

NASA-CR-192321

SAO-AXAF-DR-92-012
23 October 1992
NAS8-36123
Type 3 Document
DR#3 - Interim Rpt.

*1X 74-CR
NAS PR
152700*

(NASA-CR-192321) VETA-I X RAY TEST
ANALYSIS Interim Report
(Smithsonian Astrophysical
Observatory) 138 p

N93-26183
--THRU--
N93-26192
Unclas

G3/74 0154212

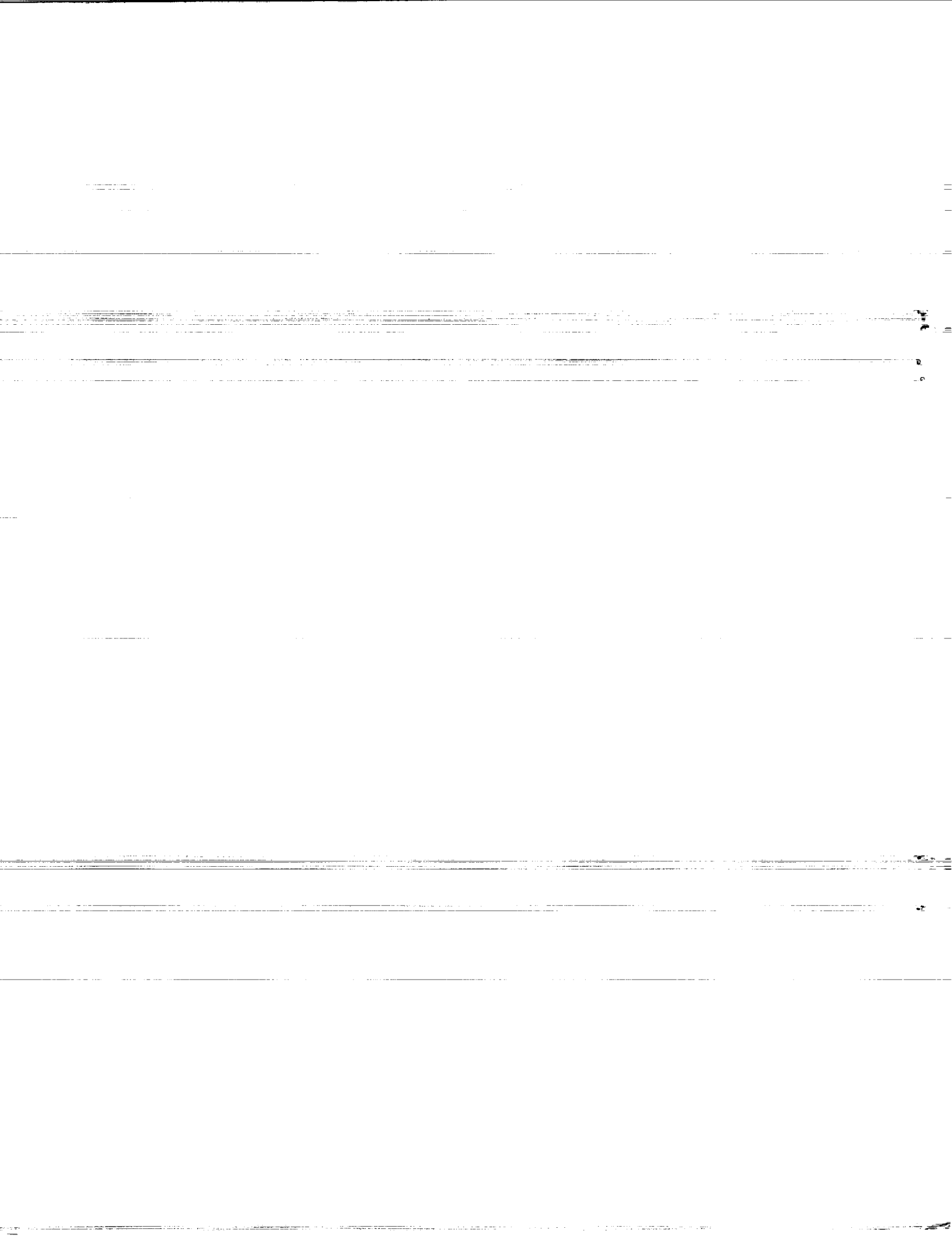
VETA-I X-RAY TEST ANALYSIS

Prepared for:

George C. Marshall Space Flight Center
National Aeronautics and Space Administration
Marshall Space Flight Center, AL 35812

Submitted by:

Smithsonian Astrophysical Observatory
60 Garden Street
Cambridge, MA 02138

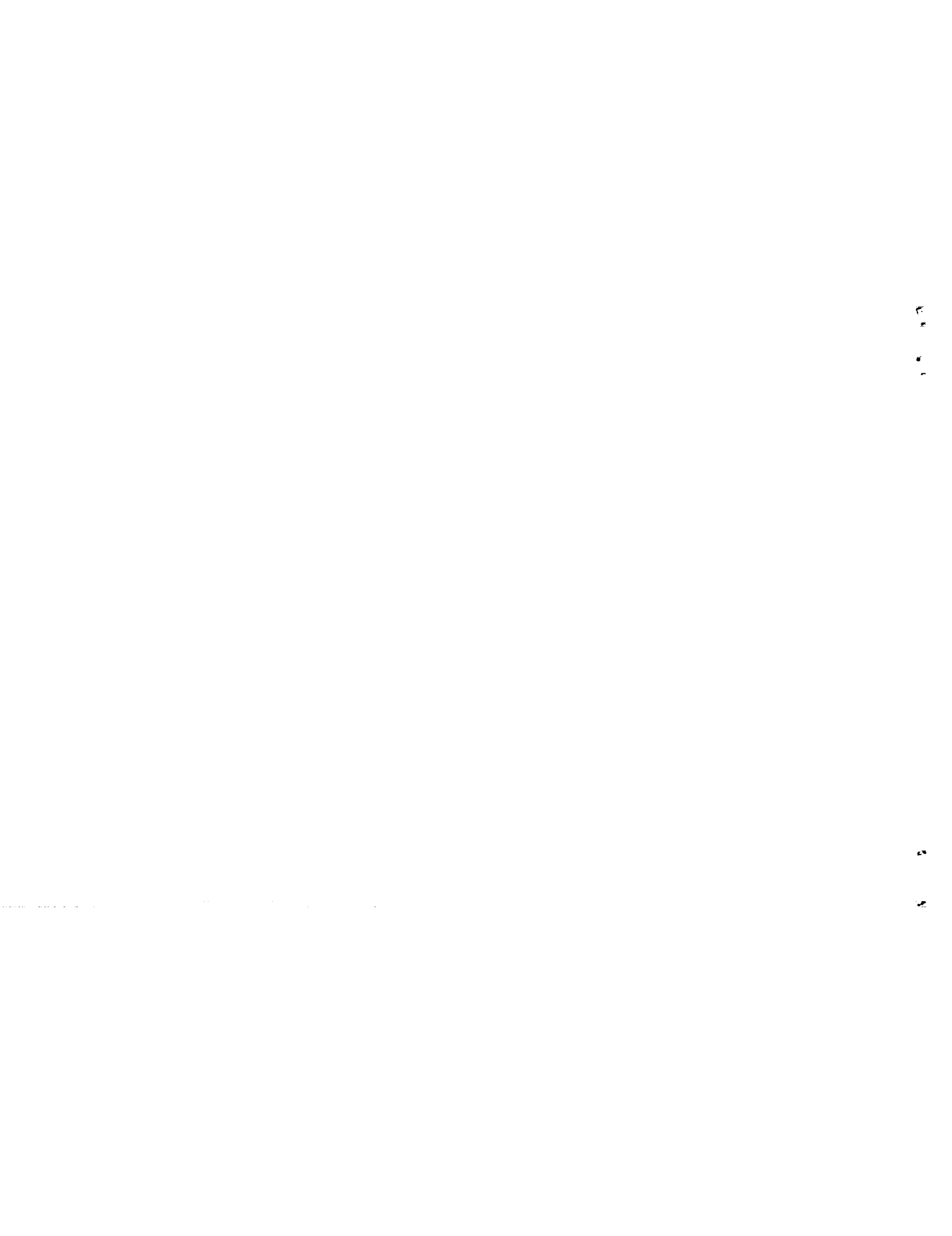


SAO-AXAF-DR-92-012
23 October 1992
NAS8-36123
Type 3 Document
DR#3 - Interim Rpt.

VETA-I X-RAY TEST ANALYSIS

Prepared for:
George C. Marshall Space Flight Center
National Aeronautics and Space Administration
Marshall Space Flight Center, AL 35812

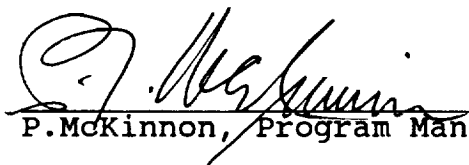
Submitted by:
Smithsonian Astrophysical Observatory
60 Garden Street
Cambridge, MA 02138



Smithsonian Astrophysical Observatory

Contract: **NAS8-36123, AXAF Mission Support**
Title: **VETA-I X-RAY TEST ANALYSIS**
Document No.: **SAO-AXAF-DR-92-012**
DR No.: **DR-3**
Data Type: **3**
Release Date: **23 October 1992**
Revision Level: **Basic Release, Rev "-"**

Approvals


P. McKinnon, Program Manager 10/23/92
Date

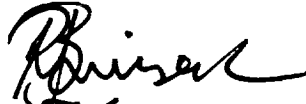
1
2
3

4
5

VETA-I X-RAY TEST ANALYSIS

An interim Report Prepared by

R.J.V. Brissenden



G. Chartas



M. D. Freeman



J.P. Hughes



E.M. Kellogg



W. A. Podgorski



D. A. Schwartz



P. Zhao



Approved by

D.A. Schwartz

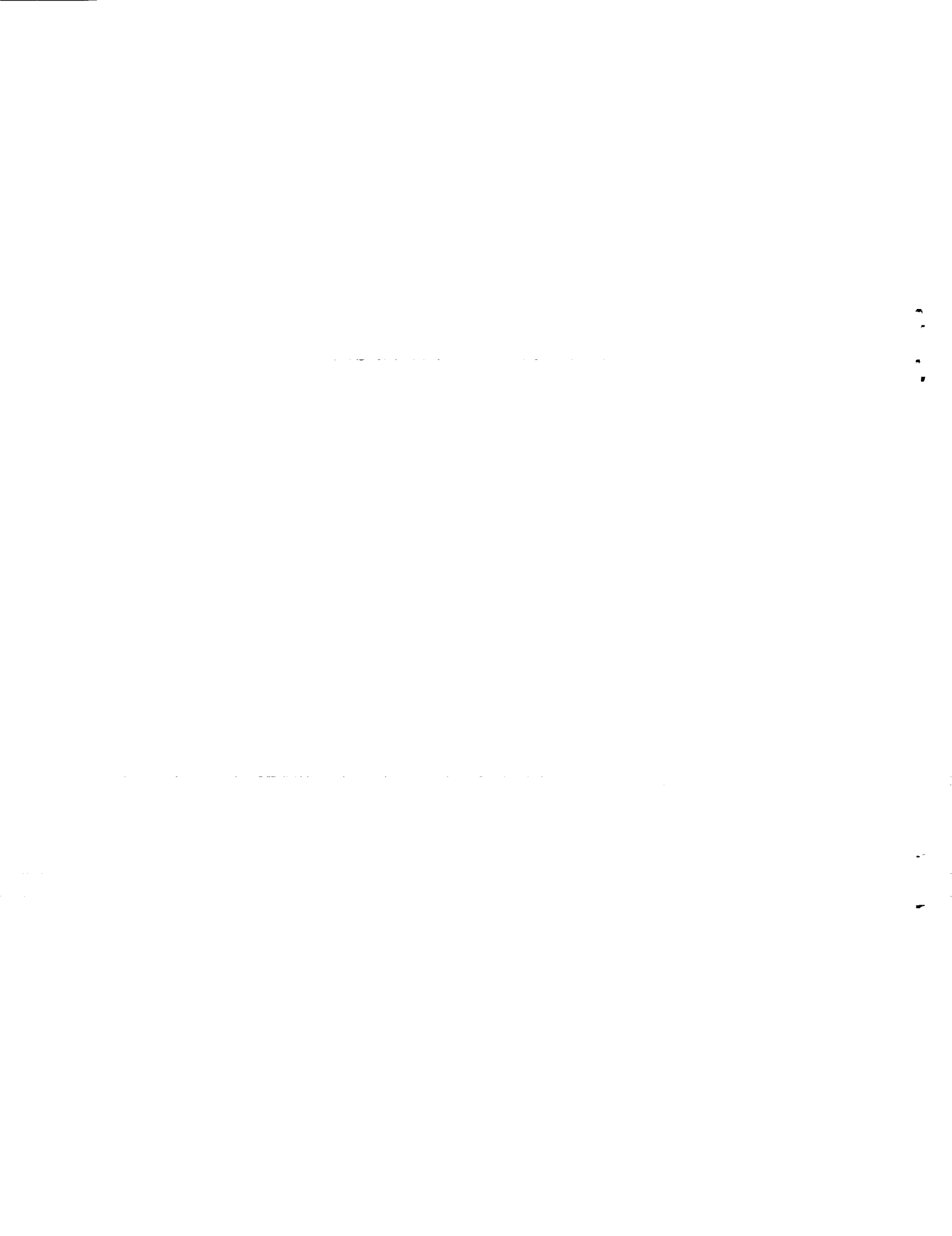


Smithsonian Astrophysical Observatory
60 Garden St.
Cambridge MA 02138



Table of Contents

- I. Foreword
- II. "Intensity Distribution of the X-Ray Source for the AXAF VETA-I Mirror Test"
- III. "VETA-I X-Ray Detection System"
- IV. "VETA X-Ray Data Acquisition and Control System"
- V. "Correcting X-Ray Spectra Obtained from the AXAF VETA-I Mirror Calibration for Pileup, Continuum, Background and Deadtime"
- VI. "AXAF VETA-I Mirror Encircled Energy Measurements and Data Reduction"
- VII. "Precision of the Calibration of the AXAF Engineering Test Article (VETA) Mirrors"
- VIII. "Image Analysis of the AXAF VETA-I Mirror"
- IX. "Surface Finish Quality of the Outer AXAF Mirror Pair Based on X-Ray Measurements of the VETA-I"
- X. "The X-Ray Reflectivity of AXAF VETA-I Optics"



FOREWORD

This interim report presents some definitive results from our analysis of the VETA-I X-ray testing data. It also provides a description of the hardware and software used in the conduct of the VETA-I X-ray test program performed at the MSFC X-ray Calibration Facility (XRCF). These test results also serve to supply data and information to include in the TRW final report required by DPD 692, DR XC04. To provide an authoritative compendium of results, we have taken nine papers as published in the SPIE Symposium, "Grazing Incidence X-ray/EUV Optics for Astronomy and Projection Lithography," vol. 1742, and have reproduced them as the content of this report.

These papers are as follows:

P.Zhao et al., "Intensity Distribution of the X-Ray Source for the AXAF VETA-I Mirror Test." This paper describes a novel pinhole camera arrangement for measuring the size and detailed intensity distribution of the X-ray generator used for the VETA-I testing.

W.A.Podgorski et al., "VETA-I X-Ray Detection System." This paper provides an overview of all the hardware provided and used by SAO to carry out the Veta-I testing.

R.J.V.Brissenden et al., "VETA X-ray Data Acquisition and Control System." This paper describes the computer system architecture and software used for the conduct of the VETA testing, and the test data archive.

G.Chartas et al., "Correcting X-ray Spectra Obtained from the AXAF VETA-I Mirror Calibration for Pileup, Continuum, Background and Deadtime." This paper describes the initial stages of the data reduction, which consist of extracting the true counting rate attributable to X-ray line photons, from the broad pulse height distribution which is measured.

P.Zhao et al., "AXAF VETA-I Mirror Encircled Energy Measurements and Data Reduction." This paper describes some of the measurements taken after the VETA testing in order to understand the precision of the pinhole motions. It also gives a detailed discussion of the correction for the effect of the transmission of the mesh supporting the proportional counter window. This correction results in our final encircled energy estimates.

D.A.Schwartz et al., "Precision of the Calibration of the AXAF Engineering Test Article (VETA) Mirrors." This paper presents an error analysis showing how well the measurements of encircled energy were made.

M.D.Freeman et al., "Image Analysis of the AXAF VETA-I Mirror." This paper presents analysis of the 2-dimensional scans of the image core with an 0.2 arcsec diameter pinhole, to unfold the facility effects and present the intrinsic mirror performance.

J.P.Hughes et al., "Surface Finish Quality of the Outer AXAF Mirror Pair Based on X-Ray Measurements of the VETA-I." This paper analyzes the results of the FWHM scans, the encircled energy measurements, and the wing-scan measurements in order to deduce the intrinsic circumferential slopes and constraints on the surface deviation amplitudes for spatial frequencies above 0.1 mm^{-1} .

E.M.Kellogg et al., "The X-ray Reflectivity of AXAF VETA-I Optics." This paper confronts our measurements of the absolute effective area with theoretical predictions for the reflectivity of Zerodur. This leads to issues on the composition of Zerodur, on extrapolation of wing-scan data to the entire focal plane, on contamination of the glass, and on the relation between synchrotron and MSFC X-Ray Calibration Facility measurements.

In addition, much other information appears in our two previous reports:

"AXAF VETA-I X-Ray Testing: Quick Look Results," SAO-AXAF-AR-91-080, 15 November 1991.

"AXAF VETA-I X-Ray Testing: Preliminary Analysis Report," SAO-AXAF-AR-92-002, 10 January 1992.

Key results:

Development of a complete data reduction and analysis system, including understanding of effects which were only revealed during the actual testing.

Performance of the data reduction and analysis for all the proportional counter pinhole data.

Development of a knowledge base of what off-line characterization is needed of the XRCF, prior to HRMA calibration. This includes pinhole images of the X-ray generator assembly (XGA), measurements of the XGA filter thicknesses, and line to continuum ratios for the different targets as a function of the full range of XGA operating voltages and currents.

Development of a computer system architecture and archive which can serve for the HRMA calibration. The lessons learned allow us the first precise definition of requirements for a Master Control Computer system for HRMA calibration.

Measurements of intrinsic P1/H1 properties, including

circumferential slope errors, model dependent constraints on correlation amplitudes at various scales, and micro-roughness amplitude vs. index of an assumed power law shape of the spatial power spectrum distribution function.

Measurements of parameters incidental to the veta-I test, and relevant to the HRMA calibration; e.g., particulate and molecular contamination of the mirrors; unfolding of mechanical distortions; needs for spatial and temporal monitoring of X-ray generator uniformity; and a data base for estimation of the time duration of HRMA testing.

Compilation of a rich set of "lessons learned" to expedite the planning and conduct of the HRMA and HRMA/SI calibration process.

Future work remains in the following areas:

An investigation of the sensitivity of the data reduction to the use of nominal VETA reflectivity vs. energy for the bremsstrahlung continuum, rather than more precise reflectivity vs. energy which might result from analysis of synchrotron measurements, or by simply iterating the present best fit to effective area.

Study results of the sealed BND vs. the flow BND, to assess possible spatial non-uniformity of the X-ray beam from the top vs. the bottom of the VETA aperture.

Re-investigate detailed effects of dust scattering, considering the recent information on the distribution of cerium oxide particles on the mirror surface, and incorporate into the overall VETA model of surface roughness.

Update the VETA model with a raytrace using a higher resolution interface to represent the mechanical displacements, to include distortions of flexures. This model must also include effects of the adhesives. We are also awaiting data which we have requested on the thermal gradients during the VETA testing, and the Kodak models of the ensuing thermal distortions.

Quantitative confrontation of the ring focus data to such updated VETA models. Assess the general utility of ring focus testing for the HRMA calibration. Explain the origin of the apparent multiple ring structure.

Reassess what models of the P1/H1 surface deviations are consistent with both the X-ray data, and the final metrology data, when the latter becomes available.

Assess the degree of consistency, and identify any inconsistencies, between the X-ray data and the final P1/H1 optical metrology.

Provide the ASC with the archival VETA test data base.

Provide the ASC with the models and tools used to analyze the VETA-I test data.

Assessment of the errors in measuring absolute effective area. Utilize the error estimates from the VETA test to produce error budget predictions for the HRMA calibration.

Assess a quantitative limit to the amount of hydrocarbon on the surface of the actual VETA-I.

The above work, and other effects which may be revealed as significant in our further processing, will be reported in internal SAO memos, as studies relative to our monitoring of the HRMA contractor, and as reports of our Calibration Task Team activities.

Conclusion:

The VETA-I X-ray test program was a spectacular success. The primary objective, that of measuring the intrinsic FWHM of the P1/H1 was <0.5 arcsec, was achieved, despite the initial mechanical test configuration for which the raw data showed a larger FWHM. Secondary objectives of assessing how well a mirror could be calibrated clearly establish that measurements of the HRMA can be made in the regime of 1%, and give much detailed information on equipment and procedures to accomplish this. Development of a prototype tool to estimate test time has already led to a confident scheduling of the HRMA and HRMA/SI XRCF calibration timeline. Many of the software analysis tools, the software architecture, and the data abase archiving formats, will be directly applicable to the ASC tasks for oversight of AXAF calibration.

Intensity Distribution of the X-Ray Source for the AXAF VETA-I Mirror Test

Ping Zhao, Edwin M. Kellogg, Daniel A. Schwartz, and Yibo Shao

Harvard-Smithsonian Center for Astrophysics
60 Garden Street, Cambridge, MA 02138

M. Ann Fulton

ES-65, Marshall Space Flight Center, AL 35812

ABSTRACT

The X-ray generator for the AXAF VETA-I mirror test is an electron impact X-ray source with various anode materials. The source sizes of different anodes and their intensity distributions were measured with a pinhole camera before the VETA-I test. The pinhole camera consists of a 30 μm diameter pinhole for imaging the source and a Microchannel Plate Imaging Detector with 25 μm FWHM spatial resolution for detecting and recording the image. The camera has a magnification factor of 8.79, which enables measuring the detailed spatial structure of the source. The spot size, the intensity distribution, and the flux level of each source were measured with different operating parameters.

During the VETA-I test, microscope pictures were taken for each used anode immediately after it was brought out of the source chamber. The source sizes and the intensity distribution structures are clearly shown in the pictures. They are compared and agree with the results from the pinhole camera measurements.

This paper presents the results of the above measurements. The results show that under operating conditions characteristic of the VETA-I test, all the source sizes have a FWHM of less than 0.45 mm. For a source of this size at 528 meters away, the angular size to VETA is less than 0.17 arcsec which is small compared to the on ground VETA angular resolution (0.5 arcsec, required and 0.22 arcsec, measured). Even so, the results show the intensity distributions of the sources have complicated structures. These results were crucial for the VETA data analysis and for obtaining the on ground and predicted in orbit VETA Point Response Function.

1. INTRODUCTION

The Advanced X-ray Astrophysical Facility (AXAF) is NASA's third Great Space Observatory, scheduled to be launched in the late 1990s.¹ The main element of AXAF is its X-ray telescope which consists of four nested Wolter Type-I mirror pairs. The Verification Engineering Test Article-I (VETA-I), made of Zerodur with a diameter of 1.2 meters, is the uncoated outmost pair.² Its mirror figures and surface quality were measured using an electron impact X-ray source at the X-ray Calibration Facility (XRCF) of the Marshall Space Flight Center (MSFC) from August to October of 1991. X-rays generated in the source chamber traveled 528 meters inside a X-ray Guide Tube before reaching the VETA, and were then focused in the focal plane 10 meters behind the VETA. Four types of measurement were made as listed below with their required precisions:

- Full Width Half Maximum (FWHM, expected less than 0.5 arcsec). ± 0.05 arcsec.
- Encircled Energy. $\pm 2\%$.
- Effective Area. $\pm 5\%$.
- Ring Focus.

Ideally, a point source with a pure monochromatic line for each energy should be used. But the pure

monochromatic X-ray source does not exist and it is also impossible to construct a point source within a finite distance. Therefore we had to measure the X-ray source spatial and spectral distribution as they were generated in the source chamber. This paper deals with the source spatial distribution. The spectral distribution is discussed elsewhere in this Volume.³

The source size and intensity distribution measurement was made at XRCF in June of 1991. The following sections discuss the techniques we used for the measurement, the method we used to analyze the data, and the results. Section 2 briefly describes the X-ray generator of XRCF used for the VETA test. Section 3 explains the pinhole camera setup and the measurement. Section 4 shows the images taken by the pinhole camera and discuss the data analysis process. Section 5 presents the source anode pictures taken during the VETA-I test. Section 6 gives the final results.

2. VETA-I X-RAY GENERATOR

The X-ray Generator Assembly (XGA) at XRCF is housed in the source chamber building and interfaces to the Guide Tube through a 6 inch vacuum gate valve. The other end of the 500 meter Guide Tube is connected with the giant VETA test vacuum chamber in the control building. Figure 1 is a schematic diagram of the XGA. From right to left there are: An alignment telescope port connected to the end of the Guide Tube; then there are bellows and the 6 inch Gate valve. Next to it is the source/filterwheel chamber which houses the filter wheel holding up to nine X-ray filters of different material. Rotating a big feedthrough nob on the top of the chamber enables us to change the filters with in two seconds and without breaking the vacuum. At the end there is the X-ray Generator Head, which houses the X-ray source that produces X-rays by electron bombardment of various anode materials. There is (not shown in the figure) a 2.75 inch gate valve and bellows in between the filterwheel chamber and the Generator Head. The whole XGA is mounted on a Newport optical table. Figure 2 is a simplified view of the X-ray source, which basically consists of a tungsten filament cathode and a target anode made of various materials. Each anode has a conical shape surface with an angle of 30 degrees from horizontal and 10.7 mm diameter at the bottom. The

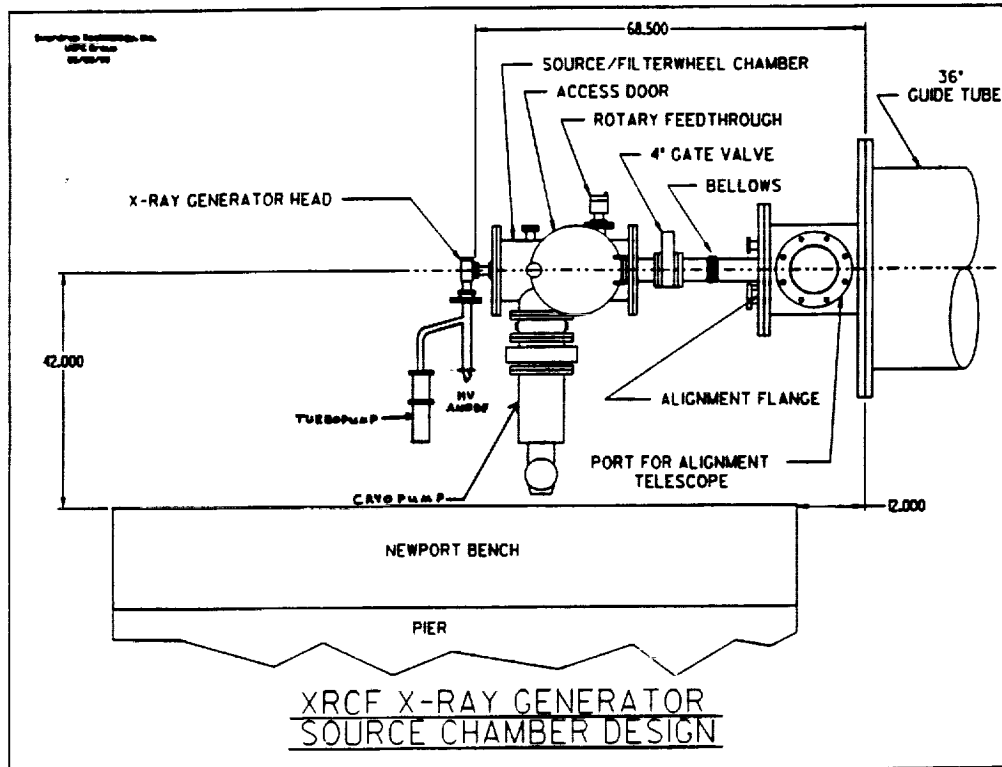


Figure 1: XRCF X-ray Generator Assembly.

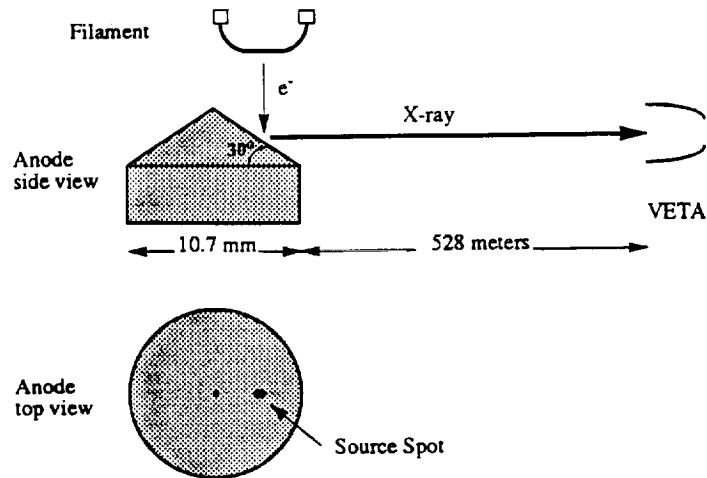


Figure 2: XRCF X-ray Source for the VETA Test.

electron beam, emitted from a heated 0.9 mm diameter tungsten filament located 10 mm above the anode, is accelerated and focused (with a bias focus cap) to a small spot on the target anode. The X-rays produced as a result of the electron - target interaction are projected through a X-ray filter then down the Guide Tube to the experiment. The X-ray source size is limited by the dimensions of the electron impact area rather than by an aperture. The output of the X-ray source is principally characteristic of K and L lines from the anode material superimposed on a bremsstrahlung continuum. The X-ray energy and flux may therefore be controlled by proper selection of target material and electron beam energy, which is controlled by the anode voltage. Proper selected filters are used to suppress the bremsstrahlung continuum and low energy photons. Generally, filters are made of the same material as the target since the characteristic emission energy of an element is slightly below the absorption edge energy. A pure element is therefore "transparent" to its own emission lines. Filter thicknesses were generally chosen to attenuate the X-ray beam by a factor of 2 to 5 at the wavelength of interest. Five anode targets (aluminum, carbon, copper, molybdenum and zirconium) were used for the VETA-I test. Their characteristic X-ray lines with mean line energy, operating anode voltages and corresponding filter thicknesses are listed in column 1 through 4 of Table 1.

3. X-RAY SOURCE SIZE MEASUREMENT

Understanding that the knowledge of the source size is crucial to the VETA test and the subsequent data analysis, a pinhole camera measurement of the source size was planned and carried out between June 18 and 20, at the XRCF. Figure 3 is a schematic diagram of the measurement setup. It is the same setup as shown in Figure 1, except instead of the Guide Tube a High Resolution Imager (HRI) is connected to the 6 inch gate valve and, instead of the filterwheel, a filter/pinhole holder is inserted near the X-ray Generator Head. The X-ray Generator Head is the actual one later used for the VETA test. The pinhole is a laser drilled 30 μm diameter circular hole on a 12.5 μm thick gold foil. The HRI is a microchannel plate detector with an area of 26.4 x 26.4 mm^2 and 25 μm FWHM resolution.⁴ Its axis is tilted 2 degree from the X-ray pipe axis to increase the sensitivity. The distances are 170.7 mm between the source and the pinhole and 1500.9 mm between the pinhole and the HRI. This configuration gives a magnification factor 8.79. Therefore this pinhole camera has a 2.8 μm resolution for the source spots, which enables measuring the detailed spatial structures of the source. Keep in mind that 0.5 arcsec for VETA is 1.28 mm at the source. We will use this as a scale in the following figures and tables. Source spot from six anodes were measured with this pinhole camera. Table 1 lists representative measurements that have a good electron beam focus and source spot. From columns 5 to 10, there listed filters, anode voltage, emission current, integration time, HRI counts, and filename for each run. Please note that copper anode was not measured but later used for the VETA test, while magnesium and silicon anodes were measured but not used for VETA test. Because most of the

Table 1. X-ray Sources for the VETA and Pinhole Test

X-ray Line	Energy keV	VETA Test		Pinhole Test					
		Filter μm	V kV	Filter μm	V kV	I mA	T sec	HRI cnts	File
Al-K	1.488	Al 10.0	8.0	None	8.00	0.18	30	7045	a.3.1
				None	8.01	0.106	90	13737	t.20
				Al 25.4	8.06	2.01	45	6124	t.23
C-K	0.277	Poly 2.0	4.0	None	2.10	0.17	300	9450	c.2.1
				None	5.03	0.40	30	6196	c.3.3
				Poly 12.7	5.02	2.01	30	6118	c.4.1
Cu-L	0.932	Cu 0.5	7.0						
Mo-L	2.334	Mo 2.0	17.0	None	7.00	0.50	15	4233	m.3.5
				None	8.00	0.10	60	5803	m.2.3
				Ag 2.0	9.02	0.50	20	4765	m.4.4
Zr-L	2.067	Zr 2.08	12.0	None	9.00	0.15	30	5507	z.3.2
				Ag 2.0	9.04	0.60	30	4809	z.4.2
				Ag 2.0	10.05	0.75	30	9113	z.4.3
Mg-K	1.254			None	6.00	0.50	30	7785	mg.3.1
				Al 25.4	8.02	4.01	30	3377	mg.4.1
Si-K	1.741			None	5.06	0.10	400	5497	s.2.2
				None	7.08	0.50	45	5763	s.3.2
				None	7.00	0.75	30	3993	s.4.3

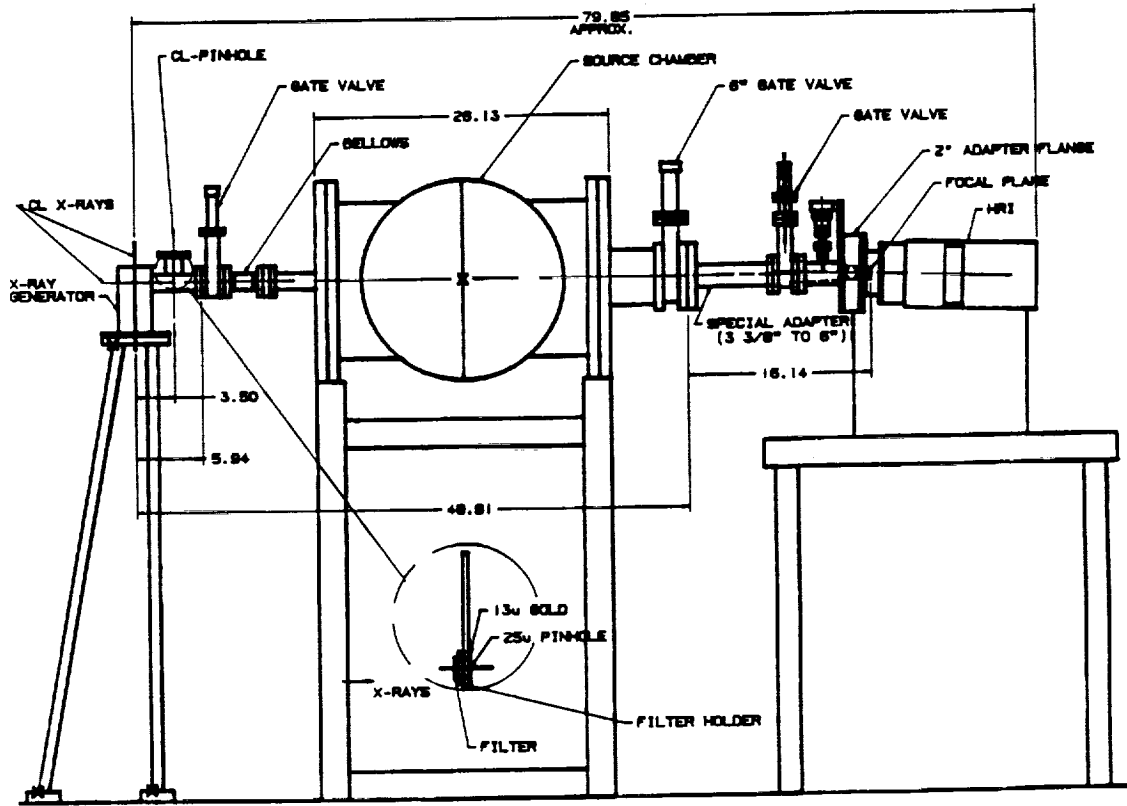


Figure 3: XRCF X-ray Source Size Measurement Setup.

VETA test X-ray filters were not available at that time, all of the low flux runs used no filters, and the high flux runs used filters not exactly matching the ones later used in the VETA test. This should not affect the source size because the filters were only used to suppress the continuum which is much weaker than the lines. The X-ray generator operating conditions (viz., emission current and bias voltage) were selected to be representative of those later used during the VETA-I test. The integration time was chosen to have at least 3000 HRI counts.

4. X-RAY SOURCE IMAGES AND DATA ANALYSIS

The recorded HRI data were stored on floppy diskettes and then transferred to our Sun Work Station. The data were analyzed and displayed with IRAF/PROS (Image Reduction and Analysis Facility / Post-Reduction Off-line Software) software system. We did deconvolution of the image by using Lucy's technique,⁵ considering a tophat function as the Point Spread Function (PSF) of the 30 μm pinhole. Because the size of the pinhole PSF on the HRI (0.294 mm) is much smaller than that of the source image (see Figure 4), deconvolution of the image can hardly make any difference. Therefore we chose not to spend the time for image deconvolution. All the figures shown in this paper are from the original data.

Figure 4 shows one of the X-ray source images from an aluminum target. Figure 4(a) is a contour plot of the image with contour levels equal to 2, 10, 20, 35, 50, 65, 80, 90, 100 percent of the peak intensity. The X and Y axes are the horizontal and vertical directions of the source spot, respectively. Figure 4(b) is a 3D plot of the same image with $1 \times 1 \text{ mm}^2$ area in the X-Y plane and intensity in the Z direction. The little circle in Figure 4(a) indicates the size of the 30 μm pinhole Point Spread Function on the HRI. It is much smaller than the source image size. Therefore the deconvolution process was not necessary. Figures 5 through 9 show the same kinds of plots for carbon, molybdenum, zirconium, magnesium, and silicon targets,

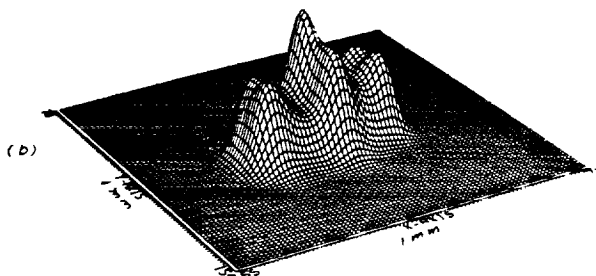
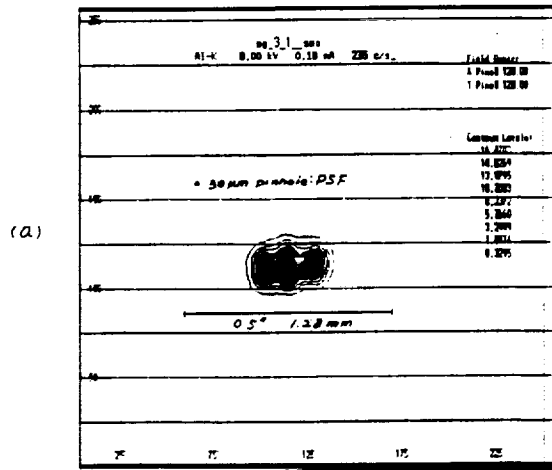


Figure 4: Aluminum Source Image.

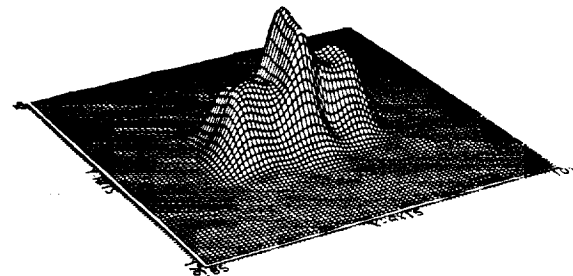
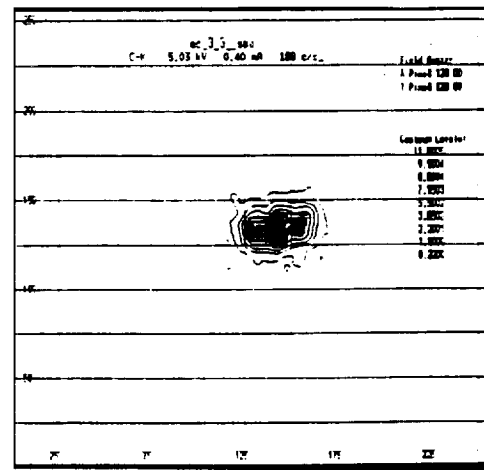


Figure 5: Carbon Source Image.

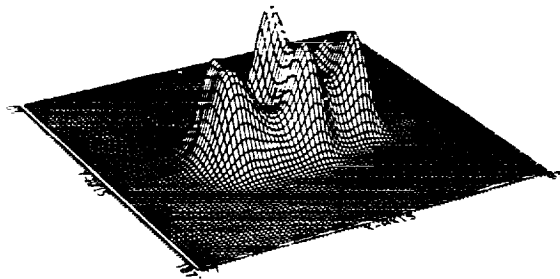
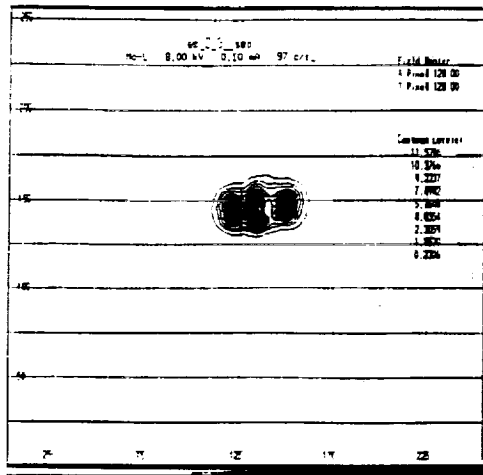


Figure 6: Molybdenum Source Image.

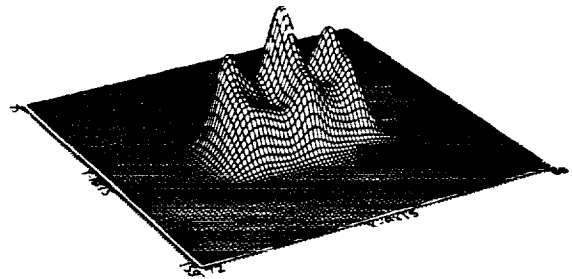
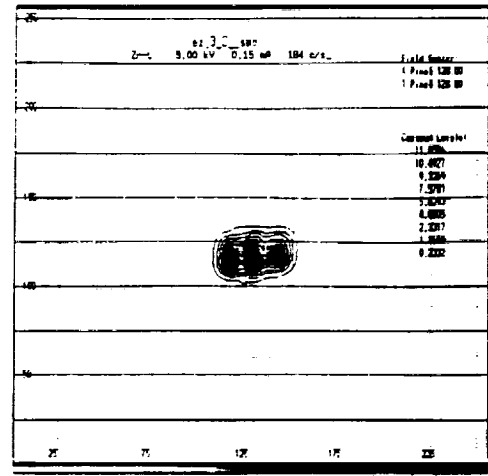


Figure 7: Zirconium Source Image.

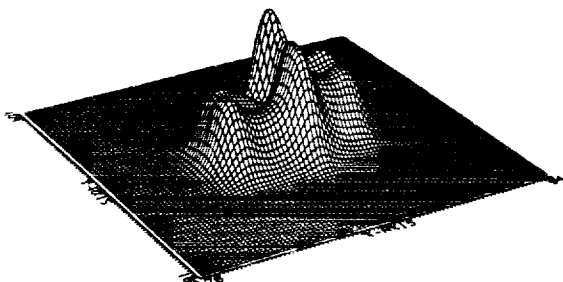
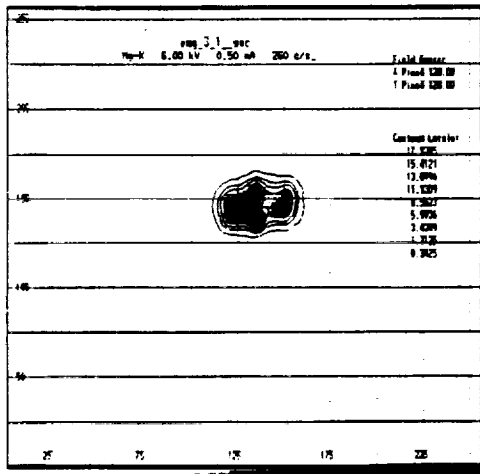


Figure 8: Magnesium Source Image.

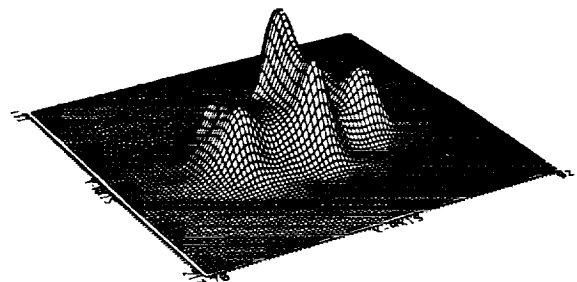
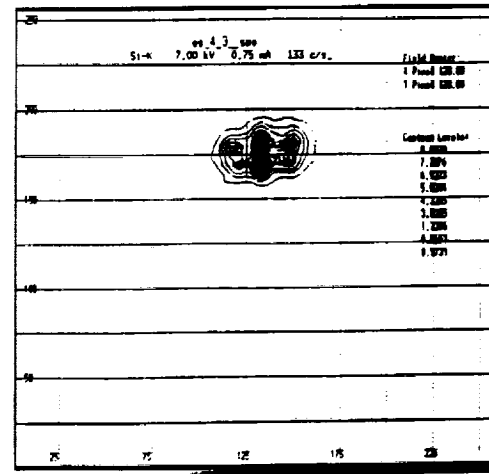


Figure 9: Silicon Source Image.

respectively. It is seen that all the images are about the same size and have similar structures. Generally speaking, the source spots are much smaller than 1.28 mm or 0.5 arcsec and a little narrower in the vertical direction (Facility Z-axis) than the horizontal direction (Facility Y-axis). A distinctive feature for all the images is that there are three intensity stripes along the vertical direction, which can also be seen in the anode pictures in the next section. This is probably due to the surface fine structure of the source filament. Figure 10 shows four microscope pictures of the filament, with magnification factors 35, 339, 1340 and 2820, respectively. There are many fine stripes along the filament. Because the electrons are most likely being

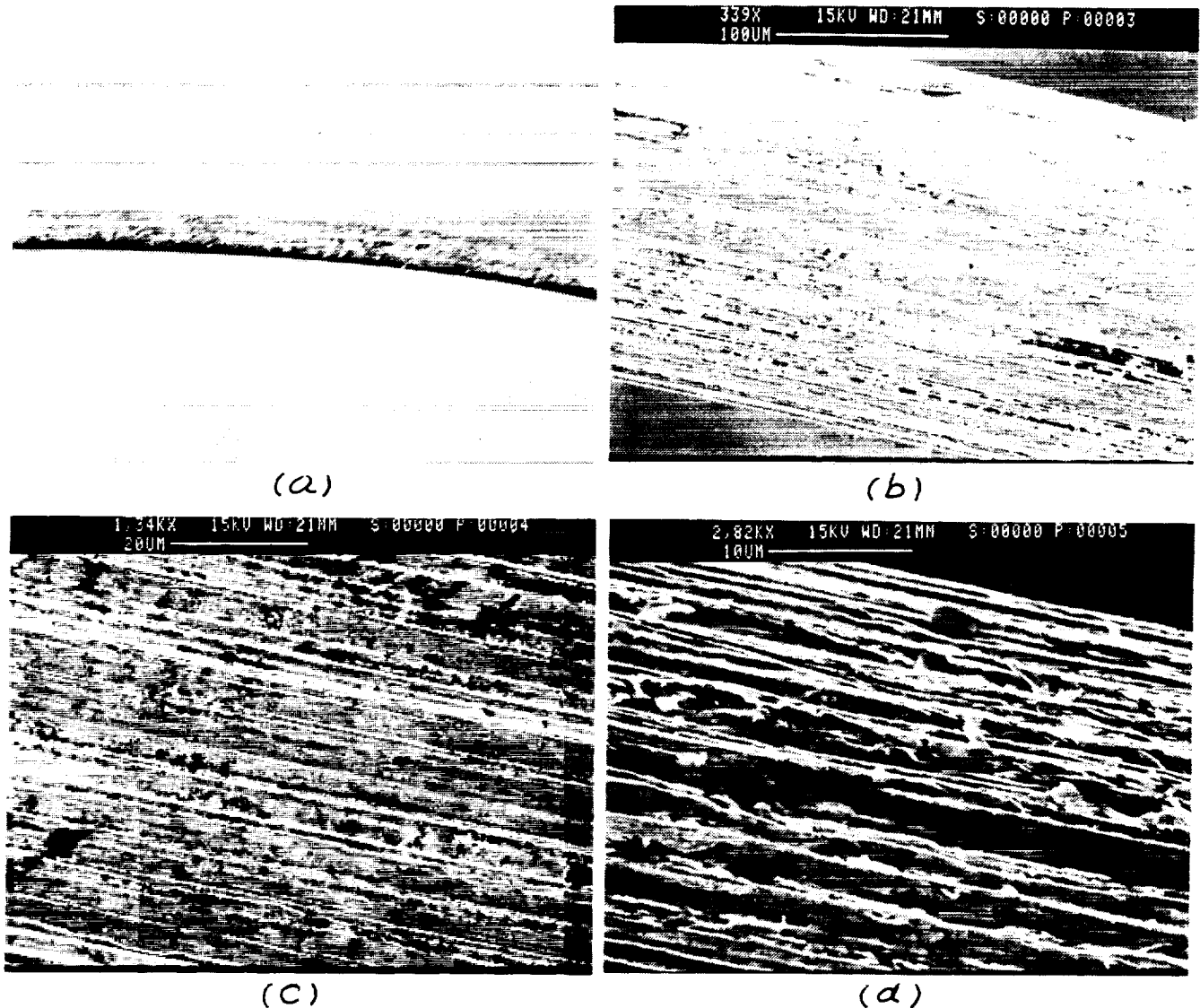


Figure 10: X-ray Source Filament Pictures. Magnification factors are (a) 35, (b) 339, (c) 1340 and (d) 2820. There are many fine stripes along the filament, which caused the three intensity peaks in the source.

emitted at the peak of the stripes and the filament is aligned in the X-ray direction, electron beams hit the anode target in this striped pattern. From the VETA point of view, the stripes are in the vertical direction, which agrees with the images recorded.

Figures 11 through 16 are the image profiles projected onto Y and Z axes. The image features mentioned above are clearly shown in these projection profiles. Since these are not Gaussian or any other type of regular profiles, we give six parameters to characterize the source size. They are the RMS, FWHM, and Full Width

Al-K (1.488 keV) Source Image Projection File: ea_3_1.t

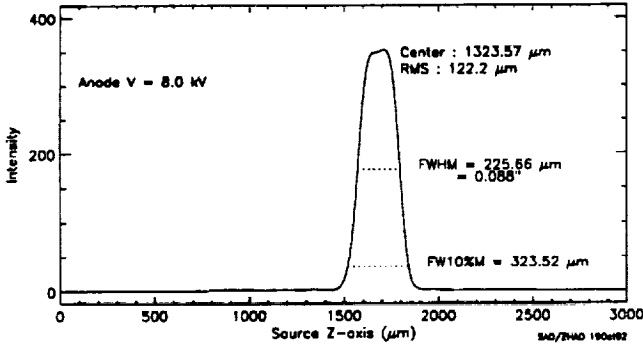
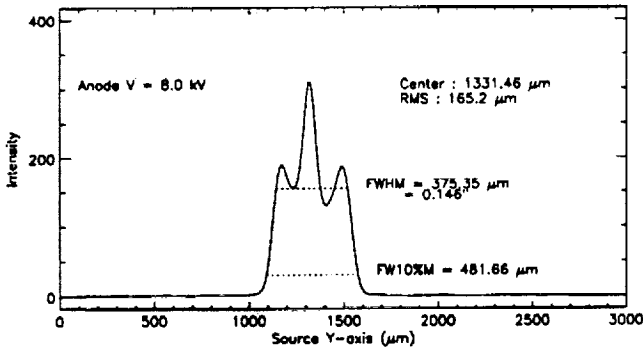


Figure 11: Aluminum Source Image Projection Profile.

C-K (0.277 keV) Source Image Projection File: ec_3_3.t

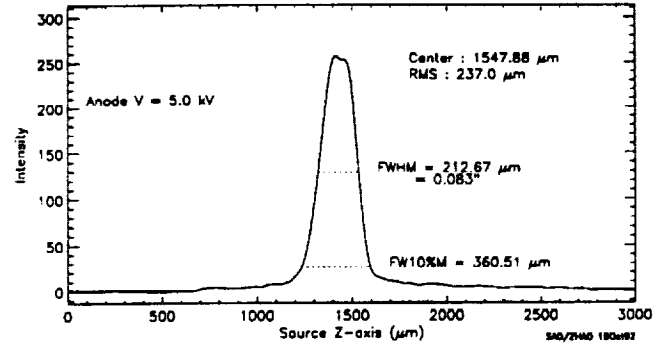
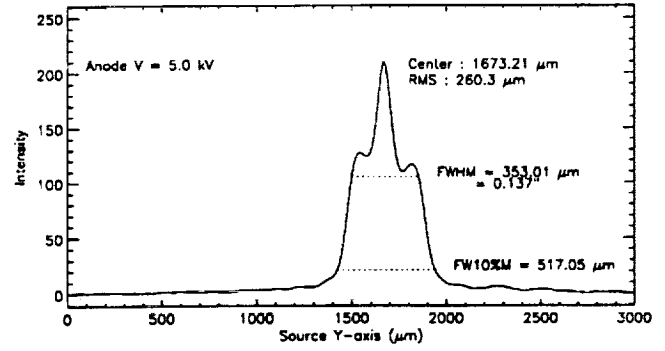
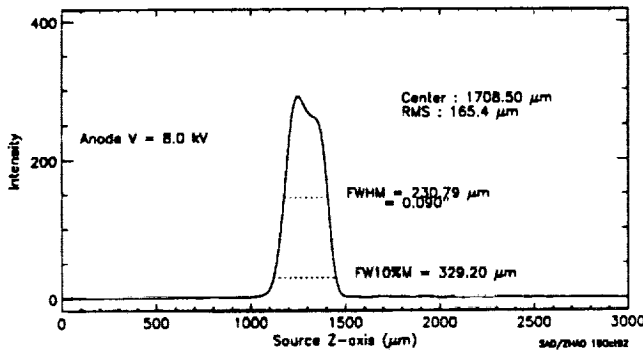
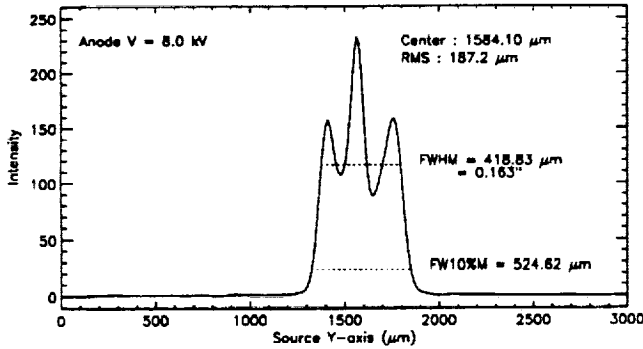


Figure 12: Carbon Source Image Projection Profile.

Mo-L (2.29 keV, 2.39 keV) Source Image Projection File: em_2_3.t



Mo-L (2.29 keV, 2.39 keV) Source Image Projection File: em_4_4.t

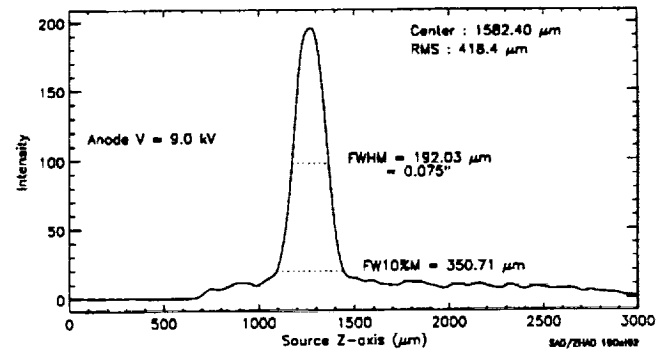
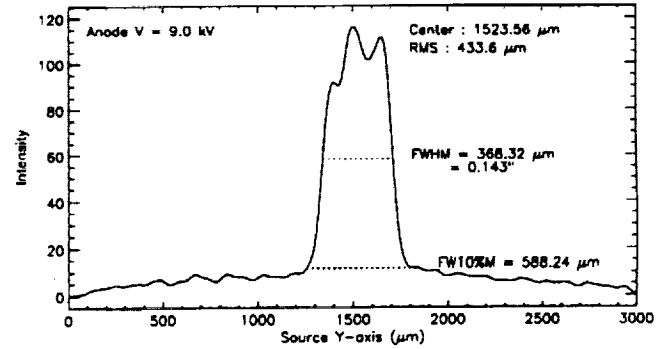
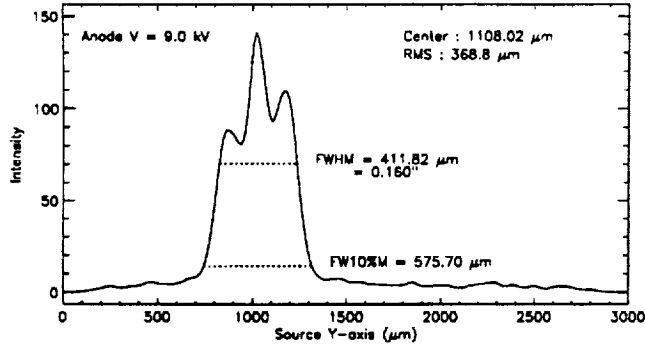


Figure 13: Molybdenum Source Image Projection Profile.

Zr-L (2.04 keV, 2.12 keV) Source Image Projection File: ez_4_2.t



Zr-L (2.04 keV, 2.12 keV) Source Image Projection File: ez_4_3.t

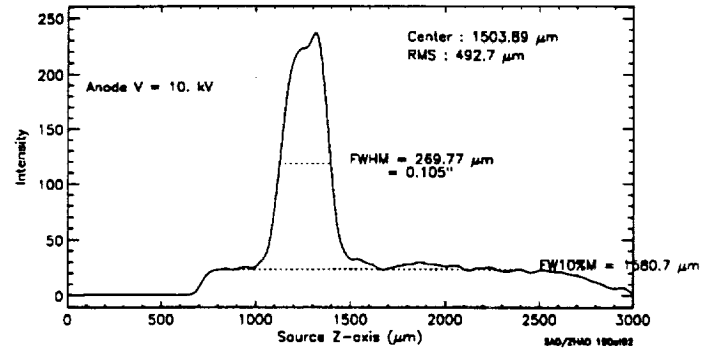
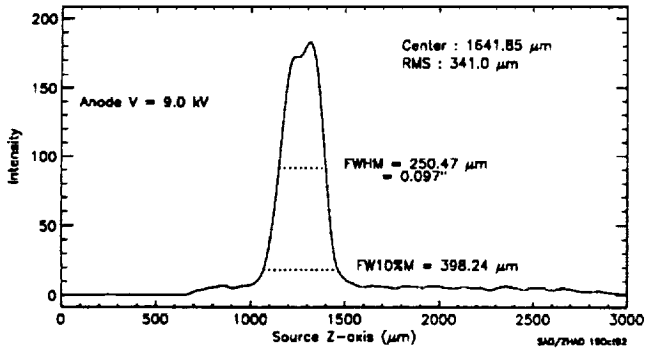
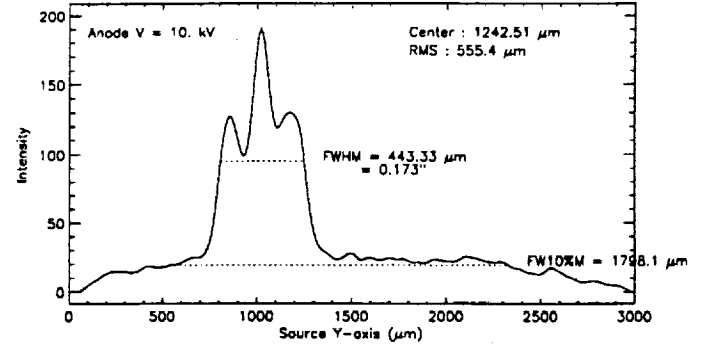
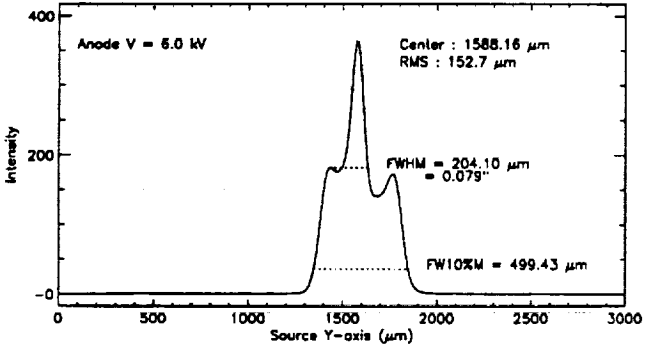


Figure 14: Zirconium Source Image Projection Profile.

Mg-K (1.254 keV) Source Image Projection File: emg_3_1.t



Si-K (1.741 keV) Source Image Projection File: es_4_3.t

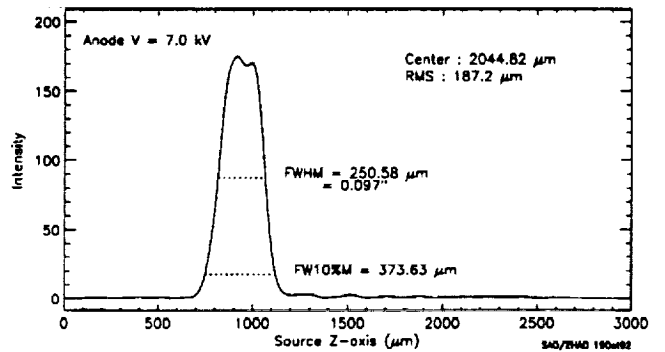
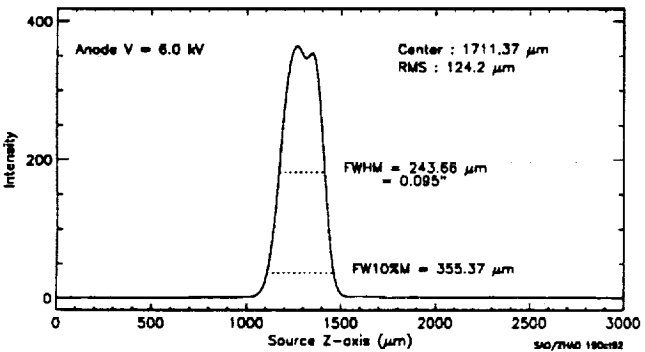
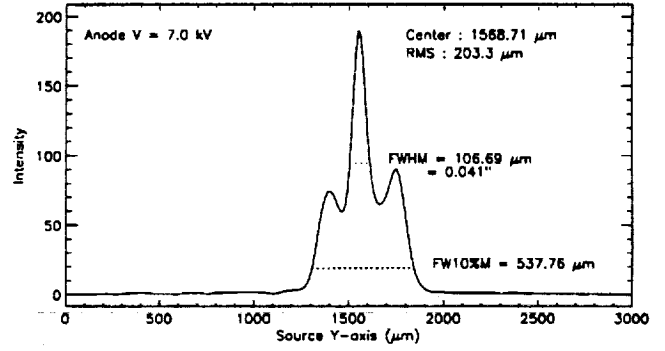


Figure 15: Magnesium Source Image Projection Profile.

Figure 16: Silicon Source Image Projection Profile.

10% Maximum (FW10%M) in Y and Z directions. For all the images, the FWHM is less than 0.45 mm or 0.35 mm in horizontal or vertical directions, respectively. For aluminum and carbon targets, the pinhole test results here give the actual source intensity distribution for the VETA test since the operating conditions are the same for both tests. For molybdenum and zirconium targets, the anode voltage was set higher during the VETA test in order to achieve desired beam flux. Especially for molybdenum, the anode voltage for VETA test is 17 kV but the highest voltage used for the pinhole test is only 9 kV. This is mainly because the source molybdenum filter used for the VETA test was labeled incorrectly. A two micron molybdenum filter was requested but the actual thickness of the filter was 5.25 micron, found in the spectrum analysis after the VETA test.³ This difference reduced the Mo-L line beam flux by a factor of 9. Without knowing that the thicker filter was used during the VETA test, the anode voltage was increased to obtain an adequate flux level. Therefore the pinhole test results do not reflect the real intensity distribution of the molybdenum and zirconium source during the VETA test. However, we still can use the pinhole test results to make an estimate. As we can see in Figure 13 and 14, a certain amount of halo appears around the source intensity peak when the anode voltage is increased, but the peak width and shape stayed about the same. We will show in the next section that this was true even for the VETA operating voltage.

5. X-RAY SOURCE ANODE PICTURES

During the VETA test, three microscope pictures, with magnification x7, x12.5 and x35, were taken for each used anode immediately after it was brought out from the X-ray Generator Head. Figure 17 shows the x7 and x35 pictures for the aluminum anode. Figures 18 through 21 shows the same pictures for the other four anodes used for the VETA test. These pictures were taken directly above the anode - a view angle 90 degrees from the VETA. The spots where electron beam hit the target and the X-rays were generated clearly match the source images taken by the pinhole camera, especially the three intensity stripes. The spot sizes from the pictures agree with the pinhole test results (Because the anode surface is 30 degrees from the horizontal, the source size in the vertical direction is the length of the spot in the picture divided by $\sqrt{3}$). However, the copper anode picture, which was not measured in the pinhole test, shows a different and bigger

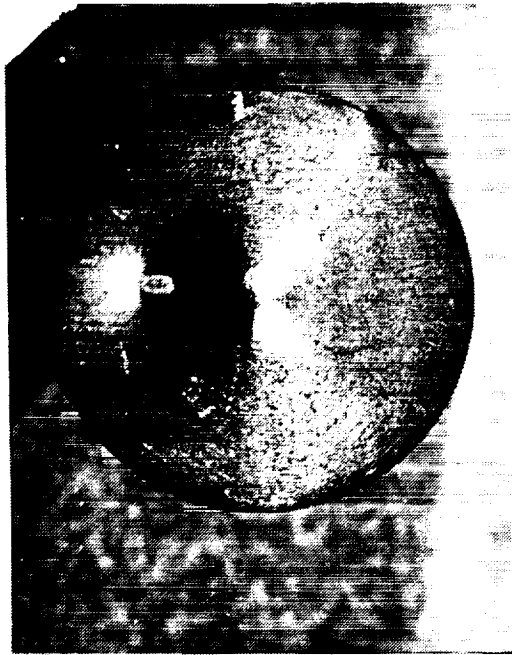


7X Aluminum Anode



35X Aluminum Anode

Figure 17: Aluminum Source Anode Pictures. x7 (left), x35 (right). Actual anode size: 10.7 mm diameter.

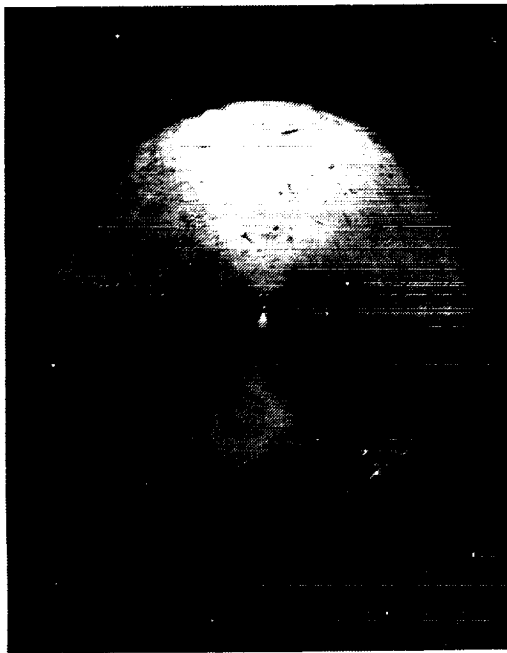


7X Carbon Anode

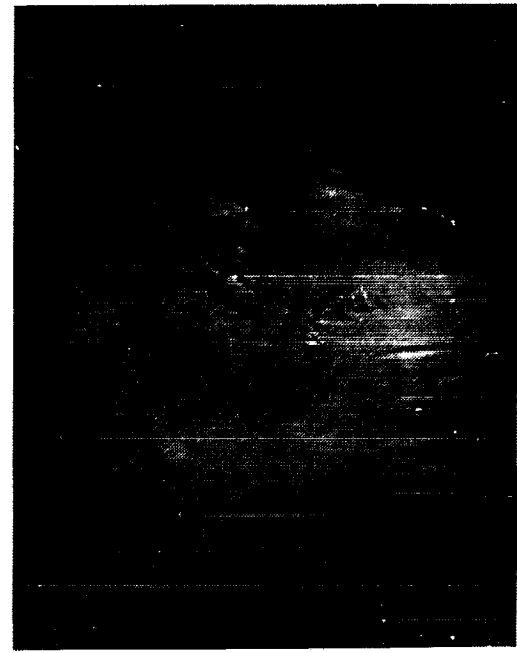


35X Carbon Anode

Figure 18: Carbon Source Anode Pictures. $\times 7$ (left), $\times 35$ (right). Actual anode size: 10.7 mm diameter.

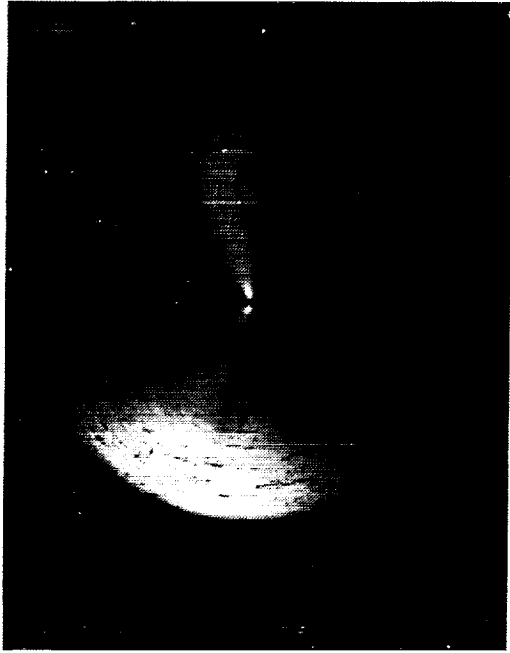


7X Copper Anode

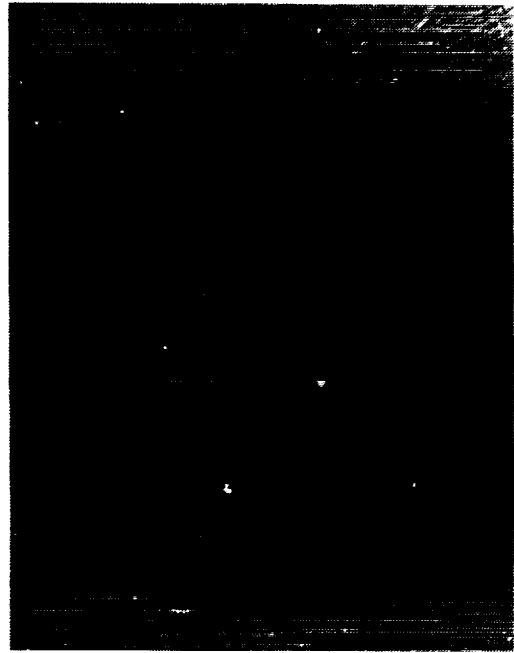


35X Copper Anode

Figure 19: Copper Source Anode Pictures. $\times 7$ (left), $\times 35$ (right). Actual anode size: 10.7 mm diameter.

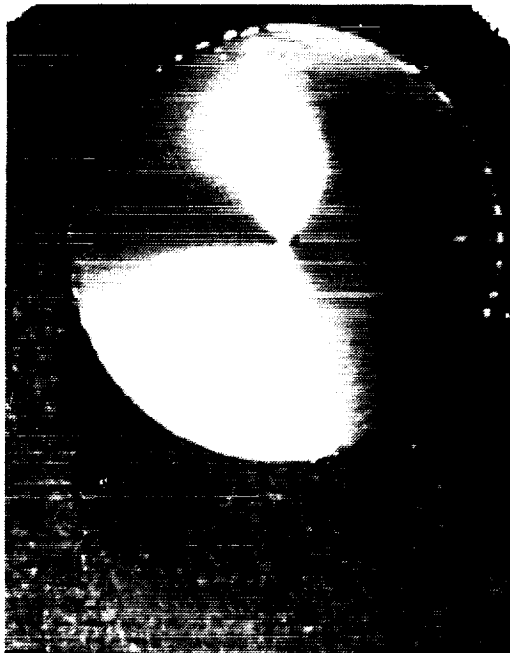


7X Molybdenum Anode



35X Molybdenum Anode

Figure 20: Molybdenum Source Anode Pictures. $\times 7$ (left), $\times 35$ (right). Actual anode size: 10.7 mm diameter.



7X Zirconium Anode



35X Zirconium Anode

Figure 21: Zirconium Source Anode Pictures. $\times 7$ (left), $\times 35$ (right). Actual anode size: 10.7 mm diameter.

Table 2. X-ray Source Intensity Distribution Measurement Results

X-ray Line	Energy keV	Anode V kV	Width in	RMS		FWHM		FW10%M	
				mm	arcsec	mm	arcsec	mm	arcsec
Al-K	1.488	8.0	Y	.165	0.065	.375	0.147	.481	0.188
			Z	.122	0.048	.225	0.088	.323	0.126
C-K	0.277	5.0	Y	.260	0.102	.353	0.138	.517	0.202
			Z	.237	0.093	.212	0.083	.360	0.141
Cu-L ^a	0.932	7.0	Y	.23	0.09	.52	0.20	.66	0.26
			Z	.14	0.06	.25	0.10	.36	0.14
Mo-L	2.334	9.0 ^b	Y	.433	0.169	.368	0.144	.588	0.230
			Z	.418	0.163	.192	0.075	.350	0.137
Zr-L	2.067	10.0 ^b	Y	.555	0.217	.443	0.173	.1798	0.702
			Z	.492	0.192	.269	0.105	.1580	0.618
Mg-K	1.254	6.0	Y	.152	0.060	.204	0.080	.499	0.195
			Z	.124	0.049	.243	0.095	.355	0.139
Si-K	1.741	7.0	Y	.198	0.077	.397	0.155	.515	0.201
			Z	.177	0.069	.234	0.091	.342	0.134

^a Width estimated from anode photo.

^b Below the VETA operating voltage.

spot. We only made a rough estimate of its size based on our understanding of other anode pictures.

6. RESULTS AND DISCUSSIONS

Table 2 lists the final results of the X-ray source intensity distribution measurements. For each source size, it lists RMS, FWHM and FW10%M in both horizontal (Y) and vertical (Z) directions. For all the targets, the source sizes were smaller than the measured VETA FWHM. For the aluminum and carbon sources, of which we used to measure the FWHM of the VETA, the measurements were done under the same operating conditions as the VETA test. For molybdenum and zirconium sources, the measurements were done at a lower anode voltage than the VETA test. Combining the results of the pinhole test and the anode pictures, we conclude these two source sizes should still be the same even though there are more halos around the peaks. The copper source, of which we didn't make pinhole measurement, has a bigger size based on the anode picture. An accurate measurement of the VETA encircled energy and effective area was made only with the aluminum, carbon and zirconium sources.^{6,7} The results of this X-ray source measurement were used to analyze the VETA data, to deconvolve the point spread function, to characterize the mirror surface figure and to predict its in orbit performances.^{8,9}

7. ACKNOWLEDGEMENTS

We would like to thank Adrian Roy and Martin Zombeck for the pinhole camera testing and data taking. We also thank David Watson for operating the source and providing useful information about the XRCF X-ray Generator. This work was supported under NASA contract # NAS8-36123.

8. REFERENCES

1. M. C. Weisskopf, "The Advanced Astrophysics Facility: An Overview," *Astrophysical Letters & Communications*, Vol. 26, pp. 1-6, 1987.
2. E. M. Kellogg, R. J. V. Brissenden, K. A. Flanagan, M. D. Freeman, J. P. Hughes, M. T. Jones,

M. Ljungberg, P. Mckinnon, W. A. Podgorski, D. A. Schwartz, and M. V. Zombeck, "Calibration of the Verification Engineering Test Article-I (VETA-I) for AXAF using the VETA-I X-ray Detection System," *Proc. SPIE*, Vol. 1546, pp. 2-12, 1991.

3. G. Chartas, K. A. Flanagan, J. P. Hughes, E. M. Kellogg, D. Nguyen, M. V. Zombeck, M. Joy, and J. J. Kolodziejczak, "Correcting X-ray spectra obtained from the AXAF VETA-I mirror calibration for pileup, continuum, background and deadtime," *Proc. SPIE*, this volume, 1992.

4. W. A. Podgorski, K. A. Flanagan, M. D. Freeman, R. G. Goddard, E. M. Kellogg, T. J. Norton, J. P. Ouellette, A. G. Roy, and D. A. Schwartz, "VETA-I X-ray detection system," *Proc. SPIE*, this volume, 1992.

5. L.B. Lucy, "An iterative technique for the rectification of observed distributions," *Astronomical Journal*, Vol. 79, pp. 745-754, 1974.

6. P. Zhao, M. D. Freeman, J. P. Hughes, E. M. Kellogg, D. Nguyen, M. Joy, and J. J. Kolodziejczak, "AXAF VETA-I mirror encircled energy measurements and data reduction," *Proc. SPIE*, this volume, 1992.

7. E. M. Kellogg, G. Chartas, D. Graessle, J. P. Hughes, L. Van Speybroeck, P. Zhao, M. C. Weisskopf, R. F. Elsner, and S. L. O'Dell, "The X-ray reflectivity of the AXAF VETA-I optics," *Proc. SPIE*, this volume, 1992.

8. J. P. Hughes, D. A. Schwartz, A. Szentgyorgyi, L. Van Speybroeck, and P. Zhao, "Surface finish Quality of the Outer AXAF mirror pair based on X-ray measurement of the VETA-I," *Proc. SPIE*, this volume, 1992.

9. M. D. Freeman, J. P. Hughes, L. Van Speybroeck, J. W. Bilbro, M. C. Weisskopf, "Image analysis of the AXAF VETA-I mirror," *Proc. SPIE*, this volume, 1992.

VETA-1 X-ray Detection System

W. A. Podgorski, K. A. Flanagan, M. D. Freeman
R. G. Goddard, E. M. Kellogg, T. J. Norton
J. P. Ouellette, A. G. Roy, D. A. Schwartz

Smithsonian Astrophysical Observatory
60 Garden St.
Cambridge, MA 02138
(617)495-7000

1. ABSTRACT

The alignment and X-ray imaging performance of the Advanced X-ray Astrophysics Facility (AXAF) Verification Engineering Test Article-I (VETA-I) was measured by the VETA-I X-Ray Detection System (VXDS). The VXDS was based on the X-ray detection system utilized in the AXAF Technology Mirror Assembly (TMA) program, upgraded to meet the more stringent requirements of the VETA-I test program. The VXDS includes two types of X-ray detectors; 1) a High Resolution Imager (HRI) which provides X-ray imaging capabilities and 2) sealed and flow proportional counters which, in conjunction with apertures of various types and precision translation stages, provide the most accurate measurement of VETA-I performance. Herein we give an overview of the VXDS hardware including X-ray detectors, translation stages, apertures, proportional counters and flow counter gas supply system and associated electronics. We also describe the installation of the VXDS into the Marshall Space Flight Center (MSFC) X-Ray Calibration Facility (XRCF). We discuss in detail the design and performance of those elements of the VXDS which have not been discussed elsewhere; translation systems, flow counter gas supply system, apertures and thermal monitoring system.

2. INTRODUCTION

The Advanced X-ray Astrophysics Facility (AXAF), will be the third of NASA's Great Observatory series, having been preceded by the Hubble Space Telescope and Gamma Ray Observatory, and to be followed by Space Infra Red Telescope Facility. The AXAF, managed by NASA's Marshall Space Flight Center (MSFC), will be the largest imaging x-ray telescope flown in this century, will have the best angular resolution and will have response to higher energy, 10 keV, than any prior high resolution imaging telescope. A more complete description of the AXAF may be found in references 1 and 2.

A major technical challenge of the AXAF program is the fabrication of the AXAF Wolter Type 1 X-ray optics to tolerances never before having been achieved in such large X-ray optics. Fabrication of smaller optics to the required tolerances was demonstrated in the TMA program. However, it was decided that the fabrication technology for large optics should be demonstrated by test prior to proceeding with the full AXAF program. The VETA-I test program was thus instituted. In this program the largest pair of AXAF optics was to be fabricated to final tolerances, mounted in a test mount and tested in X-rays to demonstrate conclusively that the performance requirements had been met.

An X-ray test of the 10 meter focal length AXAF optics would require a new test facility, the X-ray Calibration Facility (XRCF), built at MSFC in place of the existing XRCF which had been used for calibration of the Einstein Observatory (HEAO-B) and testing of the TMA.

Testing of the VETA-I to the required levels would also require more accurate X-ray test equipment than had been previously available. An X-ray Detector Assembly (XDA) had been developed by the Smithsonian Astrophysical Observatory (SAO) for testing of the TMA. It had been utilized at MSFC in the HEAO-B XRCF for two TMA tests and a number of other tests of various X-ray systems. It was decided to upgrade the XDA for testing of the VETA-I.

Additions and modifications made to the TMA XDA to make it suitable for VETA-I testing included: 1) thin window flow proportional counters for low energy testing and new sealed proportional counters with better performance, 2) new, more accurate four-axis translation system for proportional counter scans, 3) new apertures for the proportional counters, 4) flow counter gas supply system, 5) new supporting structure for beam normalization proportional counters, 6) thermal monitoring system and 7) integrated workstation control and data acquisition system. Retained in the system were the HEAO-B breadboard HRI and its data acquisition system and the basic structure and drive mechanisms which provided instrument

designated as the VETA-I X-ray Detector Assembly(XDA). The VETA-I XDA is illustrated in Figure 1, and is shown pictorially in Figure 2 as it was installed in the MSFC XRCF for the VETA-I test. The VETA-I XDA co-ordinate axes are also shown in Figure 1. The origin of the XDA co-ordinate system is fixed with respect to the XDA base and is nominally located at the focus of the VETA-I when the XDA is properly positioned for testing. The XDA co-ordinates are nominally parallel to the XRCF facility co-ordinates when the XDA has been properly aligned. The XDA X axis is along the VETA-I optical axis, positive towards the VETA-I from the XDA. The XDA Z axis is nominally vertical, positive up, and the Y axis is nominally horizontal, completing a right-handed co-ordinate system.

The XDA structure and the arrangement of the XDA translation axes are shown in Figure 1. The X-ray detectors are mounted on the "XDA Top Plate", which is capable of being translated in the X and Y directions. These translation stage motions are designated as "PRIMX" and "PRIMY", with the stage motion sign convention illustrated in Figure 1(large arrows). The "PRIMX" motion is utilized to adjust the focus position of the XDA such that the detector focal plane is coincident with the VETA-I focus. The "PRIMY" motion is primarily utilized to select the detector to be used, the HRI or a proportional counter. It is also utilized to adjust the Y position of the XDA such that the selected proportional counter aperture is within reach of the counter translation stages (discussed below). The HRI is mounted on a Z axis translation stage whose motion is designated as "HRIZ", with a positive stage motion being upwards. The XDA FPC and SPC and apertures for these counters are carried by an integrated set of four translation stages, two in the Y direction and two in the Z. The counters and apertures make up a sub-assembly designated as the counter/aperture translation system, or "CAT". This entire sub-assembly mounts on the Top Plate of the XDA.

The translation stage arrangement of the CAT is shown in both Figures 1 and 2. From "ground" on the XDA Top Plate the stage order is PCAY, PCAZ, PCY and PCZ. The proportional counter apertures are carried on structure which is carried by both PCAY and PCAZ. The counters themselves are carried by all four stages. This arrangement allows selection of the counter and aperture combination to use by movement of the PCY and PCZ stages such that the chosen counter is positioned behind the chosen aperture. The counter and aperture together can then be moved relative to the X-ray beam by movement of the PCAY and PCAZ stages.

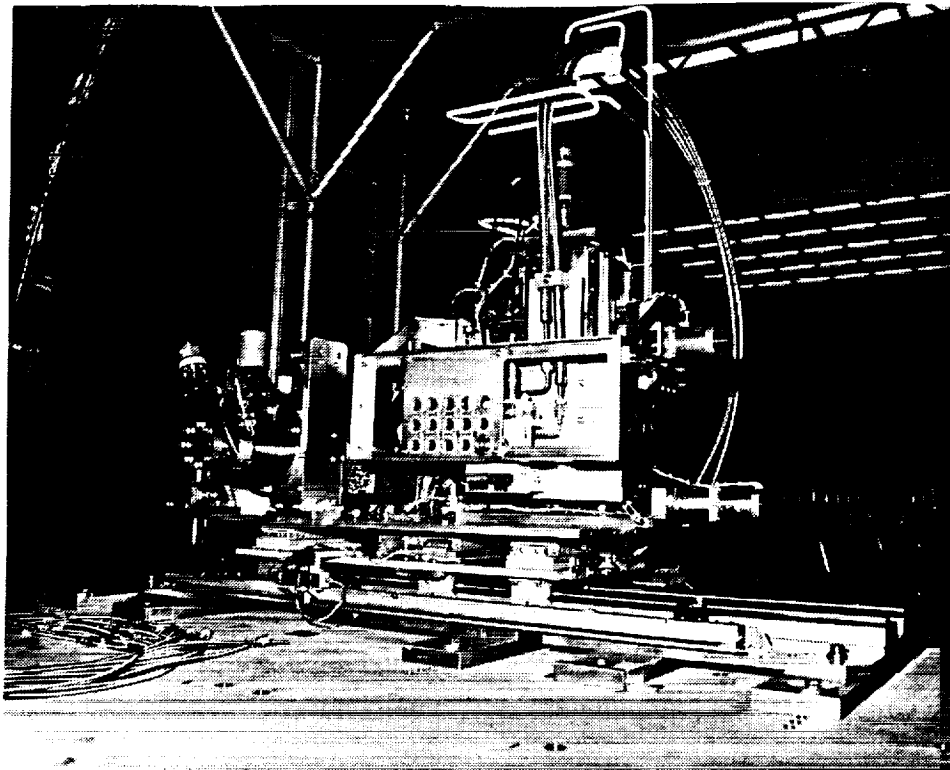


Figure 2. VETA-I XDA Installed in XRCF

3.3 Beam Normalization Detectors

An FPC and an SPC were also located on a structure, shown in Figure 3, just in front of the VETA-I (towards the source from the VETA-I). Their position was such that they intercepted the X-ray beam just outside of the VETA-I aperture annulus and inside the overall beam limits, which were set by the size of the X-ray guide tube. They were used to monitor the X-ray flux incident on the VETA-I and thereby allow normalization of data from the focal plane detectors. These proportional counters were designated as "beam normalization detectors(BND)".

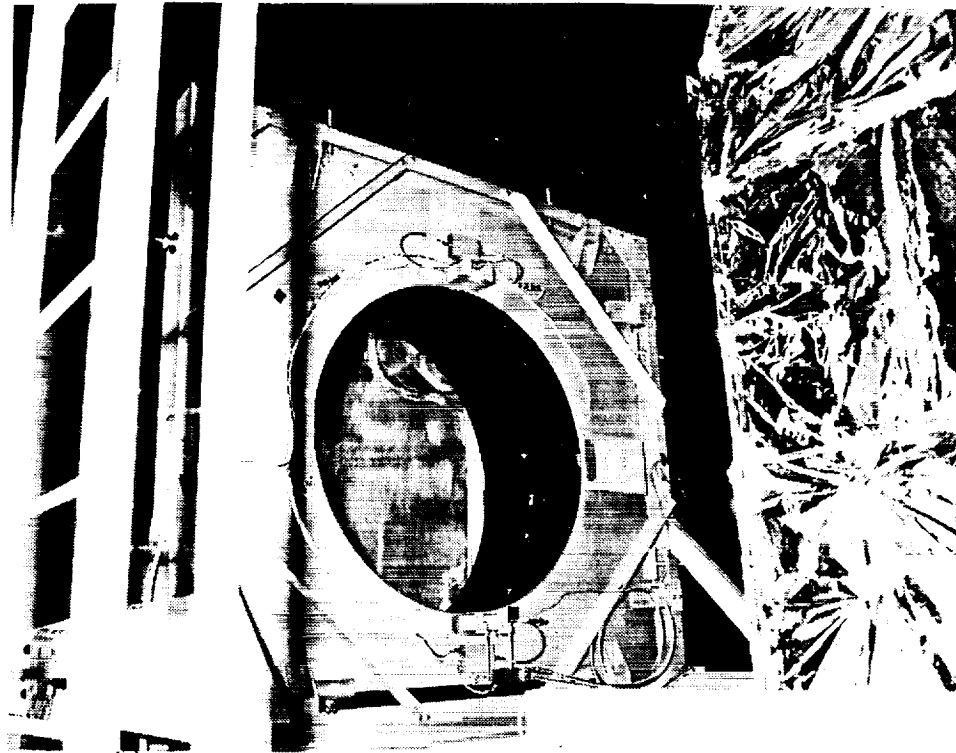


Figure 3. VXDS Beam Normalization Detectors

3.4 Flow Counter Gas Supply System

Operation of the XDA and BND FPC's required a flow counter gas supply system(GSS). The GSS was located outside of the XRCF vacuum chamber and supplied gas through flexible hoses and feed-thrus into the chamber. The GSS is shown in Figure 4. The GSS was capable of supplying either methane or P10(90% argon, 10% methane) at a controlled pressure between 100 and 1000 torr. Safety systems were also incorporated to prevent dumping of flow counter gas into the chamber through a failed flow counter window.

3.5 Thermal Monitoring System

A Thermal Monitoring System(THM) was incorporated to measure temperature at 20 locations throughout the VXDS hardware. Thermistors were utilized along with a Hewlett-Packard Model 3852A data acquisition system. Temperatures monitored included each proportional counter, each XDA motor, the GSS accumulator and various points on the XDA structure.

3.6 X-ray Data Acquisition and Control System

The X-ray Data Acquisition and Control System(XDACS) included both the electronics and cabling needed to run the detectors, translation stages and gas supply system as well as the extensive computer control system used to operate the system and to store and analyze the test data. The XDACS is discussed by Brissenden(this volume).

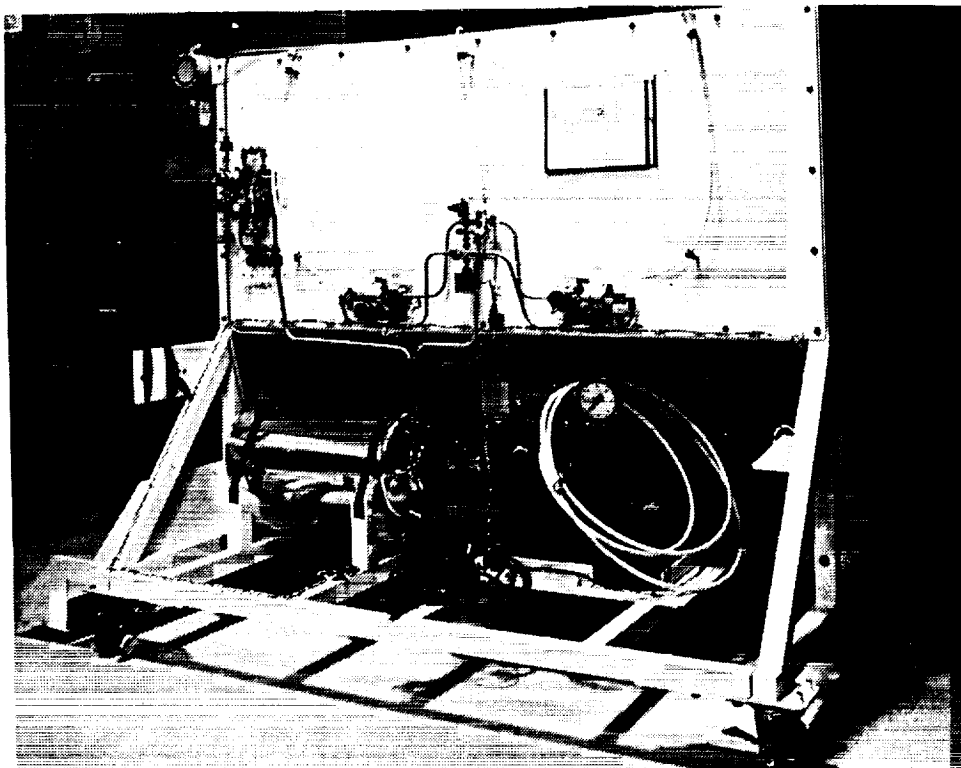


Figure 4. Flow Counter Gas Supply System

4. TRANSLATION STAGE PERFORMANCE

4.1 PRIMX, PRIMY and HRIZ Translation Stages

The translation stage performance requirements varied from stage to stage, depending on the function of the stage and its' heritage. The PRIMX, PRIMY and HRIZ stages were carry-overs from the TMA XDA and had a resolution of 2.5μ . The PRIMX and PRIMY stages incorporated Sony Magnascale linear position sensors which were used for closed loop control of position through the XDACS. The HRIZ stage did not have a position sensor and was controlled in an open loop mode by counting steps. Each of these three stages incorporated an absolute zero indicator and limit switches at the ends of travel.

The absolute accuracies of the PRIMX or HRIZ stages were not critical to the performance of the VXDS. The function of the PRIMX stage was to adjust the focus position of the XDA. The depth of focus of the VETA-I(on the order of 100μ) and the knowledge of the focus position of the apertures($\pm 10\mu$) and HRI focal plane were large when compared with the repeatability of the stage($\pm 2.5\mu$). Also, the focus position was always measured relative to the PRIMX zero reference position. As long as this did not shift we could always move the XDA to the correct focus position for each detector well within the accuracy needed. The HRIZ accuracy was not critical since it was utilized only to position the HRI, an imaging detector with a one inch field-of-view, in the vertical axis.

The PRIMY stage was utilized for large moves to select either the HRI or proportional counters for use and also for small moves to place the chosen proportional counter aperture on-axis. The use of PRIMY for aperture positioning was dictated by the limited travel of the PCAY stage as compared with the extent of the apertures in the Y direction. The XDACS software was developed in such a way that a given aperture could be placed on-axis (that is, the center of the aperture co-located with

the current definition of the X-ray beam center) by any valid combination of PRIMY and PCAY stage positions which yielded the correct sum of the two. The accuracy requirement for PRIMY was therefore driven by the need to repeatably locate the beam with different combinations of PRIMY and PCAY stage position. The positioning resolution of the PRIMY stage was 2.5μ (one motor step). The readout resolution was 1μ and the manufacturers specified accuracy for the readout was better than $\pm 10\mu$ over 1 meter of travel).

During the VETA-I test some difficulty was experienced with maintaining accurate beam center positions. The problem was that we could not always return to an aperture in which the beam had been "centered" (that is, located in Y and Z axes) and find the beam still near the center of that aperture (the beam drift was monitored and was not significant). The differences in beam center position were often 30μ to 50μ or sometimes more. In addition, we could not always locate the beam in a new aperture, even though we had carefully centered the beam in a different aperture and had very accurate knowledge of the relative positions of all of the apertures. This did not always occur, however. It was finally determined that the beam center errors occurred when the PRIMY axis had been moved to either reach a new aperture or to come back to the original aperture, but with a different combination of PRIMY and PCAY. The result of the problem was to lengthen the test times somewhat, due to the need to perform "beam centering" procedures each time the aperture was switched. The results of the tests were not compromised, however.

After the VETA-I test a series of measurements were made to determine the accuracy of the PRIMY stage. These were made using an HP laser position measuring system, and are documented in reference 3. The results are shown in Figure 5, wherein the PRIMY position errors are plotted vs. commanded move distance. The Figure shows PRIMY errors to be on the order of 0.6μ to 0.8μ per millimeter move. The sense of the error is that the true distance moved (measured by the HP laser) is always less than the indicated move (as measured by the Sony Magnascale) on the PRIMY stage. In the next generation of X-ray detection equipment the PRIMX, PRIMY and HRIZ stages will be replaced, thereby correcting this problem.

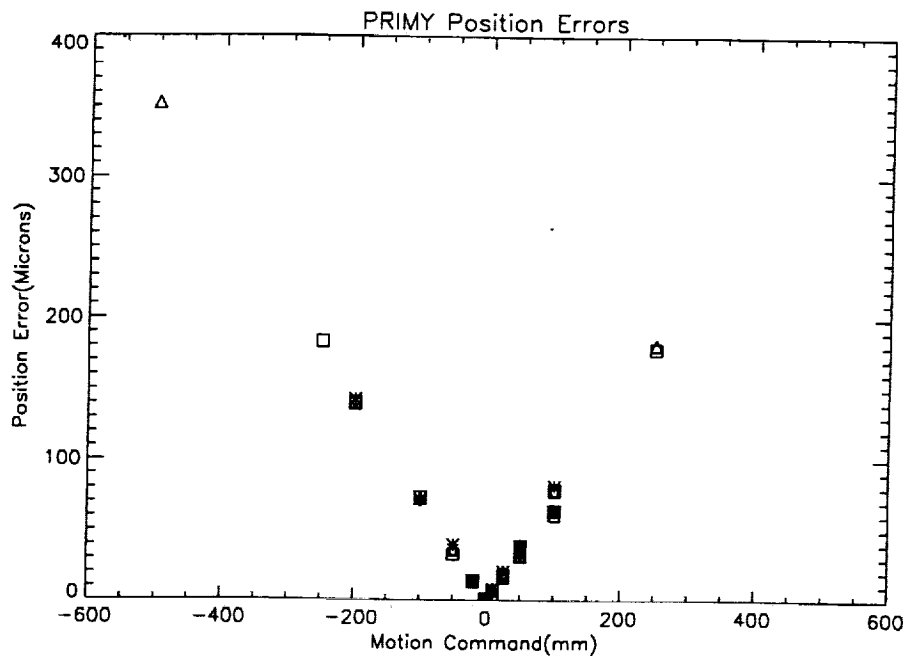


Figure 5. PRIMY Position Errors

4.2 PCY, PCZ, PCAY and PCAZ Translation Stages

As discussed above in Section 3.2 the PCY and PCZ stages on the CAT were used to move the selected proportional counter behind the selected aperture. The required positioning accuracies (including readout inaccuracy) for the PCY and PCZ stages

were $\pm 5\mu$ over the entire travel range (approximately 200mm) of each stage. Testing using an HP laser position measuring system verified that these accuracies were met.

The PCAY and PCAZ stages were used both to select an aperture for use and to perform various types of scans through the X-ray beam, with the proportional counter held fixed behind the selected aperture. One dimensional scans in either the Y or Z axis and a two dimensional raster scan in both Y and Z were used extensively in the VETA-I test. The accuracy desired for aperture selection was $\pm 3\mu$ over the entire range of travel (approximately 100mm for PCAY and 150mm for PCAZ), even though the PRIMARY stage was not as accurate. The reason for this was to allow very accurate aperture to aperture moves using PCAY and PCAZ alone. Apertures were grouped together such that the smaller apertures could be reached by PCAY and PCAZ moves only. Figures 6 and 7 show acceptance test data for the PCAY and PCAZ stages. Positioning errors are plotted over the entire travel range of each stage. In each case the $\pm 3\mu$ error limits were met.

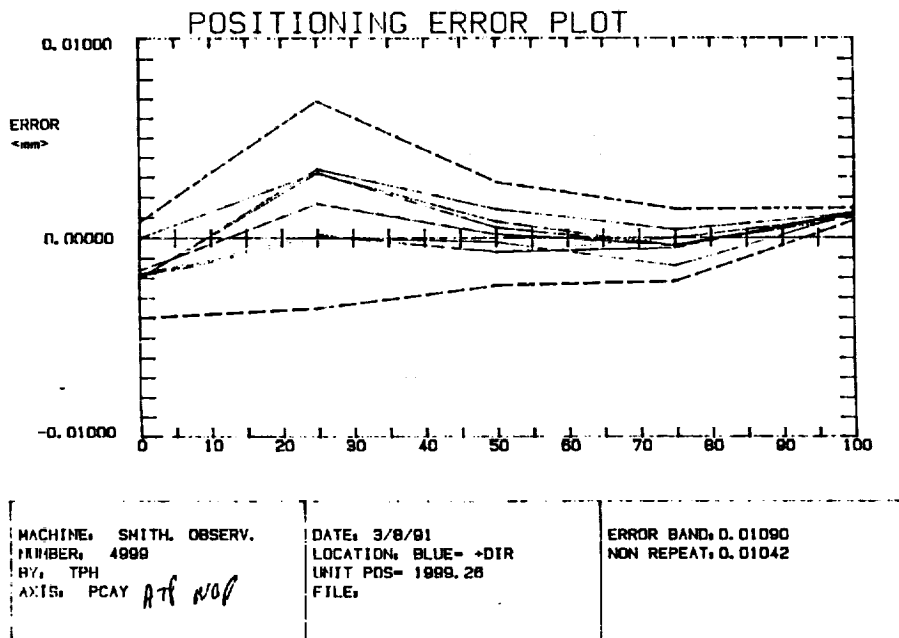


Figure 6. PCAY Stage Position Errors - Full Travel

The most demanding use (in terms of accuracy) of the PCAY and PCAZ stages was to perform the one and two dimensional scans. These scans were typically small in extent, with very small scan steps. A typical one dimensional scan would be to scan the 5μ aperture in either Y or Z in steps of 2μ over a range of 200μ . A typical two dimensional scan would utilize the 10μ aperture, scanning in steps of 10μ over a 19×19 scan matrix (190μ by 190μ). For these short scans we utilized a "motor incremental mode" of scanning. In this mode the encoder feedback was NOT used, and the movement was made by motor steps alone. In addition, the scans were performed in such a manner as to remove translation stage backlash. For example, when performing a two-dimensional raster scan all rows were scanned in the same direction, and the stage was always moved beyond (to the left of) the first point in the row so that the backlash was taken out in the rightward move to the first scan point in the row. Using this mode the errors were below 1μ at any scan point. This accuracy was demonstrated using the HP laser position measurement system. A typical test run is shown in Figure 8, wherein position error is plotted vs. stage position for a 30μ scan in steps of 5μ . The maximum error in this case was 0.2μ . A 1μ scan position error was utilized in developing the error budgets of the VXDS. With this error the overall performance requirements were shown to be met.

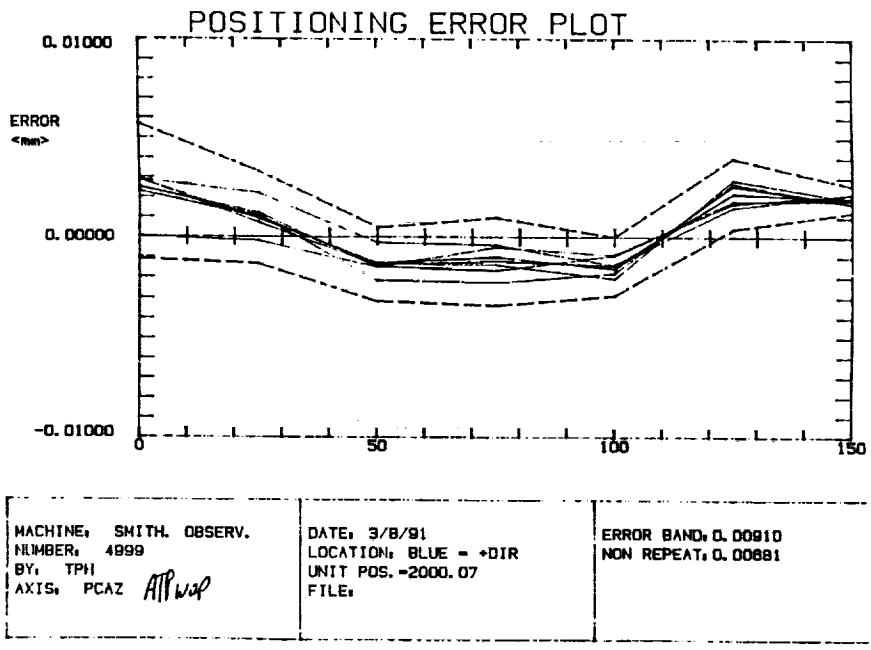


Figure 7. PCAZ Stage Position Errors - Full Travel

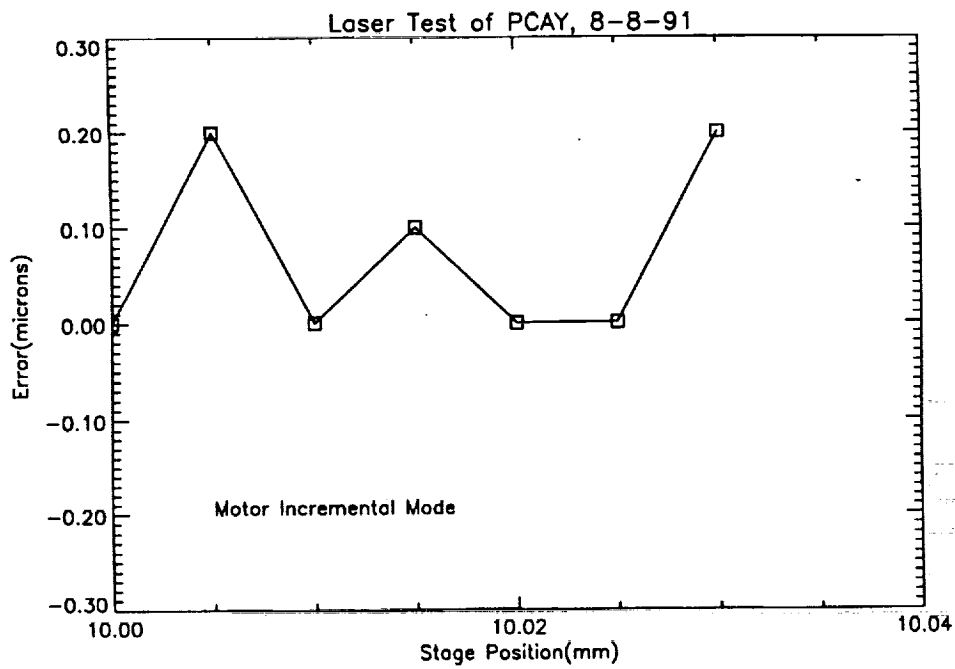


Figure 8. PCAZ Position Errors - Small Motions

5. PROPORTIONAL COUNTER APERTURES

The most accurate measurement of the performance of the VETA-I was made using proportional counters in conjunction with various types of apertures located in front of the counters. The accuracy of this approach is attributable to the high spatial resolution which can be obtained with small, precision apertures in front of the counters, good energy resolution provided by the counters and the use of the BND counters to normalize the focal plane counters during scans. The general arrangement of counters and apertures on the XDA is shown in Figures 1 and 2. In addition to the counters on the XDA, two counters were utilized for beam normalization, as discussed in Section 3.3 and shown in Figure 3. Precision apertures were also placed in front of each BND counter.

The arrangement of apertures on the XDA "aperture plate" is shown in Figure 9.

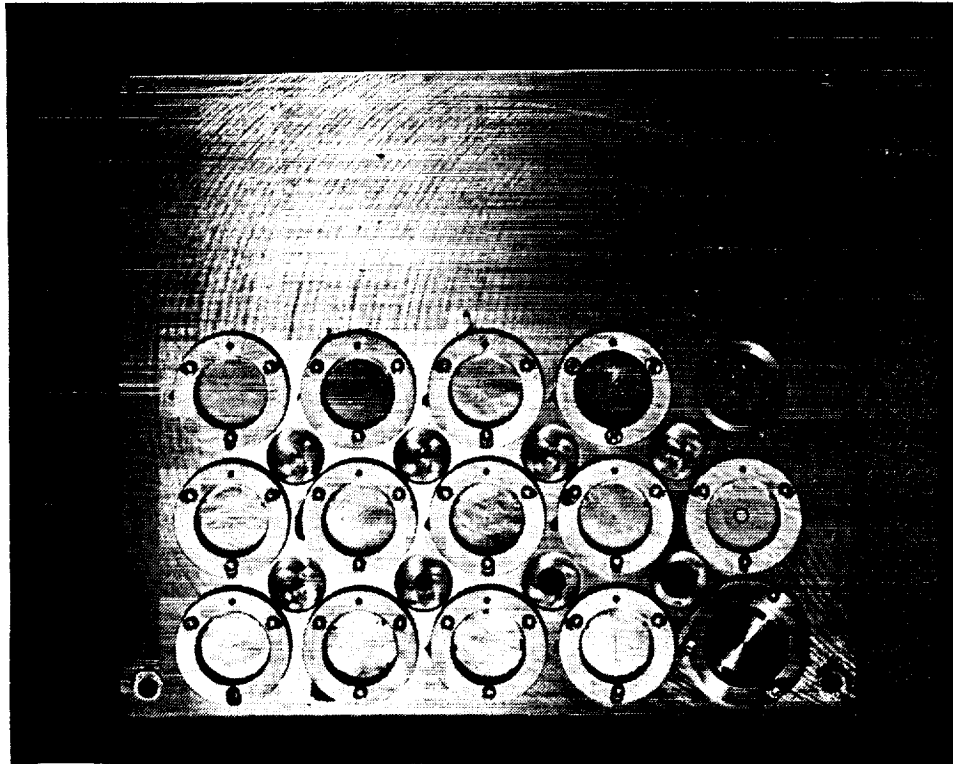


Figure 9 Apertures on XDA Aperture Plate

Three rows of aperture holders, each row containing five holders, are located on the plate. In addition, circular apertures are machined directly into the aperture plate. These machined apertures are located between the rows and columns of aperture holders. Three different types of apertures were provided:

1. Circular apertures, commonly referred to as "pinholes", even though the largest was 20mm in diameter.
2. Annular apertures with a variety of nominal diameters and annulus widths, referred to as "annuli".
3. Linear apertures, referred to as "slits", in both horizontal and vertical orientation.

A complete listing of the apertures provided on the XDA is given in Tables 1(pinholes), 2(slits) and 3(annuli). The apertures on the BND are given in Table 4. The tables provide the aperture name, nominal dimensions, open area, equivalent diameter(pinholes), method of manufacture and method of measurement. Three different fabrication techniques were used for the apertures. The smallest apertures were laser drilled into 12 μ gold foil which had been bonded into machined "aperture holders". These aperture holders were then fastened to the aperture plate, using both screws and a locating pin, and tack bonded to the plate. Other apertures were machined directly into special aperture holders and attached to the plate as described above. Finally, a number of circular apertures were machined directly into the aperture plate. Three methods of

measurement of aperture area were also used. The smallest apertures were photographed with a scanning electron microscope(SEM). The boundary curve was then digitized using precision calipers and a SEM photograph of a calibration standard, which provided a grid of lines approximately 0.46 μ apart. This calibration photo allowed compensation for SEM scale factor variation. The estimated accuracy in measurement of boundary points was better than 0.01 μ in each axis. The boundary data were then entered into the IDEAS CAD system which calculated the open area of the aperture to an accuracy of 0.02% (reference 4).

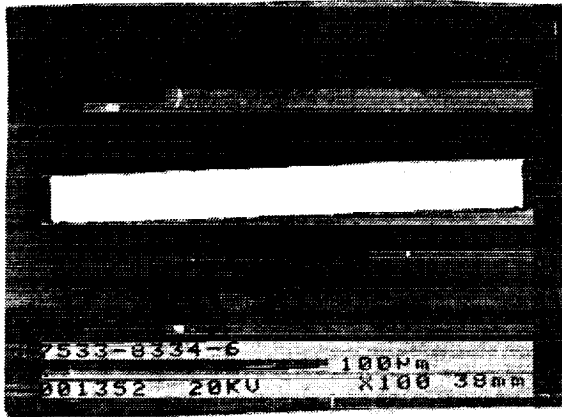
Mid-size laser drilled apertures were inspected at the laser drilling vendor's facility using an optical microscope and translation stages with an estimated accuracy of +/-0.2 μ . The boundary co-ordinates were entered into the IDEAS CAD program and the open area calculated. Larger apertures machined into the aperture plate were inspected using a two-axis video zoom system and translation stages accurate to 1 μ . Two orthogonal diameters were determined for these larger circular apertures. The average diameter was used to calculate the open area.

Aperture Name	Area (Sq mm)	Equivalent Diameter	Fabrication Method	Measurement Method
2 μ	7.707923X10-6	3.13 μ	L	SEM
5 μ	28.33479X10-6	6.01 μ	L	SEM
10 μ	104.96409X10-6	11.56 μ	L	SEM
25 μ	511.55011X10-6	25.52 μ	L	SEM
50 μ	1926.3078X10-6	49.52 μ	L	M
100 μ	7660.07X10-6	98.76 μ	L	M
300 μ	74155.591X10-6	307.28 μ	L	M
500 μ	198109.55X10-6	502.24 μ	L	M
0.75mm	0.407150	0.720mm	P	V
1.0mm	0.716303	0.955mm	P	V
1.5mm	1.824147	1.524mm	P	V
2.0mm	3.122771	1.994mm	P	V
3.0mm	6.955939	2.976mm	P	V
5.0mm	19.322051	4.960mm	P	V
7.5mm	43.556561	7.447mm	P	V
10.0mm	78.006654	9.966mm	P	V
20.0mm	313.845185	19.990mm	M	V
Fabrication Method: L=Laser drilling M=Machined P=Machined into plate				
Inspection Method: SEM=Scanning Electron Microscope M=Vendor Microscope V=Video Camera and Stages				

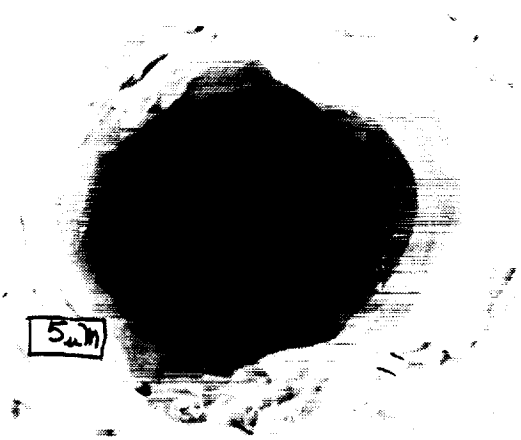
Table 1. Circular Apertures(Pinholes) on XDA Aperture Plate

The measured open area of the apertures are the geometric areas. Vignetting of the beam occurs due to the fact that the X-ray beam from the VETA-I is a converging cone with a cone angle of approximately 6.8 degrees. This factor is significant for the smaller apertures, and is taken into consideration in the test data analysis.

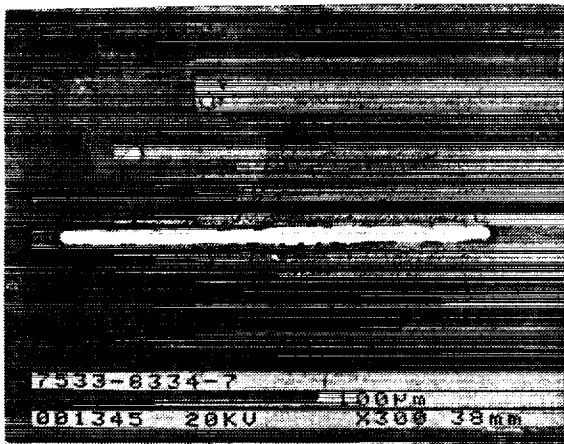
Figure 10 shows SEM photographs of several of the VETA-I apertures.



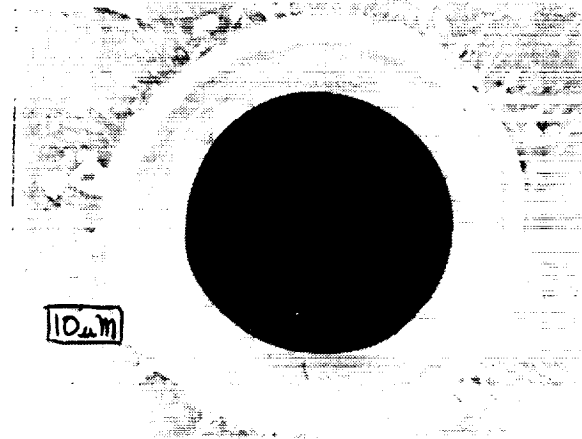
(a) 1mm x 100 μ slit



(b) 5 μ Pinhole



(c) 300 μ x 10 μ slit



(d) 10 μ Pinhole

Figure 10 SEM Photographs of Aperuures

Type	Nominal Dimensions Length x Width	Area (Sq mm)	Fabrication Method	Measurement Method
Horizontal slit	300 μ x 10 μ	0.00266520	L	SEM
Horizontal slit	1000 μ x 100 μ	0.09730713	L	SEM
Vertical slit	300 μ x 10 μ	0.00263928	L	SEM
Vertical slit	1000 μ x 100 μ	0.09480202	L	SEM
Fabrication Method: L=Laser drilling M=Machined P=Machined into plate				
Inspection Method: SEM=Scanning Electron Microscope M=Vendor Microscope V=Video Camera and Stages				

Table 2. Slit Apertures on XDA Aperture Plate

Aperture Name	Nominal Dimensions Diameter x Width	Area (Sq mm)	Fabrication Diameter	Measurement Method
100 μ Annulus	100 μ x 10 μ	0.00204820	L	M
300 μ Annulus	300 μ x 30 μ	0.01869377	L	M
600 μ Annulus	600 μ x 60 μ	0.07951131	L	M
1.0mm Annulus	1.0mm μ x 100 μ	0.27067390	L	M
4.0mm Annulus	4.0mm μ x 400 μ	4.1978070	L	M
20mm Annulus				
Fabrication Method: L=Laser drilling M=Machined P=Machined into plate				
Inspection Method: SEM=Scanning Electron Microscope M=Vendor Microscope V=Video Camera and Stages				

Table 3. Annular Apertures on XDA Aperture Plate

Part Number	Aperture Name	Area (Sq mm)	Equivalent Diameter
7533-8362 S/N 1	BND Flow Counter	314.158	20.000mm
7533-8362 S/N 2	BND Sealed Counter	315.356	20.038mm

Table 4. BND Apertures

6. FLOW COUNTER GAS SUPPLY SYSTEM

The flow counter gas supply system provided either methane or P10(90% argon, 10% methane) at a controlled pressure. Gas from the selected supply bottle was regulated to a pressure of approximately 5 psig and then fed into an accumulator via an electronically controlled "pulsing" valve. This valve would activate for a set time period whenever the measured pressure in the accumulator would drop below a computer controlled pressure setpoint. Gas from the accumulator would flow through gas lines into the XRCF vacuum chamber and to the XDA and BND flow counters, then return to the gas supply system(see Figure 4). The gas would then flow across a manually adjustable needle valve into a vacuum pump on the gas supply system. The exhaust gas from the vacuum pump was routed out of the XRCF building via an exhaust line.

Important performance characteristics for the gas supply system were its' stability about a setpoint(+/-0.5 torr), absolute accuracy of pressure regulation(+/-2 torr) and pressure repeatability(+/-1 torr). The absolute accuracy and repeatability were functions of the pressure transducer used. A pressure transducer was selected which met the accuracy and repeatability requirements. The stability requirement was met by providing a large accumulator to minimize the pressure rise caused by each gas pulse and minimizing the flow rate to the extent practical. Plots of pressure vs. time over long and short time periods are shown in Figures 11 and 12. The data show short term stability to be on the order of +/-0.2 torr.

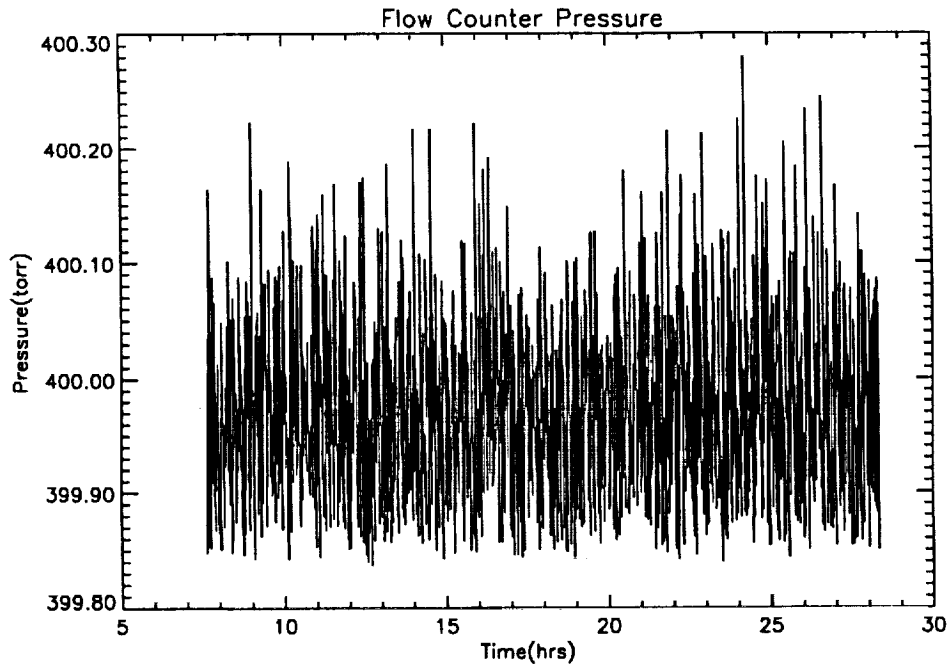


Figure 11. Flow counter gas pressure stability - long term

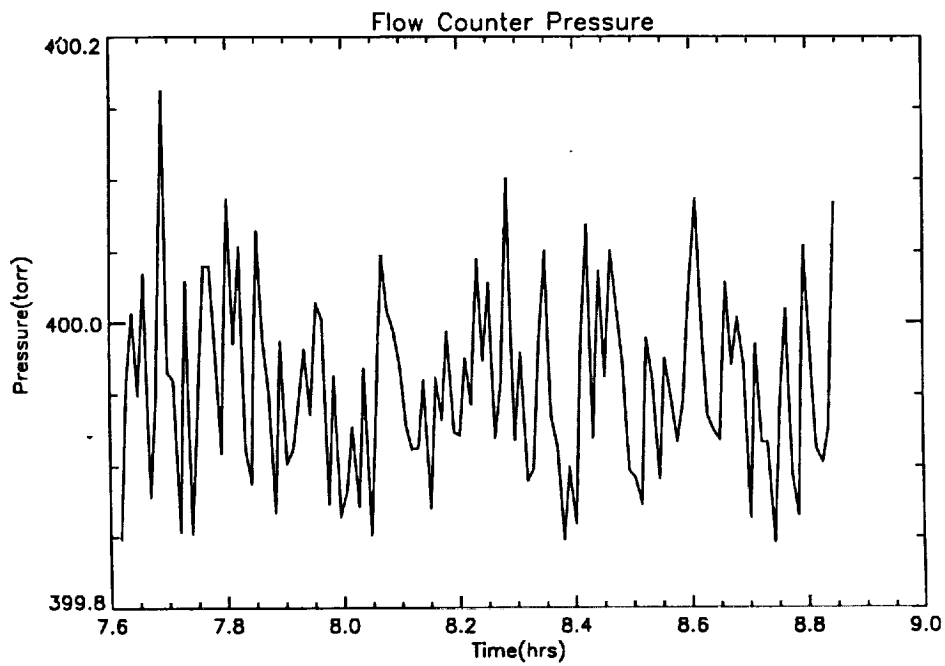


Figure 12. Flow counter gas pressure stability - short term

7. SYSTEM TEMPERATURES

Twenty thermistors were placed at critical points on the VXDS. These thermistors were read by the XDACS via the HP 3852A data acquisition system and logged in the test data files. Temperatures monitored included proportional counters, motors, various structural components and the gas supply system accumulator. The flow proportional counter temperatures were of particular importance since the counter efficiency is related to gas density. The gas supply system maintained the pressure constant in both the XDA and BND flow counters, but the density would vary, and hence the efficiency, if the gas temperatures were different. The logged temperatures were used to compensate for this effect and therefore ensure that the BND counter would properly normalize the XDA flow counter. A plot of counter temperature vs. time is shown in Figure 13.

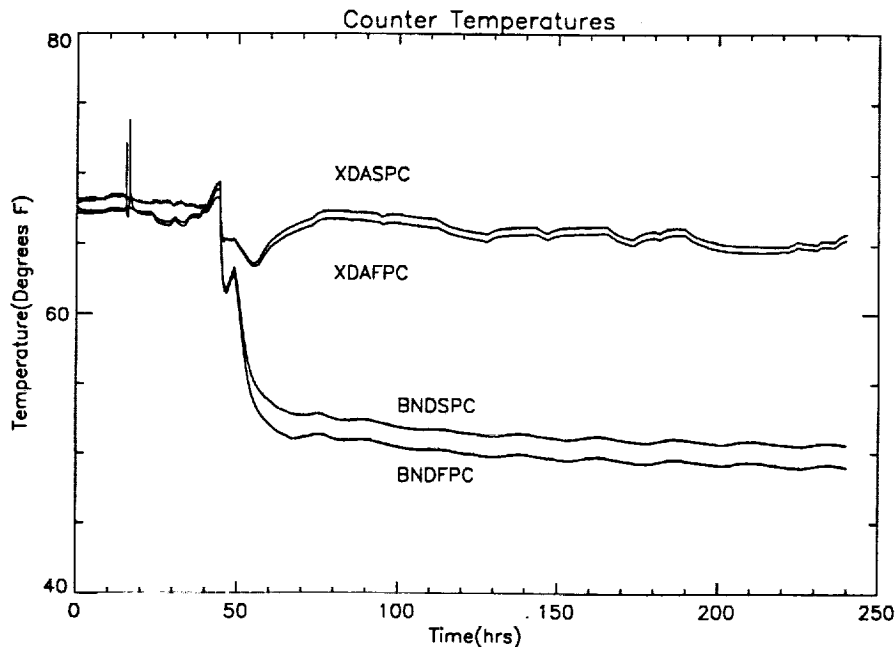


Figure 13. Proportional counter temperatures vs. time

The time duration of the plot is approximately 250 hrs, commencing near the start of the VETA-I test. A key feature shown on the plots is the large decrease in temperature of the BND counters (BNDSPC and BDNFPC) as compared with the counters on the XDA (XDASPC and XDAFPC). This was due to a cold condition which developed in the front of the XRCF vacuum chamber, near the BND. The large difference in counter (and therefore gas) temperatures made the density correction important in the data analysis.

8. CONCLUSIONS AND FUTURE WORK

The TMA XDA, an existing set of test equipment, was significantly upgraded to perform the testing on the VETA-I. The upgrades were necessary to support low energy testing (flow counters), provide enhanced accuracy (CAT & apertures), greatly improve the test efficiency and data analysis capabilities (XDACS) and to adapt the system to the new XRCF. The system was developed between mid-1989 and mid-1991 and was installed in the XRCF in June, 1991. VETA-I testing commenced in late August, 1991 and continued through late October, 1991. Additional tests were performed on the VXDS itself from December, 1991 through May, 1992.

The VXDS performed well throughout the test series, with no major failures which stopped the testing. The most significant technical problems were the failure of the XDA sealed counter and a higher than expected level of electrical noise in the XDA proportional counters. We were able to find work-arounds to both problems. Another significant issue was the effect of the flow proportional counter window mesh, which is discussed in detail in Reference 5.

The architecture of the VXDS, particularly the integrated and networked computer control system, discussed in Reference 6, was a major success. The data acquisition and analysis capabilities of the VXDS were crucial to the success of the VETA-I test.

An X-ray detection system for the AXAF High Resolution Mirror Assembly(HRMA) calibration is now being developed at SAO. The system, the HXDS, will utilize major elements of the VXDS. The dated TMA equipment will be replaced and improvements will be made to other elements where necessary. The overall control architecture of the VXDS will be carried forward to the HXDS.

REFERENCES

1. M. Weisskopf, "The Advanced X-ray Astrophysics Facility: An Overview," *Astrophysical Letters & Communications.*, vol. 26, pp. 1-6, 1987.
2. E. Kellogg, R. Brissenden, K. Flanagan, M. Freeman, M. Jones, M. Ljungberg, P. McKinnon, W. Podgorski, D. Schwartz, M. Zombeck, "Calibration of the Verification Engineering Test Article-I(VETA-I) using the VETA-I X-ray Detection System," *SPIE Volume 1546*, pp. 2-12, 1991.
3. T. Norton Internal Memorandum TJN-FY92-003, "VETA-I Test Setup Verification", December 26, 1991
4. R. Goddard Internal Memorandum RG92-02, "VETA-I Aperture Area Determination Summary", June 1, 1992
5. P. Zhao, M. D. Freeman, E. M. Kellogg, D. T. Nguyen, "VETA-I Encircled Energy and Data Reduction" *SPIE 1742-08*
6. R. J. V. Brissenden, M. T. Jones, M. Ljungberg, D. T. Nguyen, J. B. Roll, "VETA X-ray Data Acquisition and Control System", *SPIE 1742-06*.



VETA X-ray data acquisition and control system

Roger J. V. Brissenden, Mark T. Jones, Malin Ljungberg,
Dan T. Nguyen and John B. Roll, Jr.

Smithsonian Astrophysical Observatory
60 Garden Street, Cambridge, MA 02138

ABSTRACT

We describe the X-ray Data Acquisition and Control System (XDACS) used together with the X-ray Detection System (XDS) to characterize the X-ray image during testing of the AXAF P1/H1 mirror pair at the MSFC X-ray Calibration Facility. A variety of X-ray data were acquired, analyzed and archived during the testing including: mirror alignment, encircled energy, effective area, point spread function, system housekeeping and proportional counter window uniformity data. The system architecture is presented with emphasis placed on key features that include a layered UNIX tool approach, dedicated subsystem controllers, real-time X-window displays, flexibility in combining tools, network connectivity and system extensibility. The VETA test data archive is also described.

2. INTRODUCTION

The Advanced X-ray Astrophysics Facility (AXAF) Verification Engineering Test Article (VETA) consists of the largest paraboloid and hyperboloid pair of Wolter type I grazing incident mirrors contained within the AXAF telescope and represents the first elements of the flight mirror to be manufactured. The VETA P1/H1 mirror pair was aligned and tested with X-rays in the X-ray Calibration Facility (XRCF) at Marshall Space Flight Center (MSFC) during 1991 September and October. The alignment and PRF characterization was performed with the VETA X-ray Detection System (VXDS) comprised of imaging and non-imaging focal plane detectors, beam normalization and monitor detectors, motorized detector and aperture stages, gas control system, thermal monitoring system and central data acquisition and control computer system¹.

The X-ray Data Acquisition and Control System (XDACS) performs the control, data acquisition, monitoring, analysis and logging functions of the VXDS. The XDACS consists of the computers, busses, controllers and software required to perform these functions and is the subject of this paper. We describe the network and software architecture (§3 and §4), and the VETA data archive and data base used to retrieve data for detailed analysis (§5). A summary is given in §6.

3. NETWORK DESIGN AND SUBSYSTEM DESCRIPTION

The VXDS design was based on the detection system used to test the Technology Mirror Assembly (TMA), a 2/3 scale model of the next to inner AXAF mirror². The TMA test system consisted of a number of independently controlled subsystems, some of which were retained and incorporated into the VXDS. A key requirement of the VXDS design was to provide the VETA test operator with integrated procedural control and monitoring over all subsystems from a single central workstation. In order to meet this requirement a network architecture was developed that employed synchronized controllers interfaced to hardware subsystems and connected to a central SUN Microsystems 4/330 workstation via one of three different bus or network types: RS232, IEEE 488 or ethernet. A variety of bus types was required to integrate existing TMA subsystems.

The network architecture (Figure 1) shows the central workstation and peripherals, XDACS and some XRCF subsystems, analysis workstations, busses (ethernet, IEEE 488 and RS232), external network connection and InterRange Instrumentation Group (IRIG) analog time signal used for synchronization.

The subsystems shown in Figure 1 are briefly described in Table 1 and explained in more detail in Reference 1. The basic components and operation of the system are also described here to provide a context for the software description.

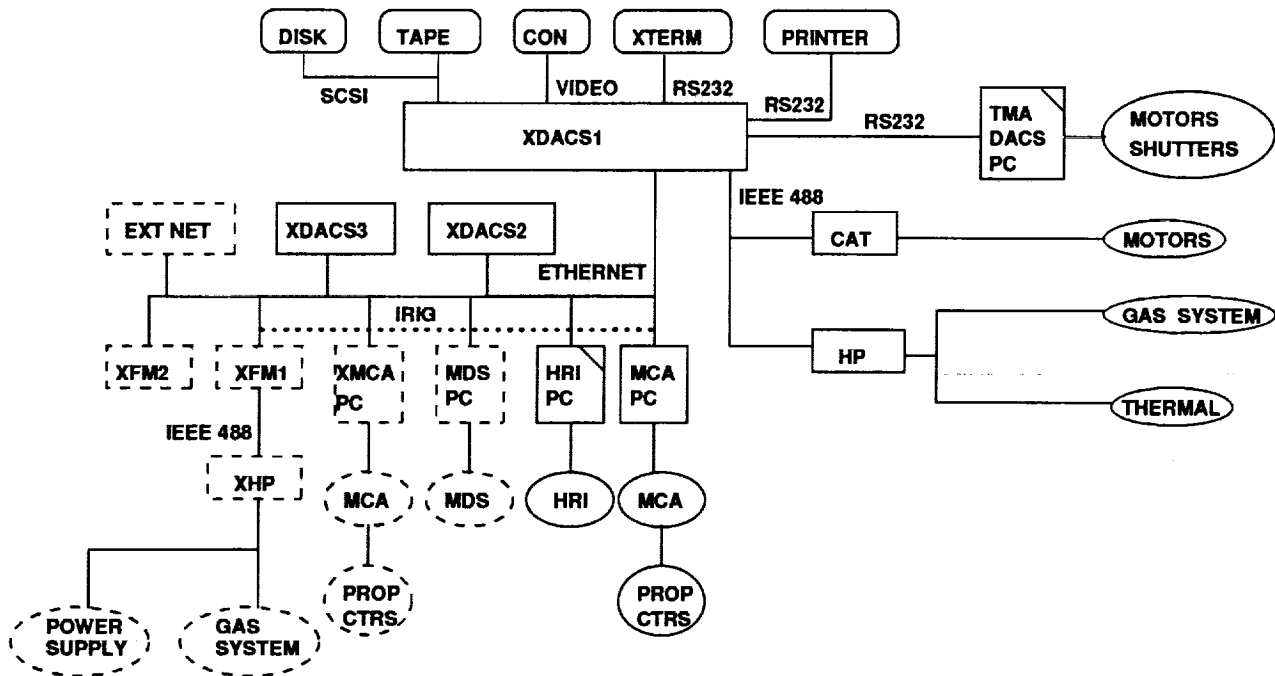


Figure 1: The XDACS/XRCF network architecture combines a variety of bus types. Hardware components are denoted by ellipses, network components (controllers and computers) by rectangles and XDACS peripherals by rectangles with rounded corners. XRCF subsystems that interface with XDACS1 but were not delivered by SAO have dashed lines. The TMA DACS and HRI subsystems were inherited from the TMA system and are marked with a diagonal line.

X-rays reflected by the VETA-I along the $-x$ axis were detected by instruments located in the focal plane (FP). The FP detectors include a High Resolution Imager (HRI), a Flow Proportional Counter (FPC) and a Sealed Proportional Counter (SPC). The SPC and FPC are mounted on orthogonal ($y-z$) motor stages behind the aperture plate which contains apertures of various sizes and shapes. The apertures include pinholes ranging from $2\ \mu\text{m}$ – 20 mm in diameter, annuli, and horizontal and vertical slits. The aperture plate is mounted on orthogonal ($y-z$) motor stages such that the counters are carried when the aperture plate moves. The counter and aperture plate motor drives constitute the Counter Aperture Translation (CAT) subsystem which is mounted on the Prime X and Prime Y coarse motor drives. The HRI motion is controlled by Prime-X, Prime Y and the HRI Z motor drive and is located in the $-y$ direction from the CAT, along Prime-Y. A set of four quadrant shutters located at the entrance to the VETA-I allows X-rays in each quadrant to be blocked for mirror alignment and focus tests. The Prime drives, HRI-Z and shutter motors are controlled by the Test Mirror Article Data Acquisition and Control System (TMA DACS) subsystem. The Prime drives, CAT and FP instrumentation are collectively called the X-ray Detection Assembly (XDA).

In addition to the FP detectors two Beam Normalization Detectors (BND), a large area flow and large area sealed proportional counter, are mounted on the BND structure located at the entrance to the VETA. The Gas Supply System (GSS) controls the type and flow of gas to the two flow counters and 19 thermistors located throughout the XDA constitute the thermal monitoring (THM) system. The central workstation and controllers constitute the XDACS which provides the controls and data acquisition functions for all subsystems. The X-ray Flux Monitor (XFM) subsystem consists of a flow and sealed proportional counter, gas system and analysis workstation and is used to monitor the X-ray source flux. The Motion Detection System (MDS)³, detects the relative motion between the FP instruments, VETA and X-ray source. The XDA, BND, GSS, THM system, XDACS, analysis workstations, MDS and XFM interfaces are collectively named the VETA X-ray Detection System (VXDS).

TABLE 1: XDACS SUBSYSTEM DEFINITION AND DESCRIPTION

SUBS.	DEFINITION	DESCRIPTION
XDACS1	X-ray Data Acquisition & Control System 1	Central controlling workstation provides operator command interface and displays. Issues low level subsystem commands, receives data and status streams, archives all data, and performs limited analysis.
XDACS2		Analysis workstation.
XDACS3		Analysis workstation.
TMA DACS	TMA Data Acquisition & Control System	TMA motor drive system provides movement in x , large scale y moves and moves the HRI in z . Four quadrant shutters located in front of the VETA may be opened and closed.
CAT	Counter Aperture Translation	Accurate ($2 \mu\text{m}$) motor stages move the focal plane proportional counters behind the aperture plate and move the aperture plate. The CAT is mounted on the TMA motor drives.
HP	Hewlett Packard	HP 3752A IEEE488 controller contains the GSS (Gas Supply System) and THM (Thermal) monitoring system cards. The GSS controls gas flow through the Focal Plane and Beam Normalization flow proportional counters and the THM provides thermal monitoring at 19 locations on the instruments, motors and structure of the XDA.
MCA	MultiChannel Analyzer	Controls and receives data from the FP and BND flow and sealed proportional counters.
MCA PC	MCA Personal Computer	Interfaces with the MCA via Ortec board. Receives commands from and transmits data to XDACS1 via TCP/IP.
HRI	High Resolution Imager	Focal plane imaging detector.
HRI PC	HRI Personal Computer	Interfaces with the HRI via custom board. Receives commands from and transmits data to XDACS1 via TCP/IP.
MDS PC	Motion Detection System PC	MDS detects relative motion between the FP instruments, VETA-I and X-ray source. The PC transmits TCP/IP packets to XDACS1.
XFM1	X-ray Flux Monitor 1	Workstation controls a smaller version of the MCA and HP (GSS and THM) subsystems. The XFM subsystem is located near the X-ray source and monitors the source flux. The software used to control and acquire data from the XFM was based on the HP and MCA software subsystems (little change was required).
XMCA PC	XFM MultiChannel Analyzer	Analogous to the MCA PC.
XFM2	X-ray Flux Monitor 2	Workstation used as a display station for XFM spectra, gas and temperature data and status.
XHP	XFM Hewlett Packard	Analogous to the HP in controlling the XFM gas system and thermal monitoring, but in addition controlled the proportional counter high voltage power supply.
EXT NET	External Network	Internet network connection.

During testing, the operator issued high level commands with appropriate parameters at the XDACS1 console. Examples of tests performed by high level commands included: generation of VETA-I alignment errors using the quadrant shutters and FP instruments (either HRI or scanning proportional counters), beam centering with successively smaller apertures, encircled energy measurements and 2-D mapping of the PRF and HRI images.

The XDACS1 acquired both autonomous and non-autonomous data during a test. For example, a 19×19 2-D scan of the PRF made with the FPC behind the $10 \mu\text{m}$ diameter circular aperture was performed by first moving the FPC behind the $10 \mu\text{m}$ pinhole and then scanning the aperture plate in a 2-D raster about the current beam center. At each point in the scan, proportional counter spectra were acquired in both the FP and BND counters and stored in files, one per point. Logs of operator keystrokes, motor positions, command parameters and low level subsystem commands were also generated. Upon completion of the scan the FP integrated line counts were normalized at each point with BND data and an image file was generated. The 361 files containing spectral data, the image file and logs constituted the non-autonomous data from the test. Data from the MDS, GSS and THM subsystems were acquired, displayed and stored continuously and independently of a given test, and were the autonomous data

streams.

Data acquired during testing were time stamped with either the XDACS1 clock or IRIG-B time signal depending on the required accuracy. The MDS data allowed time tagged events recorded by FP instruments to be corrected for excessive motion in the $y - z$ plane. Synchronization to 10 ms between the MDS, HRI, MCA and XFM was required to support such corrections, and these subsystems accessed the IRIG time signal at the controller level via a PC board. Data from other subsystems were archived with ~ 1 second accuracy. We note that the stability of the XRCF, test benches and XDA were such that MDS corrections were never needed.

The synchronization at the front-end controller level illustrates how the XDACS1 was isolated from direct hardware control. In general, the XDACS1 issued commands to the controllers and received back status and data streams. The controllers were designed to operate safely in the event of XDACS1 going off-line. Time critical data were transferred using TCP/IP (e.g., MDS, HRI and proportional counter data) and displayed with ~ 1 sec resolution and other data such as gas pressure or temperature were displayed after archiving with ~ 5 sec resolution.

4. SOFTWARE ARCHITECTURE

The software architecture is shown in Figure 2 and employs a layered structure which includes software resident on the hardware controller devices, low level and high level subsystem commands, procedural commands and the user interface including real-time displays. A brief description of each element contained within Figure 2 is given in Table 2.

The software layers allow the system to be viewed with increasing abstraction typical of an object oriented design. Information about a subsystem is available only at the appropriate layer and complex high level commands and procedures are built from simpler lower level commands. For example, the `hri` command (or object) allows the operator access only to the HRI detector, and the `xdamain` command allows access only to the motors. The `hridata` command located at a higher level has access to both the HRI and the motors and implements the concept of an HRI image taken at different locations in the focal plane. The `mcascan` command combines the acquisition of proportional counter spectra (`mcadata`), shutter motions (`flapper`) and motor stage motions (`xdamain`) to implement arbitrary scanning capability. The highest level commands apply specific analysis to data obtained from the lower levels (e.g., `mcaalign` calculates the mirror alignment error), or further combine functions (e.g., `hrialign` coordinates the shutter motion and HRI image acquisition, then calculates the mirror alignment errors).

The concept of information hiding also applies to the coordinate systems found within the XDACS1 software. The low level `xdamain` program receives motor move requests in XDA coordinates which are transformed and maintained in the motor-specific coordinates required by the motor controllers. At the highest level, the mirror alignment errors are calculated by `hrialign` and `mcaalign` in the XRCF coordinate system.

The client/server model featured in the software architecture also resulted from the object oriented design approach. For example, the implementation of `mca ds` as a server allows multiple real time displays of proportional counter data to execute simultaneously on workstations located in different locations. The clearly defined dependence of a client on a server also allows straightforward startup and shutdown sequences for the multiple processes constituting the system. The client/server model was also applied between the PC controllers and the SUN 4/330 using TCP/IP sockets.

Commands at all levels are available to the operator from the shell. High level commands are shell scripts written in korn shell (ksh) that integrate low level commands typically written in C or C++. The ksh is used both as a familiar interface for the operator and as an integration 4GL. The string manipulation and pattern matching features of ksh were used to construct file names in the high level scripts and relieved the lower level C and C++ programs from such manipulation. Other standard UNIX tools such as `awk`, `bc`, `date`, `wc`, etc., were also used extensively. The UNIX philosophy was extended to provide online documentation in the "man" page format.

The layered software architecture is extensible. New hardware subsystems may be added in a straight forward

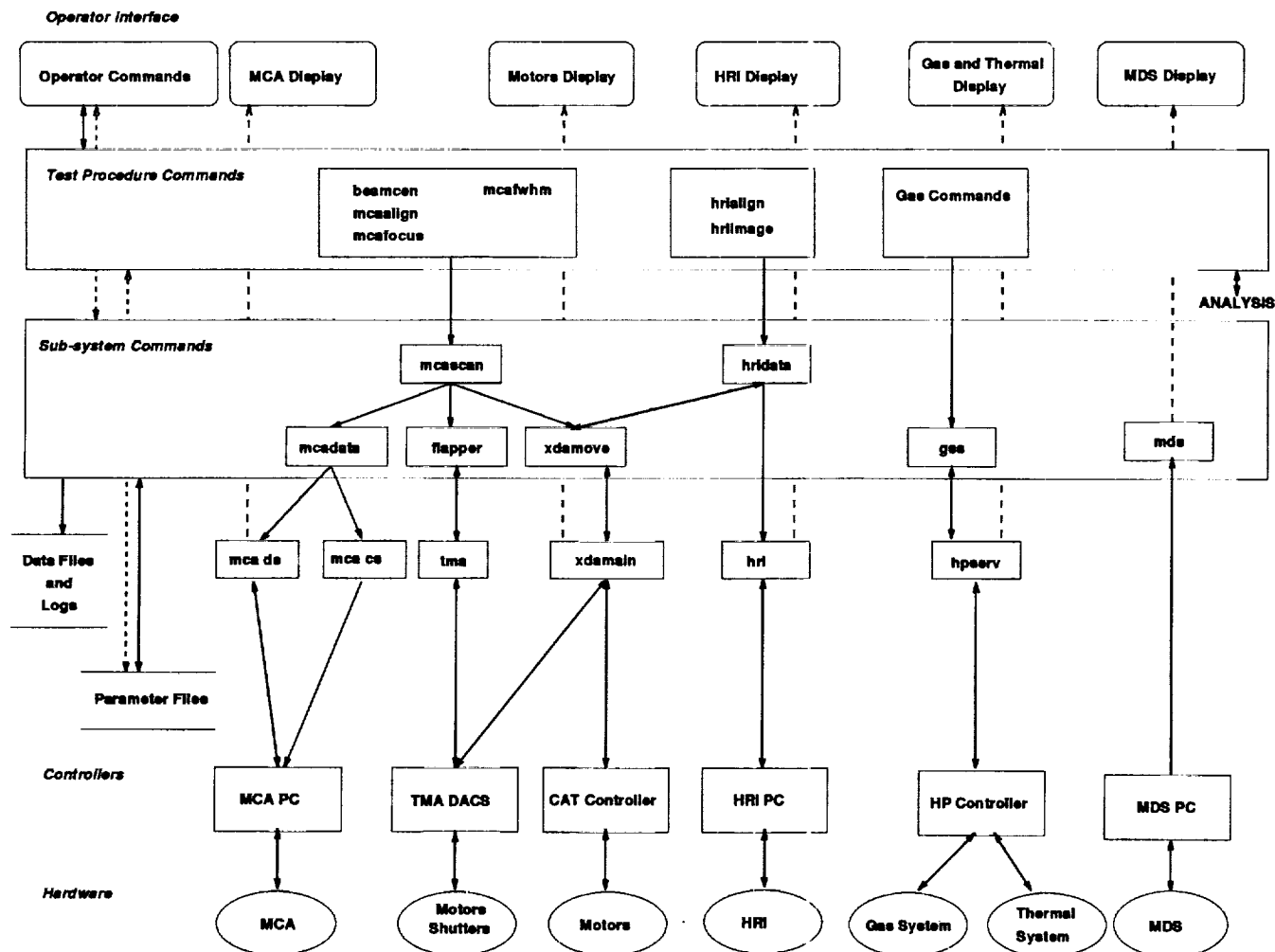


Figure 2: The XDACS software architecture employs a layered structure with hardware denoted by an ellipse and programs denoted by squares. Arrows indicate the direction of information flow (there is no significance in dashed arrows other than they pass behind another box). Commands flow down the Figure and data and status flow from the hardware up to the displays and data archive.

manner, often reusing code. Typical steps are (a) writing a hardware controller program, (b) creating a format for the archived data product, (c) writing a display/monitor program, and (d) writing the appropriate scripts to integrate with other existing subsystems.

A variety of analysis software was required by both the high level software and the operator. Access to analysis functions is shown from the **test procedure commands** layer in Figure 2 and is described at the end of Table 2. The majority of analysis routines were developed within the Image Reduction and Analysis Facility (IRAF) environment and the remaining functions were coded as standalone programs. IRAF is an analysis environment used extensively by Astronomers for multiwavelength data reduction and analysis, and provided many of the tools required for VETA test data analysis.

TABLE 2: SOFTWARE MODULE DEFINITION

MODULE	DESCRIPTION
<i>Operator Interface Layer</i>	
Operator Commands	Commands are entered at the keyboard and the operator is prompted for parameters. Statistics and status information, in addition to real-time data, are displayed as commands execute. Operator may access commands from the Test Procedure and High/Low-level Subsystem levels.
MCA Display	Displays proportional counter spectra from four MultiChannel Analyzer (MCA) buffers simultaneously in an X-window. The display program is a client of the MCA data server program (mca ds) and requests data every second. The operator may zoom on a region of interest and display specific channel counts with the cursor. Statistics and status displayed and updated include: counts in the region of interest, max and min counts, integration time and dead time.
Motors Display	Positions of motors are updated as commands execute. Current position, min and max allowed ranges and limit switch status are displayed for the three TMA motor stages, four CAT motor stages and four shutters.
HRI Display	Displays High Resolution Image (HRI) photon event data in X-window as received from the hri server. Operator may pan, zoom, alter color map and read pixel values with mouse.
Gas/Thermal Display	Displays gas pressures, valve status, temperatures and other status information with updates every 5 seconds. Parameter permitted ranges are also displayed and operator is required to acknowledge alarms for out of range conditions. The display program requests data from the hpserv server.
MDS Display	Displays Motion Detection System (MDS) data received from the mds server. Average displacements in the $y - z$ focal plane are updated each second and displayed as a scatter plot and in projection. Operator may select scale of plot.
<i>Test Procedure Command Layer</i>	
beamcen	Beam centering command. Performs 1-D counter/aperture scan in y and z centered on current beam location. Calculates centroid of each scan, updates beam center and outputs plot/data sheet. Used iteratively with smaller apertures to find X-ray beam center.
mcaalign	Generates mirror alignment errors. Performs 2-D counter/aperture scan around current beam center with the four shutters opened and closed at each scan point. Builds four images from completed scan, calculates P1/H1 mirror alignment tilt and focus errors from centroids, and outputs data sheet. Used iteratively with smaller apertures to provide VETA-I alignment corrections < 1 arcsec.
mcafocus	Generates focus error. Performs 2-D counter/aperture scan around current beam center with two shutters opened and closed at each scan point. Builds two images from completed scan, calculates the focus error, moves to new focus and outputs data sheet. Used to fine tune focus once alignment process is complete.
mcafwhm	FWHM scan. Performs 1-D counter/aperture scan around current beam center, calculates FWHM and outputs plot/data sheet. Used to characterize the VETA-I PRF.
hrialign	Generates mirror alignment errors. Acquires HRI images of the X-rays from each quadrant of the VETA-I by successively opening each shutter with the other three closed. Calculates tilt and focus errors from the centroids of each image, and generates data sheet. Used iteratively to provide VETA-I alignment corrections > 1 arcsec.
hriimage	HRI image. Acquires a single HRI image, calculates simple statistics (centroid, min, max) and generates a data sheet.

TABLE 2: SOFTWARE MODULE DEFINITION (CONT.)

MODULE	DESCRIPTION
gas commands	Gas system procedures are implemented as operator defined scripts of sequences of gas system commands, e.g., change gas, startup and shutdown procedures. Commands include open and close valves, read pressure transducers, set pressure set points and read thermistors.
<i>High-level Subsystem Command Layer</i>	
mcascan	Counter/aperture scanning program. The program is capable of performing a general 3-D scan with any counter/aperture pair. Consolidates all scanning calls from upper layers in one program and incorporates shutter (flapper) movements.
mcadata	Program is run every time data are taken with proportional counters. Clears the four MCA buffers, sets the requested integration time, starts the integration and stores the resulting spectra in an XDACS1 archive file. mcadata sends commands to the MCA command server (mca cs) and receives data from the MCA data server (mca ds).
flapper	Performs open/close operations on the four shutters located at the entrance to the VETA-I. The program is called from mcascan during alignment and focus tests such as mcaalign and mcafocus. Calls the low level tma program.
xdamove	Performs coordinated counter and aperture motor moves, backlash removal, applies offsets to current beam center if requested, determines if motors need to be moved based on current configuration and knowledge of motor accuracy, writes to high level motor log and file headers. Operates as an interface to the lower level xdamain program.
hridata	Program moves HRI to desired position and acquires a single image. Sends commands to the HRI via hri and makes motor moves with xdamain.
gss	Gas system commands, either single or as part of gas system procedures, are implemented as requests to the HP server (hp serv).
mds	Program is a client of the MDS server running on the MDS PC, makes a request every second for MDS data and passes average 1 second data to display. Stores raw and average MDS data in XDACS1 archive file.
<i>Low-level Subsystem Command Layer</i>	
mca ds	MCA data server returns MCA display client with data received from MCA PC. Communicates with MCA PC via TCP/IP.
mca cs	MCA command server passes MCA commands to the MCA PC via TCP/IP.
tma	Passes TMA commands to the TMA PC controller software via RS232. Performs low level string parsing, error checking and logging.
xdamain	The program interfaces with both the CAT and TMA motor controllers via IEEE 488 and RS232 respectively, to move motors and monitor motor status. Motor moves are made in either the XDA coordinate system (thereby hiding the motor specific coordinate systems) or in the motor specific system.
hri	Communicates with the HRI PC controller software via TCP/IP. Provides a command line interface to the HRI command set allowing exposure start and abort.
hp serv	HP server interfaces with the HP 3752A controller via IEEE488. Serves the gss client, performs bus level error checking and logging.
<i>Hardware Controller Layer</i>	
MCA PC	Software interfaces with the MCA hardware, passes on commands from the mca cs and returns data and status to the mca ds via TCP/IP. Data files are written directly to the XDACS1 archive via an NFS mounted disk.
CAT Controller	Sequences of COMPUMOTOR controller commands allow single axis motor moves and control parameters such as motor speed, limits and acceleration. The sequences are used by xdamain only and are not available to the operator.

TABLE 2: SOFTWARE MODULE DEFINITION (CONT.)

MODULE	DESCRIPTION
TMA DACS	The software was inherited from a previous test and was left unchanged. The <code>tma</code> and <code>xdamain</code> programs pass commands as strings which are executed as though they are typed by an operator at the TMA PC keyboard.
HRI PC	Software interfaces with the HRI electronics via a custom board and implements commands received via TCP/IP from the <code>hri</code> program.
HP Controller	The HP 3752A code is written in BASIC and applies the voltage-to-temperature transformation to thermistor readings, and sends and receives status from gas system commands.
MDS PC	Interfaces with the MDS hardware and executes the MDS data server process ³ .
<i>Other Architectural Elements</i>	
ANALYSIS	Software called by programs in the Test Procedure Commands layer. Analysis routines were developed in the IRAF environment ⁴ and made available from the shell. File conversions into IRAF compatible formats are performed by analysis routines. Other analysis software available included <code>PVWAVE</code> and standalone programs.
Data Files & Logs	Programs in the Subsystem Commands layer generate the XDACS1 archive data files containing raw and processed data e.g., raw MCA spectra, reduced 1-D and 2-D scan data, and raw HRI images. Logs are created at this and higher levels, e.g., gas system commands and alarms, all scan motor moves and operator commands.
Parameter Files	Each command is associated with a parameter file containing the current values, allowed ranges, type and default values of all parameters required to execute the command. The set of all parameter files are maintained in a single directory and represent a parameter data base for the entire system. The parameter files may be accessed through either a parameter interface library or from the command line ⁵ .

5. VETA DATA BASE AND ARCHIVE

During the VETA test a variety of data were archived by the XDACS1 including X-ray image data, proportional counter scan data (1D and 2D) thermal monitoring, gas system monitoring, motion stability measurements and other logging data.

The VETA test data archive was created during the VETA test as shown in Figure 3. Raw data streams were received from the various subsystems, processed and stored as formatted archive data. HRI and MCA X-ray data were stored together with a set of header keywords containing information about the data and test environment. Examples of header keywords include date, start time, finish time, integration time, operator, peak counts and filename. In the case of MCA scan tests two levels of data file were stored: raw spectra (one file for each point in the scan) and reduced scan data files containing the integrated counts as pixel values. In both cases header keywords were stored together with the data. The scan pixel values derived from the raw spectrum during the test represent "quick look" analysis since the integrated counts were derived by simply summing counts in a region of interest rather than correcting the spectrum for known physical effects.

In addition to the quick-look analysis performed during testing, more rigorous reduction and analysis was performed post-test that required flexible access to the archive. A set of data bases were constructed containing the header keywords generated during the test and information derived from the data file attributes. Data base queries typically generate a list of X-ray data filenames and their location within the archive.

The data base is comprised of four data base files in ASCII /rdb format:

- `mcahriscn`: common fields to both HRI and MCA data bases

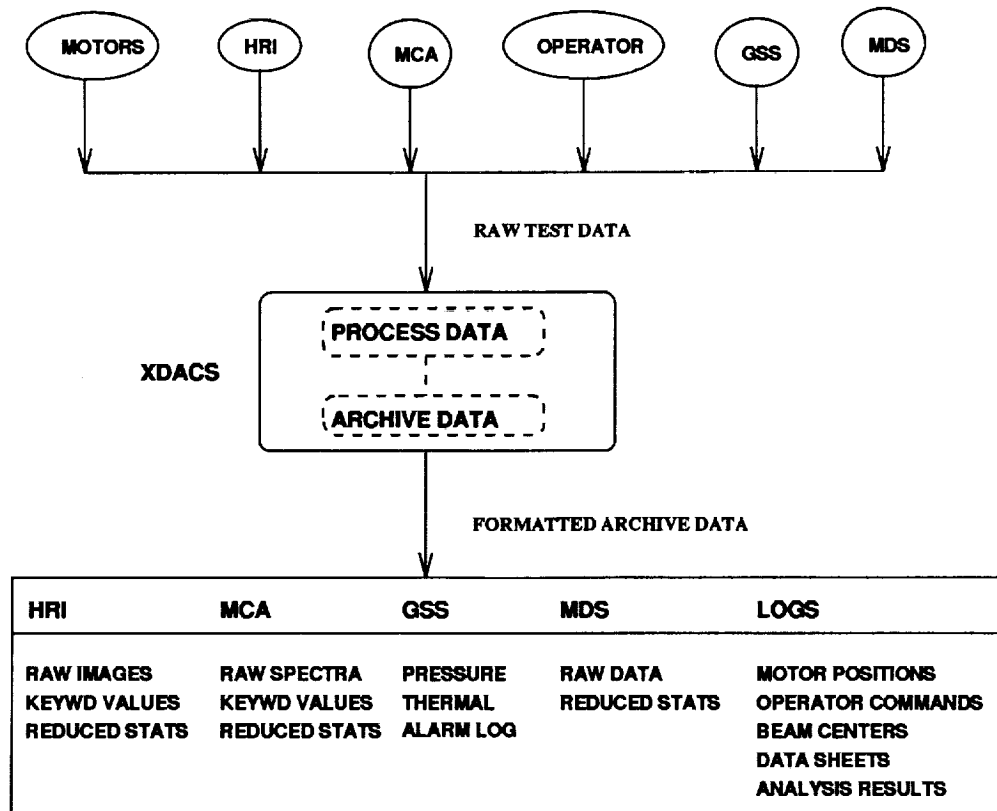


Figure 3: The VETA test data archive was constructed during the testing from both autonomous and non autonomous data streams.

- hriscn: HRI image file keywords
- mcascn: MCA scan file keywords
- mcapch: MCA raw proportional counter spectra keywords.

There are numerous fields in the data base, for example the names of the first 10 fields (of 79) within the "mcascn" data base are: scanId, aptype, bchan0, bchan1, counter, date, dcain, dcamv and dcbin.

Queries are made using /rdb in the UNIX environment, for example the command:

```
column date filename aptype < mcascn | row 'aptype=="annulus"'
```

selects the fields "date", "filename" and "aptype" from the mcascn database and then selects only those rows with the aperture type of "annulus". In this example the commands "column" and "row" are /rdb commands.

Archive extraction functions were developed to retrieve subsets of autonomous data sets such as gas system, thermal and MDS data. These subsets are combined with the data files accessed through data base queries to construct time correlated test data sets. The process is usually performed automatically using a shell script.

6. SUMMARY

We have presented the network and software architecture of the X-ray Data Acquisition and Control System used to control, archive and display data during the AXAF VETA-I X-ray test. The key features of the network architecture include: diverse hardware subsystem control from a single SUN workstation, isolation of critical functionality on

front-end controllers, integration of a variety of bus types and extensibility. The key features of the software architecture include: layered object oriented design, access to commands at all layers, client/server model, use of ksh for 4GL integration and extensibility. The VETA test data base provides convenient access to data stored in the data archive from the UNIX shell.

The VXDS system will form the basis for the next generation of equipment for testing of the assembled AXAF flight mirrors and science instruments. The software and network architecture developed for the VXDS system proved robust and will be extended to accommodate the new hardware anticipated for the next generation system.

7. ACKNOWLEDGEMENTS

The authors extend thanks to Eric Mandel for enthusiastic support throughout the system development and test, and in particular for providing so much of the parameter interface library. This work is supported by NASA contract NAS8-36123.

8. REFERENCES

1. W. A. Podgorski, *et al.*, 1992, "The VETA X-ray Detection System", this volume.
2. D. A. Schwartz, P. J. McKinnon, S. S. Murray, L. P. Van Speybroeck, M. V. Zombeck, C. C. Dailey, J. C. Reily, and M. C. Weisskopf, 1985, 2nd International Technical Symposium on Optical and Electro-Optical Applied Science and Engineering, Cannes, France, December, 1985.
3. J. Arenberg, *et al.*, 1992, "Motion Detection System", this volume.
4. D. Tody, 1986, in *Instrumentation in Astronomy VI*, ed., D. L. Crawford, Proc. *SPIE*, **627**, 733.
5. J. B. Roll, Jr. and E. Mandel, 1992, "The Parameter Interface" in NASA Workshop: *User Interfaces for Astrophysical Software*, April 14-15, Goddard Space Flight Center, ed., E. Mandel.

Correcting X-ray Spectra obtained from the AXAF VETA - I Mirror
Calibration for Pileup, Continuum, Background and Deadtime.

G. Chartas, K. Flanagan, J. P. Hughes, E. M. Kellogg, D. Nguyen, M. Zombeck
Center for Astrophysics
60 Garden Street
Cambridge, MA 02138

M. Joy and J. Kolodziejczak
Space Science Laboratory
George C. Marshall Space Flight Center
Huntsville, AL 35812

Abstract

The VETA-I mirror was calibrated with the use of a collimated soft X-ray source produced by electron bombardment of various anode materials. The FWHM, effective area and encircled energy were measured with the use of proportional counters that were scanned with a set of circular apertures. The pulsers from the proportional counters were sent through a multichannel analyzer that produced a pulse height spectrum. In order to characterize the properties of the mirror at different discrete photon energies one desires to extract from the pulse height distribution only those photons that originated from the characteristic line emission of the X-ray target source.

We have developed a code that fits a modeled spectrum to the observed X-ray data, extracts the counts that originated from the line emission, and estimates the error in these counts. The function that is fitted to the X-ray spectra includes a Prescott function for the resolution of the detector a second Prescott function for a pileup peak and a X-ray continuum function. The continuum component is determined by calculating the absorption of the target Bremsstrahlung through various filters, correcting for the reflectivity of the mirror and convolving with the detector response.

Introduction

The VETA-I (Verification Engineering Test Article-I) consists of a pair of Wolter Type-I mirrors which are intended to be used as the outermost set of the AXAF (Advanced X-ray Astrophysical Facility) telescope. A detailed description of the performance and scientific advances anticipated from AXAF observations are listed in reference¹. The improved sensitivity of the AXAF mirrors compared with those of the Einstein and ROSAT X-ray telescopes results mainly from the larger attainable effective area of AXAF over a broader energy bandwidth and the higher angular resolution resulting

from improvements in the mirror figure and surface smoothness. A natural consequence of these improvements is the need to use detectors with higher spatial and energy resolution and the need to employ more sophisticated data reduction techniques. The physical properties of the VETA-I optic measured are the FWHM, the effective area and encircled energy. Definitions of these quantities are given in Kellogg et al². For the initial analysis of the VETA-I proportional counter spectra we used a quick-look analysis technique which basically involved the summation of counts in a selected region of interest. The quick-look data provided a fair description of most of the mirrors properties with a moderate amount of analysis. In this paper we will describe a more elaborate method for analyzing the VETA-I data which leads to a determination of the mirror effective area to better than 5% and the encircled energy better than 2%. In our analysis we will apply a set of corrections for the spectral contamination of the measured proportional counter data due to the existence of a bremsstrahlung component in the X-ray source, pulse pileup effects which distort the spectrum, background and deadtime.

In section 1 we provide a brief outline of the experimental setup. A detailed description of the model employed for the data reduction is given in section 2. Finally section 3 is devoted to the presentation of the results of the VETA-I data reduction and a discussion of the effect of these corrections on the measured mirror properties.

1.0 The VETA-I calibration set up

The VETA-I calibration set-up is shown in figure 1. An electron impact X-ray source with interchangeable targets and filters is located 528 m away from the optic in order to approximate an incident plane wave. The parabola P1 and hyperbola H1 mirrors are made out of zerodur and were supported by flexures. Their relative alignment and centering were adjusted with a set of linear actuators. The X-ray flux incident on the VETA-I

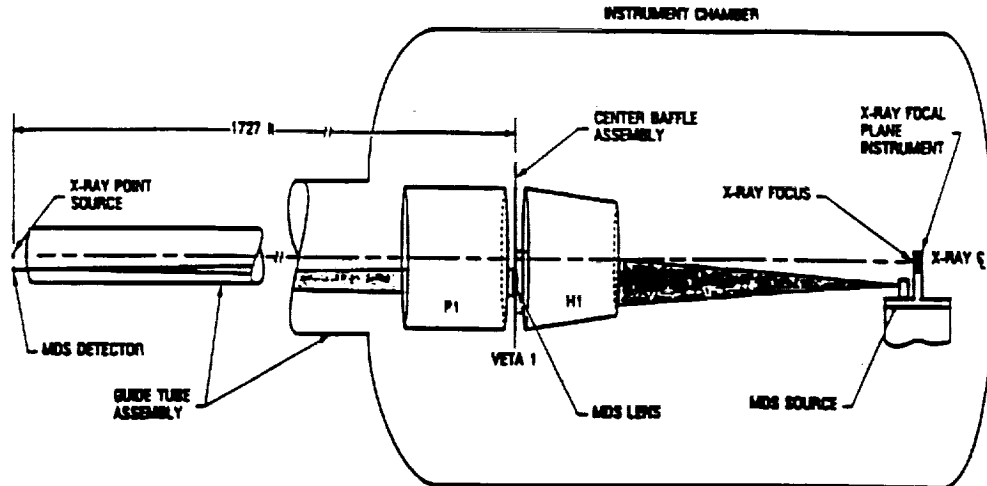


Figure 1. VETA-I calibration set up

was monitored by sealed and flow proportional counters manufactured by LND Inc. while an identical pair of sealed and flow counters were located at the focal plane of the VETA approximately 10 meters behind the optic. The flow counters have a graphite coated 1.7 μm thick polypropylene window. For energies below 1.49 keV the flow counters were filled with methane at a pressure of 250 Torr while for energies above 1.49 keV a mixture of 90% Ar and 10% methane (P10) at a pressure of 400 Torr was used. The electronics associated in acquiring the data are shown in figure 2. A set of periodic pulsers (not shown in the figure) were injected into 2 multichannel analyzer (MCA) channels in order to monitor the deadtime of the pulse height system. The focused X-ray image was scanned by translating a plate containing a set of pinholes, slits and annuli across the image with a position accuracy of approximately 1 μm .

2.0 Model of the VETA-I monitor and focal plane proportional counter spectra

The description of our model will trace the sequence of events traced by X-ray photons as they are produced through the deceleration of electrons in various targets, transmitted through filters to minimize the bremsstrahlung component, reflected by the P1-H1 mirrors and finally absorbed inside a proportional counter. The resulting pulses are fed into a multichannel analyzer which converts their relative pulse height to a channel address.

2.1 X-ray source spectrum

For the analysis of the VETA-I data we have adopted Kramers relationship for the bremsstrahlung emission of the soft X-ray source:

$$I(E) = kZ(E_{\text{max}} - E) \quad (1)$$

where E_{max} is the high voltage of the source anode, Z is the atomic number of the target and k is a fitted parameter with units of inverse energy. The spectra that we obtained from the beam monitor detectors allow a direct fit to the continuum component at energies above the characteristic X-ray lines.

2.2 Transmission of source filters and counter windows

In section 2.6 we will show that one of the main contributors to the error in the derived focal plane (XDA) and beam monitor detector (BND) events is the continuum component under the line peak. In order to minimize the bremsstrahlung intensity under the peak a source filter is used with an absorption edge slightly higher in energy than the characteristic line. The properties of the source filters used in the VETA-I test are shown in table (1). The errors quoted by the manufacturers are near 30% and are due to errors in the measuring technique. The effective source filter thickness is the thickness determined by fitting an ensemble of BND spectra and performing a grid search of filter thickness vs. the ensemble average χ^2 as shown in figure 3. The 68.3% confidence level is just χ^2_{min} (unreduced) +1. Similarly an ensemble of BND spectra are fitted in order

Proportional Counter Subsystem

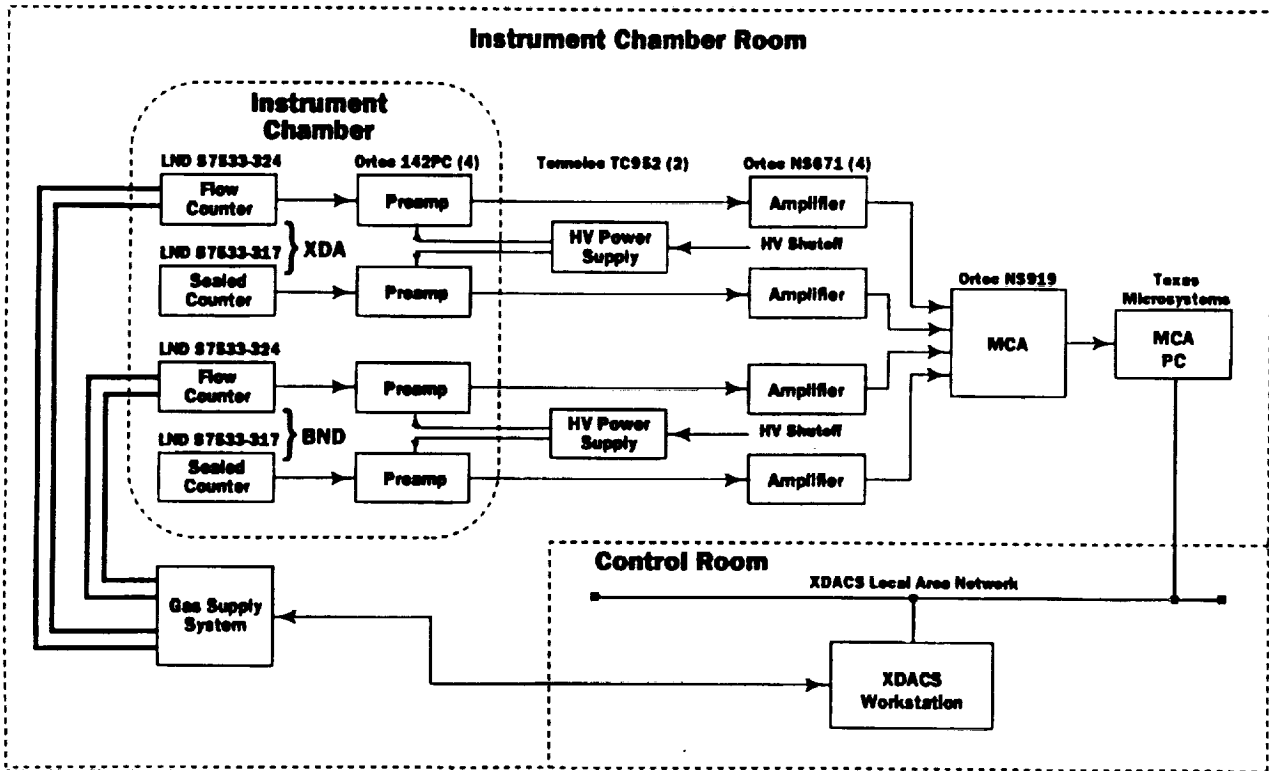


Figure 2. Proportional counter electronics

to determine the strength of line and continuum emission of the X-ray source.

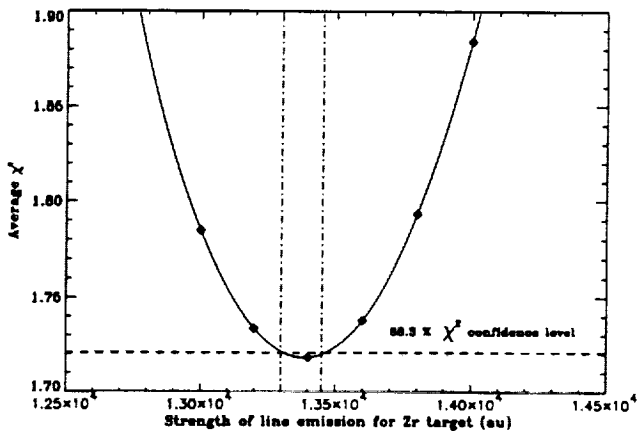
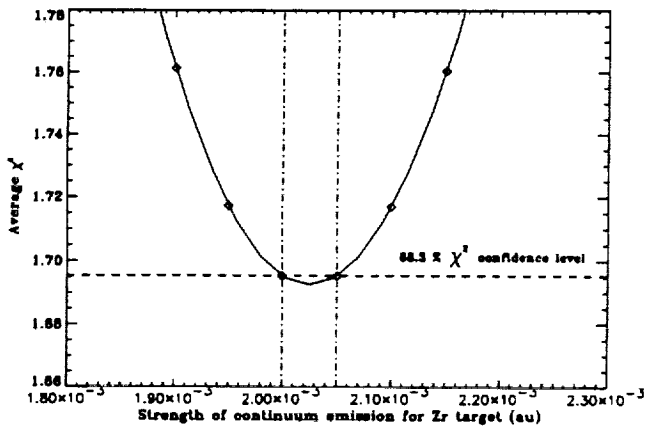
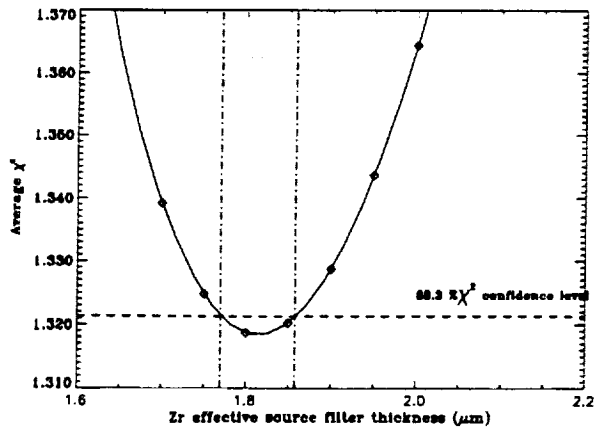


Figure 3. χ^2 grid search for source filter thickness, line strength and continuum strength

The ratio of the effective thickness to the nominal value for the thicknesses ranged between 0.9 for Zr and approximately 2.6 for Mo. An independent measurement of the Mo thickness performed in a post VETA test provided similar results for the effective filter thickness and strongly suggests an error in the labeled Mo nominal filter thickness.

Table 1:

Source filters	Nominal Thickness ρd_n	Effective filter thickness ρd_{eff}
Parylene	$2.20 \times 10^{-4} \text{ gr cm}^{-2}$	$(1.7 \pm 0.1) \times 10^{-4} \text{ gr cm}^{-2}$
Al	$2.70 \times 10^{-3} \text{ gr cm}^{-2}$	$(2.8 \pm 0.1) \times 10^{-3} \text{ gr cm}^{-2}$
Mo	$2.04 \times 10^{-3} \text{ gr cm}^{-2}$	$(5.36 \pm 0.05) \times 10^{-3} \text{ gr cm}^{-2}$
Zr	$1.29 \times 10^{-3} \text{ gr cm}^{-2}$	$(1.17 \pm 0.03) \times 10^{-3} \text{ gr cm}^{-2}$
Cu	$4.48 \times 10^{-4} \text{ gr cm}^{-2}$	$(5.82 \pm 0.5) \times 10^{-4} \text{ gr cm}^{-2}$

2.3 Resolution, efficiency and uniformity of proportional counters used in the VETA-I calibration

The resolution function $R(E)$ of a proportional counter provides the response of a counter for an incident monoenergetic beam of X-rays of energy E . Various resolution functions have been determined theoretically by studying the statistics of secondary electrons produced by the primary photoelectrons and the multiple electron avalanches initiated by each secondary electron. For energies above 2 keV the response can be approximated with a Gaussian with a mean proportional to the energy and a FWHM proportional to $E^{1/2}$. This approximation breaks down however at low energies where one observes an asymmetry in the response. This is mainly due to the small number n of avalanches produced per secondary electron ($n = \text{the energy of the electron} / \text{ionization energy}$) and consequently for low energies one does not expect, according to the central limit theorem, to obtain a Gaussian distribution.

For the present analysis the resolution of the proportional counter is approximated by a function first derived by Prescott³ which takes into account the statistics of multiple avalanches. The Prescott function has the form:

$$F(x) = \frac{N \left(\frac{m}{x}\right)^{3/4}}{\sqrt{4\pi m Q}} \exp\left(2\sqrt{\frac{mx}{Q^2}} - \frac{(m+x)}{Q}\right) \quad (2)$$

where the mean \bar{x} of the distribution is $\bar{x} = m/Q^2$ and the standard deviation is $\sigma = \sqrt{2mQ}$, Q is the Prescott

width parameter. By minimizing the Prescott function $F(x)$, $\frac{d}{dx}F(x) = 0$, one can derive the following relationship between the mean and the width parameter:

$$\frac{m}{x_{max}} = 1 + \frac{3}{2} \frac{Q}{x_{max}} + \frac{9}{16} \frac{Q^2}{x_{max}^2} \quad (3)$$

In our algorithm the m and Q parameters of the line component of the spectrum are fitted parameters. For the determination of the measured continuum component one requires to know the width parameter vs. energy in order to convolve the detector response with the modeled incident continuum component over the measured energy band.

By fitting a range of X-ray lines we have produced an empirical expression for $Q(E)$ for E in the range of 0 to 2.5 keV:

$$Q(E) = a_0 E + a_1 E^2 + a_2 E^3 + a_3 E^4 \quad (4)$$

with $a_0 = 0.08514$, $a_1 = -0.13751$, $a_2 = 0.08026$, $a_3 = -0.01552$

The measured energy resolution and Prescott Q parameter for the proportional counters used in the VETA test are shown in figure 4.

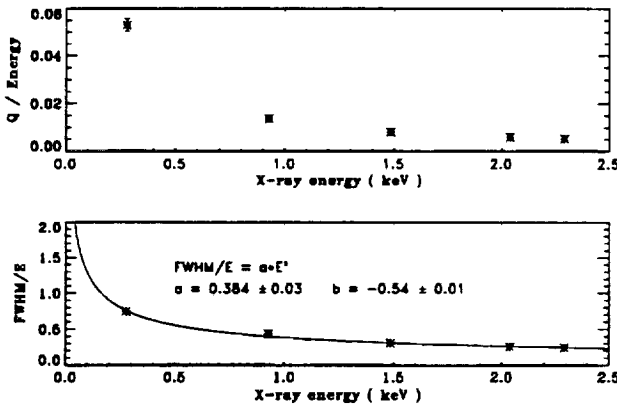


Figure 4. Measured Prescott Q parameter and proportional counter energy resolution

2.4 Peak pileup correction

Soft X-ray spectra obtained during the VETA -I calibrations show evidence of peak pileup at high counting

rates. Each pileup count corresponds to 2 events that were not separately detected in the multichannel analyzer. At energies below the 1.49 keV Al line the poor detector energy resolution does not allow a direct determination of the pileup component. The pileup peak represents a small distortion to the spectrum and is corrected for by performing a simultaneous fit to the line and pileup peak. This fit provides a relation between the percent pileup counts and the total event rate. The measured pileup versus total event rate is shown in figure 5.

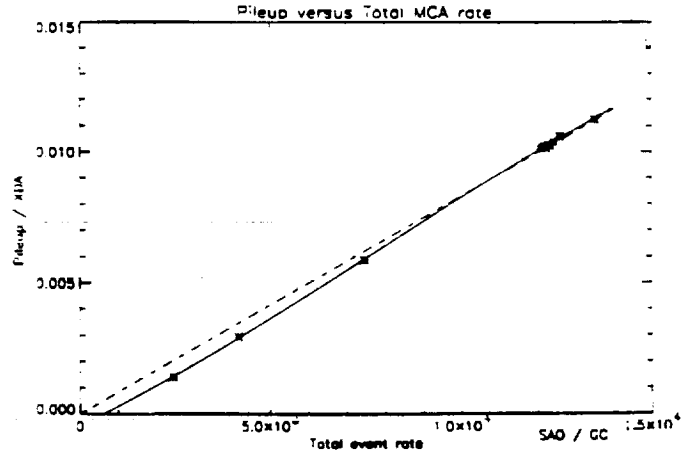


Figure 5 Measured pileup rate vs. total MCA event rate

We have compared our results to a theoretical model presented in Johns and Yaffe⁴ which predicts that the percent pileup follows the equation:

$$\frac{N_{pu}}{N_{XDA}} = (1 - e^{-2\rho\tau}) \quad (5)$$

where N_{XDA} are the total number of focal plane events originating from the X-ray line, N_{pu} are the photon events that are piled up, ρ is the average photon event rate (from all MCA channels) and τ is the characteristic time of the MCA. The theoretical prediction is also shown in figure 5. The fitted value for τ is $1.85e-7$ sec. The measured pileup fraction $f(\rho)$ is fit to a 3rd degree polynomial:

$$f(\rho) = b(1)\rho + b(2)\rho^2 + b(3)\rho^3$$

where $b(1) = 4.845e-7$, $b(2) = 5.876e-11$, $b(3) = -2.441e-15$

2.5 Extraction of X-ray line counts

The function that describes the model fitted to the focal plane spectrum has the form:

$$f_{XDA}(i) = f_{line}(i) + f_{cont}(i) + f_{pu}(i) + f_{bgd}(i) \quad (6)$$

where $f_{XDA}(i)$ are the counts in the MCA pulse height channel i , f_{line} is the X-ray line component which includes all excited K and L lines and their escape peaks and is attenuated by the mirror reflectivity, f_{cont} is the continuum part of the spectrum which also contains the fluorescence radiation that escapes the counter and the effect of the mirror reflectivity, f_{pu} is the pileup component and f_{bgd} is the normalized for live time background. In the calculation of the continuum and line component we perform a convolution of the detector response $R(E_i, E_j)$ with the incident X-ray spectrum. The incident spectrum is a sum of ni X-ray lines of strength $a_1 * s(E_j)$, where $s(E_j)$ is the relative intensity of line E_j obtained from reference⁵, and a bremsstrahlung emission $Brem(E_k)$ of strength a_2 . For the focal plane spectrum we include the effect of reflectance off the mirror by multiplying with the model effective area $A(E_j)$ as determined by ray tracing the P1-H1 mirror surface and using Henke 90 optical constants for zerodur. The input model effective area of the VETA-I is shown in figure 6 together with the energies at which the calibration was performed.

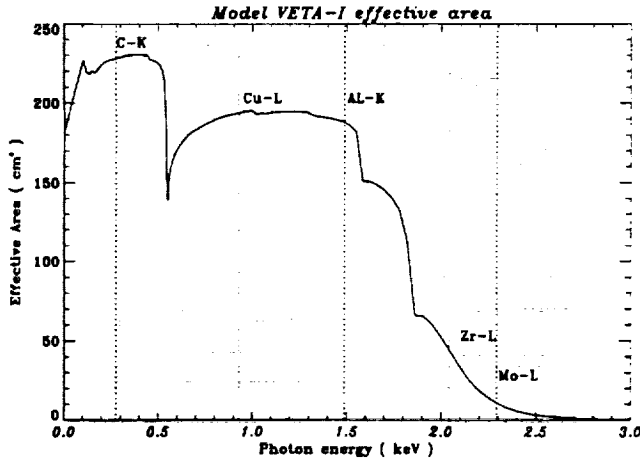


Figure 6. Input model effective area of the VETA-I

The line component of equation (6) is calculated by using the expression:

$$f_{line}(i) = a_1 \sum_{j=1}^{ni} s(E_j) T_f(E_j) T_w(E_j) Abs(E_j) A(E_i)$$

$$\times [(1 - esc(E_j, E_i)) R(E_i, E_j) + esc(E_j, E_i) R(E_i, E_j - E_i)]$$

For the continuum component we used:

$$f_{cont}(i) = a_2 \sum_{k=1}^{ph} T_f(E_k) T_w(E_k) Abs(E_k) Brem(E_k) \times [(1 - esc(E_k, E_i)) R(E_i, E_k) + esc(E_k, E_i) R(E_i, E_k - E_i)]$$

T_f and T_w are the transmission of the source filter and counter window respectively, $Abs(E_j)$ is the efficiency of the counter, $esc(E_i, E_j)$ is the probability of a fluorescence photon of energy E_i escaping from the counter times the fluorescence yield.

The background component is normalized to take into account differences in the live time between the background run and the test run. $f'_{bgd}(i)$ is the measured background MCA spectrum.

$$f_{bgd}(i) = \frac{t_{int} \times (1 - dt_{bgd})}{t_{bgd} (1 - dt_{MCA})} f'_{bgd}(i)$$

where t_{int} is the integration time, t_{bgd} is the integration time of the background run, dt_{bgd} and dt_{MCA} are the deadtime of the background run and test run respectively.

For extracting the counts that originated from the X-ray line emission we begin by fitting the model function of equation (6) to the spectrum using a Marquardt nonlinear least squares routine. We select a region of interest (ROI), determined by the XDA MCA channels (m_0, m_1) and BND MCA channels (n_0, n_1), around the line peak and sum the measured pulse height counts. We then subtract the fitted continuum component in the ROI, subtract the pileup in the ROI, add the fitted line counts outside the ROI, add two times the total pileup counts (every pileup count corresponds to two events detected as one count) and finally subtract the normalized background counts. The extracted line counts for the focal plane detector $XDA_{p,c,b}$, corrected for pileup, continuum and background effects, are given by the expression:

$$XDA_{p,c,b} = \sum_{i=m_0}^{m_1} S_{XDA}(i) + \sum_{i=0}^{m_0-1} f_{line}(i) + \quad (7)$$

$$+ \sum_{i=m_1+1}^{m_{max}} f_{line}(i) + 2. \times N_{pu} - \sum_{i=m_0}^{m_1} f_{pu}(i) -$$

$$- \sum_{i=m_0}^{m_1} f_{cont}(i) - \frac{t_{int} \times (1. - dt_{bgd})}{t_{bgd} \times (1. - dt_{XDA})} f_{bgd}$$

The extracted line counts for the beam monitor detector $BND_{c,d}$, corrected for continuum and background are:

$$BND_{c,d} = \sum_{i=n_0}^{n_1} S_{BND}(i) + \sum_{i=0}^{n_0-1} f_{line}(i) +$$

$$+ \sum_{i=n_1+1}^{n_{max}} f_{line}(i) - \sum_{i=n_0}^{n_1} f_{cont}(i) -$$

$$\frac{t_{int} \times (1. - dt_{bgd})}{t_{bgd} \times (1. - dt_{BND})} f_{bgd}$$

where $S_{XDA}(i)$ and $S_{BND}(i)$ are the counts in pulse height channel i from the total focal plane and beam monitor proportional counter spectra, dt_{XDA} and dt_{BND} are the deadtime in the MCA channels that contain the XDA and BND spectra respectively.

The BND count rate is significantly lower than the XDA count rate and pileup effects are less than 0.1% and for this reason we have not included a pileup correction for the beam monitor spectra.

2.6 Error analysis implemented in spectral extraction

The objective of the VETA-I calibration was to measure the encircled energy with 2% precision and the effective area to 5%. In the present analysis we will present the calculated 1σ error components of the measured effective area that are due to fitting errors, pileup effects, bremsstrahlung, continuum, background subtraction and the deadtime correction. We now proceed in propagating errors through equations (7) and (8) that give the focal plane and beam monitor line events, in terms of the corresponding quantities in counts and percent deadtime.

$$\sigma_{XDA_{d,p,c,b}}^2 = \sigma_{XDA_{d,p,c}}^2 \left(\frac{1}{1 - dt_{XDA}} \right)^2 +$$

$$+ \sigma_{dt_{XDA}}^2 \left[\frac{XDA_{p,c,b}}{(1 - dt_{XDA})^2} \right]^2 \quad (9)$$

Subscripts d,p,c and b to a quantity refer to deadtime, pileup, continuum and background corrections to that quantity. $XDA_{p,c,b}$ are the counts in the XDA spectrum originating from line emission and corrected for pileup, continuum and background. The error contributions from each effect can be seen in the following equations where we have neglected errors in the deadtime for the background, which contributes less than 0.05%. The error in the focal plane counts is:

$$\sigma_{XDA_{p,c,b}}^2 = \sum_{i=m_0}^{m_1} S_{XDA}(i) + \sum_{i=0}^{m_0-1} f_{line}(i) +$$

$$+ \sum_{i=m_1+1}^{m_{max}} f_{line}(i) + 4. \times \sigma_{pu}^2 + \sigma_{pufit}^2 +$$

$$+ \sigma_{f_{cont}}^2 + \left(\frac{t_{int} \times (1. - dt_{bgd})}{t_{bgd} \times (1. - dt_{XDA})} \right)^2 \times \sum_{i=m_0}^{m_1} f_{bgd}(i) \quad (10)$$

For the error in the beam monitor counts we neglect the pileup terms due to the relatively low count rates measured in the BND detector.

$$\sigma_{BND_{c,b}}^2 = \sum_{i=n_0}^{n_1} S_{BND}(i) + \sum_{i=0}^{n_0-1} f_{line}(i) +$$

$$+ \sum_{i=n_1+1}^{n_{max}} f_{line}(i) + \sigma_{f_{cont}}^2 +$$

$$\left(\frac{t_{int} \times (1. - dt_{bgd})}{t_{bgd} \times (1. - dt_{XDA})} \right)^2 \times \sum_{i=n_0}^{n_1} f_{bgd}(i) \quad (11)$$

σ_{pu} is the standard deviation in the pileup counts, σ_{pufit} is the standard deviation of the pileup counts in the region of interest (m_0, m_1). The errors due to the deadtime correction are:

$$\sigma_{dt_{XDA}}^2 = \left(\frac{\sum_{i=m_4}^{m_5} S_{XDA}(i) - \sum_{i=m_2}^{m_3} S_{XDA}(i)}{t_{int} \times f_{p1}^2} \right)^2 \sigma_{fp1}^2 +$$

$$+ \left(\frac{1}{t_{int} \times f_{p1}} \right)^2 \times \left((0.289)^2 + \sum_{i=m_3}^{m_4} S_{XDA}(i) \right)$$

$$\sigma_{dt_{BND}}^2 = \left(\frac{\sum_{i=b_4}^{n_5} S_{BND}(i) - \sum_{i=b_2}^{n_3} S_{BND}(i)}{t_{int} \times f_{p2}^2} \right)^2 \sigma_{fp2}^2 +$$

$$\left(\frac{1}{t_{int} \times f_{p2}} \right)^2 \times \left((0.289)^2 + \sum_{i=n_3}^{n_4} S_{BND}(i) \right)$$

The pulse height channels over which the pulser counts appear in the XDA and BND MCA spectra are (m_4, m_5) and (n_4, n_5) respectively. Since the pulser used for the deadtime correction was periodic, the error in the pulser counts as measured in the MCA is :

$$\sqrt{\int_0^1 (x - \mu)^2 P(x) dx} = 0.289 \text{ counts}$$

while the error in the injected pulser rate is : $f_p = 0.289/t_{puls}$, where t_{puls} is the time over which pulser rate is measured.

The errors in determining the continuum component from the fit are:

$$\sigma_{f_{cont, XDA}}^2 = \sum_{j=0}^{np} \left[\sigma_{a(j)} \frac{\partial}{\partial a(j)} \sum_{i=m_0}^{m_1} f_{cont, XDA}(i) \right]^2$$

$$\sigma_{f_{cont, BND}}^2 = \sum_{j=0}^{np} \left[\sigma_{b(j)} \frac{\partial}{\partial b(j)} \sum_{i=n_0}^{n_1} f_{cont, BND}(i) \right]^2$$

The summations are performed over the np variables $a(j)$ for the XDA spectrum and $b(j)$ for the BND spectrum) of the continuum component;

source filter thickness, line strength, continuum strength, the Q Prescott parameter of the detector response, the m Prescott parameter and the model scaling factor.

3.0 Results and discussion

In figure 7 we present fits and their residuals to the beam monitor and focal plane spectra for Al, Zr, C and Mo source targets. The continuum component for the carbon spectrum was measured in a post VETA test where the proportional counter gain was set appropriately such that the high energy continuum could be fitted. A set of apertures with pinhole diameters ranging from 5 μ m to 20 mm were placed at the focal plane in front of the XDA proportional counter in order to measure the encircled energy at different radii. The calculated encircled energy using both quick look and fitting techniques are presented in figure 8. The difference between encircled energy calculated by each method is very noticeable for Zr and Mo. This can be explained by referring to the model effective area of the mirror in figure 6. Notice that near Zr the effective area curve is very steep. This implies that the attenuation of the continuum component in the XDA spectrum will be strongly dependent on energy, resulting in a line to continuum ratio in the region of interest quite different from the one measured in the BND spectrum.

Since the largest error component in determining the line counts in a spectrum originates from the continuum subtraction one desires to minimize the continuum counts in the ROI by selecting a ROI as small as possible around the X-ray line peak. Obviously for detectors with better energy resolution one may select narrower ROI's thus reducing the error due to the continuum subtraction. We have investigated the sensitivity of the calculated line events in the spectrum with the selected region of interest and found that it is insignificant. The variation of the calculated encircled energy with selected region of interest for both the quick look analysis technique and the spectral fitting technique is shown in figure 9. Notice that the quicklook analysis technique is very sensitive to the selected region of interest. Initial values for the effective area used in the fit to the focal plane spectra were obtained by ray tracing the VETA-I mirror and using optical constants as measured by Henke et al. The next iterative step is to repeat the analysis using the effective area as determined from the fits to the spectra as input to the code.

In table 2 we present the measured 1 sigma uncertainties in the XDA and BND line events. The error in the ratio XDA/BND at a certain energy reflects the measured uncertainty in determining the encircled energy (EE) at that energy, since the EE for our experimental setup is approximately $\pi \times \text{XDA/BND}$.

The energy scale of the pulse height channels is also determined with an iterative procedure. We initially locate the pulse height channel that corresponds to the peak of the smoothed spectrum. This value is used as an initial guess for the fitting routine which after a certain number of iterations provides the pulse height channel that corresponds to the maximum of the fitted line component of the spectrum. The pulse height

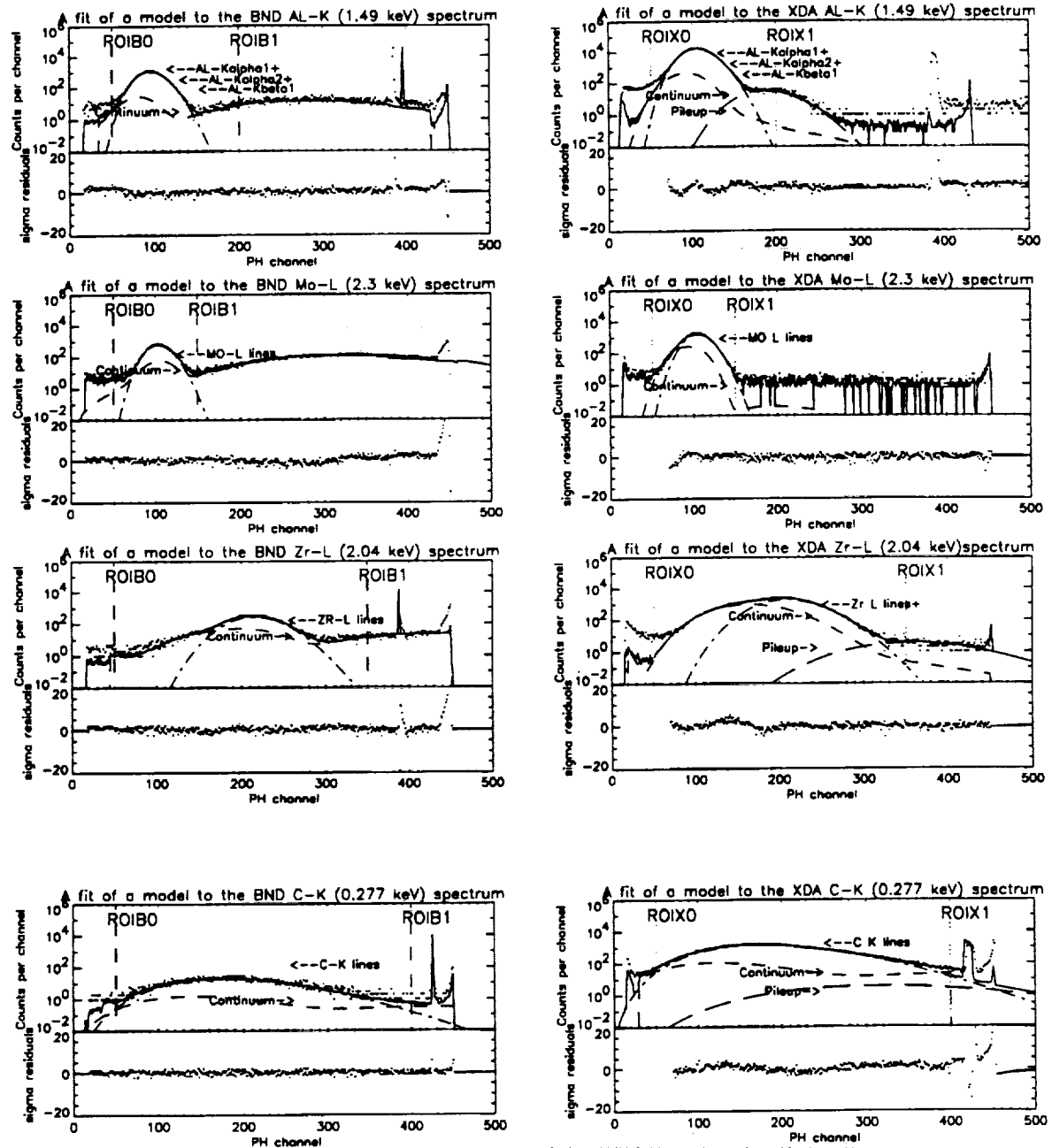


Figure 7. Fits and residuals of a model to Al,Zr,Mo and C VETA-I spectra

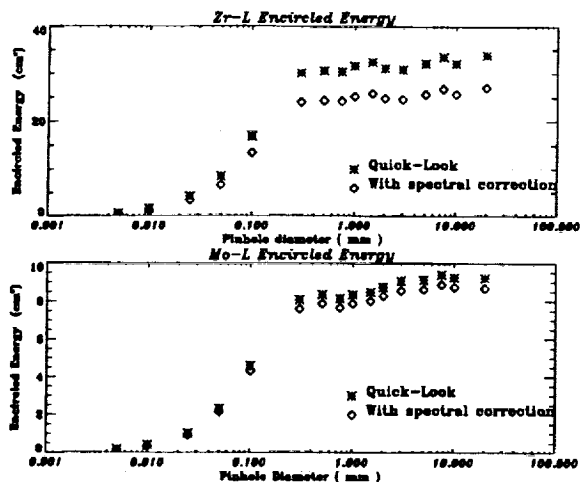


Figure 8. Measured encircled energy using both quick-look and fitting techniques

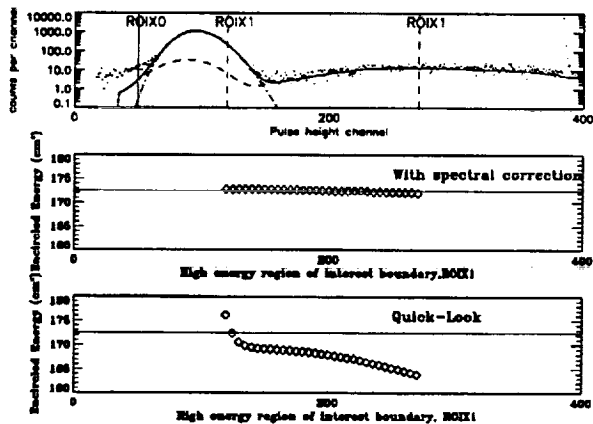


Figure 9. Variation of the measured encircled energy with selected region of interest for both the quick look analysis technique and the spectral fitting technique

energy scale is then recalculated using the corrected value for the line peak location. This procedure is especially effective when dealing with low count spectra and spectra with large continuum components.

The effects of X-ray transmission attenuation due to the proportional counter window mesh are

treated in a separate paper by Zhao et al⁶.

Table 2: Measured 1 sigma uncertainties in the XDA and BND line events

	C	Cu	Al	Zr	Mo
σ_{XDA}	0.37%	0.2%	0.17%	0.53%	0.68%
σ_{BND}	0.20%	1.1%	0.15%	0.66%	1.2%
$\frac{\sigma_{XDA}}{\sigma_{BND}}$	0.42%	1.2%	0.23%	0.85%	1.4%

Acknowledgments

We would like to acknowledge Dan Schwartz, Diab Jerius and Ping Zhao for useful conversations. The work reported here has been supported in part by NASA Contract NAS8 - 36123

References

1. Astro. Lett. and Communications, 1987, Vol. 26
2. Kellogg et al, SPIE 1992, this conf.
3. J. R. Prescott, "Photomultiplier single-electron statistics and the shape of the ideal scintillation line." Nuc. Ins. and Meth. 22 1963.
4. P. C. Johns and M. J. Yaffe, "Correction of pulse height spectra for peak pileup effects using periodic and random pulse generators." Nuc. Ins. and Meth. A225 1987.
5. S. I. Salem, S. L. Panossian and R. A. Krause, "Experimental K and L relative X-ray emission rates."- Atomic Data and Nuclear Data Tables 14, 1974.
6. Zhao et al, SPIE 1992, this conf.

AXAF VETA-I Mirror Encircled Energy Measurements and Data Reduction

Ping Zhao, Mark D. Freeman, John P. Hughes, Edwin M. Kellogg, and Dan T. Nguyen

Harvard-Smithsonian Center for Astrophysics
60 Garden Street, Cambridge, MA 02138

Marshall Joy and Jeffery J. Kolodziejczak
ES-65, Marshall Space Flight Center, AL 35812

ABSTRACT

The AXAF VETA-I mirror encircled energy was measured with a series of apertures and two flow gas proportional counters at five X-ray energies ranging from 0.28 to 2.3 keV. The proportional counter has a thin plastic window with an opaque wire mesh supporting grid. Depending on the counter position, this mesh can cause the X-ray transmission to vary as much as $\pm 9\%$, which directly translates into an error in the encircled energy. In order to correct this wire mesh effect, window scan measurements were made, in which the counter was scanned in both horizontal (Y) and vertical (Z) directions with the aperture fixed. Post VETA measurement of the VXDS setup were made to determine the exact geometry and position of the mesh grid. Computer models of the window mesh were developed to simulate the X-ray transmission based on this measurement. The window scan data were fitted to such mesh models and corrections were made. After this study, the mesh effect was well understood and the final results of the encircled energy were obtained with an uncertainty of less than 0.8%.

1. INTRODUCTION

The Verification Engineering Test Article-I (VETA-I), made of Zerodur with a diameter of 1.2 meters, is the uncoated outmost mirror pair of The Advanced X-ray Astrophysical Facility (AXAF), the third of NASA's four Great Space Observatories.¹ Its mirror figures and surface quality were measured at the X-ray Calibration Facility (XRCF) of the Marshall Space Flight Center (MSFC) from August to October of 1991.² X-rays generated by an electron impact source³ 528 meters away were focused by the VETA to its focal plane, which is 10 meters behind the VETA. The focused X-rays were then detected and measured with the VETA X-ray Detecting System (VXDS) built by SAO.⁴ Four types of results were obtained, i.e. Full Width Half Maximum (FWHM), Encircled Energy, Effective Area, and Ring Focus. All the measurements were done with X-ray detectors placed in the focal plane, except the Ring Focus measurements, which were done in the Ring focal plane (about 21 mm in front of the focal plane).

We first give some definitions:

Total Effective Area (or simply **Effective Area**): The total power reflected by the VETA into 2π steradians, measured in units of cm^2 . It is equal to the projected area of an equivalent mirror with 100% reflectivity, or a projected area of $P1 \times R^2(E, \theta)$, where P1 is the Paraboloid mirror of the VETA and R is the mirror reflectivity as a function of X-ray energy and grazing angle.

Encircled Energy: The fraction of the power reflected from the mirror that passes through an aperture of radius r , in the focal plane. It is measured in units of the effective area or cm^2 as a function of r . Therefore it is also called *encircled effective area*.

Fractional Encircled Energy: The Encircled Energy normalized to that contained in the largest

aperture used for the measurement, 20 mm diameter (= 6.88 arcmin).

The requirements for the VETA-I test was to measure the FWHM (expected to be better than 0.5 arcsec) to ± 0.05 arcsec precision, the Fractional Encircled Energy to $\pm 2\%$, and the Effective Area to $\pm 5\%$.

In this paper we discuss the VETA encircled energy and effective area measurements and their data reduction for up to the 20 mm diameter aperture. The total effective area involves wing scan measurement and is discussed in another paper in this volume.⁵ Two major corrections were made to the raw data. The first is the spectrum correction with which we take care of the spectrum contamination taken by the proportional counter. The second, an even bigger correction, is the counter window mesh correction. The first correction is discussed by another paper in this volume.⁶ This paper mainly deals with the second correction.

In the following sections we discuss the techniques used for the measurements, the method used for the wire mesh correction, and the results. Section 2 describes the VETA encircled energy measurements and explains the X-ray detector window mesh effect. Section 3 is about the Post VETA Measurement. Section 4 discusses the computer mesh models. Section 5 gives the mesh effect correction. And section 6 lists the final results of the VETA encircled energy.

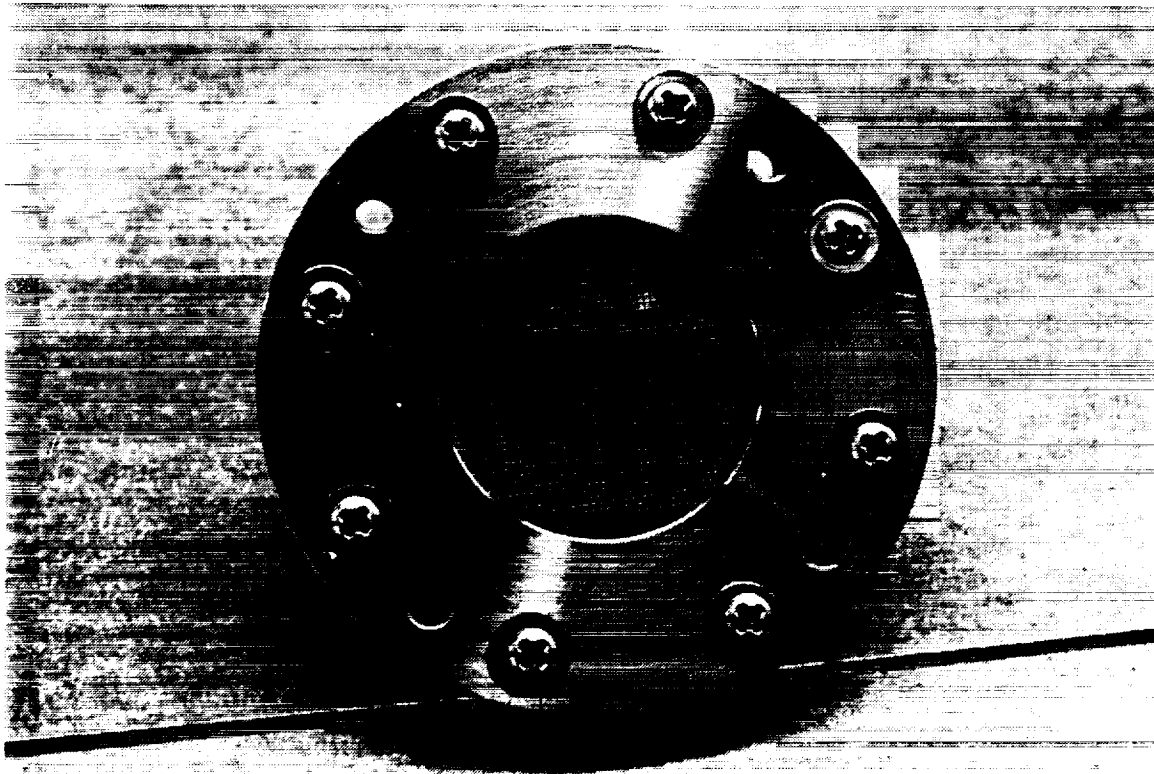


Figure 1: VXDS Flow Proportional Counter Window. The mesh supporting grid is made of gold wire with $50.8 \mu\text{m}$ diameter and $529.17 \mu\text{m}$ pitch.

2. VETA-I ENCIRCLED ENERGY MEASUREMENTS AND WIRE MESH EFFECT

VETA encircled energy measurements were made at five different X-ray energies, i.e. C-K (0.277 keV), Cu-L (0.932 keV), Al-K (1.488 keV), Zr-L (2.067 keV) and Mo-L (2.334 keV). The X-rays focused by the VETA pass through an aperture of radius r , in the focal plane, and detected by a flow gas proportional

counter placed 25 mm behind the focal plane. There are 16 apertures with diameters of 0.005, 0.01, 0.025, 0.05, 0.1, 0.3, 0.5, 0.75, 1, 1.5, 2, 3, 5, 7.5, 10, 20 mm. The aperture 0.005 through 0.5 mm are laser drilled pinholes on 99.9% pure and 12.5 microns thick gold foil. The 0.75 mm or larger apertures were machine drilled on aluminum plate with irridite coating. We have taken the scanning electron microscope pictures of the laser drilled pinholes. Their actual sizes and shapes are slightly different from a perfect circle with quoted diameters, which is discussed by another paper in this volume.⁴ Each aperture was placed in the focal plane of the VETA-I and centered on the peak of the VETA Point Spread Function (PSF). The photon counts, counted by the flow gas proportional counter (also called X-ray Detection Assembly counter or XDA counter), through each aperture then represents the integral of the PSF out to the radius of that aperture. The encircled energy is measured by comparing the counting rate to that obtained in an identical flow counter, the Beam Normalization Detector (BND), of very well known area, exposed to the same incident beam in the entrance plane of the P1. Depending on the source intensity, the integration time was chosen to ensure both detectors receiving enough counts so the statistical error is less than 1%. The VETA effective area is calculated as

$$\text{Effective Area (r)} = \frac{\text{XDA Counts (r)}}{\text{BND counts}} \times \text{BND area}$$

where BND area = $\pi \text{ cm}^2$ with an uncertainty of 0.05%.

The flow proportional counter is filled with either 125 torr methane for a low energy line (C-K) or 400 torr P10 gas (10% methane and 90% argon) for higher energy lines (Cu-L, Al-K, Zr-L and Mo-L). It has a thin polypropylene window with an opaque wire mesh supporting grid which prevents the window from breaking under differential pressure. The wire is made of gold with $50.8 \mu\text{m}$ diameter and the average mesh period is $529.17 \mu\text{m}$ (see Figure 1). When the window is uniformly illuminated, which is the case for the BND counter, the transmission is 81.72% due to the wire mesh effect. But it is not so simple for the XDA counter. As shown in Figure 2, the X-ray photons from the focal point expand into a ring of about 3 mm diameter when they strike the counter window, which is located 25 mm behind the focal plane. Depending

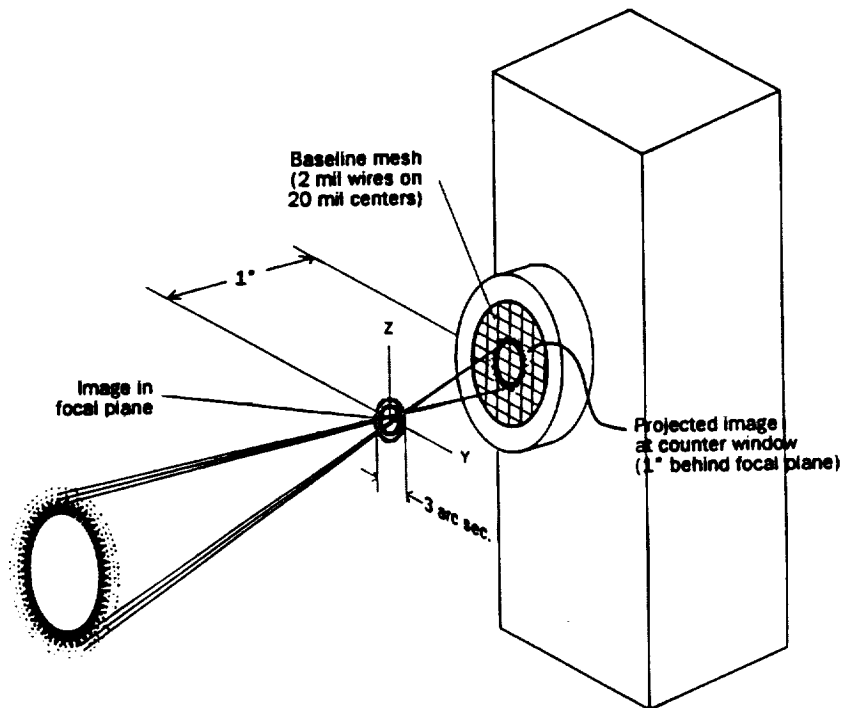


Figure 2: Counter Window Wire Mesh Effect. The X-ray photons form a ring pattern when they enter the counter window. Depending on the phase of the mesh grid relative to the photon ring, the X-ray transmission can vary from 75% to 92%.

WINDOW SCAN MEASUREMENTS

0.600 mm scan = 9 steps x 0.075 mm stepsize
 or = 11 steps x 0.060 mm stepsize

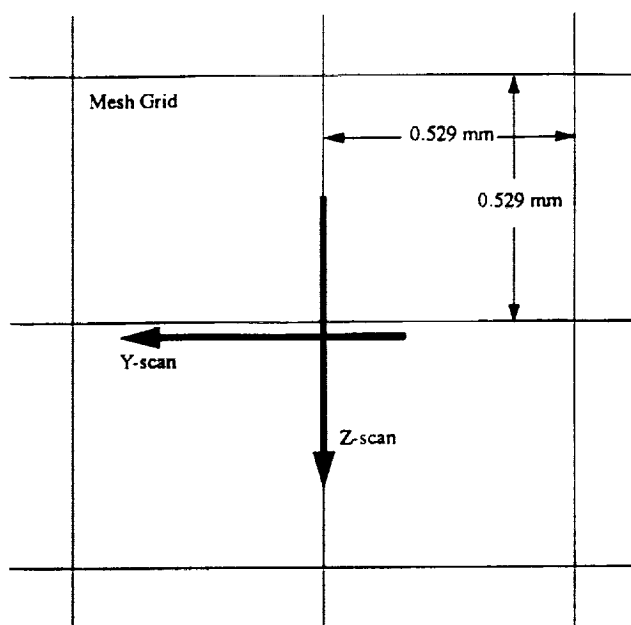


Figure 3: The planned VETA Encircled Energy Window Scan Measurement. The arrows indicate the Y and Z positions of the aperture center with respect to that of the mesh grid. The transmission maximum occurs when the aperture center is at one of the mesh grid intersection, except for the 20 mm aperture, in which the transmission minimum occurs. The scan maximum occurs when the aperture center crosses one of the mesh wire, also except for the 20 mm aperture, in which the transmission minimum occurs.

on the phase of the mesh grid relative to the photon ring, the X-ray transmission can vary from 75% to 92%, which directly translates into an error of the encircled energy. Obviously we had to take this mesh effect very seriously in order to fulfill the measurement precision requirements.

To measure the counting rate modulation due to the wire mesh and to make appropriate transmission corrections, the window was scanned in both Y and Z directions with the aperture fixed. Three sources (Al, C and Zr) and 11 apertures (0.3 through 20 mm) were used for the window scan measurements. The procedure was to: 1) make a scan in Y direction; 2) find the location with the highest counts; 3) offset the counter to this location; 4) make a scan in Z direction. Each scan is a 600 μm span with 9 or 11 steps (see Figure 3). Integration time is chosen to ensure enough counts (> 10000) for each step. Figure 4 is the Quick-look data of some typical scans, generated during the VETA test. The mesh modulation effect is clearly seen. Figure 5 is the Quick-look data for 2 and 10 mm apertures which shows something we could not understand at that time: the window Z-scans have much higher counts than the Y-scans. Obviously they were not done as planned because otherwise the highest point of the Y-scan curve should agree with the middle point of the Z-scan curve. Figure 6 shows all the quick-look window scan data for the Al-K line. It shows the 20 mm aperture window scan and the Z-scans for the 2 and 10 mm aperture are distinctively higher than the rest of the window scans. Compared with the wire mesh models (see Section 5), a simple analysis (we leave this to our reader as a little fun exercise) concludes that all the window scans were not done as planned. This was caused by a computer error and it complicated the data reduction. In order to make the mesh correction, we had to fully understand how the window scan measurements were actually done and the exact geometry of the apertures and counter setup. Therefore we planned the Post VETA

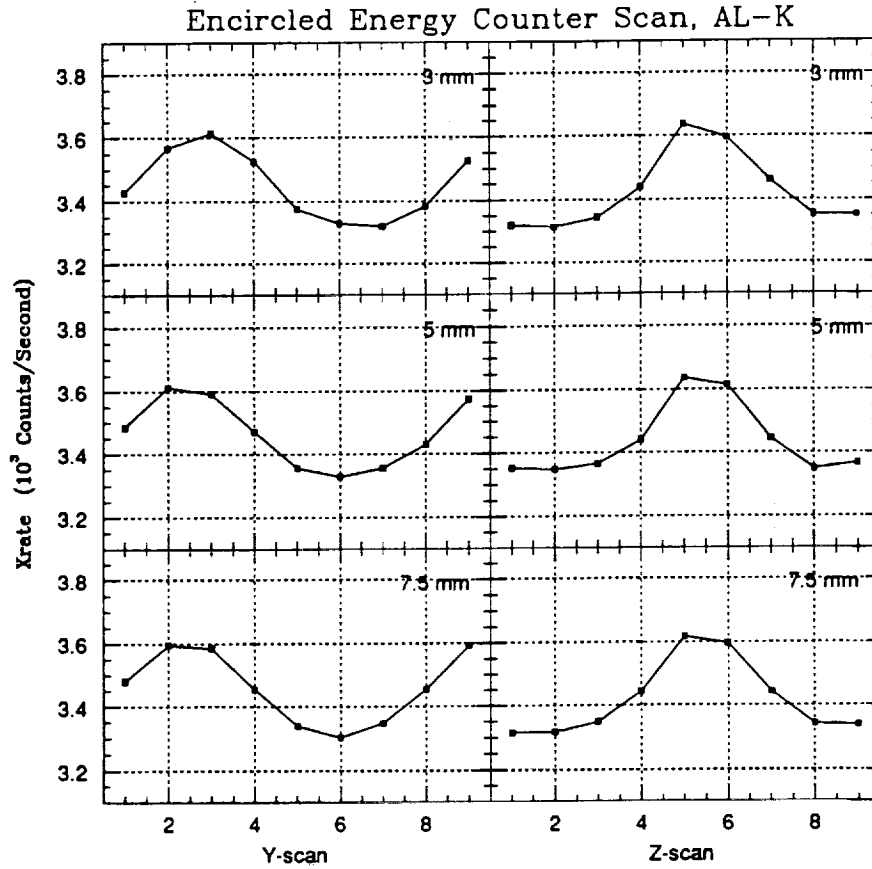


Figure 4: VETA Encircled Energy Window Scan Quick-look Data. Al-K source, aperture 3 - 7.5 mm.

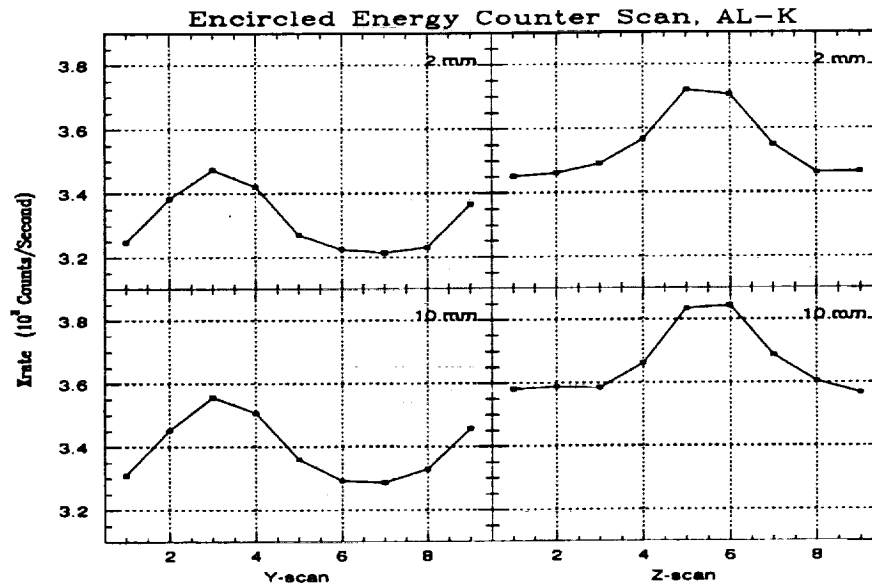


Figure 5: VETA Encircled Energy Window Scan Quick-look Data. Al-K source, aperture 2 and 10 mm. The Z-scans have much higher counts than Y-scans. It indicates that these window scan measurements were not done as planned.

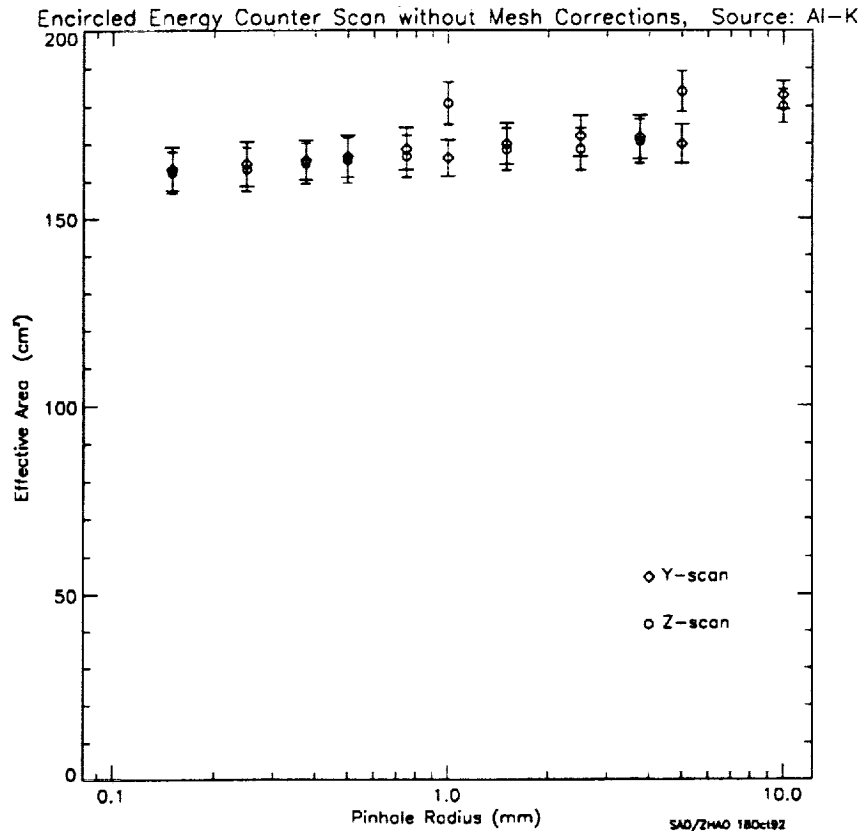


Figure 6: VETA Encircled Energy vs. aperture size Quick-look Data. Al-K source. The 20 mm aperture window scans and the Z-scans for the 2 and 10 mm aperture are distinctively higher than the rest of the window scans.

Measurement which was carried out in March of 1992 at XRCF.

3. POST VETA MEASUREMENTS

Two Post VETA Measurements were made. The first one was the mechanical measurement which solely supported the window mesh effect analysis. The second one was the X-ray measurement which measured the beam uniformity, filter thickness, detector response etc., in supporting the whole VETA data analysis and HRMA (High Resolution Mirror Assembly) test planning. In the mechanical measurement we measured: 1) the mesh grid periodicity; 2) the mesh wire orientation; 3) relative Y and Z positions between the VETA focal points and the wire mesh as well as the counter window bezel; 4) VETA focal point to wire mesh distance (along the X axis). Depending upon the region on the window, the mesh periodicity varies between 499 μm to 564 μm . The mesh wires are laid within 0.2 degrees from the horizontal and vertical directions. A motor log recorded all the motor positions during the VETA test. We used this motor log to repeat all the moves and measured the aperture and counter positions. Figure 7 shows the actual positions on the window mesh where the X-rays enter the window for different scans and apertures. It is seen that the Y-scans and Z-scans were actually made at different parts of the window. There are actually six locations on the window where data were taken: window Y-scan, Z-scan and window fixed measurement for 2 and 10 mm apertures; window Y-scan, Z-scan and window fixed measurement for other apertures. There was a so called Prime-Y move, which moves the whole XDA assembly in order to reach different parts of the detector, during the VETA test. We later found this Prime-Y move had a 0.1% error - it was 100 μm short for a 100 mm move - and also its repeatability was not very good. But our motor log regards every move as accurate as its read out. Therefore the positions shown in Figure 7 are only good to $\pm 20 \mu\text{m}$. More accurate window positions

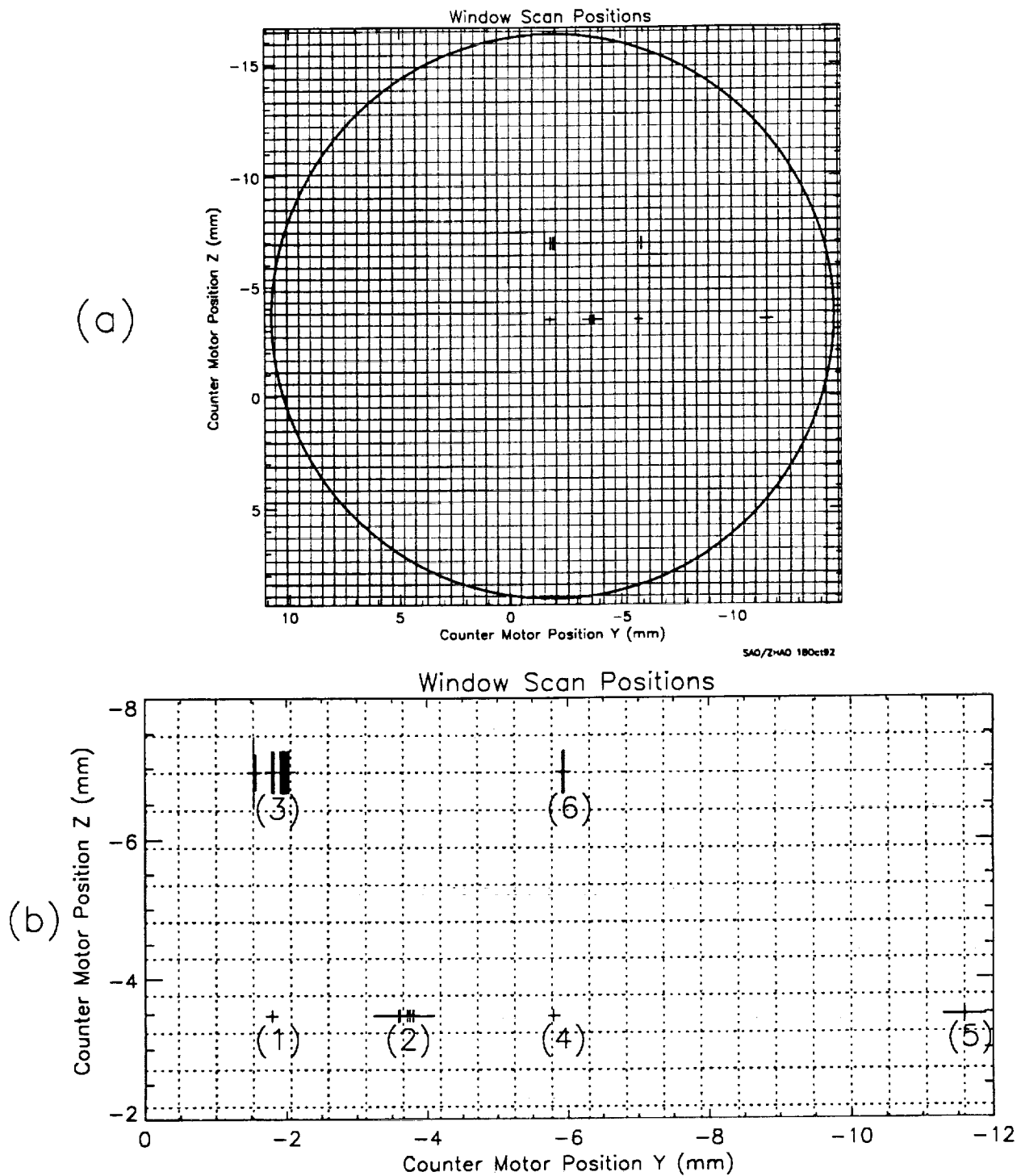


Figure 7: Window Scan Positions. A result of the Post VETA Measurements. (a) shows the relative positions of the window bezel (big circle), mesh grid and the aperture center positions where the measurements were made (little crosses). (b) shows a magnified portion of (a). The measurements were bunched at six locations. Location (1), (2) and (3) are for the rest of the apertures. Location (4), (5) and (6) are for 2 and 10 mm apertures. Location (1) and (4) were also for the planned window scan measurements. But the actual window Y-scan measurements were made at (2) and (5). The actual window Z-scan measurements were made at (3) and (6).

were obtained by fitting the VETA data to the mesh models (see next two sections). Because the window slightly bulged out under the pressure, the VETA focal point (the center of the 5 μm aperture was used to refer to this point) to wire mesh distances were measured at all six positions shown in Figure 7 under 125 and 400 torr differential pressures. The results are in Table 1.

Table 1. VETA Focus to Window Mesh Distance

Source	Gas & Pressure	Aperture Size		
		0.005-7.5 mm	2 & 10mm	20mm
C	Methane/125 Torr	24.940 mm	24.940 mm	29.012 mm
Al,Cu,Mo,Zr	P10/400 Torr	24.703 mm	24.814 mm	28.775 mm

4. WIRE MESH COMPUTER MODELS

Computer models of the window mesh were developed to simulate the X-ray transmission based on the exact XDA geometry and our knowledge of the VETA.⁷ First, ray-trace image files of X-ray on the counter window were generated by using the OSAC package. The ray-trace included the effects of residual gravitational distortions, scatterings for different energies, despace due to the uncut glass, apodization, finite source sizes and their intensity distribution, finite source distance, mirror surface figures, and mirror support strut. For all five sources and different focuses to mesh distances, there are 14 ray-trace image files generated and each contains 50000 photons. We then laid each ray-trace image on top of a mesh wire grid model and calculated the number of photons blocked by the wire grid. The mesh grid model was then moved in both Y and Z directions with the ray-trace image fixed to simulate the window scan, and transmission was calculated for each move. Figure 8 shows the ray-trace image of the Al-K source on top of the wire grid for one fixed position. Figure 9 shows the mesh transmission model for the Al-K source with a 2-dimensional scan of 81x81 positions. It is seen that the mesh effect is very strong. For 20 mm aperture, the transmission is the minimum when the center of the aperture is at one of the intersections of the mesh grid. For other apertures, the transmission is the maximum in that case. Depending on the counter position, the X-ray transmission can vary between 75% and 92%. There are 14 such mesh models corresponding to 14 ray-trace files as mentioned above.

5. WIRE MESH CORRECTIONS

To make the mesh effect correction, we had to first fit the data to the mesh model to find the accurate Y and Z positions of the window scan. The correction was then made by comparing the percentage of transmission at these positions in the mesh model to the BND counter mesh transmission. The quick-look data shown in section 3 provide a preliminary result during and immediately after the VETA test. The spectrum fitting analysis was done for all the VETA encircled energy data to correct spectral contamination including bremsstrahlung continuum, pulse pileup, background and deadtime.⁶ The spectrum corrected data were then used to fit with their corresponding mesh models with a minimum χ^2 . The initial fit was made based on the window scan positions measured during the post VETA measurement. The VETA motor log gives the relative positions between Y-scan and Z-scan for each aperture. More accurate fit was then obtained by combining the initial fit and the motor log. This process was like fitting a two dimensional data to the mesh model, even though the data were only from two one dimensional scans perpendicular to each other. The data fit the mesh model very well. The reduced χ^2 for each window Y and Z scan pair fit ranges from 0.4 to 1.4 with the average around 1. Figure 10 (a) and (b) show one of the typical fits. The fitting process located the exact relative positions between the aperture and the window mesh. The XDA transmission rate at these positions was then calculated using the mesh model. The mesh corrections were finally made by multiplying the spectrum corrected data with the BND transmission rate (81.72%) and dividing it by the calculated XDA transmission rate. Figure 10 (c) and (d) show the corrected encircled energy window scan data. It is seen that the mesh modulation effect is removed.

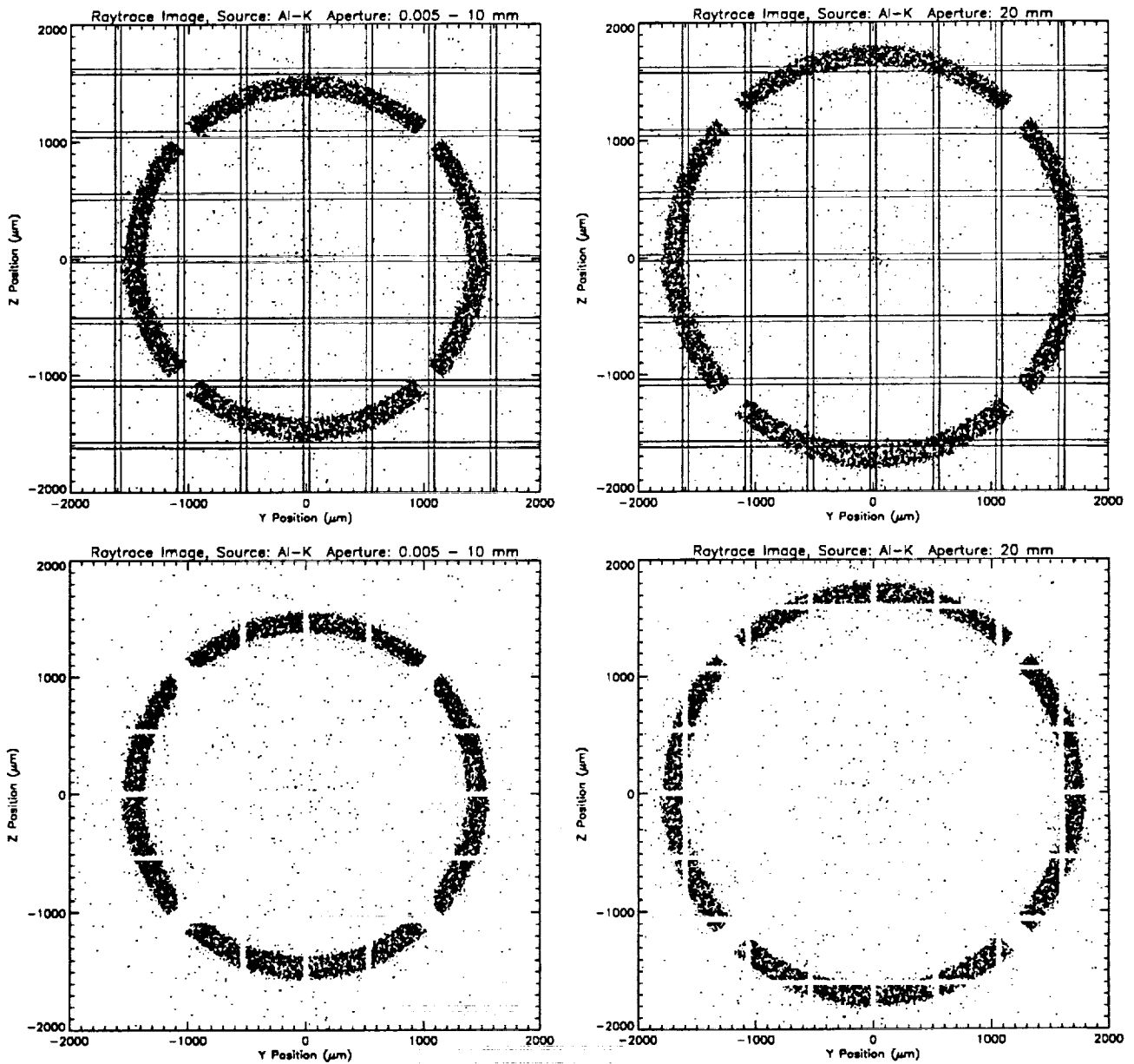
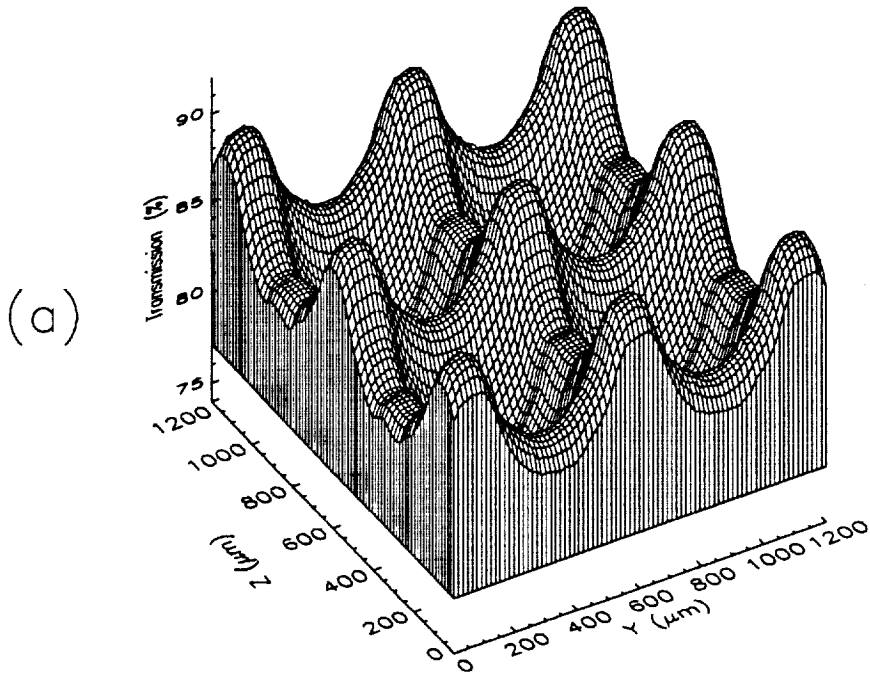


Figure 8: Raytrace Image on Mesh grid Model. Al-K source. (a) and (b) show, one fixed counter position, the 50000 photon raytrace images on top of the mesh grid model for 0.005 - 10 mm apertures and 20 mm aperture, respectively. (c) and (d) show the mesh transmission pattern for the same raytrace images.

Mesh Window Transmission Model
Source: AL-K Aperture: 0.005 - 10 mm



Mesh Window Transmission Model
Source: AL-K Aperture: 20 mm

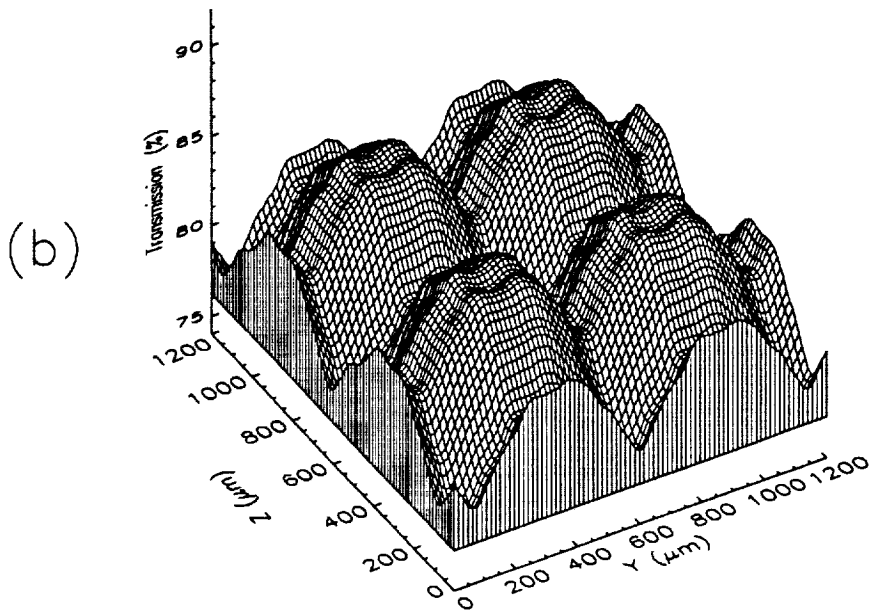
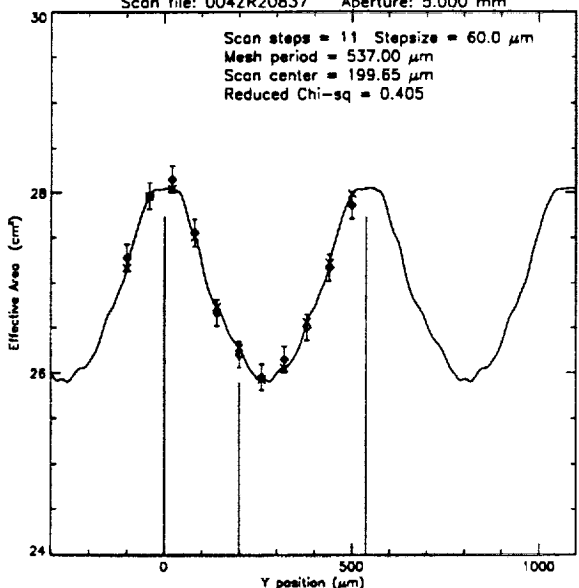
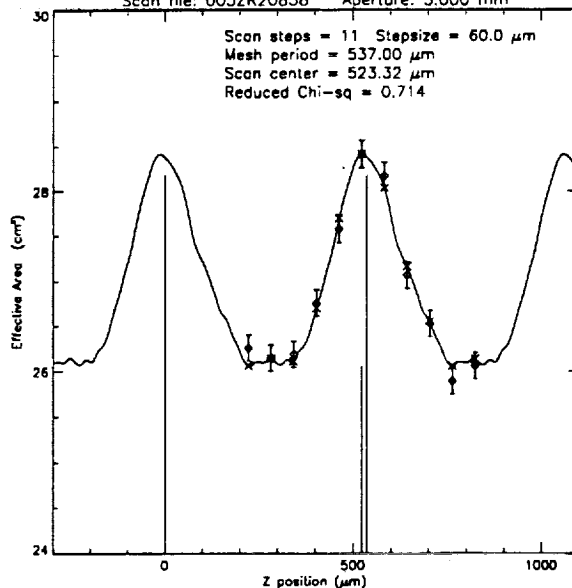


Figure 9: Window Mesh Transmission Models. Al-K source. (a) is the model for 0.005 to 7.5 mm apertures, in which a maximum transmission occurs when the Y-Z coordinates of the aperture center is at a mesh wire intersection. (b) is the model for 20 mm aperture, in which a minimum transmission occurs when the Y-Z coordinates of the aperture center is at a mesh wire intersection. Depending on the counter position, the X-ray transmission can vary between 75% and 92%.

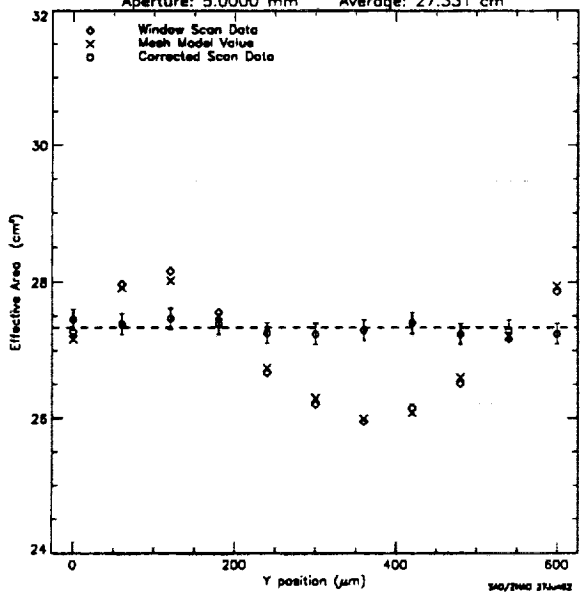
Window Scan Data fitted with the Mesh Transmission Model
 Model file: mesh537_E_2.07_FDIST_24703
 Scan file: 004ZR20837 Aperture: 5.000 mm



Window Scan Data fitted with the Mesh Transmission Model
 Model file: mesh537_E_2.07_FDIST_24703
 Scan file: 005ZR20838 Aperture: 5.000 mm



Window Scan Data with Mesh Transmission Corrections
 Window Scan file: 004ZR20837
 Aperture: 5.0000 mm Average: 27.331 cm²



Window Scan Data with Mesh Transmission Corrections
 Window Scan file: 005ZR20838
 Aperture: 5.0000 mm Average: 27.557 cm²

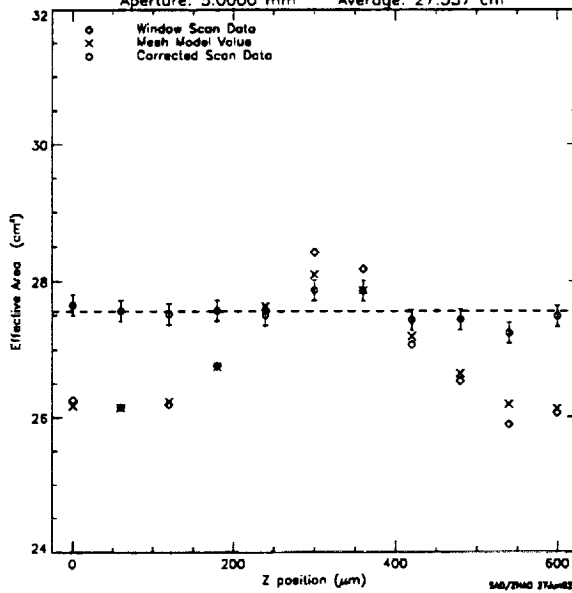


Figure 10: A Typical Window Scan Data Fit to The Mesh Model. Zr-L source, 5 mm aperture. Top two figures show the Y and Z scan data fit to the mesh model. Bottom two figures show the same data after the mesh correction. The mesh modulation effect is removed.

The window scan measurement only covered three sources (Al, C and Zr) and 11 apertures (0.3 mm through 20 mm). Before the window scan measurements, we did the window fixed measurement for all five sources and 16 apertures (0.005 through 20 mm). Instead of scanning the counter, only one fixed counter position was used for each aperture. In order to make mesh effect corrections for the window fixed measurements, we had to know their exact counter positions. We do have a motor log which gives the relative counter positions between all the window scan and window fixed measurements. However, there were prime-Y moves during the measurement which make the motor log not very reliable. But we did the beam centering for apertures ranging from 0.005 mm to 0.3 mm. The 0.3 mm aperture was the only one used for both window scan and beam centering thus it linked the window fixed data and the window scan data. There was no or very small Prime-Y move between 0.005 and 0.3 mm aperture window fixed measurements. With this information, we were able to accurately locate the counter positions for apertures from 0.005 mm to 0.3 mm window fixed measurements and hence to make their mesh effect corrections. For the final results, we use the window scan data for 0.3 to 20 mm apertures and window fixed data for 0.005 to 0.1 mm apertures. Because there was no window scan measurement for Cu and Mo sources, we could only rely on our motor log to make some rough mesh corrections for these two sources. Therefore the results for these two sources have bigger errors.

6. FINAL RESULTS OF THE VETA-I ENCIRCLED ENERGY

Table 2 gives the final results and their errors for the VETA encircled energy. The final errors are less

Table 2. VETA-I Encircled Energy units: cm^2

Aperture size (mm)	X-ray lines				
	C-K 0.277 keV	Cu-L 0.932 keV	Al-K 1.488 keV	Zr-L 2.067 keV	Mo-L 2.334 keV
0.005	4.375	3.362	2.959	0.516	0.155
0.010	8.839	8.471	7.498	1.352	0.349
0.025	31.651	24.662	24.302	3.636	0.954
0.050	65.126	49.312	49.001	7.270	2.129
0.100	123.797	97.395	94.425	14.521	4.271
0.300	214.293	167.884	165.682	24.939	7.784
0.750	217.538	181.863	166.690	25.664	8.011
0.500	220.655	186.698	168.720	26.085	7.987
1.000	217.422	179.857	169.617	26.207	8.164
1.500	219.620	180.507	170.602	26.536	8.233
2.000	217.813	178.935	170.995	27.119	8.374
3.000	222.311	186.224	173.035	26.982	8.999
5.000	220.197	174.568	173.674	27.445	9.040
7.500	221.697	190.402	174.769	27.691	9.272
10.000	219.958	185.656	174.259	27.804	8.772
20.000	223.037	182.731	179.007	28.706	8.497
Total Error	0.562%		0.612%	0.795%	
Error due to Mesh Correction	0.422%		0.470%	0.772%	

than $\pm 0.8\%$ for Al, C and Zr sources, which exceeded the requirements ($\pm 2\%$) by a factor of 2.5. Figures 11, 12 and 13 are the plots of the encircled energy vs. the aperture sizes before and after the mesh corrections for Al, C and Zr sources. These results were then used to compare with the expected values to get the VETA point spread functions and the mirror surface figures.⁷ they were also used to obtain the VETA total effective area and mirror reflectivity.⁵

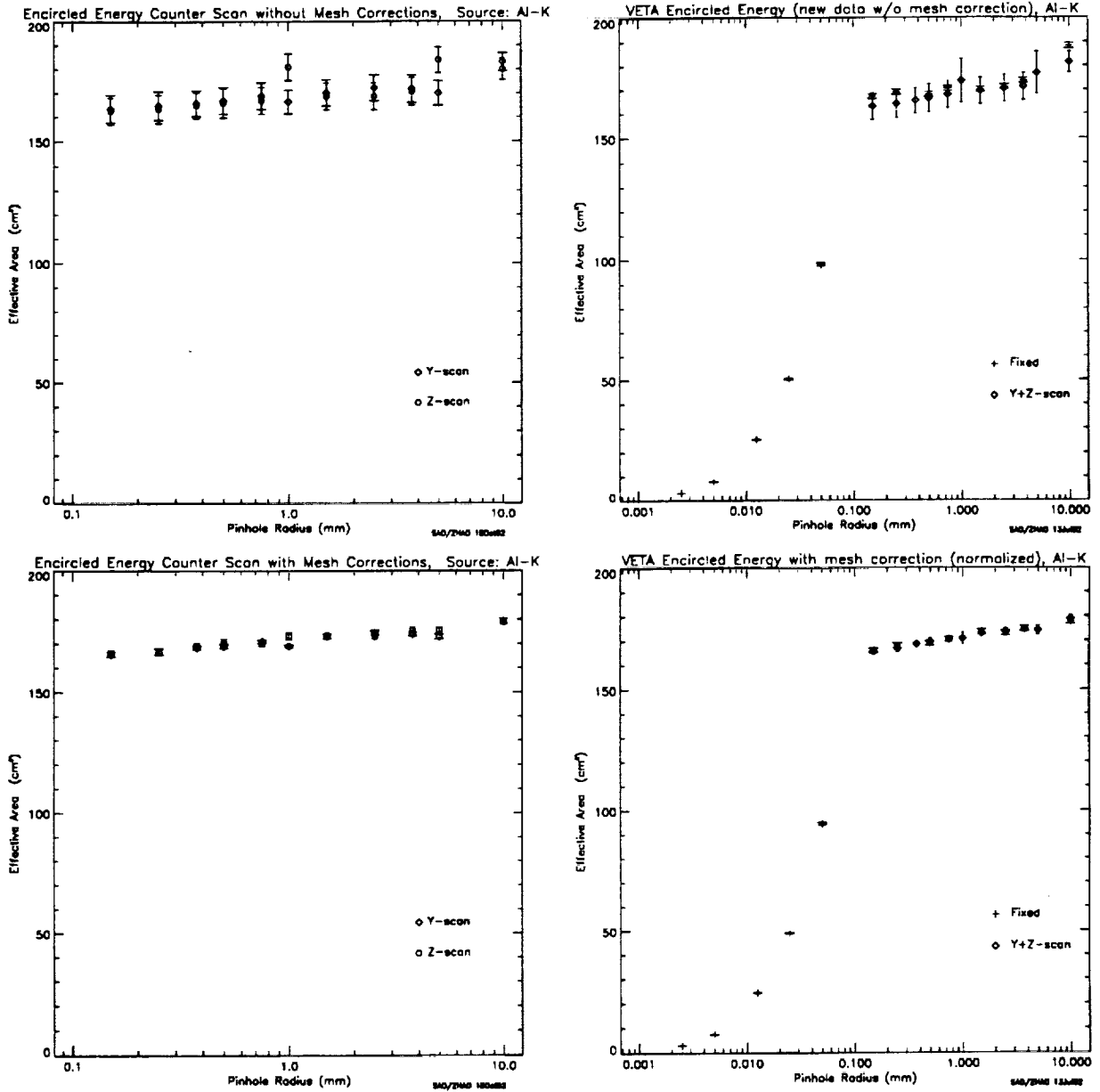


Figure 11: The VETA-I Encircled Energy before (above) and after (below) the Mesh Corrections. Al-K source.

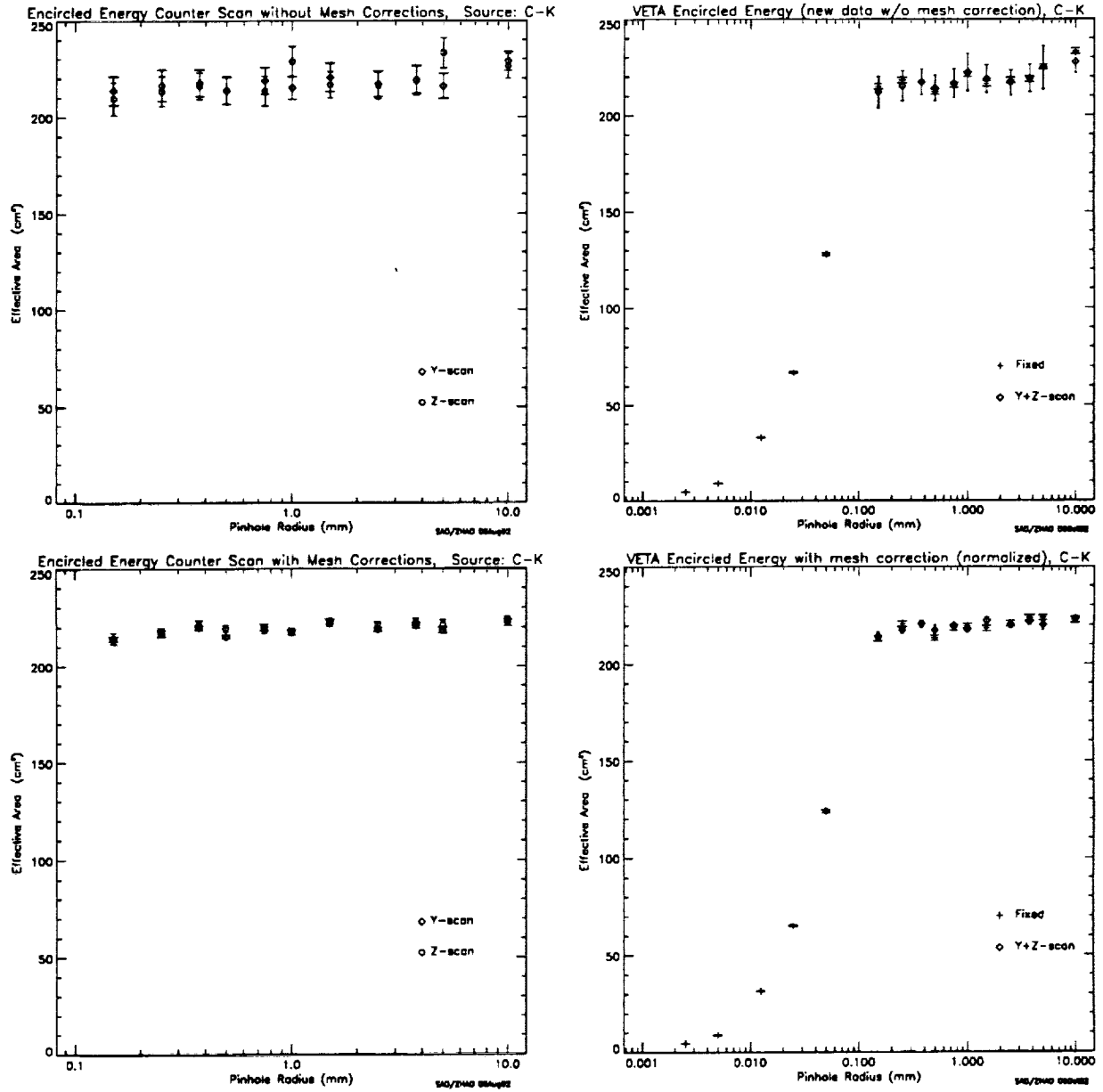


Figure 12: The VETA-I Encircled Energy before (above) and after (below) the Mesh Corrections. C-K source.

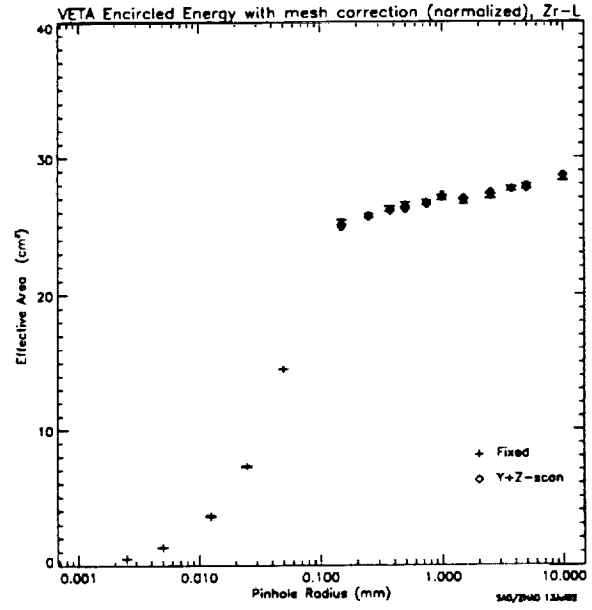
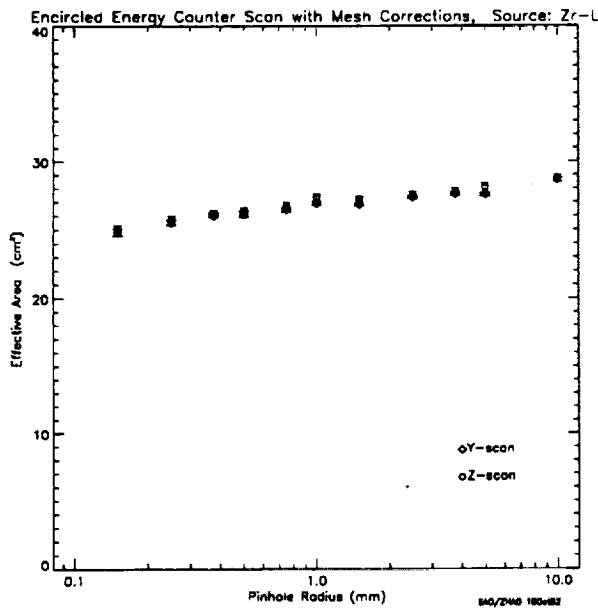
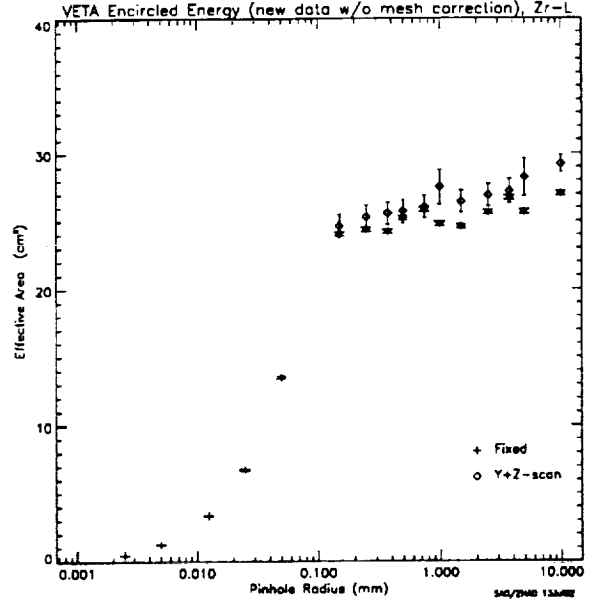
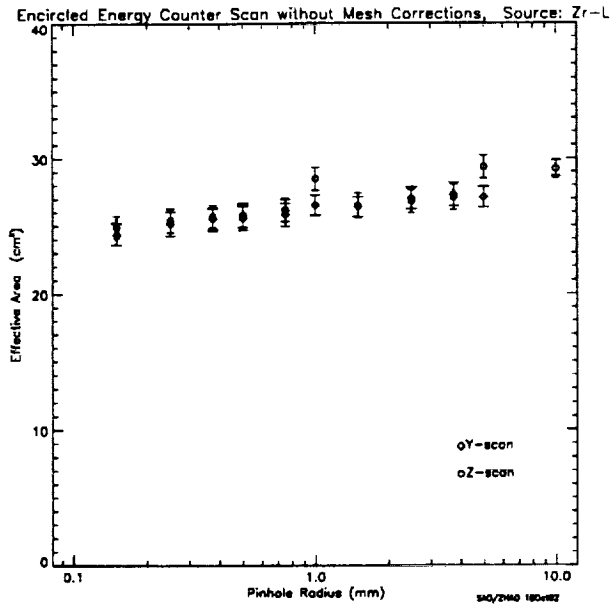


Figure 13: The VETA-I Encircled Energy before (above) and after (below) the Mesh Corrections. Zr-L source.

7. ACKNOWLEDGMENT

We would like to thank Roger Brissenden, George Chartas, Mark Jones, Tim Norton, William Podgorski, John Roll, and Dan Schwartz for their help during the course of this work. This work was supported under NASA contract # NAS8-36123.

8. REFERENCES

1. M. C. Weisskopf, "The Advanced Astrophysics Facility: An Overview," *Astrophysical Letters & Communications*, Vol. 26, pp. 1-6, 1987.
2. E. M. Kellogg, R. J. V. Brissenden, K. A. Flanagan, M. D. Freeman, J. P. Hughes, M. T. Jones, M. Ljungberg, P. Mckinnon, W. A. Podgorski, D. A. Schwartz, and M. V. Zombeck, "Calibration of the Verification Engineering Test Article-I (VETA-I) for AXAF using the VETA-I X-ray Detection System," *Proc. SPIE*, Vol. 1546, pp. 2-12, 1991.
3. P. Zhao, E. M. Kellogg, D. A. Schwartz, Yibo Shao, and M. A. Fulton, "Intensity distribution of the X-ray source for the AXAF VETA-I mirror test," *Proc. SPIE*, this volume, 1992.
4. W. A. Podgorski, K. A. Flanagan, M. D. Freeman, R. G. Goddard, E. M. Kellogg, T. J. Norton, J. P. Ouellette, A. G. Roy, and D. A. Schwartz, "VETA-I X-ray detection system," *Proc. SPIE*, this volume, 1992.
5. E. M. Kellogg, G. Chartas, D. Graessle, J. P. Hughes, L. Van Speybroeck, P. Zhao, M. C. Weisskopf, R. F. Elsner, and S. L. O'Dell, "The X-ray reflectivity of the AXAF VETA-I optics," *Proc. SPIE*, this volume, 1992.
6. G. Chartas, K. A. Flanagan, J. P. Hughes, E. M. Kellogg, D. Nguyen, M. V. Zombeck, M. Joy, and J. J. Kolodziejczak, "Correcting X-ray spectra obtained from the AXAF VETA-I mirror calibration for pileup, continuum, background and deadtime," *Proc. SPIE*, this volume, 1992.
7. J. P. Hughes, D. A. Schwartz, A. Szentgyorgyi, L. Van Speybroeck, and P. Zhao, "Surface finish Quality of the Outer AXAF mirror pair based on X-ray measurement of the VETA-I," *Proc. SPIE*, this volume, 1992.

Precision of the Calibration of the AXAF Engineering Test Article
(VETA) Mirrors.

D.A. Schwartz, G. Chartas, J.P. Hughes, E.M. Kellogg, and P. Zhao
Smithsonian Astrophysical Observatory

ABSTRACT

Measurements of the VETA encircled energies have been performed at 5 energies within 16 radii ranging from 0.05 to 200 arcseconds. We report here on the analysis of the accuracy of those measurements. A common "error tree" structure applies, and we present representative numbers for the larger terms. At 0.277, 1.5, and 2.07 keV, and for radii of 3 arcsec and larger, our measurements have estimated 1 sigma errors of 0.6 to 1.5 percent. Effects of measurement statistics and of the VETA test mount limit the accuracy at smaller angles, and modulation by the counter window support structure together with the imperfect position repeatability limit the accuracy for the 0.93 and 2.3 keV energies. We expect to mitigate these limitations when calibrating the complete AXAF flight mirror assembly.

1. INTRODUCTION: CALIBRATION OF AXAF

The Advanced X-ray Astrophysics Facility (AXAF) will be a long-lived international observatory for performing high resolution imaging and spectroscopic studies in the 0.1 to 10 keV range. The scientific objectives of AXAF are to investigate the nature of celestial objects, the physics of fundamental processes in the universe, and the history and evolution of the universe. To fully exploit the information obtained requires that we know the response of the X-rays mirrors to a calibration accuracy of order 1%.

We have been investigating techniques for calibrating the flight mirrors in conjunction with previous measurements proving the technology of mirror fabrication. We have previously reported results from measurements of a Technology Mirror Assembly (TMA; Schwartz et al. 1986; VanSpeybroeck et al. 1986; Wyman et al. 1986) and of an improved version of this assembly designated TMA-II, (VanSpeybroeck et al. 1989). The Verification Engineering Test Article (VETA) consisted of the outermost pair of the nested set of AXAF mirrors, comprising the actual flight mirror. Previous results have been reported in Kellogg et al (1991b), in internal SAO reports (Brissenden et al. 1991; 1992), and appear in several papers in this volume. The present paper addresses X-ray measurements of the VETA from the point of view of how accurate a calibration was performed.

Our objective for the VETA calibration was 5% accuracy for the effective area and 2% accuracy for the encircled energy. These were unusual and ambitious goals, which were largely achieved. This requirement forced much attention to details, of which some were unusual and unanticipated (cf., Chartas et al. 1992; Zhao et al. 1992a,b).

The next section discusses the philosophy and objectives of calibration in more detail. In general, the error from photon counting statistics can be made less than 1% since it is usually feasible to acquire more than 10^4 counts, so that ability to understand the systematic effects determines the final precision. Section 3 presents the principles of the calibration measurements. Our key technique is to measure the ratio of counts in nominally identical detectors, so that many effects, (e.g., variability of the X-ray generator, dead time in the common electronics), cancel to first order. Section 4 presents our detailed analysis of how accurate are the VETA calibration measurements. Papers in this volume by Hughes et al. (1992) and Kellogg et al. (1992) address how well we can use this information to deduce the true properties of the VETA.

2. CALIBRATION OBJECTIVES

To understand the rationale of the calibration program, we must clearly define the purposes of calibration. In simplest form, a "calibration" is a measurement that can stand alone to provide definitive numerical conversion of on-orbit data into physical quantities. An approximation to this situation might be the conversion of a counting rate measured in a ten arcsec circle in the focal plane at some off-axis angle, into a broad band flux. The calibration

process might have allowed us to determine a single "average area" number to divide into the measured counting rate.

In X-ray astronomy the flux conversion actually depends on the form of the incident spectrum, and calibration is a much more complex process. It is clearly not possible to reproduce on the ground every possible measurement that could be made on-orbit. That would require sampling the product of all possible energies, times a range in each of two off-axis angles, times a range of focal plane locations, times all possible image sizes of interest. The way the actual flight data is analyzed is by construction of semi-analytical models of the telescope and detectors, and using these models to interpolate and extrapolate continuously to the exact parameter values of any given observation. Thus the second major purpose of a calibration is to verify that the models used are valid.

The third purpose of the calibration is to overdetermine the numerical parameters appearing in the models. This allows determination of best-fit values, error estimates, and allowed ranges of parameters, to any given confidence level.

In cases where the models prove inadequate (e.g., unacceptable fits to the data for any values of the free parameters), the calibration process must provide sufficient data to refine the models. Examples of such refinement might be measuring on a finer grid of data points for interpolation, or replacing the usual assumption of azimuthal symmetry with a detailed functional dependence.

The most general calibration model of a telescope is the point response area:

$$dA(E, \theta, \vartheta, y, z, x, i) \quad (1)$$

where $dA/(dydz)$ is the infinitesimal effective absolute area per unit solid angle in the image plane, to a broad parallel beam of X-rays of energy E , incident at polar angle θ and azimuthal angle ϑ to the telescope optical axis, and imaged at the angular position y, z in a plane parallel to the on-axis Gaussian focal plane but displaced by a distance x . The two polarization states are indexed by i . X-ray reflectivity depends only slightly on the polarization state, and we do not consider this further for the VETA calibration. For the flight mirror, the significance of polarization correction will be investigated.

Operationally, one of the most important functions is the absolute encircled energy area,

$$A_r(E, \theta, \vartheta, x) = \int_0^r dA \, dy \, dz \quad (2)$$

Henceforth we will specialize to the case of the VETA measurements, which were made on-axis, $\theta=0$, ϑ indeterminate, and in focus, $x = 0$. Dropping ϑ , the effective area is defined as

$$A_{eff}(E) \equiv A_{r=\pi/2}(E, 0, 0). \quad (3)$$

Other important quantities are the dimensionless point response function, $f = dA/A_{eff}$, and the encircled energy fraction A_r/A_{eff} .

In this paper we will deal with the encircled energy area, as measured within the available apertures (Podgorski et al. 1992). Effective area will be considered as a limiting case of encircled energy, and treated in more detail by Kellogg et al. (1992).

3. PRINCIPLES OF THE VETA CALIBRATION MEASUREMENTS

Figure 1 illustrates the fundamental principle of our calibration. A broad, uniform, parallel beam of X-rays of monochromatic energy E illuminates both the VETA X-ray mirror and a beam normalization detector (BND) immediately adjacent to the VETA. The BND is provided with a large mechanical aperture of a precisely known area, A_1 . In the focal plane, X-rays which pass through a precisely measured pinhole of angular radius, r , illuminate a focal plane X-ray detector assembly (XDA) which is nominally identical to the BND assembly. These detectors are thin window, gas proportional counters, with a gas flow system to replenish the gas which leaks out through

the windows. Analog pulses resulting from X-ray interactions in the BND and focal plane detectors are processed through nominally identical electronics, and are presented to a common analog to digital converter, the MultiChannel Analyzer (MCA), resulting in numbers N_1 and N_2 counts, respectively. We then can express the desired encircled energy area as

$$A_r = A_1(N_2/N_1). \quad (4)$$

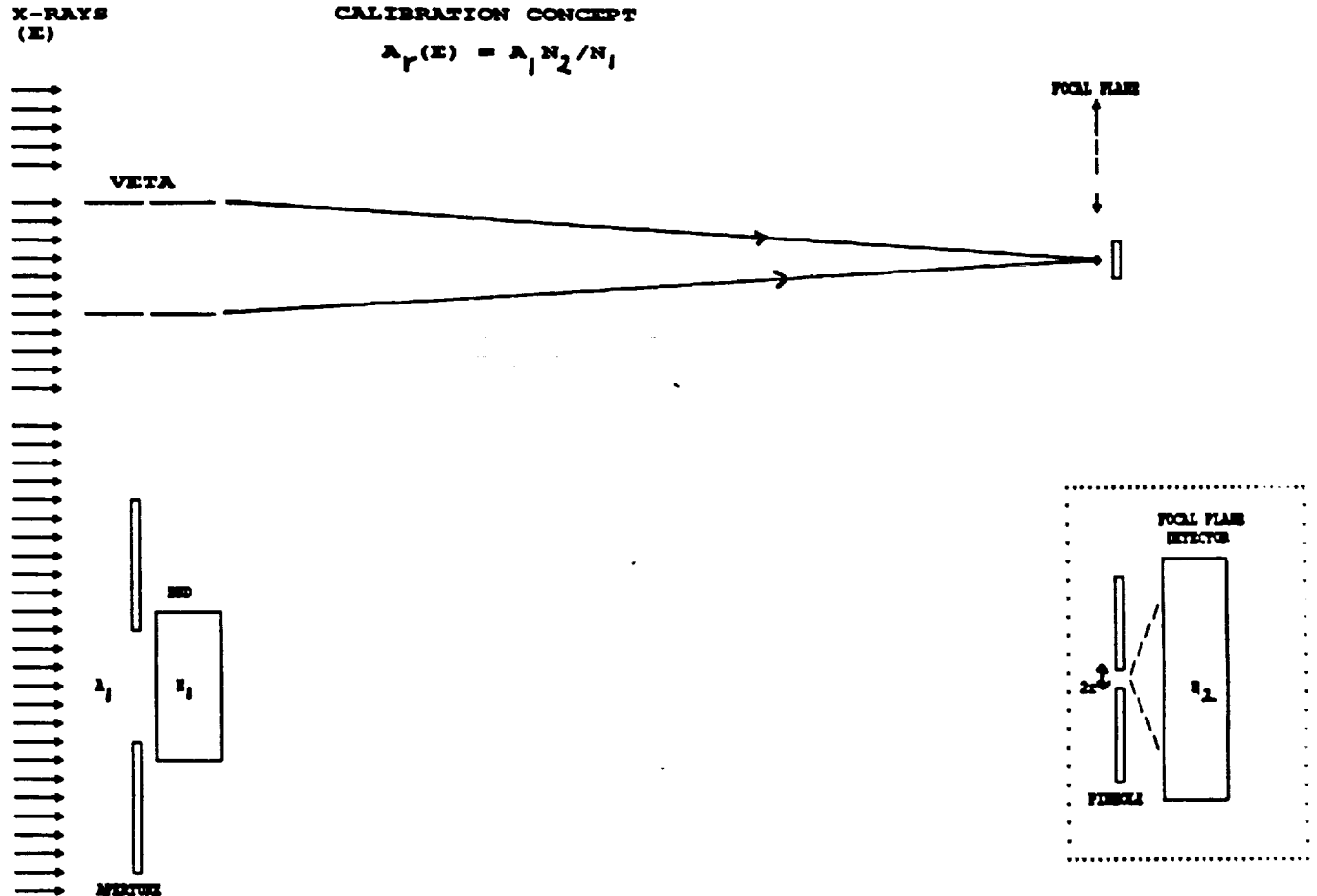


Figure 1. Cartoon of the concept of calibration of an X-ray mirror. The VETA reflects X-rays to the focal plane. The comparison of focal plane counts to counts in an identical detector adjacent to the VETA, provides the required information. The x-ray focus area is enlarged to the lower right. (Figure is not to scale.)

The remaining task of this paper is to construct the error analysis tree, accounting for the extent to which the actual experiment deviates from the above idealization. In this paper we only deal with the errors affecting the accuracy of the measurement. Specifically, the fact that the X-rays are diverging from a source of finite size at finite distance must be considered in converting from our measured parameters to the true VETA model. Since the VETA as such will not be used as a flight instrument, we do not attempt the on-orbit performance estimate in this paper (but cf., Freeman et al. 1992; Hughes et al. 1992;) For the error *analysis* tree presented here we take a data oriented approach, in contrast to the hardware oriented approach presented by Kellogg et al. (1991a) in discussing the error *budget* tree, prior to performing the measurements.

We can see some potential difficulties by reference to Figure 1. We must ask to what extent is the X-ray beam uniform, so that the mean flux over the VETA is identical to that over the A_1 aperture. Zhao et al. (1992) discussed the correction due to the fact that the X-rays form a ring on the focal plane detector, whereas they uniformly

illuminate the BND detector. Finally, the X-ray beam consists of broad bremsstrahlung continuum, underlying the idealized emission line spectrum. Chartas et al. (1992) discuss the process of extracting those counts attributable to the line emission.

4. ANALYSIS OF THE CALIBRATION ACCURACY

4.1 Top Level Encircled Energy Area

Our measurements employed 5 different energies, and 16 different pinhole sizes. Rather than present 80 detailed error analyses leading to the precise uncertainty for each measurement, we want to emphasize the error analysis structure that applies to all measurements. Thus in the discussion below we may quote a range of error values, or nominal values which apply very closely, but not necessarily precisely, to many of the measurements.

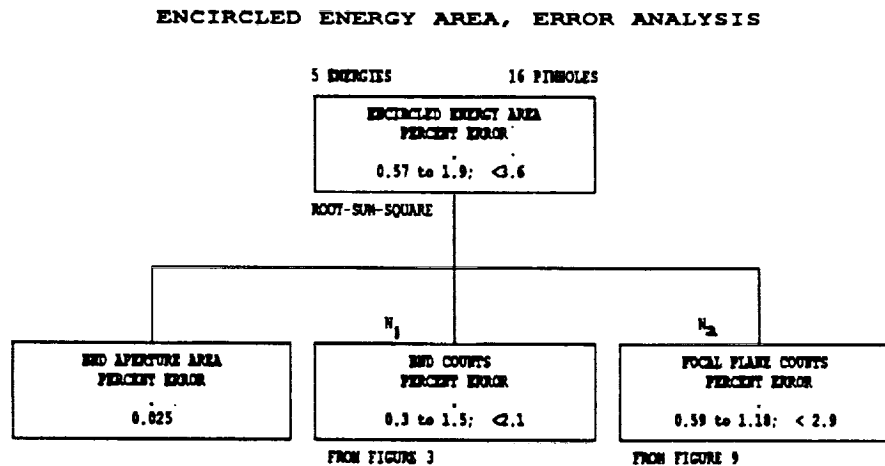


Figure 2. Top level error analysis. The final error in ENCIRCLED ENERGY AREA is shown as the root-sum-square of the three terms on the right hand side of equation (4), where N_1 are the BND COUNTS, and N_2 are the FOCAL PLANE COUNTS. The error analysis for N_1 is shown in figure 3, and the error analysis for N_2 is shown in figure 9.

Figure 2 shows the top level of the error analysis tree, based on equation (4). We intend that the three lower terms be combined as a root-sum-squares, to give the net error in the upper box. Thus we attempt to analyze systematic errors which affect both detectors in only one place: as if the BND were correct and the focal plane had a relative error, (or vice versa). The BND aperture is a 20 mm diameter hole, drilled in 1/8th inch aluminum, so that its area is 3.142 cm². The diameter is measured with a precision Jo block to an estimated accuracy of 0.025%. Effects due to vignetting by the finite thickness of the aperture, and to penetration of the Al plate by X-rays of the energies present in the bremsstrahlung continuum, are estimated at less than 10⁻⁵.

A more accurate description is given by equation (5):

$$A_p(E) = A_1 * (B_1 / B_{VETA}) * (N'_2 / t_2) / (N'_1 / t_1), \quad (5)$$

which considers the ratio of the true counting rates, with the live time ratio (t_1/t_2) and the ratio of flux on the BND, B_1 , to flux on the VETA, B_{VETA} , both taken as nominally 1. The primes denote the counts from the X-ray lines,

rather than the total counts in the detectors. These counts, N'_2 and N'_1 , are determined from fits to the proportional counter pulse height spectra, as discussed by Chartas et al. (1992).

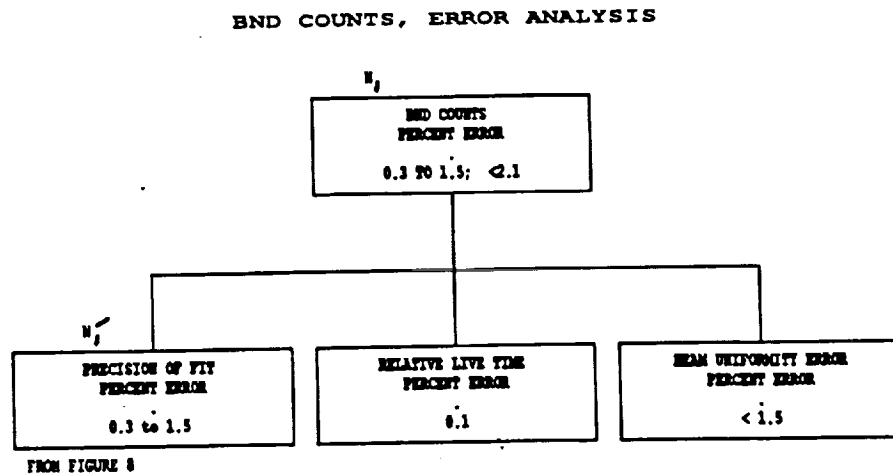


Figure 3. Analysis of the error in the BND COUNTS. The top box represents the net error in N_1 , and the lower left box the error in determining N'_1 . The error in N'_1 is analyzed in figure 8. Data on the RELATIVE LIVE TIME is shown in figure 4, and data relative to the BEAM UNIFORMITY ERROR is shown in figure 5.

Figure 3 shows the top level error analysis for the idealized BND counts, N_1 , and Figure 9 for the idealized focal plane counts, N_2 .

4.2 Error Analysis of the Beam Normalization Detector Counts.

To estimate the live time in each detector chain, we insert a pulse generator of known rate into a portion of the pulse height spectrum where we do not expect significant X-ray counts. Figure 4 plots the dead time determined in this manner for the BND and focal plane counts, separately, as a function of the total counting rate of the MCA. We also plot the dead time measurement which is generated internally by the MCA. We attribute the small differences among these curves, and the fact that they do not have zero intercept, as due to low level noise pulses which do not register as MCA counts, and vary due to different noise levels in different detectors. Our nominal operating point is about 5000 s^{-1} , giving a relative error of 0.1%. We analyze this error as applying to the incident flux determined by the BND.

We find no evidence for spatial irregularity of the X-ray beam which would cause the BND to sample a flux different from the VETA. Unfortunately we were not able to do the extensive experimentation necessary to provide stringent limits. Ideally, we would scan one BND in space over the area in front of the VETA, and compare its counting rate to an identical fixed BND detector in order to separate effects of time variability in the X-ray generator. This is planned to be carried out prior to and subsequent to calibration of the actual flight mirrors. At present we have some limited information obtained by scanning the focal plane detector in the broad beam at the focal plane, after the VETA had been removed. Figure 5 shows the ratio of the focal plane (scanning) to BND (fixed) total counts, vs. the position of the focal plane detector over a 600 mm scan in the horizontal direction, with the Al source. If this scan were a fair sample of the VETA aperture, we would quote the maximum allowed rms of the ratio about its mean value, and after root-sum-square subtraction of the counting rate statistics, as the limit to the beam non-uniformity. Instead, to attempt to be more conservative, we quote the total 1.5% change obtained by an eyeball straight line fit to the data. Although this was a horizontal scan, we note that the BND is displaced vertically from the telescope axis. We

may expect that the beam non-uniformity depends on the filter used with each target in the X-ray generator, and thus is specific to each X-ray energy.

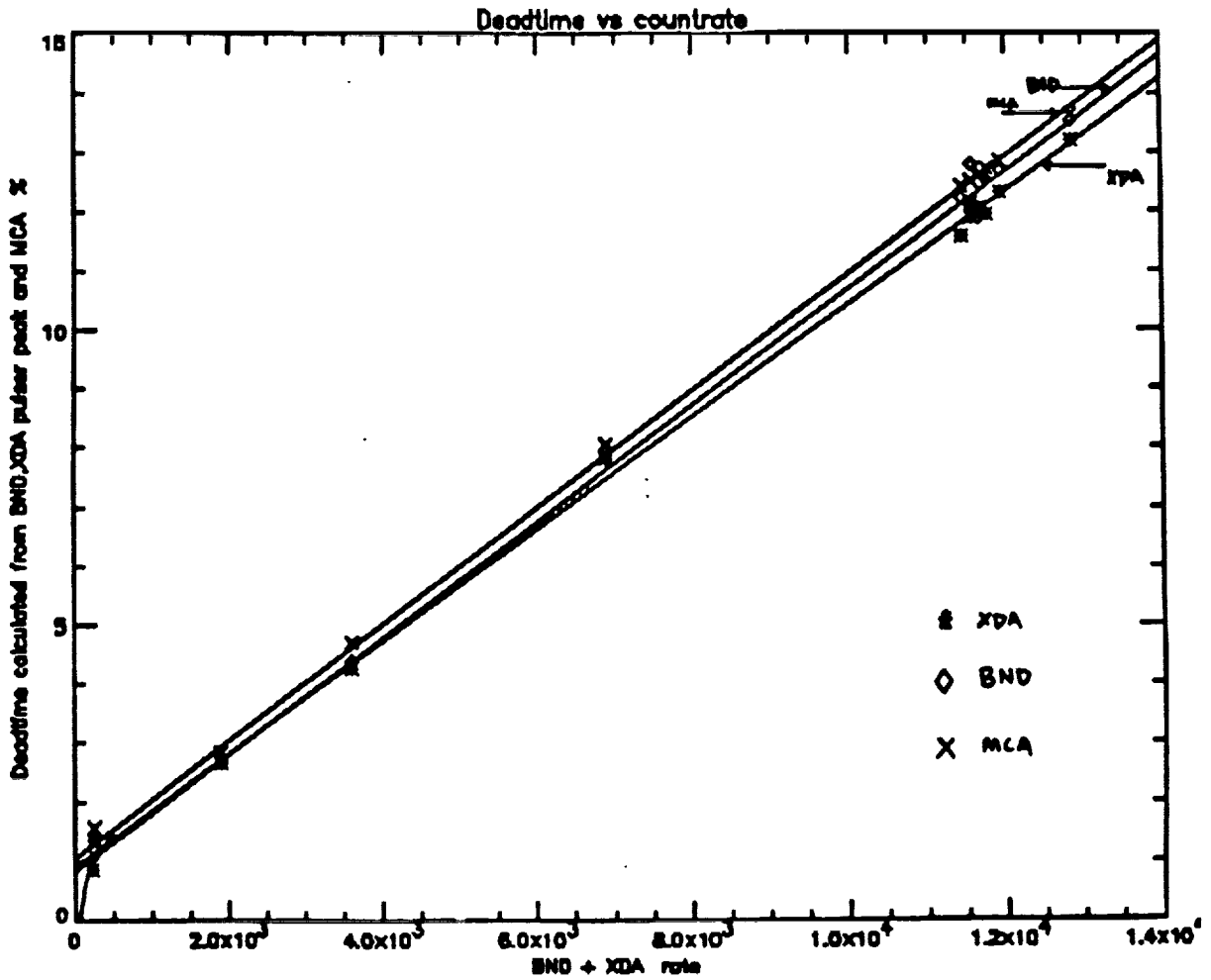


Figure 4. Percent dead time is plotted vs total (i.e., BND plus XDA) counting rate. The dead time is estimated in three different ways: MCA designates the expected dead time as generated by the MCA electronics; BND designates dead time estimated by a pulse generator of known rate through the BND electronics chain, and XDA designates dead time estimated by the same pulse generator through the XDA electronics chain.

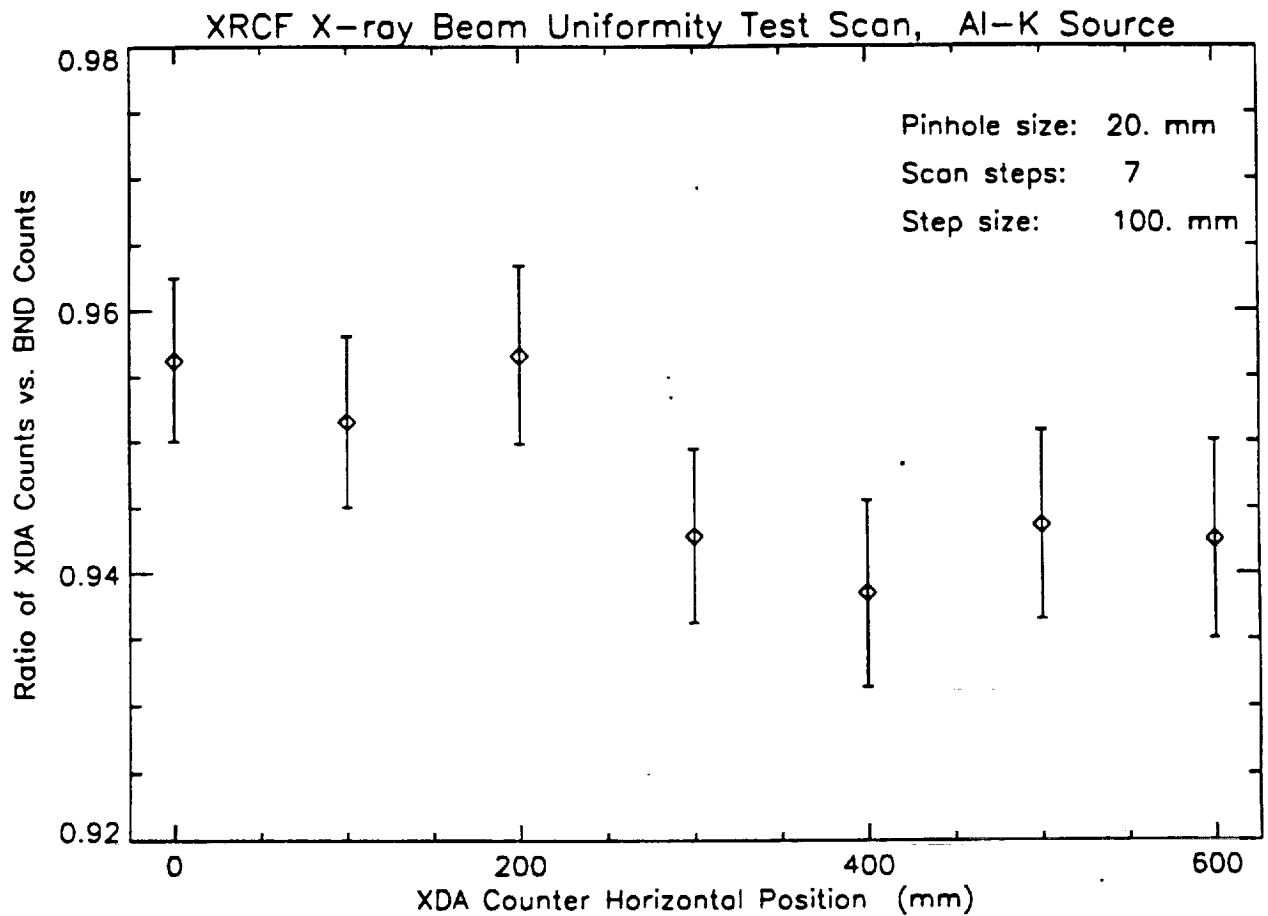


Figure 5. Beam uniformity scan for the Al 1.5 keV x-rays. The ratio of the XDA to BND detector is plotted vs. the horizontal (Y-axis) position of the XDA detector in the focal plane.

An example of the expected shape of the X-ray spectrum incident on the BND and VETA is shown in Figure 6. For this molybdenum target, the continuous histogram shows the bremsstrahlung continuum extending up to 17 keV, corresponding to the setting of the generator high voltage. The notch above 2.3 keV is due to using a Mo filter to reduce this continuum. Mo has a complex of L-shell lines around 2.3 keV, with the five strongest spread over the region 2 to 2.5 keV. In all our fitting, we treat the multiple K or L shell lines with fixed ratios as tabulated in Salem et al. 1974, and treat the total line flux resulting in the fits as being at the weighted mean energy. The bremsstrahlung continuum shape is taken to be the thick target result, $\frac{dn}{dE} \propto \alpha(E_{max} - E)/E$, where n is the number of bremsstrahlung x-rays at energy E , and E_{max} is the electron acceleration voltage.

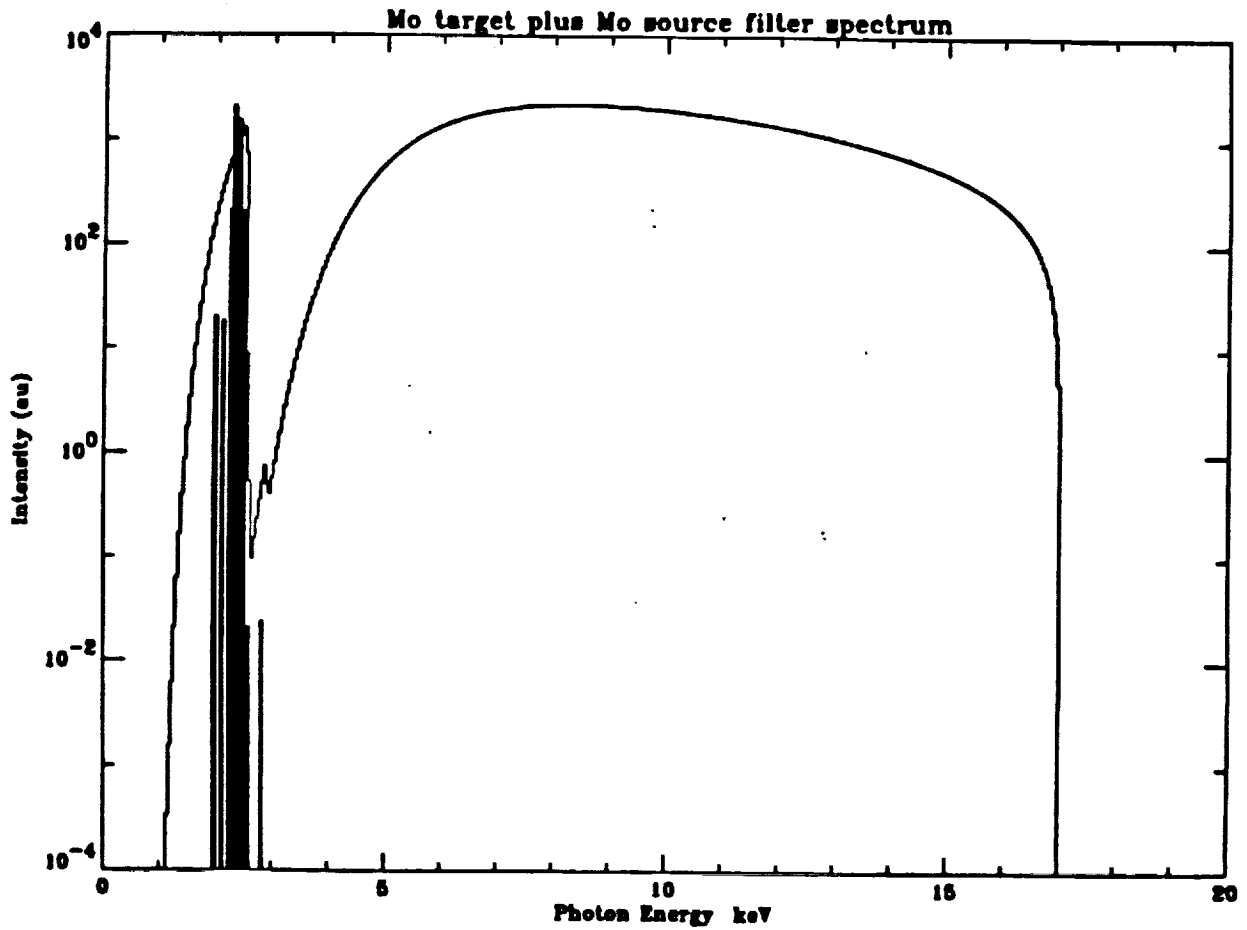


Figure 6. Deduced shape of the spectrum from the molybdenum target, incident on the BND detector. We see the bremsstrahlung continuum, and the complex of L-shell lines centered on 2.33 keV. The intensity is in arbitrary units, plotted in 50 eV wide bins.

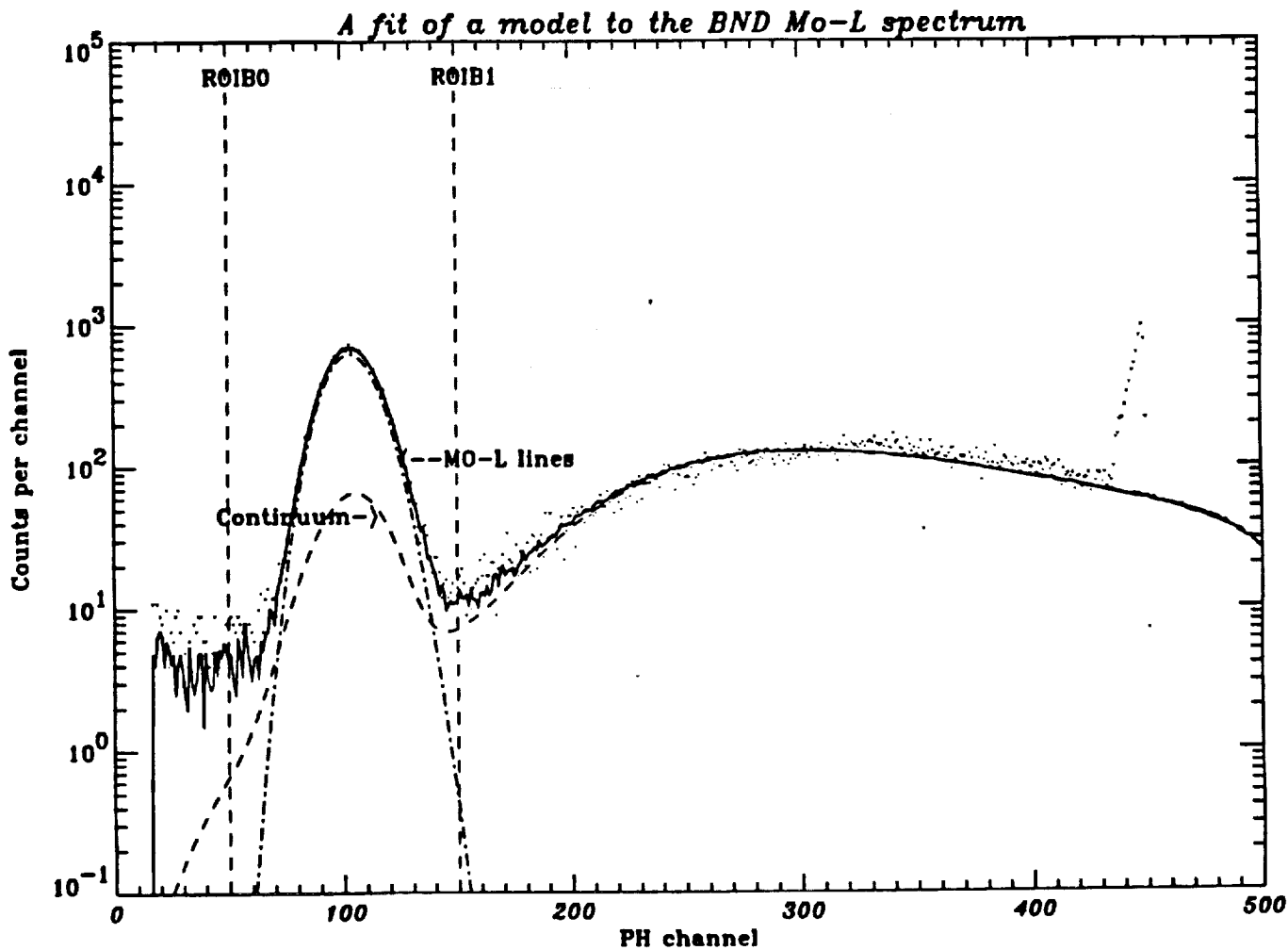


Figure 7. Response of the BND pulse height analysis, dots, compared with that expected by fitting the counter response to the input model of figure 6. The peak at channel ~ 100 is the response to all the L-shell lines, smeared out by the detector resolution. The lower solid line is the fit to the bremsstrahlung continuum, and the upper continuous line is the sum of the line and continuum component. The data analysis depends on the fit within the pair of vertical dashed lines designated ROIB0 and ROIB1 (see Chartas et al., 1992). (The measured counts pile up around our upper threshold, at about channel 450.)

Figure 7 is a typical pulse height spectrum observed in the BND for Mo X-rays. The key feature of the proportional counter response is that its modest energy resolution greatly broadens and blends all the X-ray lines, and also smooths out the sharp features due to the filter. In our data analysis, we subtract non-X-ray background, and perform fits to determine the strength of the lines, the continuum normalization, the energy resolution parameter using a Prescott response function, and the peak channel of the X-ray lines. As discussed by Chartas et al. (1992), we take the actual counts in the region of interest, shown as the vertical dashed lines, and subtract the number of counts determined by the fit to the bremsstrahlung continuum.

Figure 8 shows the analysis of the precision of extracting the X-ray line counts from the BND according to the process just described. The number of total counts in the region of interest is typically a few thousand to less than 100,000, so we show a 0.4 to 1.5 percent error in the statistics of the line peak counts. Generally, the X-ray generator flux is observed to be stable in time over a few minutes to a few hours, so we average from 2 to 20 different BND spectra in order to obtain one single fit with which to compare a series of focal plane measurements. This reduces the net error to the 0.1 to 1% range.

PRECISION OF BND FIT, ERROR ANALYSIS

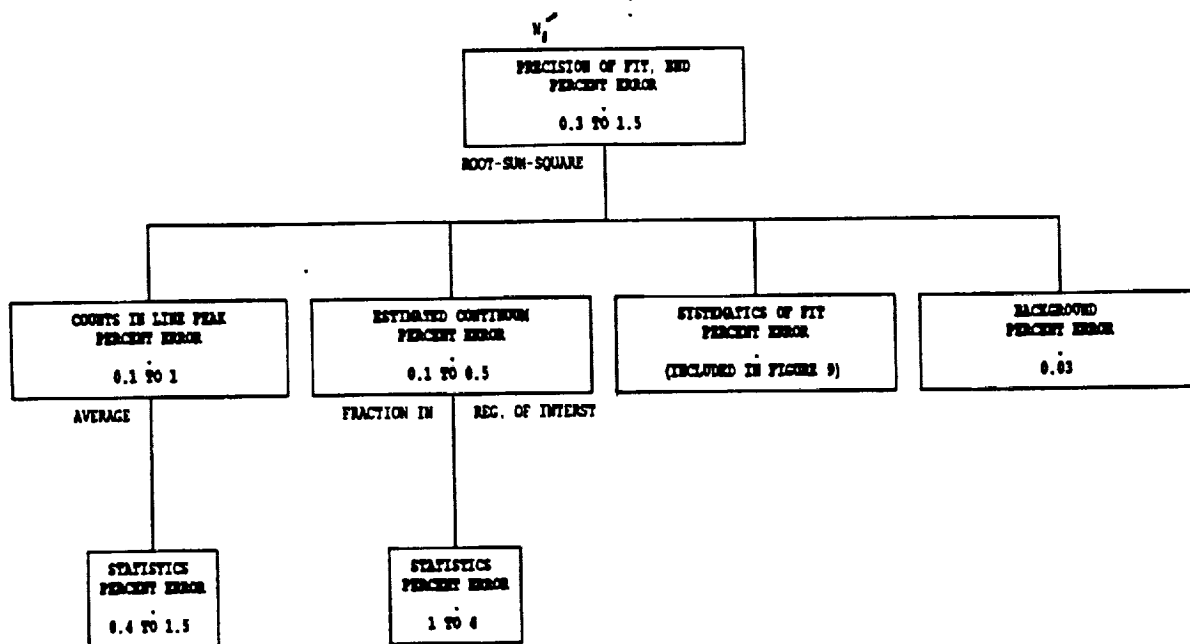


Figure 8. Analysis of the uncertainty in N'_1 , the fit to the number of counts from the X-ray line as measured in the BND detector. The error is dominated by the Poisson fluctuations in the number of counts in the line peak and in the continuum. The systematic errors of the fit are all attributed to the XDA counts, since it is only errors in the ratio of XDA to BND which affect the encircled energy results.

The number of counts inferred as the continuum contribution ranges from ~600 to 10,000, so its flux is approximately determined to 1 to 4% of its own value. When averaged, and expressed as a fraction of the line flux, the estimated error ranges from 0.1 to 0.5%.

In the figure, we include a term to allow for errors which result from the systematics of the least-squares-fit process. These arise due to parameters which are kept fixed, e.g., the X-ray generator high voltage or the proportional counter window thickness, for which the value assumed may be incorrect. For analysis purposes we will assess all these effects when we consider the focal plane detector errors, since it is only the error in the ratio of counts that affects encircled energy.

We measure non-X-ray background when the gate valve to the X-ray generator is closed. We typically integrate long enough to acquire 1000 counts, so that the background flux is known to $\sim 3\%$. The BND counting rates are always 100 times higher than background, so that this gives only 0.03% effect on the fitted counts.

We assume all other effects are each less than 0.1%, and we do not discuss them further since they contribute negligibly to the root-sum-square error. An example is the exact choice of the "region of interest" boundaries, as shown by Chartas et al. 1992 (their Figure 9).

4.3 Error Analysis of the Focal Plane Detector Counts.

Figure 9 presents the top level analysis of the focal plane detector counts. The relative live time box is repeated here for completeness, but has zero entry since we formally included its effects in the BND rate.

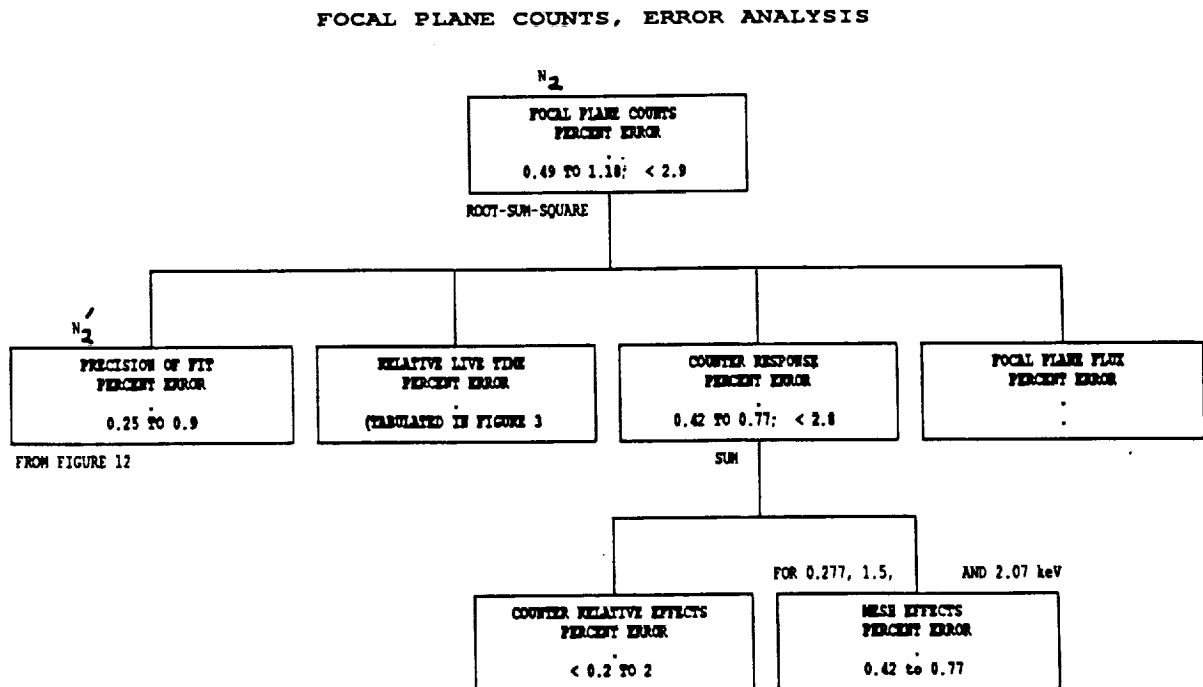


Figure 9. The error analysis for N_2 , the idealized number of counts in the focal plane detector. PRECISION OF FIT error is shown in figure 12. The FOCAL PLANE FLUX error term would enter in the discussion of the true absolute effective area, but is shown blank here. MESH EFFECTS are discussed in Zhao et al. (1992).

The "counter response" term is intended to include intrinsic differences in the focal plane detector relative to the BND detector, (omitting terms due to "systematics of fit" discussed in figure 12). The primary effect is due to the window support mesh, as discussed in detail by Zhao et al. (1992). For the C-K (0.277 keV), Al-K (1.49 keV), and Zr-L (2.07 keV) lines the estimated residual uncertainty after performing the correction is 0.5%. For the Cu-L (0.93 keV), and Mo-L (2.3 keV) lines we did not scan the counter windows behind the pinholes as is necessary to perform the correction. In this case we assume the $\pm 8\%$ full range of the possible correction is a uniform distribution (for which the rms is $1/\sqrt{12}$), and therefore take $16\%/\sqrt{12} = 4.4\%$ as the error.

The term "counter relative effects" is intended to account for unexpected ways in which the BND and focal plane detectors differed. (Expected possible differences are analyzed in the "systematics of fit" term in figure 12.) It was planned that we would correct for these unexpected differences by simply swapping the positions of the two counters and comparing the ratios of counts in the swapped vs. normal positions. Unfortunately, the window on the BND

counter was broken before this swap could be performed. The transparency of the actual window is an important determinant of the proportional counter response, so it is not valid to perform the swap with a replaced window and use it to correct the VETA data. Instead, we studied the ratios with the counters swapped for the replaced window, and interpret the apparent difference as an upper limit to the error. In the case of Al-K X-rays the two ratios, for the raw counting rate data, were 1.037 and 1.039, while for Cu-L X-rays the ratios were 1.063 and 1.042. We thus show 0.2 to 2 percent as an upper limit to this error term. We treat the actual error as zero. From this data, we estimate that for the flight mirror we will be able to perform this correction to within a residual 0.2% error.

In figure 10 we show the estimated X-ray generator spectrum from the Al target. We see the Al-K lines (solid), and the bremsstrahlung continuum (dotted) modified by the Al filter. The dot-dash line indicates the expected spectral shape incident on the focal plane. Because the VETA mirror response cuts off sharply above 2 keV, the continuum spectrum is significantly modified. Figure 11 shows the pulse height spectrum as recorded in the focal plane proportional counter. We notice the continuum contribution is reduced, relative to the BND spectra. We also see a broad peak at about twice the Al-K energy. This is due to pile up of Al-K X-rays, since we are typically counting at several thousand per second. Although prominent on the graph, it is less than 1% of the Al line counts, and it is known to within a few percent of its own estimated value (from figure 5 of Chartas et al. 1992), so that it gives less than a few hundredths percent error to the focal plane counts.

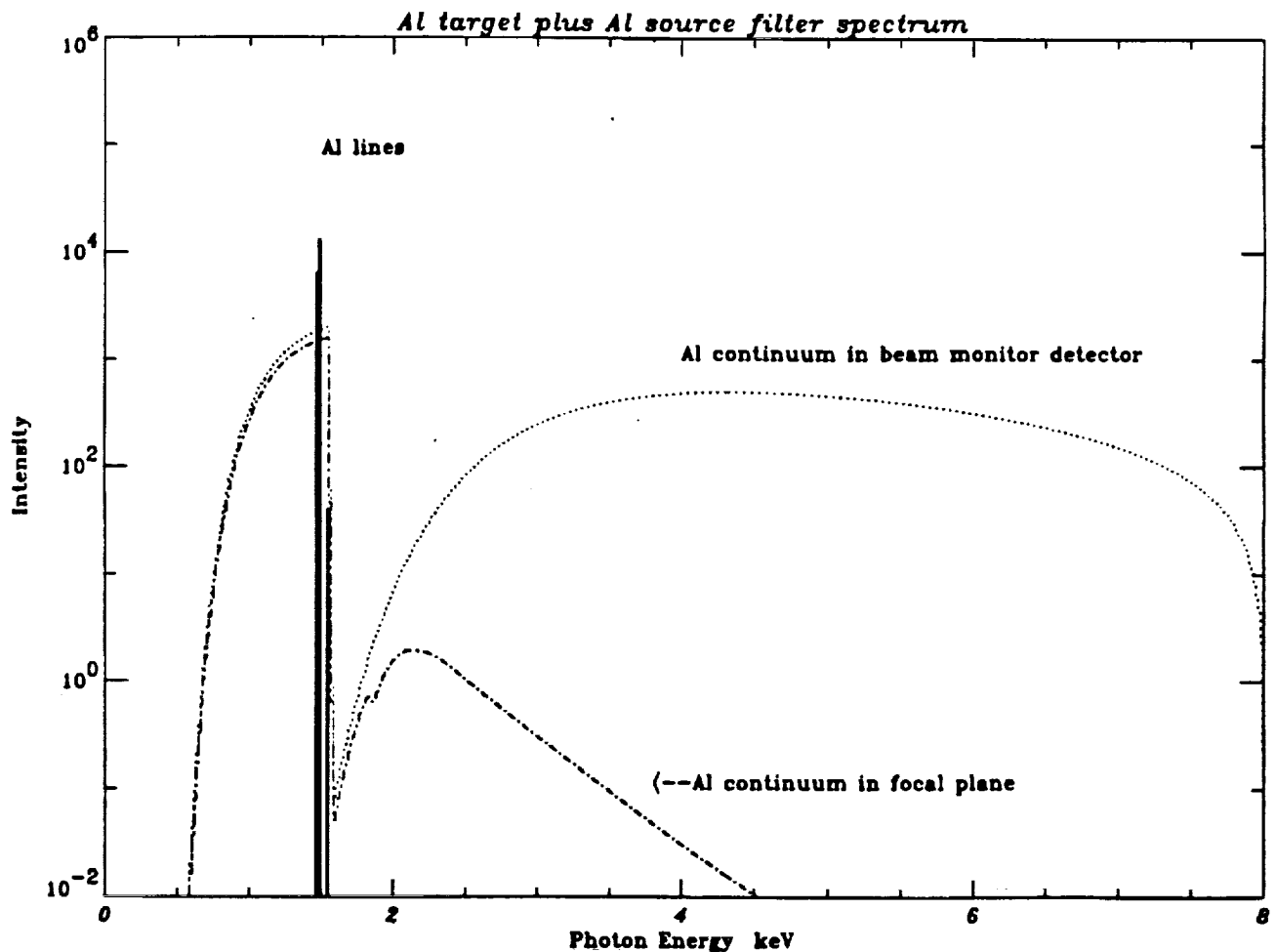


Figure 10. Deduced shape of the spectrum from the aluminum target, as incident on the VETA (dotted line) and incident on the XDA detector after reflection by the mirror (dash-dot line). We see the bremsstrahlung continuum, and the K-shell lines centered on 1.49 keV. The intensity is in arbitrary units.

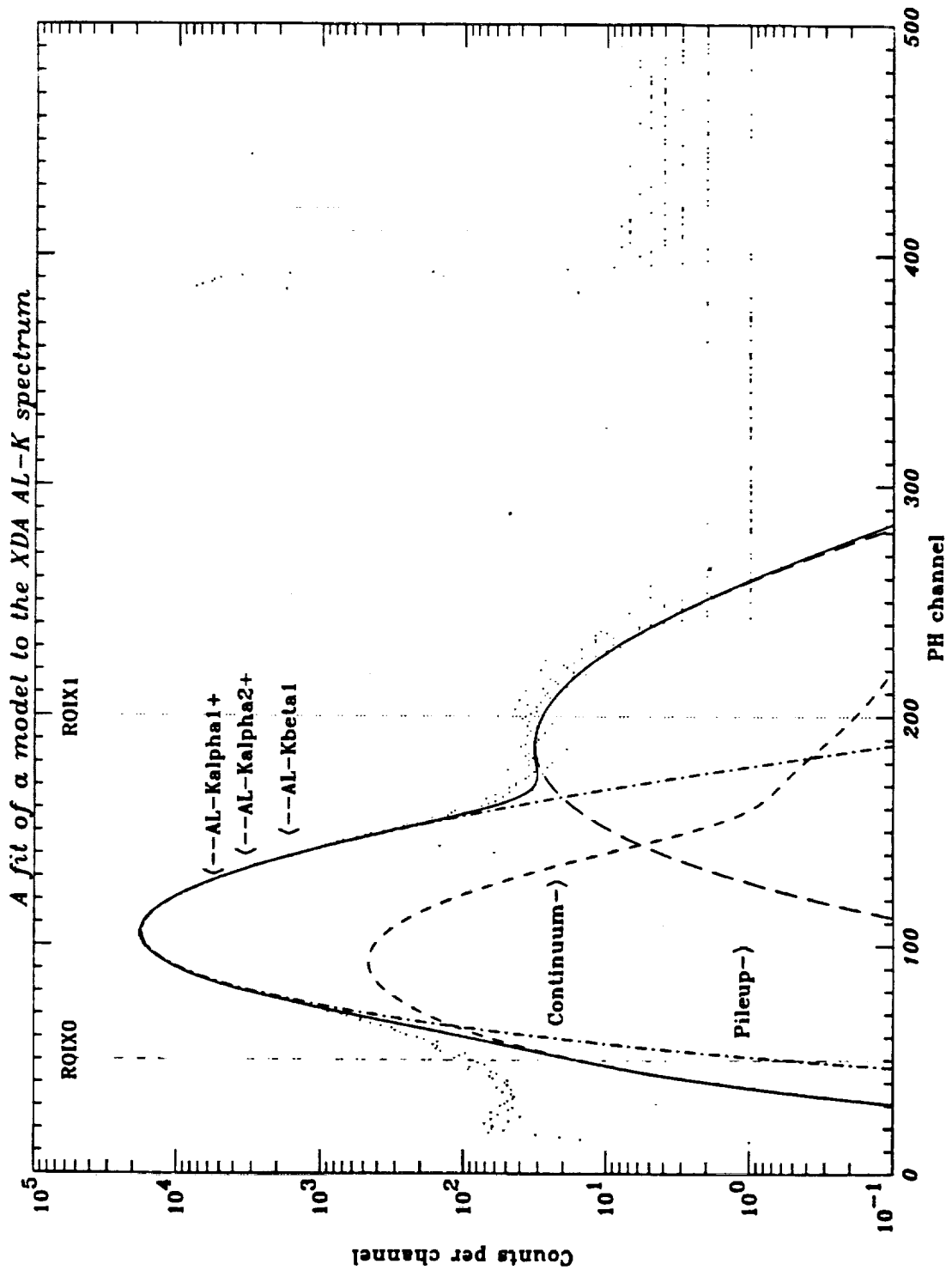


Figure 11. Response of the XDA pulse height analysis, dots, compared with that expected by fitting the counter response to the input model of figure 10. The peak at channel ~ 100 is the response to the K-shell lines, smeared out by the detector resolution. The peak at channel ~ 200 is from pulse pile-up. The short dashed line is the fit to the bremsstrahlung continuum, and the upper solid line is the sum all components. The data analysis depends on the fit within the pair of vertical dashed lines designated ROIX0 and ROIX1 (see Chartas et al., 1992). (The pulser used for dead time estimation peaks at about channel 390.)

Figure 12 analyzes the precision of fitting to the line counts in the focal plane detector. The data analysis proceeds by taking all the measured counts within the region of interest indicated by the vertical lines, subtracting the fit to the continuum, subtracting that part of the fit to the pile up peak which falls within the region of interest, and adding twice the total number of counts fit to the entire pile up peak, since these pile up events are each two 1.49 keV X-rays.

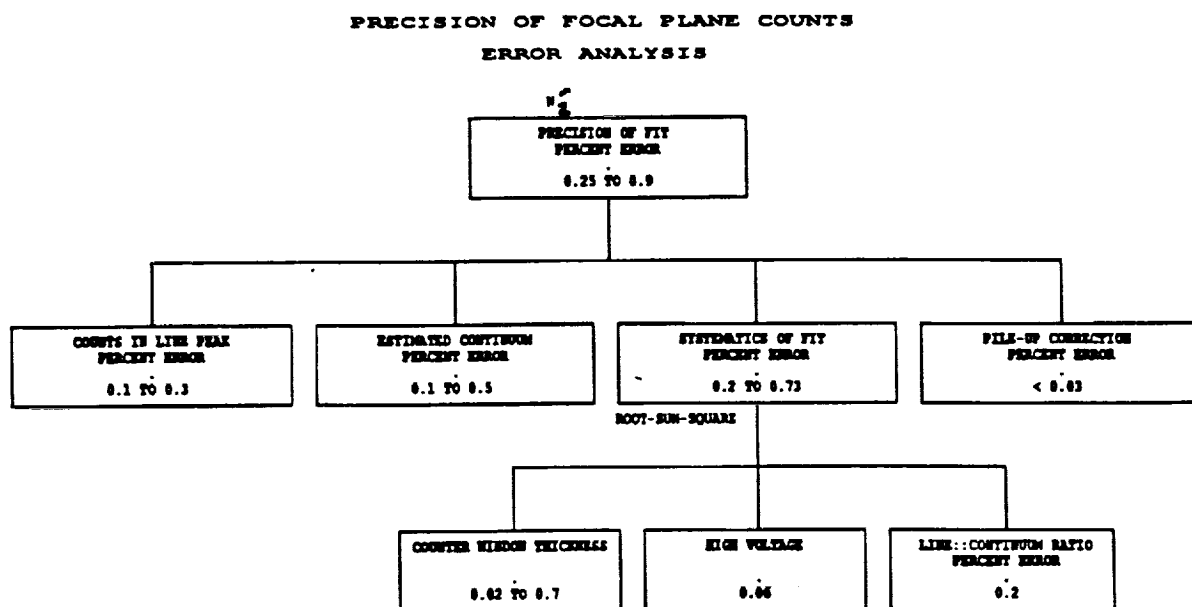


Figure 12. Error analysis for N_2' , the fit to the number of counts in the X-ray line. The COUNTS IN LINE PEAK and ESTIMATED CONTINUUM boxes are the Poisson statistical errors. See text for SYSTEMATICS OF FIT errors.

Counts in the line peak are typically 10^5 to 10^6 , giving a 0.1 to 0.3 percent error. The pile-up correction itself is about 1 to 3%, known to an accuracy of about 1%. The background is known to about 3%, but is less than 0.001 of the line counts. The significant new term in this error tree is that due to the systematics of the fit. The three dominant terms are due to the counter window thickness, the ratio of the line to continuum counts in the incident X-ray spectrum, and the high voltage setting of the X-ray generator. Each of these is held as a fixed, given parameter during the fit to determine the number of counts in the X-ray line.

We perform a sensitivity analysis to assess the effects of those terms. Figure 13 shows the effect of varying the proportional counter window thickness from its nominal value of 1.7 ± 0.2 microns. The top panel for each energy (13a for 1.49 keV, 13b for 0.277 keV), shows how the number of fitted counts changes as a function of fixing different window thickness parameters. The bottom panel shows the percentage error. The effect is greatest at the lowest energy, C-K where the window is most opaque.

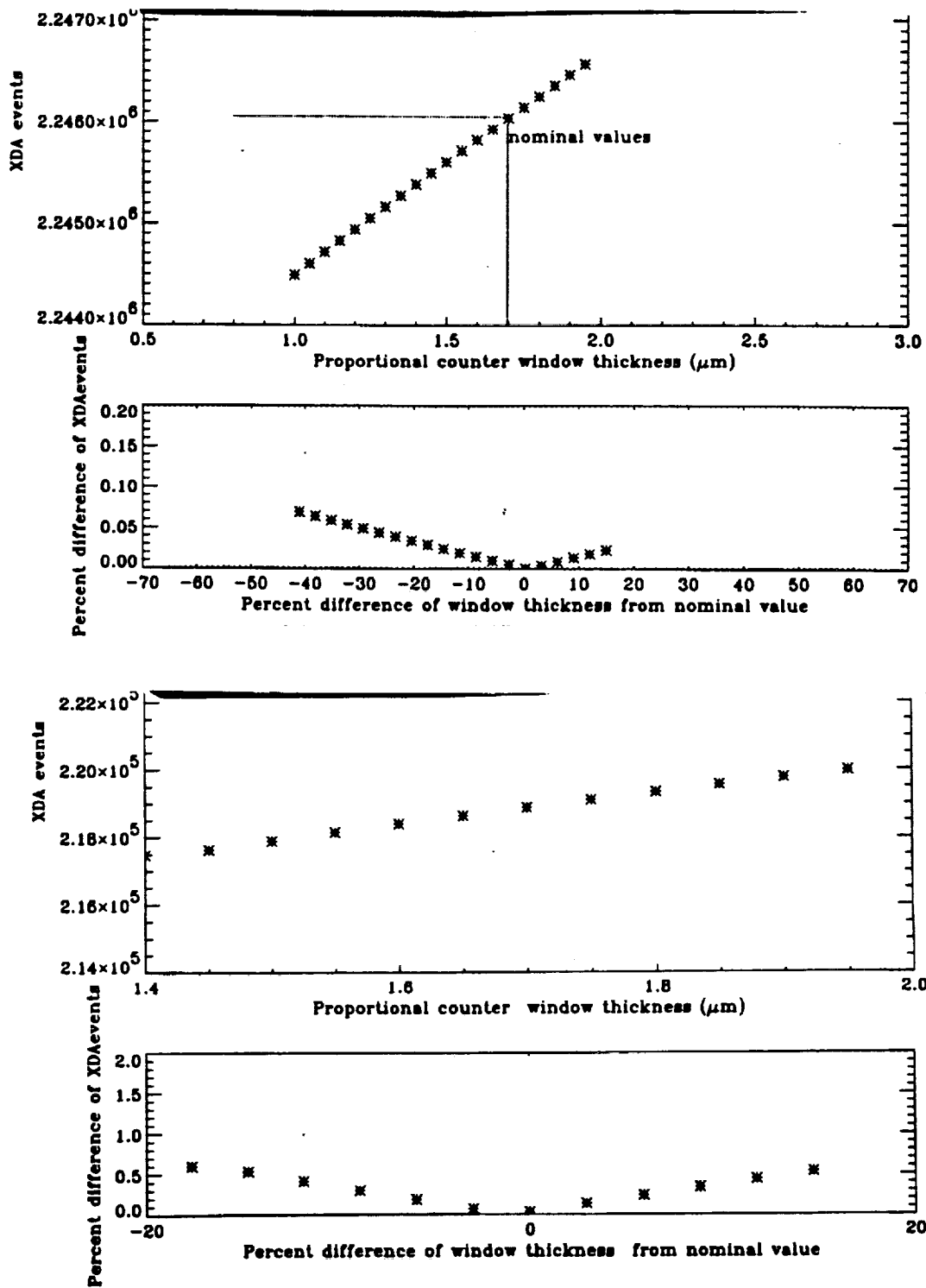


Figure 13. Systematic change of the deduced line counts for Al-K X-rays (fig. 13a, upper 2 graphs) and for C-K X-rays (fig. 13b, lower 2 graphs), vs. the true proportional counter window thickness. The bottom panels of 13a and 13b show the percentage change in deduced line counts vs. the percentage change in window thickness. The nominal error in knowledge of the window thickness is 0.2 microns.

Figure 14 shows the effect of varying the assumed value of the high voltage setting of the X-ray generator, on the fitted counts from Al. Within the assumed 1% tolerance on the generator setting, the deduced counts change by less than 0.06%.

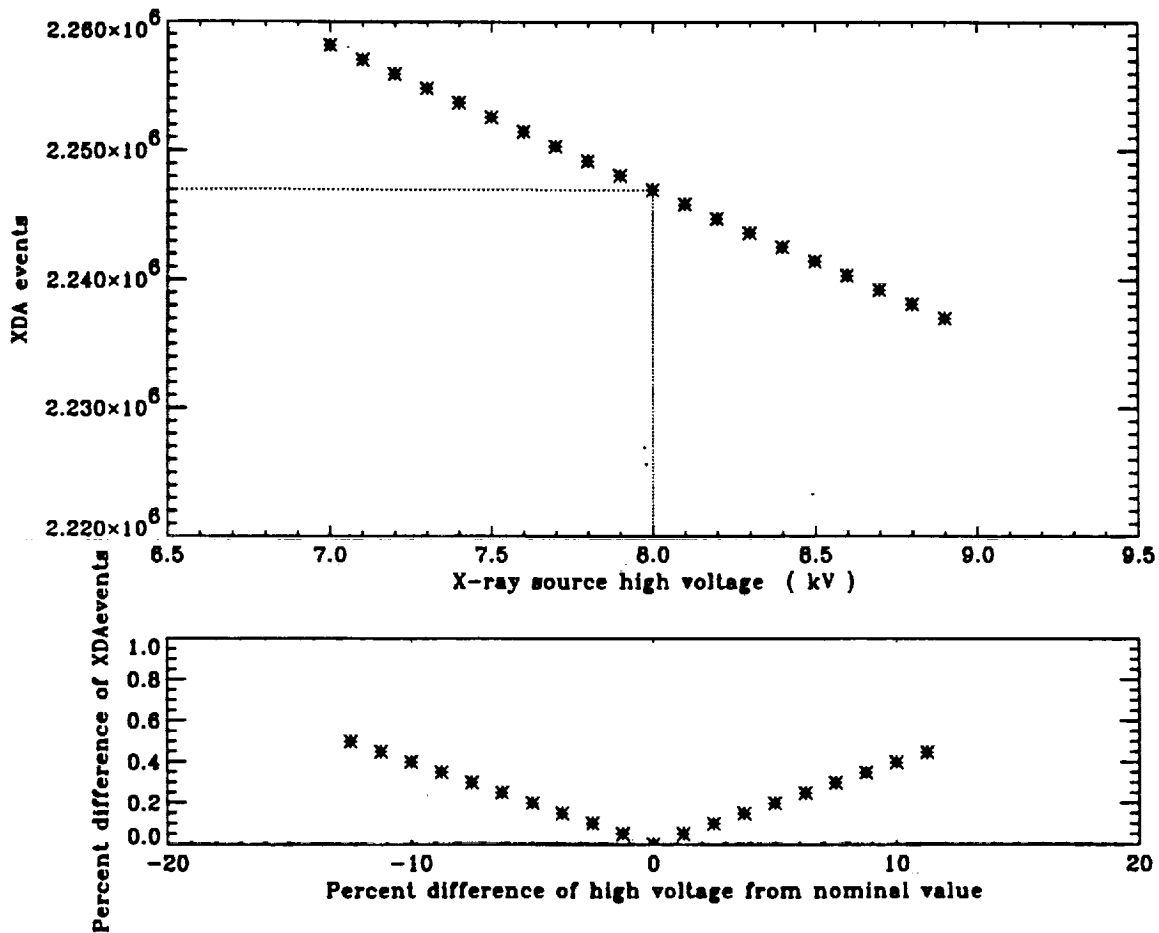


Figure 14. Systematic change of the deduced line counts for Al-K X-rays vs. the true high voltage setting of the X-ray generator. The assumed accuracy of the high voltage setting is 1%.

In fitting the focal plane counts, we assume that the incident X-ray line to bremsstrahlung continuum ratio is the same as determined from the fit to the BND data, and modified subsequently by the mirror reflectivity. Figure 15 shows how the line strength and continuum strength parameters are independently fitted to the BND data. The range of variation of the ratio is taken from the extremes on the 95% confidence contour, and applied in figure 16 to the analysis of the sensitivity of the Al counts, resulting in a 0.2% error.

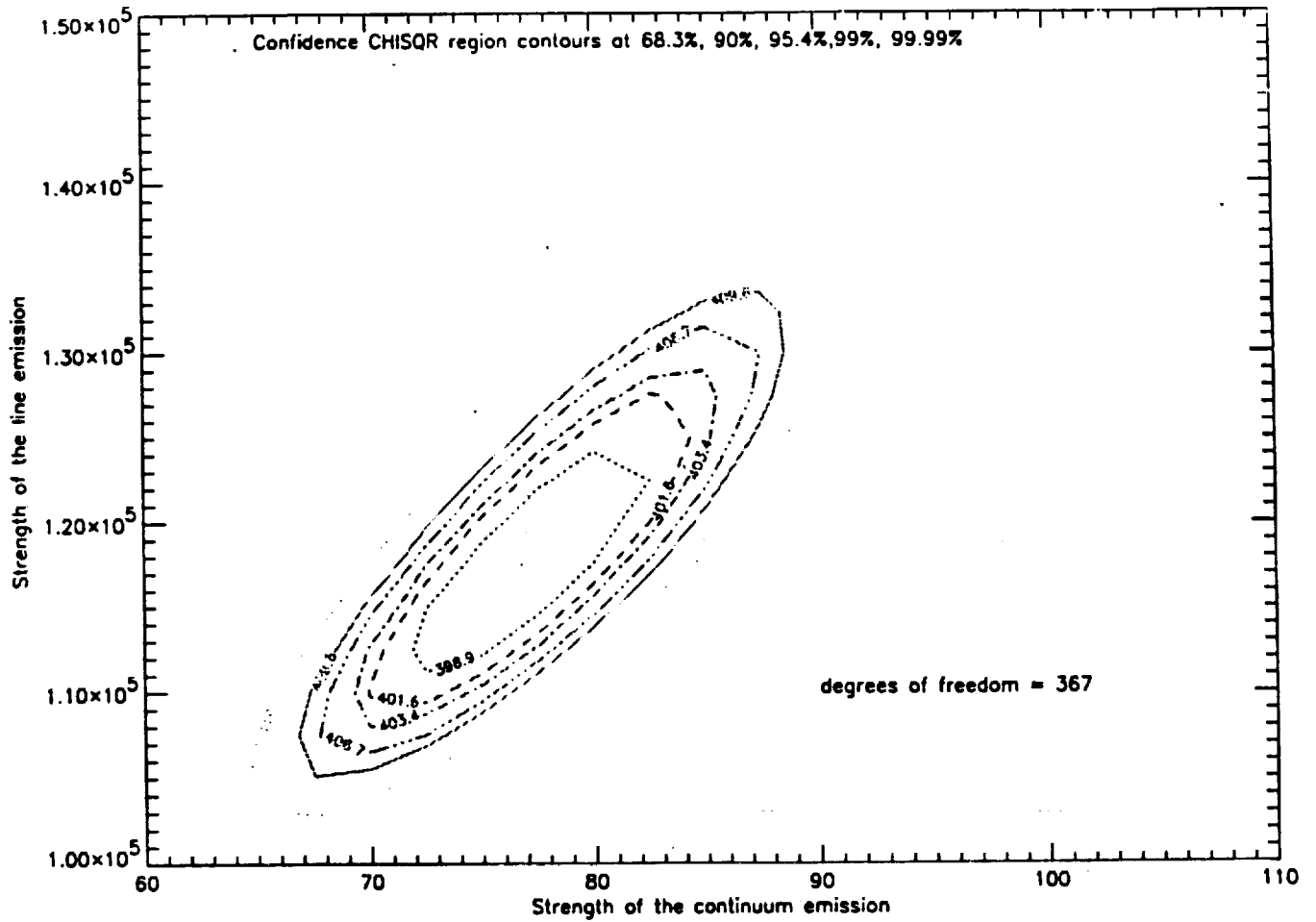


Figure 15. Chi-squared contours for jointly determining the line strength and the continuum strength from the BND data for the Al target. We take the extreme range of variation of the ratio of line to continuum flux (about 5%), along the 95% confidence contour, to estimate the uncertainty of the focal plane counts due to this systematic error.

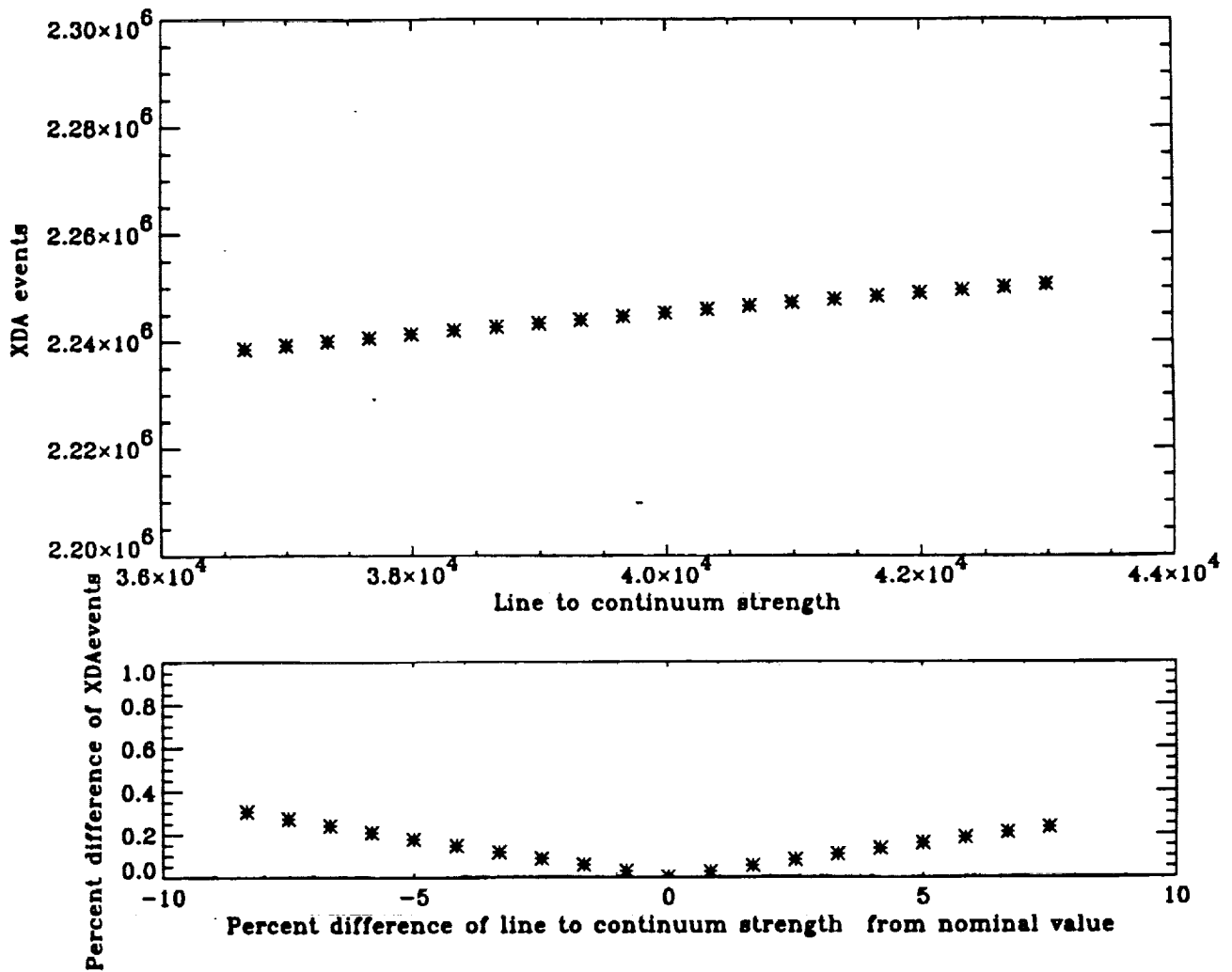


Figure 16. The upper panel shows the systematic change of the deduced line counts for Al-K X-rays vs. the true value of the line to continuum strength (plotted in arbitrary units). The lower panel shows the percentage error in Al line counts vs. the assumed percentage error in the ratio. The nominal error in the ratio is $\sim 5\%$, to 95% confidence.

4.4 Summary

Figure 17 summarizes the error estimates for the 3 most reliable energies, and for pinholes of diameter 3 arcsec and larger. The proportional counters could not be centered at the same precise position behind the pinholes of radius 20 and 100 arcsec as for the other pinholes, and this may be reflected in a slightly larger error for some of those data points. Within the internal accuracy of the estimates of the error of each point, the errors are probably consistent with the mean for all pinhole sizes of each given energy: 1.07% for 0.277 keV, 0.75% for 1.49 keV, and 0.89% for 2.07 keV. It is reasonable that the errors would be the same, since this range of pinhole radii all contain greater than 80% of the encircled energy.

ENCIRCLED ENERGY ERROR

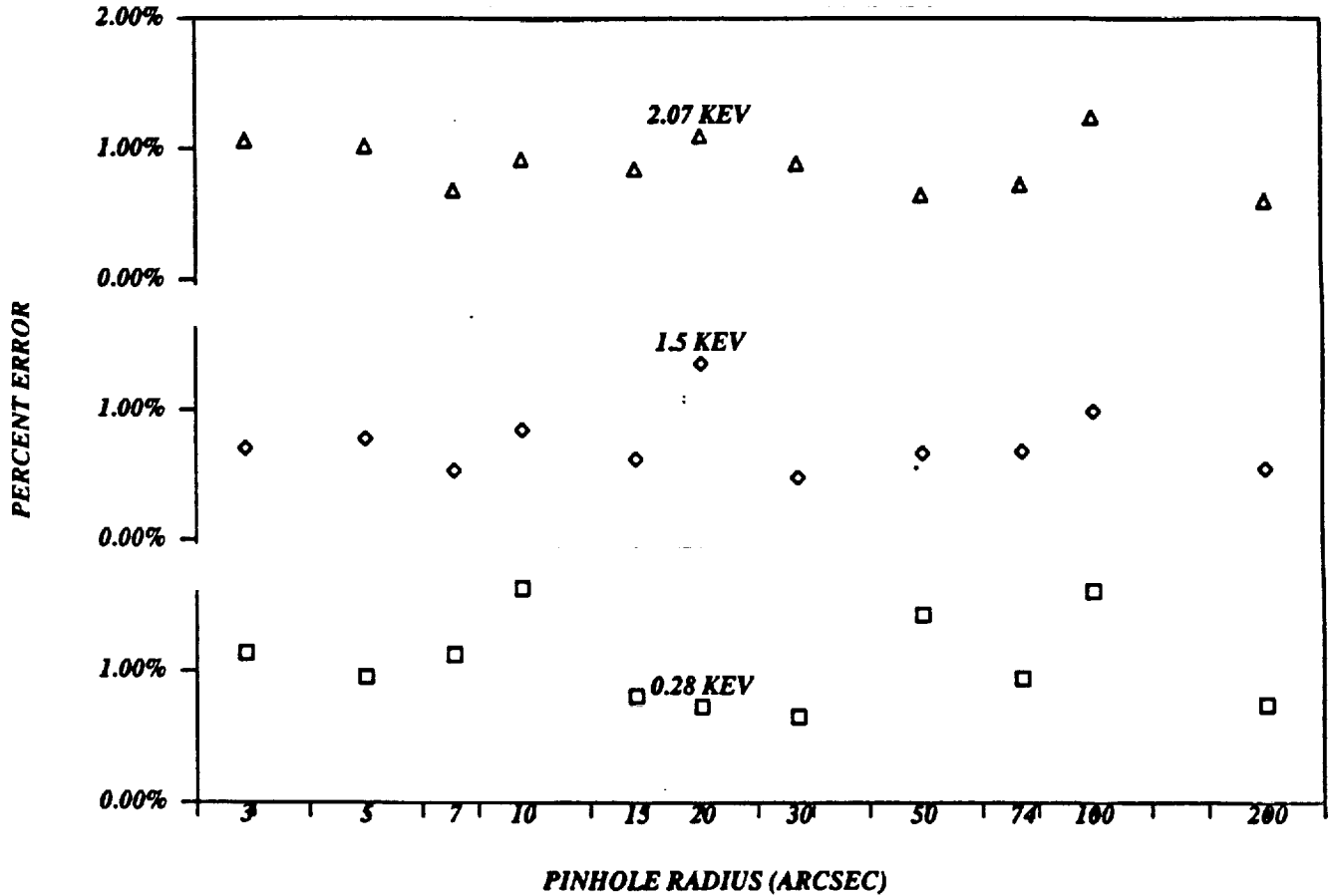


Figure 17. Percentage error on the Encircled Energy Area, for pinholes of radius 3 arcsec and larger, at the C-K, Al-K, and Zr-L X-ray lines. The scatter for the different size pinholes is consistent with a constant error of 1.07% at 0.277 keV, 0.75% at 1.5 keV, and 0.89% at 2.07 keV.

Assuming the error for each energy is constant, independent of pinhole size, we use the rms scatter of the 11 data points to calculate the precision to which we have estimated the mean error at each energy. We find 0.35% for 0.277 keV, 0.24% for 1.49 keV, and 0.20% for 2.07 keV, as the uncertainty in how well we know the errors at those energies. This justifies quantitatively our ignoring some of the errors of magnitude less than 0.1%.

The precision of making VETA measurements makes us optimistic that we can achieve our goal of predicting the on-orbit AXAF telescope performance to a precision of order 1%. The correction of ground calibration data to on-orbit prediction also depends on the accuracy of the models of how the telescope will distort in the presence of gravity. This uncertainty is expected to be of order 1% itself, therefore we desire to improve the ground measurements by another factor of ~ 2 , but will encounter diminishing returns for further improvement beyond that point. Understanding the counter effects of window thickness and mesh shadowing, and obtaining increased characterization of the X-ray spectrum produced by the generator, offer significant error reduction. In addition, we know that for the VETA test we were subject to systematic errors due to X-ray beam spatial irregularities and systematic counter differences. Direct measurement and correction for these effects is planned for the AXAF flight mirror calibration.

5. ACKNOWLEDGMENTS

We thank M. Birkinshaw and H. Tananbaum for comments on the manuscript. R.Brissenden, J. Chappell, M. Freeman, D. Graessle, M. Jones, M. Joy, J. Kolodziejczak, D. Nguyen, T. Norton, W. Podgorski, J. Roll, P. Slane and L VanSpeybroeck all played important roles in carrying out the VETA-I tests and analyses. We thank many MSFC, TRW, and EKC personnel for heroic efforts in preparing facilities and supporting the execution of the test. This research was supported in part by NASA contract NAS8-36123.

6. REFERENCES

- Brissenden, R.J.V., Hughes, J.P., Kellogg, E.M. and Zhao, P., Internal SAO report SAO-AXAF-AR-91-080, 15 November 1991.
- Brissenden, R.J.V., Chartas, G., Hughes, J.P., Kellogg, E.M. and Zhao, P., Internal SAO report SAO-AXAF-AR-92-002, 10 January 1992.
- Chartas, G., Flanagan, K.A., Hughes, J.P., Kellogg, E.M., Nguyen, D., Zombeck, M., Joy, M., and Kolodziejczak, J. 1992, *SPIE Proceedings*, 1742, (this volume).
- Hughes, J.P., Schwartz, D.A., Szentgyorgyi, A., VanSpeybroeck, L., and Zhao, P. 1992, *SPIE Proceedings*, 1742, (this volume).
- Kellogg, E.M., Chartas, G., Graessle, D., Hughes, J.P., VanSpeybroeck, L., Zhao, P. Weisskopf, M.C., Elsner, R.F., and O'Dell, S.L., 1992, *SPIE Proceedings*, 1742, (this volume).
- Kellogg, E.M., Brissenden, R.J.V., Flanagan, K.A., Freeman, M., Hughes, J.P., Jones, M., Ljungberg, M., McKinnon, P., Podgorski, W., Schwartz, D.A., Zombeck, M., 1991a, *SPIE Proceedings*, 1546, 2.
- Kellogg, E.M., et al. 1991b, [abstract], *B.A.A.S.*, 23, 1349.
- Podgorski, W.A., Flanagan, K.A., Freeman, M.D., Goddard, R.G., Kellogg, E.M., Norton, T.J., Ouellette, J.P., Roy, A.G., and Schwartz, D.A., 1992, *SPIE Proceedings*, 1742, (this volume).
- Salem, S.I., Panossian, S.L., and Krause, R.A. 1974, *Atomic and Nuclear Data Tables*, 14.
- Schwartz, D.A., McKinnon, P.J., Murray, S.S., Primini, F.A., VanSpeybroeck, L.P., Zombeck, M.V., Dailey, C.C., Reily, J.C., and Weisskopf, M.C. 1986, *SPIE Proceedings*, J.L. Culhane, ed., 587, 10.
- VanSpeybroeck, L.P., McKinnon, P.J., Murray, S.S., Primini, F.A., Schwartz, D.A., Zombeck, M.V., Dailey, C.C., Reily, J.C., Weisskopf, M.C., Wyman, C.L., Glenn, P., and Slomba, A. 1986, *SPIE Proceedings*, J.L. Culhane, ed., 597, 20.
- VanSpeybroeck, L.P., Reid, P., Schwartz, D.A., and Bilbro, J., *SPIE Proceedings*, 1160, 94.
- Wyman, C.L., Dailey, C.C., Reily, C., Weisskopf, M., McKinnon, P.J., Schwartz, D.A., and VanSpeybroeck, L.P., 1986, *SPIE Proceedings*, J.L. Culhane, ed., 597, 2.
- Zhao, P., Freeman, M.D., Hughes, J.P., Kellogg, E.M., Nguyen, D.T., Joy, M., and Kolodziejczak, J.J. 1992b, *SPIE Proceedings*, 1742, (this volume).
- Zhao, P., Kellogg, E.M., Schwartz, D.A., Shao, Y., and Fulton, M.A. 1992a, *SPIE Proceedings*, 1742, (this volume).

Image Analysis of the AXAF VETA-1 X-ray Mirror

M. Freeman, J. Hughes, L. Van Speybroeck

Smithsonian Astrophysical Observatory
60 Garden St.
Cambridge, MA 02138
(617)495-7000

J. Bilbro, M. Weisskopf

Space Sciences Laboratory
NASA / George C. Marshall Space Flight Center
ES 65, Huntsville, Alabama 35812
Phone (205)544-5498 FAX (205)544-7754

ABSTRACT

Initial core scan data of the VETA-1 x-ray mirror proved disappointing, showing considerable unpredicted image structure and poor measured FWHM. 2-D core scans were performed, providing important insight into the nature of the distortion. Image deconvolutions using a raytraced model PSF was performed successfully to reinforce our conclusion regarding the origin of the astigmatism. A mechanical correction was made to the optical structure, and the mirror was tested successfully (FWHM 0.22 arcsec) as a result.

1. INTRODUCTION

The Verification Engineering Test Article - 1 (VETA-1) was a subset of the High Resolution Mirror Assembly (HRMA), the AXAF flight optics. It consisted of the outer mirror pair (P1/H1) in the polished but uncut and uncoated state. The goal of the VETA-1 test was to demonstrate the feasibility of polishing grazing incidence x-ray optics to the level required by the stated AXAF mission requirements. The Congressionally-mandated milestone was a FWHM of 0.5 arcsec for the optic, to be reported by mid-September. The VETA-1 and its associated test hardware were placed in the X-ray Calibration Facility (XRCF) at NASA's Marshall Space Flight Center (MSFC) during the last weeks of August, 1991. Pumpdown of the chamber began on the evening of Friday, Aug. 30. It was found that 2-3 days were required to achieve thermal stabilization at vacuum before running critical tests. Using the VETA X-ray Detection System (VXDS) and a quadrant shutter placed behind the mirror, relative alignment of the optical elements was performed, first using the VXDS imaging detector, and then the VXDS proportional counters and apertures. By Monday, Sept. 2, the alignment and focus adjustments were complete, and we began detailed pinhole scan measurements of the VETA-I image.

Initial one-dimensional (1-D) core scans through the image center at the best RMS focus showed a marked bimodal shape in the intensity distribution (Fig. 1). Even after many 1-D scans, the unexpected shape and large variation of measured FWHM with scan position and direction did not yield the needed understanding of the image, instead indicating significant two-dimensional (2-D) structure. In addition, the measured FWHM was not sufficiently better than 0.5 arcsec to avoid concerns of measurement

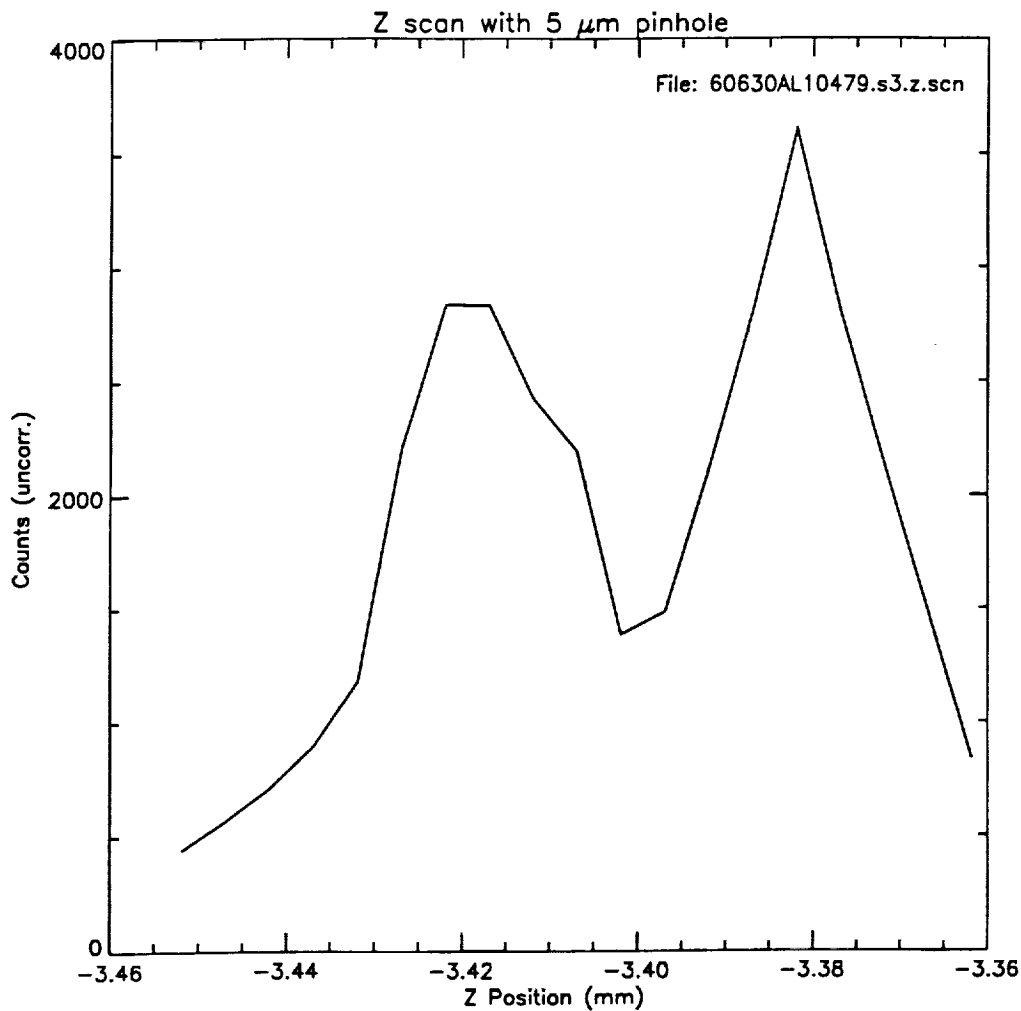
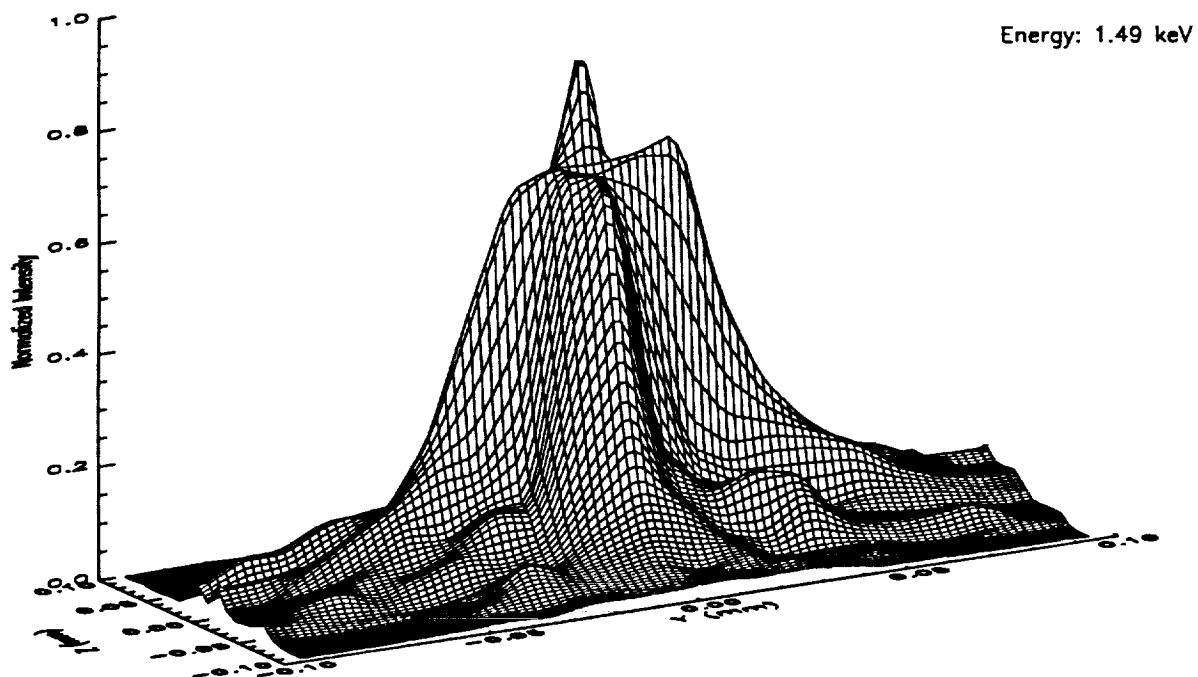


Figure 1. One-Dimensional Core Scan (Sept. 2, 1991)

error. It was determined that to provide a better understanding of the image, it was necessary to perform a 2-D raster scan of the entire image core. Weighing image detail against test time, a 19 by 19 raster pattern using the 10 μm pinhole was chosen, producing a sampled image of the inner 4 arcsec core of the point response function (PRF).

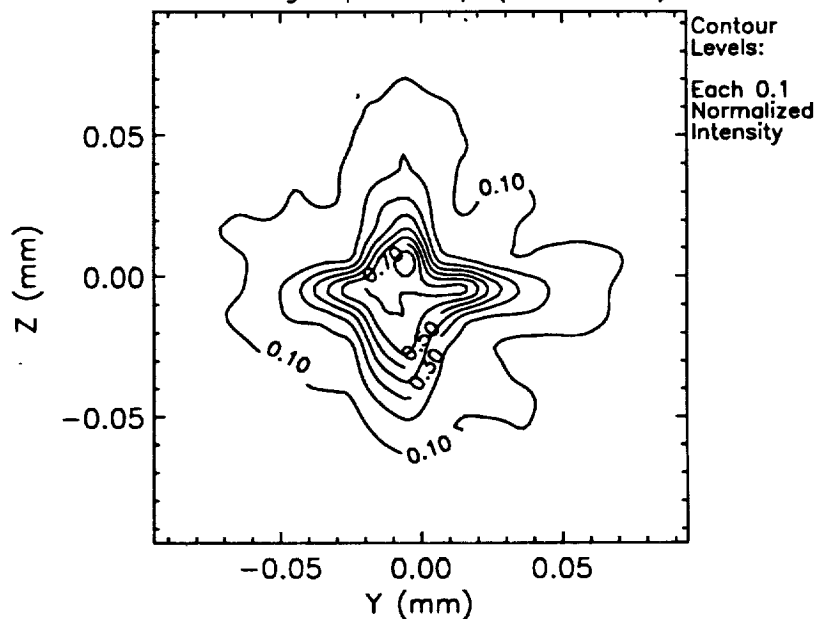
2. INITIAL 2-D CORE SCANS

The first complete 2-D scan (ID: 10579) of the image, taken 6 days into the test (Sept. 5), is shown in Fig. 2, in (a) as an isometric intensity plot, and (b) as iso-intensity contours. This pattern of isometric view followed by contours will be used throughout for image display. The 19 by 19 data were resampled in the following images by 4 in each axis for visualization. An aluminum anode target, which produces characteristic line radiation at approximately 1.488 keV, and the flow proportional counter (FPC) were used. Note that the intensity corresponds to the number of counts accumulated from the FPC spectra in an operator defined region-of-interest (ROI). No corrections were made for deadtime, since the deadtime was dominated by the Beam Normalization Detector (BND) count rate, making the *relative* deadtime correction over the image only of order a few percent. Pulse pile-up



(a) Isometric intensity plot

Full image span 190μ (3.8 arcsec)



(b) Isointensity Contours

Figure 2. 19 x 19 Scan with 0.010 mm Pinhole
File: 1000AL10579.scn

corrections were also ignored for these analyses, but are expected to be of order a few percent, since the source intensity was controlled to limit the maximum count rate.

The image showed a significant "cross" structure. The alignment of the cross with the gravity vector provided an indication of the origin of the distortion (the y-axis of the images shown [labelled Z] is the anti-gravity direction). Although it was known that gravity produced ovalization of the optics, no raytrace predictions of the most recent Kodak finite element model of the optics in the test configuration had been performed by SAO. Work began immediately to perform these analyses. In addition, we compared the focal position measured using only the top and bottom mirror quadrants to that of only the left and right, and found them to differ by approximately 600 μm .

3. MODEL POINT SPREAD FUNCTION

A NASTRAN Finite Element Analysis (FEA) model of the VETA-I in the test configuration was obtained by SAO from Eastman Kodak, the load in this case being the body forces due to gravity. The resultant predicted distortion, after removal of the rigid body effects, was primarily ovalization with a magnitude of 4.95 μm (zero to peak) for the paraboloid (P1) and 3.43 μm for the hyperboloid. SAO produced an independent ANSYS model, with predicted values within 20% of the EKC model. Using SAO-developed software and OSAC, a raytrace code developed by Perkin-Elmer (P. Glenn et. al.), the FEA model data was fit with Legendre-Fourier polynomials and raytraced. Included in the raytrace model and the subsequent post-processing were the following effects:

1. Finite Source Distance (518.16 m)
2. Finite Source Size (.22 arcsec dia.)
3. P1-H1 Despace (109.03 mm)
4. Calculated Gravitational Distortion (above)
5. Zerodur Reflectivity at 1.488 keV
6. $\Delta\Delta R$ errors (RMS = 0.098 arcsec, from HDOS)
7. Circumferential slope errors: 6.446 μrad (P1) and 9.745 μrad (H1)
8. Sag errors: 1585 \AA (P1) and 447 \AA (H1)
9. Axial slope errors:
 - a. Low frequency gaussian core: 0.158 arcsec
 - b. Mid-frequency PSD term: 25 \AA (18 mm correlation length)
 - c. Upper Mid-frequency PSD term: 10 \AA (0.35 mm correlation length)
 - d. High frequency PSD term: 7 \AA (0.018 mm correlation length)

The first four will be referred to as 'Facility Effects': Inclusion of just these terms is equivalent to assuming a perfect mirror in the test configuration. No residual misalignment of P1 to the X-ray Calibration Facility (XRCF) or P1 to H1 was assumed. Excellent relative positional stability of the source, optics, and detectors was realized based on inspection of the Motion Detection System (MDS) data. For this reason, we decided to ignore the effects of vibration in the simulation. Finally, the focal plane ray file was sampled to simulate the actual 10 circular pinhole scan.

The results are shown in Fig. 3 (a) and (b), exhibiting good qualitative agreement with the measured image. An algorithm was created to perform a simple image subtraction by scaling the simulation to the peak of the measured image, then aligning them for minimum RMS difference. This resulted in an RMS residual of 3.7%, a peak residual of 33.5%, and a correlation coefficient of 0.961. These data and the measured focus difference pointed more strongly to the 1g ovalization as the source of the image distortion, although work continued to determine if there were reasonable alternate hypotheses. At this point, engineering personnel from the Eastman Kodak Co. (EKC), the designers of the mirror support structure, began to consider possible ways to correct the problem. SAO, TRW and MSFC staff desired even more concrete evidence that this was indeed the cause, since the solution would most likely involve breaking vacuum, making mechanical changes to the VETA-1 assembly, and another pumpdown. With only days left before the FWHM needed to be reported, such a significant loss of test time could only be contemplated if the confidence that it would correct the problem was *very* high.

4. DECONVOLUTION AND SUPPORTING DATA

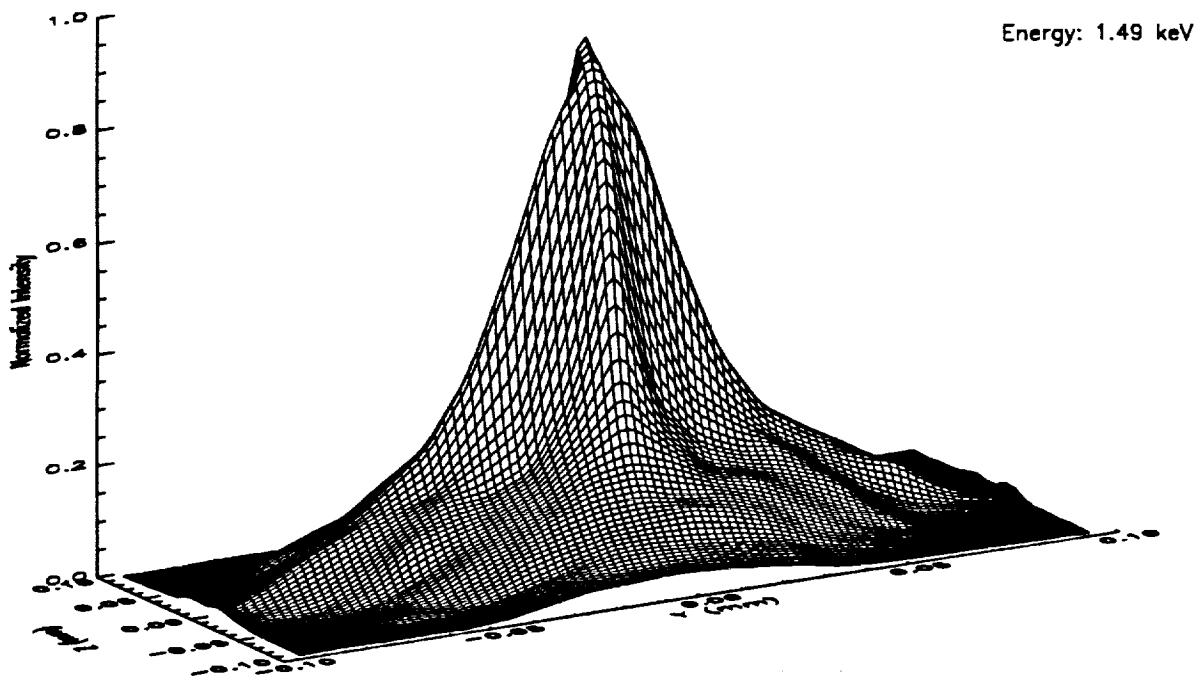
Given that the fit to of the model to the data was reasonable, deconvolution of the facility effects from the raw data was attempted. The assumption was made that the superposition of the facility effects (F), such as the gravitational distortion or the finite source distance (see above), and the "true" imaging performance of P1/H1 (P) could be represented as a two-dimensional convolution to yield the test data (D):

$$D = F \otimes P \equiv \int_{-\infty}^{\infty} F(R-r)P(r)dr.$$

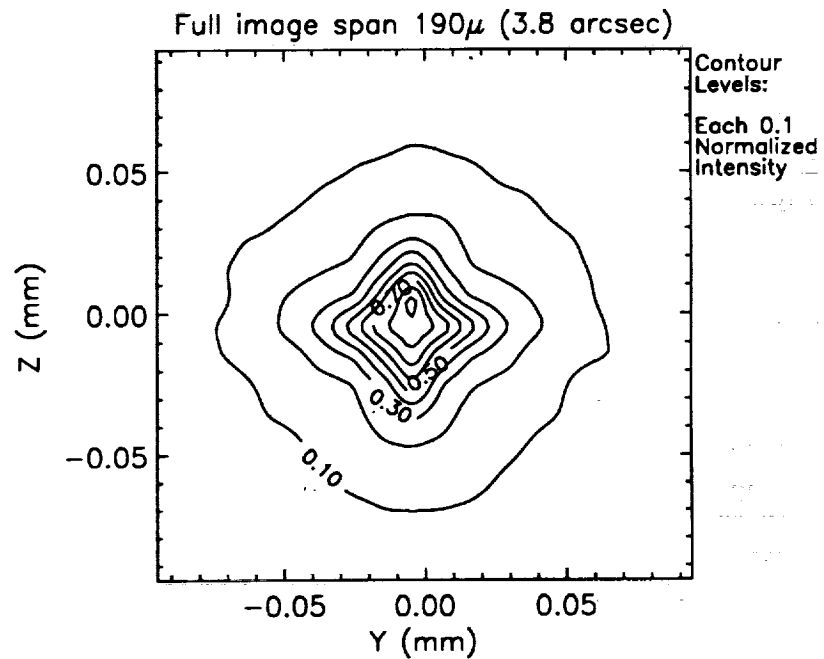
The ultimate aim of the restoration was to restore the 'true' imaging performance of P1/H1, ie. remove the 'facility effects'.

The general approach entailed resampling the 10 μm pinhole 19x19 point raster scan image onto 1 $\mu\text{m} \times 1 \mu\text{m}$ pixels, to yield D . The convolution kernel F was defined by running a raytrace of a perfect mirror (i.e., without $\Delta\Delta R$, circumferential slope, sag, or axial slope errors) in the test configuration, including only the facility effects as enumerated above. This was output as a FITS image with 1 $\mu\text{m} \times 1 \mu\text{m}$ pixels. This image is shown in Figure 4. Two standard techniques for deconvolution were then used: Wiener filter deconvolution and a nonlinear recursive restoration scheme described by Richardson and for astronomical use by Lucy^{[1][2]}. Note that both of these deconvolution techniques are available under IRAF (package: stsdas.playpen). The Richardson-Lucy (R-L) technique has been heavily employed for deconvolution of HST images^[3].

Wiener filter deconvolution is a simple Fourier quotient technique which uses estimates of the noise and signal power spectrum (PS) to obtain an optimally-filtered result. In our application the noise PS was assumed to be white and was computed from the input image. The PS of the convolution kernel F was assumed to be noiseless, which is only approximately correct since the raytrace which produced this function used a finite number of rays. A low pass filter (4 pixel sigma) was applied in the frequency domain. The results are shown in Figure 5. The technique restores a point image with a full width half maximum (FWHM) of 0.24 arcsec. However there is a significant amount of "ringing" in the image, which appears as ripples in the zero level. This is often the case with this type of deconvolution technique and arises because of the sharp digital filter and the lack of a constraint requiring the restoration of positive counts only.

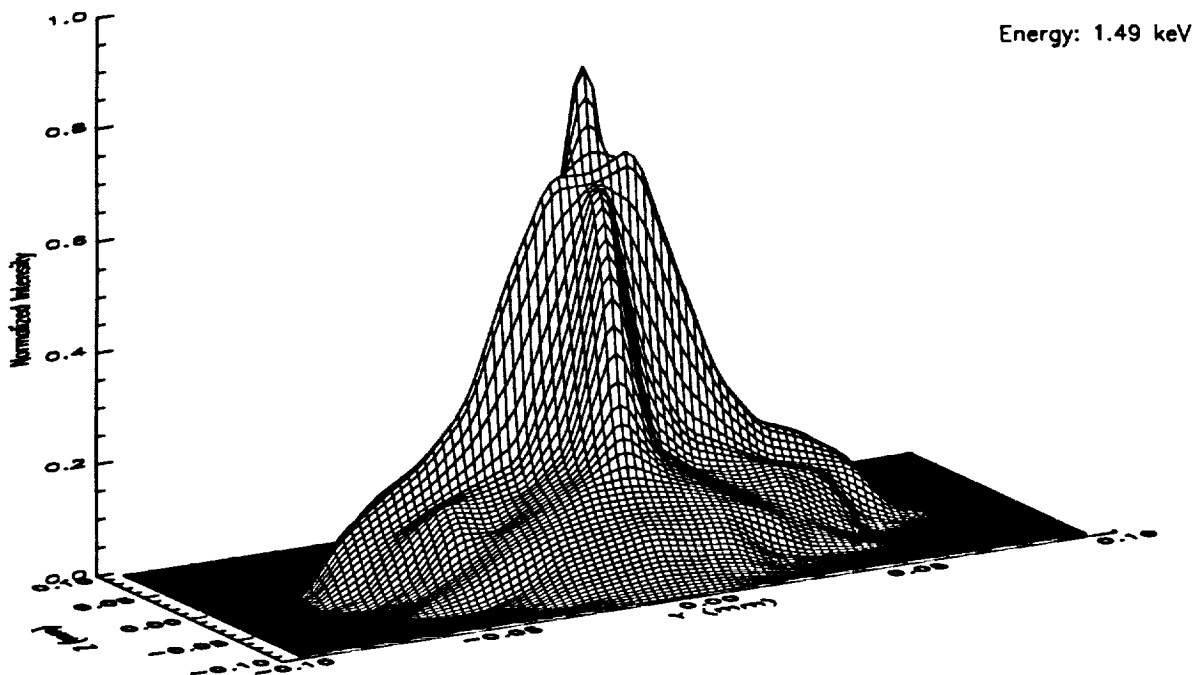


(a) Isometric intensity plot

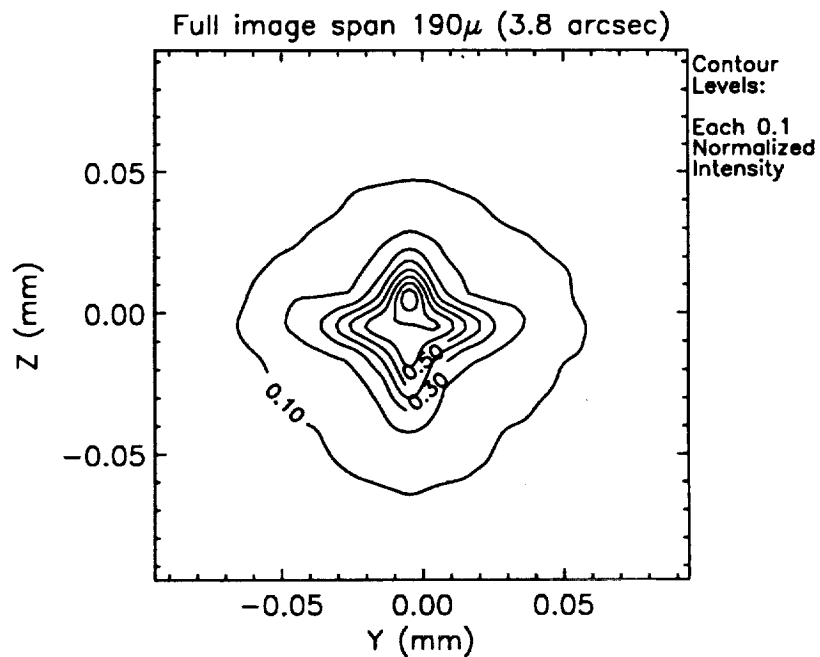


(b) Isointensity Contours

Figure 3. SAO Raytrace Prediction of VETA-I Performance
EKC Structural Model of 1g Deformation

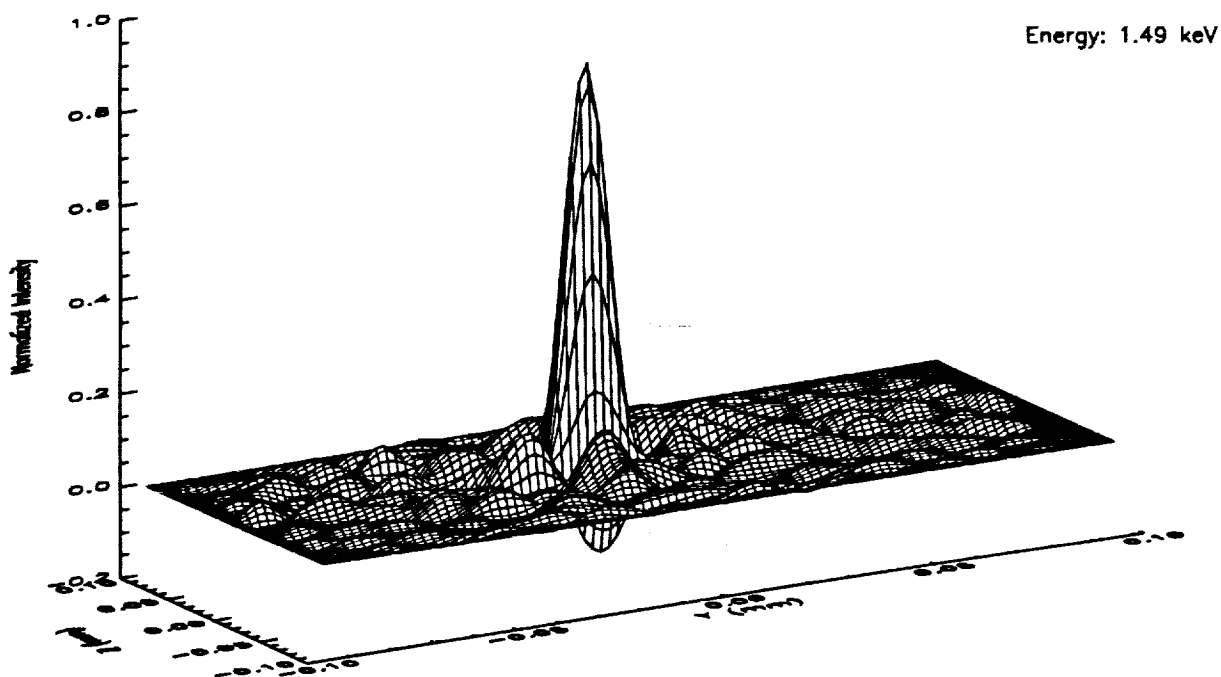


(a) Isometric intensity plot

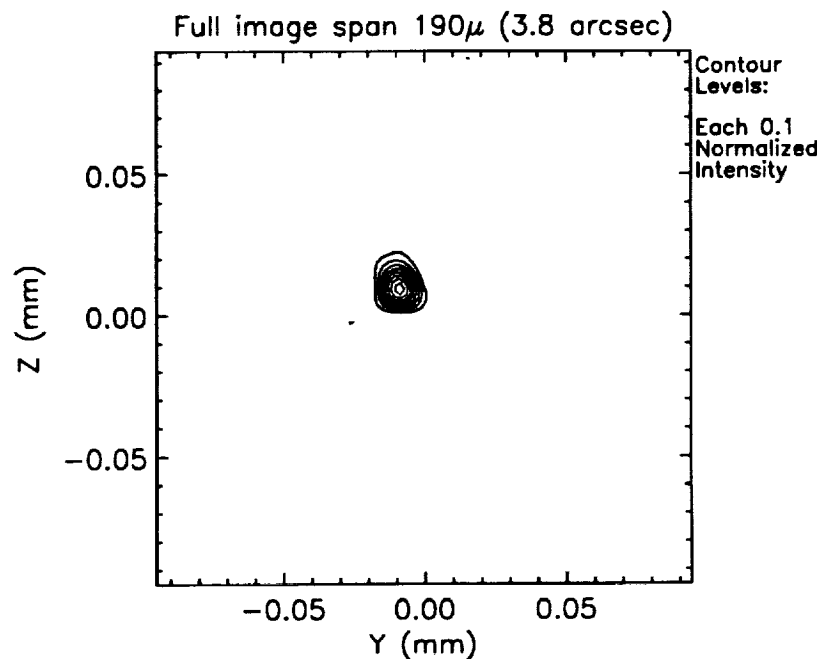


(b) Isointensity Contours

Figure 4. Facility Effects PSF
(Gravity(EKC), Finite Source Size & Distance, and Despace)



(a) Isometric intensity plot



(b) Isointensity Contours

Figure 5. Wiener Deconvolution of 19x19 Scan 10579 using Facility Effects PSF

The R-L image deconvolution requires that the restored data be non-negative everywhere. Furthermore it insists on *statistical* agreement between the observed data and the rectified estimate, instead of *exact* agreement and employs χ^2 as the figure of merit. One well-known shortcoming of this approach is the lack of a built-in stopping rule. We found that during the first 10 or so iterations the change in χ^2 was rapid, while after about 50 standard iterations the change in χ^2 from iteration to iteration became very small. During the test period, we used this to indicate convergence. Figure 6 shows the restored image from this technique after 8 accelerated (equivalent to ~ 50 standard) iterations. The FWHM of the imaged point source is 0.21 arcsec.

5. MIRROR GRAVITY OVALIZATION CORRECTION AND RESULTS

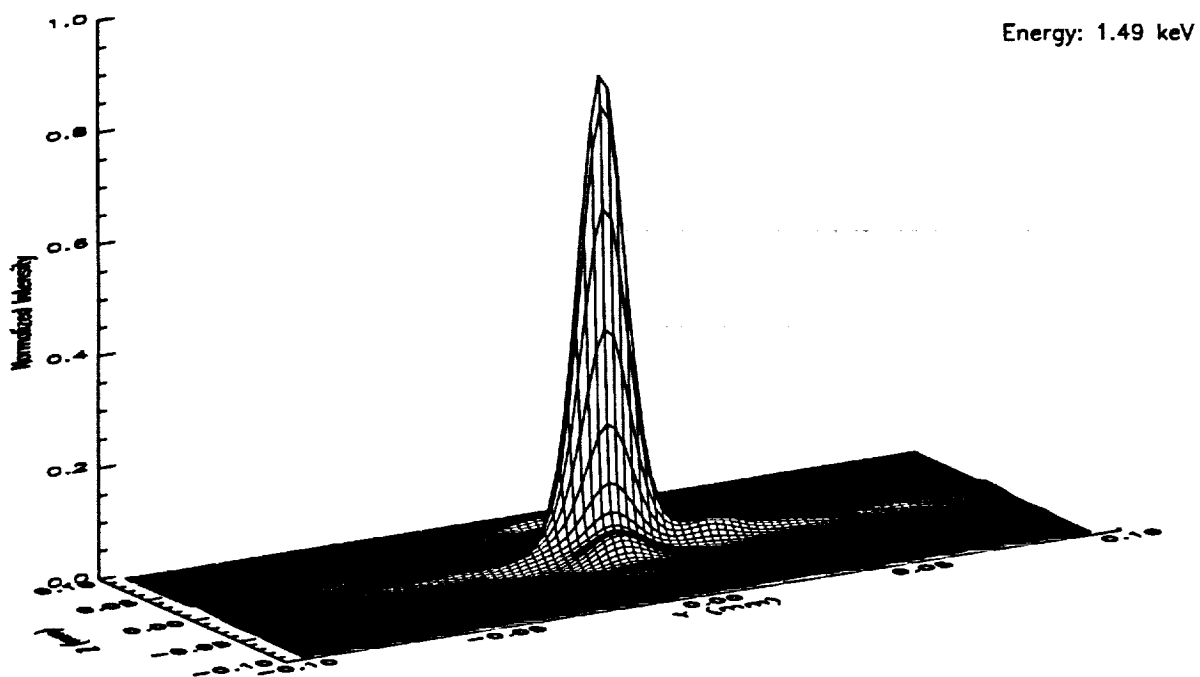
All indications were that we had a correct hypothesis for the source of the image distortions. EKC had determined that a force could be applied to the mirror support rings which would correct the majority of the ovalization and related distortion. The data and a correction plan were presented to appropriate project management personnel on Monday, Sept. 9. Approval was given to implement the correction, and repressurization was begun as soon as the necessary hardware had been fabricated by EKC. After the required 3 days of stabilization, realignment of the optics began on Sept. 15. Two days later, on Sept. 17, the first 19 x 19 scan after the 1g correction had been applied was performed. The results are plotted in Figure 7, showing a much improved PRF. Later that same day we measured the FWHM with 1D scans using the 5 μ m pinhole to be 0.22 arcsec, the figure reported to the Congress and announced publicly.

The corresponding OSAC raytrace model PSF of the new facility effects is shown in Figure 8. Using the same R-L deconvolution technique, we obtained the deconvolved image (after 8 accelerated iterations) shown in Figure 9.

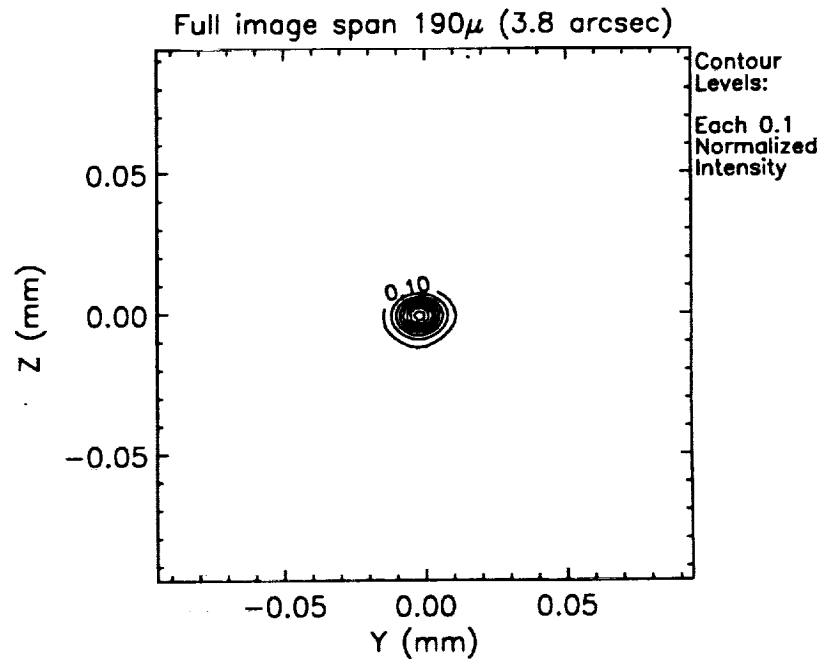
6. DISCUSSION OF THE R-L DECONVOLUTION RESULTS

It was noted during the test work, and in subsequent processing of test images, that the Richardson-Lucy algorithm would produce continuous improvement in the estimated mirror performance for many iterations, albeit at a decreasing rate. Although the deconvolution work during the test was used primarily to establish correlation between the measured image and a model, it would be desirable to develop a "stopping rule" such that an estimate of the true mirror performance (ie. removing the facility effects) might be made.

To investigate more completely the behavior of the restoration as a function of the number of iterations, we employed the Accelerated R-L algorithm^[4] in an IDL/PV-WAVE™ implementation available from the ST-ECF. In our application, we saw an improvement in convergence rate of 5-8 over the standard R-L algorithm. This allowed us to quickly "push" the restoration to the equivalent of hundreds of standard iterations. Figure 10 shows the the FWHM plotted for both the pre- and post-correction restorations, as well as the measured value and that produced by the Wiener filter. As noted, the restoration continued to improve the image well beyond the measured value, although no direct comparison can be made since the measured FWHM includes all facility effects, most significant in this case being the source size effect. Although not evident in the restorations shown at 8 iterations, the effects of 'over-restoring' the image can be seen in Figure 11, the restoration of scan 20057 after 32 accelerated R-L iterations. Here the data variations in the outer regions of the image are beginning to be restored as separate "sources". This is inconsistent with our physical situation, and emphasizes the importance of exercising caution in the use of this technique.

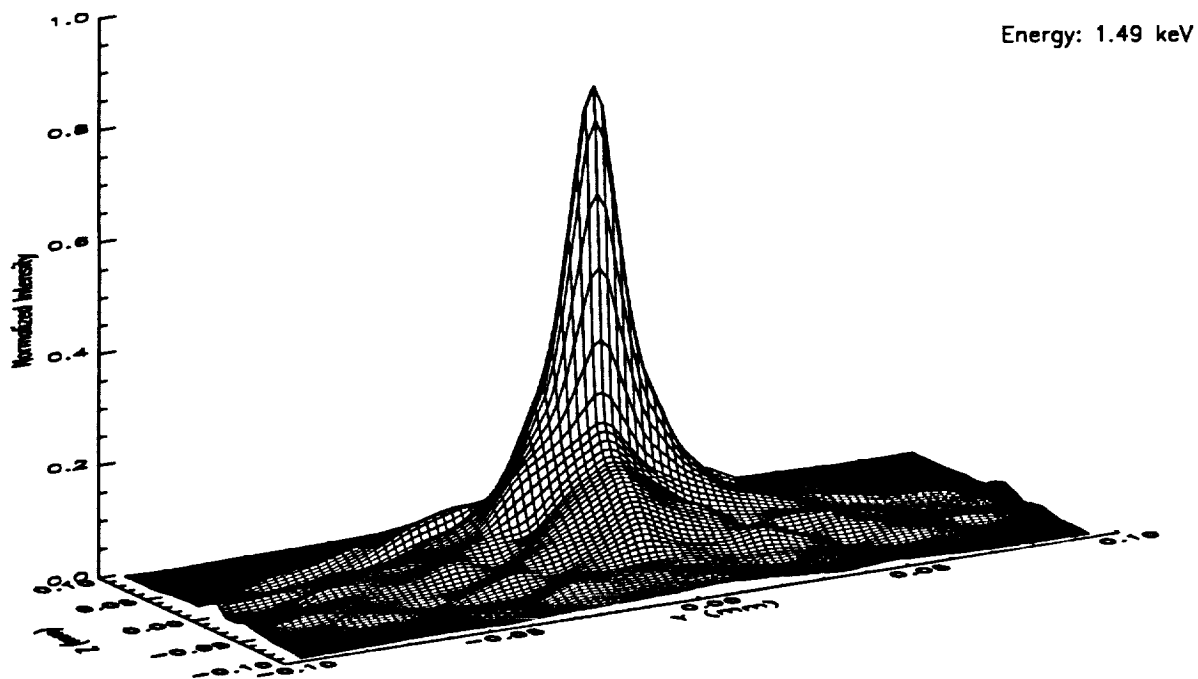


(a) Isometric intensity plot

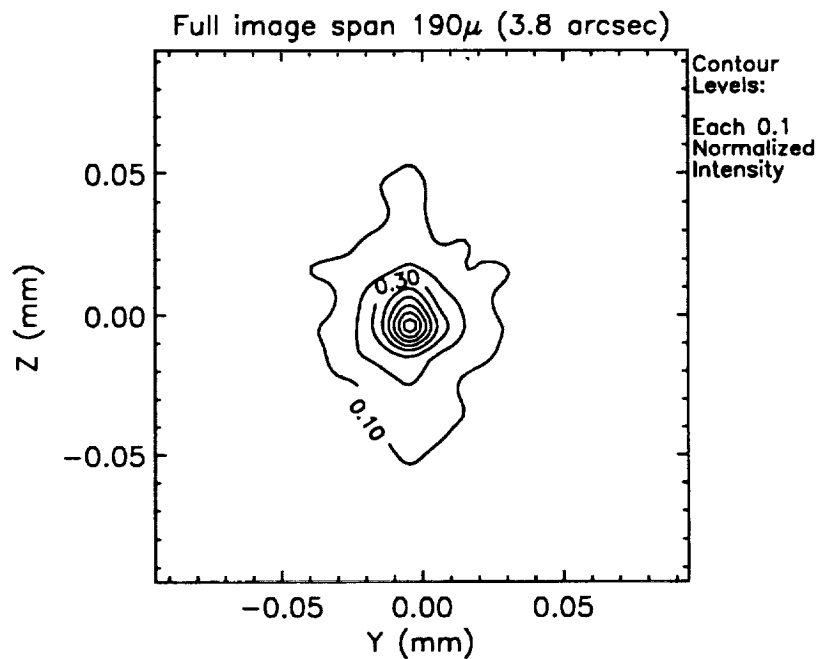


(b) Isointensity Contours

Figure 6. R-L (accel) Deconvolution of 19x19 Scan 10579 using Facility Effects PSF (8 iterations)

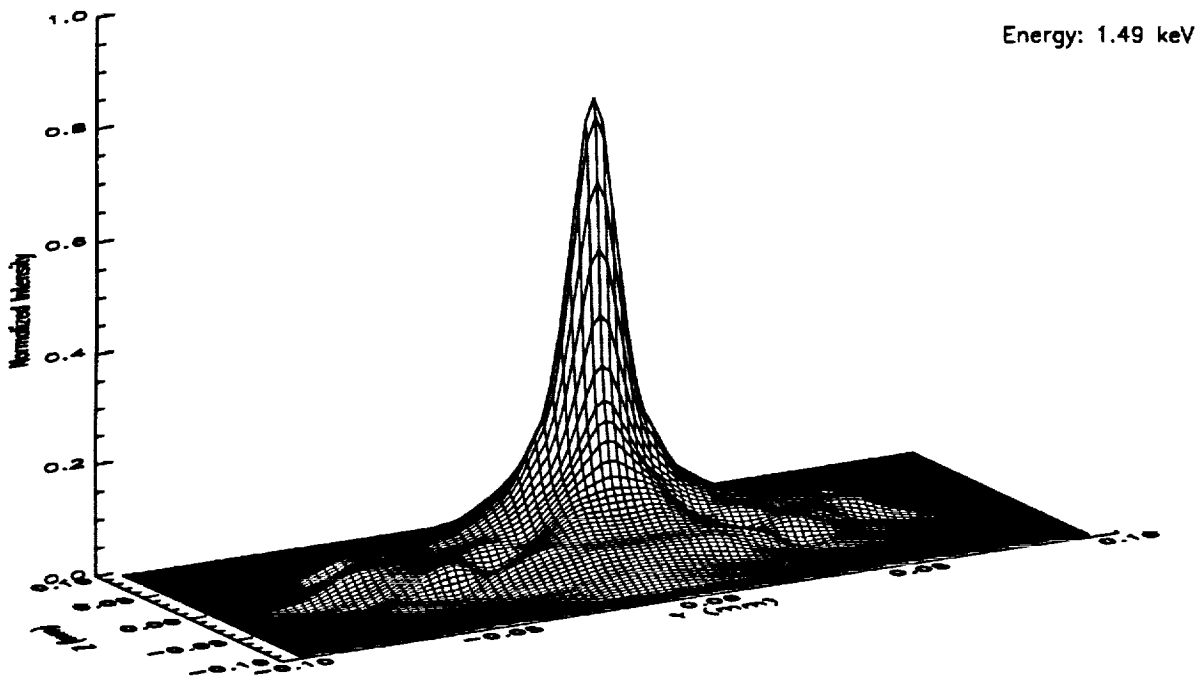


(a) Isometric intensity plot

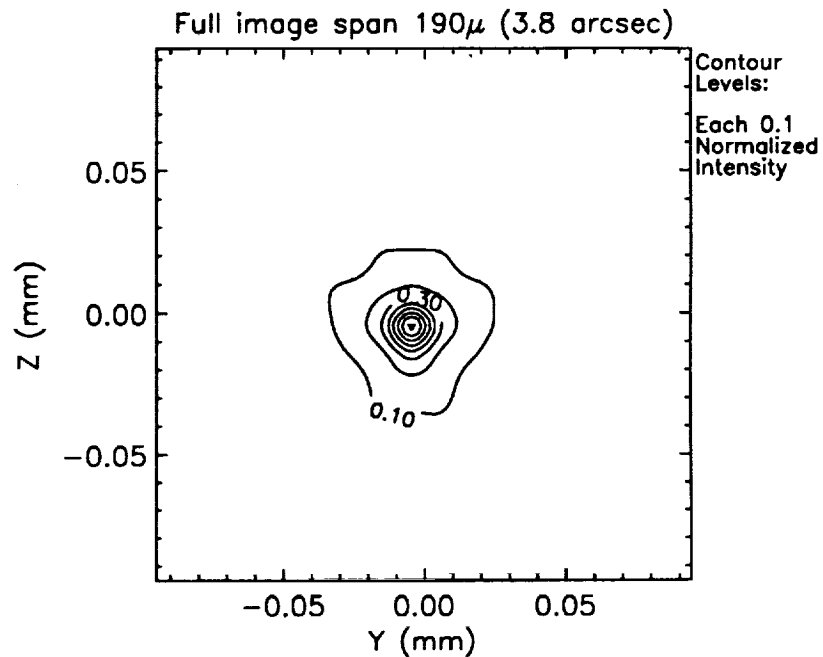


(b) Isointensity Contours

Figure 7. 19 x 19 Scan with 0.010 mm Pinhole
File: 002AL20057.scn

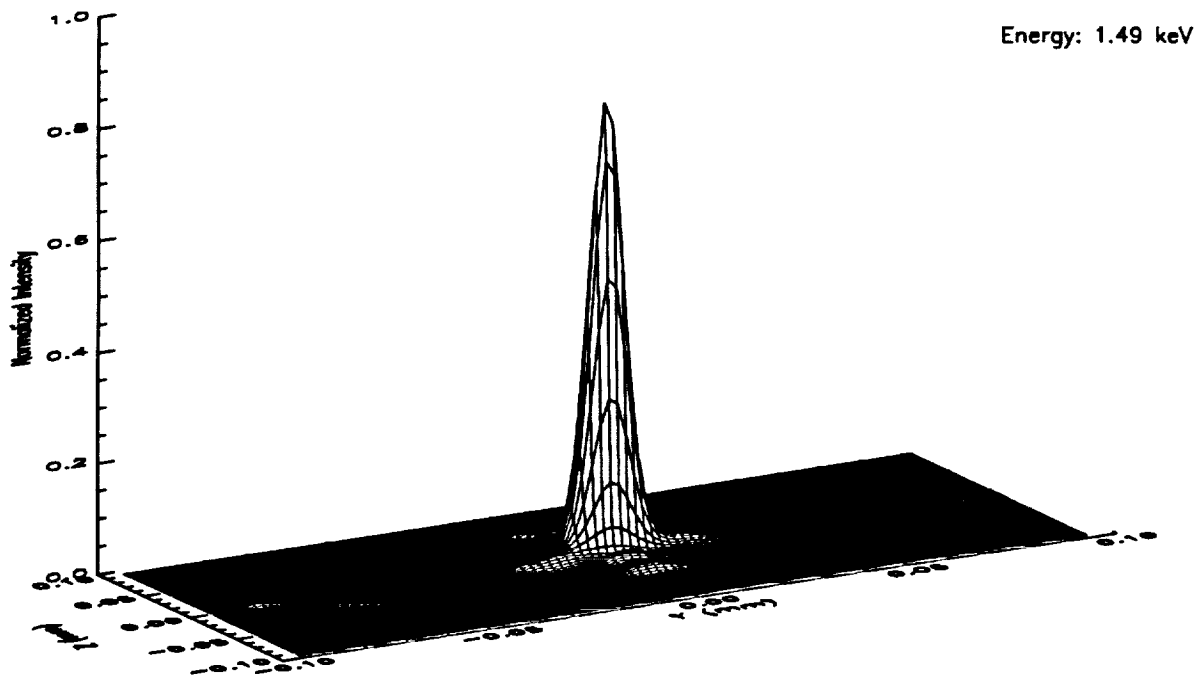


(a) Isometric intensity plot

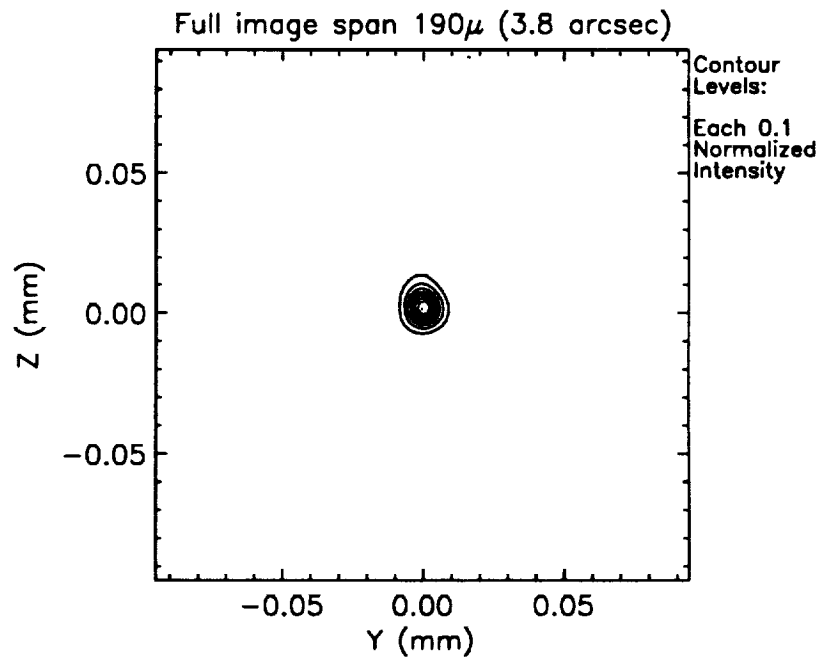


(b) Isointensity Contours

Figure 8. Facility Effects PSF with Modeled 1g Correction (Gravity(EKC), Finite Source Size & Distance, and Despacing)



(a) Isometric intensity plot



(b) Isointensity Contours

Figure 9. R-L (accel) Deconvolution of 19x19 Scan 20057 using Facility Effects PSF (8 iterations)

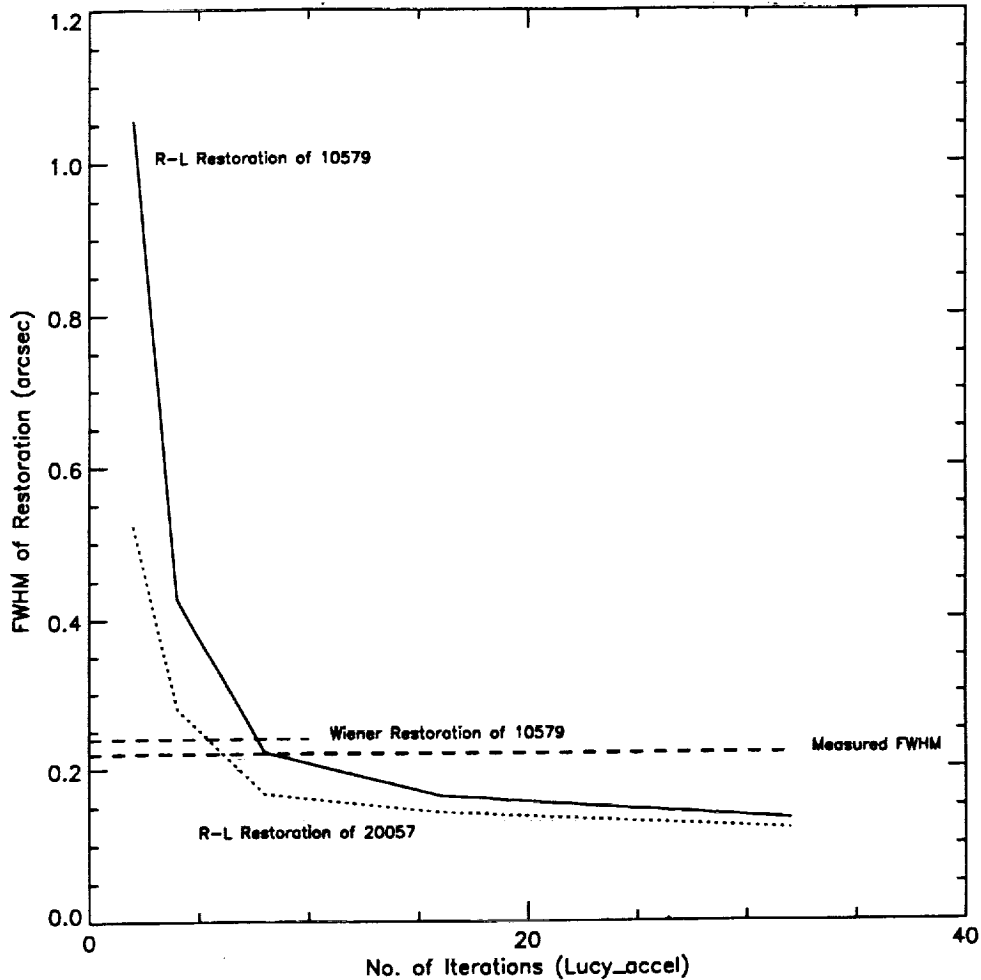
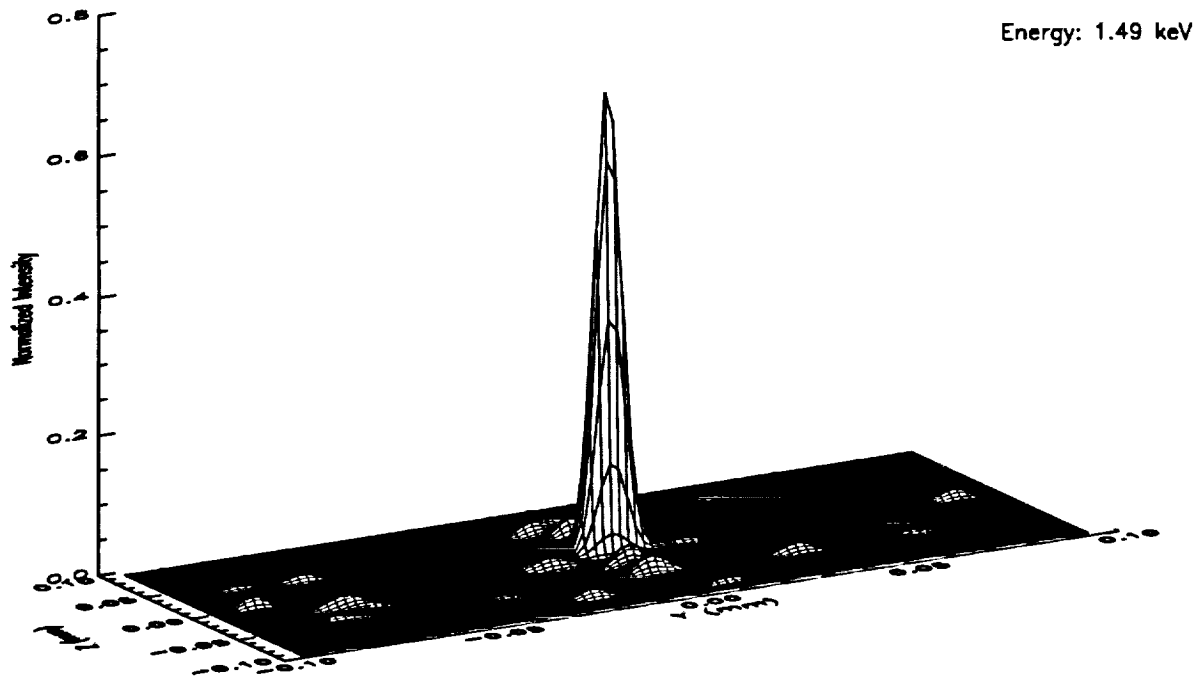


Figure 10. FWHM of Image during Restoration

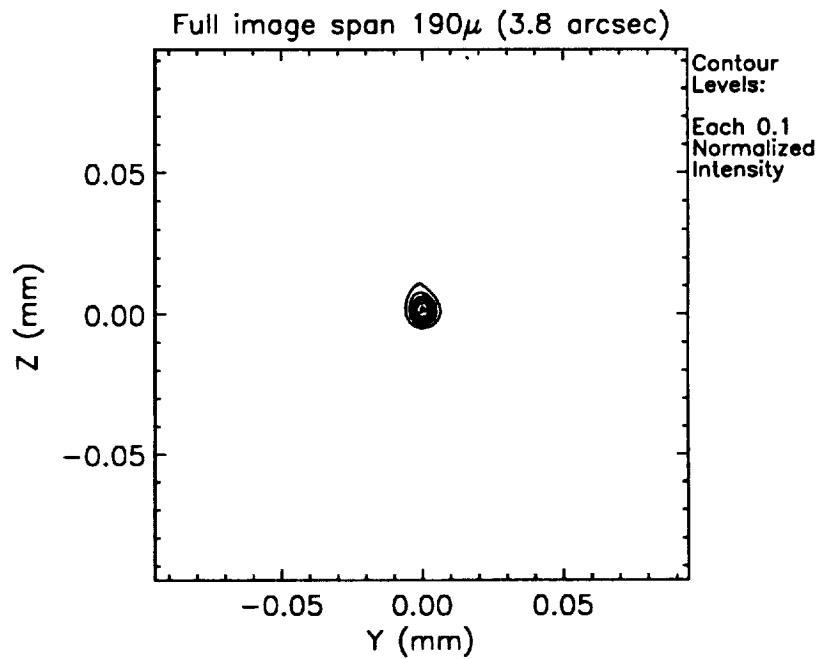
7. CONCLUSIONS AND FUTURE WORK

The measurement of the VETA-1 FWHM within specification and on time was accomplished through hard work by the test and analysis personnel of SAO, TRW, Eastman Kodak, and MSFC. The information necessary to make the important real-time correction to the optic was derived in large part from analysis work, especially the R-L deconvolution, performed in parallel with the test. We believe this method of application, where certain known or modeled effects are deconvolved from measured data to produce a more useful representation of the system performance, is applicable to many measurement problems.

More work is necessary in the development of a R-L "stopping rule" for this application. We intend to pursue investigations of image frequency content and the statistics related to the knowledge of the model PSF as possible avenues for the development of such a rule. This work will be an important part of providing definition for the test of the HRMA.



(a) Isometric intensity plot



(b) Isointensity Contours

Figure 11. R-L (accel) Deconvolution of 19x19 Scan 20057 using Facility Effects PSF (32 iterations)

ACKNOWLEDGEMENTS

We are grateful to H.-M. Adorf of the ST-ECF for providing the new implementation of the accelerated R-L algorithm, a useful interpolation scheme for subsampling images, and many helpful suggestions related to the application of the R-L technique.

REFERENCES

3. B. H. Richardson, *J. Opt. Soc. America* **62**, 55, 1972.
3. L. B. Lucy, "An iterative technique for the rectification of observed distributions", *Astron. J.* **79-6**, 745-754, June 1974.
3. H.-M. Adorf, J. R. Walsh, and R. N. Hook, "Restoration Experiments at the ST-ECF", *Proc. Workshop The Restoration of HST Images and Spectra*, R. L. White and R. J. Allen (eds.), Space Telescope Science Institute, Baltimore MD, 21-22 Aug. 1990.
4. H.-M. Adorf, J. R. Walsh, R. N. Hook, and F. D. Murtaugh, "Accelerating the Richardson-Lucy Algorithm", 1992 (unpublished).

Surface Finish Quality of the Outer AXAF Mirror Pair
Based on X-ray Measurements of the VETA-I

John P. Hughes, Daniel Schwartz,
Andrew Szentgyorgyi, Leon Van Speybroeck, and Ping Zhao

Harvard-Smithsonian Center for Astrophysics
60 Garden Street, Cambridge, MA 02138

ABSTRACT

We employ the X-ray measurements of the VETA-I taken at the X-Ray Calibration Facility (XRCF) of the Marshall Space Flight Center (MSFC) to extract information about the surface finish quality of the outermost pair of AXAF mirrors. The particular measurements we consider are one dimensional scans of the core of the point response function (PRF) (full width half maximum [FWHM] scans), the encircled energy as a function of radius, and one dimensional scans of the wings of the PRF. We discuss briefly our raytrace model which incorporates the numerous effects present in the VETA-I test, such as the finite source distance, the size and shape of the X-ray source, the residual gravitational distortions of the optic, the despace of the VETA-I, and particulate contamination. We show how the data constrain the amplitude of mirror surface deviations for spatial frequencies greater than about 0.1 mm^{-1} . Constraints on the average amplitude of circumferential slope errors are derived as well.

1. INTRODUCTION

One of the principal goals of the Advanced X-ray Astrophysics Facility (AXAF) is to perform sensitive, high spatial resolution imaging over a broad X-ray bandwidth. This capability is provided in large part by the High Resolution Mirror Assembly (HRMA), which consists of a set of nested Wolter Type-I mirrors. In the summer of 1991, the Verification Engineering Test Article (VETA-I), consisting of the outermost pair of HRMA shells (P1/H1) assembled into a mounting fixture, was delivered to the XRCF for X-ray testing. The main purpose of the test was to demonstrate FWHM imaging performance of better than $0.5''$ for the optic. An additional secondary goal was verification of the optical surface metrology. Since schedule pressures made it impossible to obtain complete final metrology of the polished surfaces, it was decided to use the X-ray data itself to estimate the surface finish quality of P1/H1.

We consider three types of data in this paper: (1) one-dimensional scans of the core of the PRF at the single X-ray energy of 1.488 keV; (2) encircled energy as a function of radius for three X-ray energies: 0.277, 1.488, and 2.067 keV; and (3) one dimensional large angle scans of the wings of the PRF for five X-ray test energies: 0.277, 0.932, 1.488, 2.067, and 2.334 keV. As we show below, the first data set is most constraining of the circumferential slope errors on the surface. The second data set is most sensitive to the power spectral density (PSD) of surface irregularities over spatial frequencies of $f = 0.05 - 24 \text{ mm}^{-1}$. The last data set is sensitive to the amount of particulate contamination on the surface in addition to the PSD of surface irregularities over $f = 1 - 100 \text{ mm}^{-1}$.

The shape of the VETA-I PRF in the core within a radius of about $100 \mu \approx 2''$ (we assume a focal plane scale of $0.02''/\mu$ throughout this paper) was determined largely by the test conditions. For example, the optics were not cut to their nominal flight lengths, which meant that it was impossible to space them properly. The optical elements were separated by a despace of 109.03 mm in addition to the nominal design spacing. The finite source distance also degraded the imaging performance in the core. In order to faithfully reproduce these and other effects in the FWHM scans and encircled energy data, it was required that a raytrace calculation be performed. On the other hand the data taken far from the core, such as the wing scan data, could be handled analytically.

2. RAYTRACE MODEL

Our calculation for the X-ray performance of the VETA-I consists of two parts: (1) the raytrace program OSAC (Optical Surface Analysis Code) written by P. Glenn, and (2) a stand-alone post-processing program developed at SAO.

OSAC incorporates the mirror surface prescription (including low order error terms, such as axial sag) and various VETA-I ground calibration effects: the finite source distance (518160 mm, measured from the front of the VETA-I), the despace, and gravitational distortions. The latter were implemented in OSAC as a set of Fourier-Legendre coefficients which were determined from fits to NASTRAN finite element analysis models of the VETA-I in the test configuration.

SAO's post processing software was able to include the measured intensity distribution of the XRCF X-ray source,¹ obscuration due to the aperture support struts, an arbitrary axial focus location, and circular pinholes of arbitrary size placed at arbitrary positions in the focal plane. Scattering of X-rays due to particulate contamination on the surface is also included.²

Various mirror fabrication errors: $\Delta\Delta R$, circumferential slope, and axial slope errors, were implemented in the post processing software. Values for the first error term were obtained from the mirror manufacturer, Hughes Danbury Optical Systems (HDOS) (P. Reid, private communication). The VETA-I test data were not very sensitive to this error term. The magnitude of circumferential slope errors was parameterized as a (one-dimensional) normally distributed quantity, and the direction of scatter was taken to be orthogonal to the axial slope direction. Our results show that the FWHM data scans were somewhat sensitive to the magnitude of this error. Axial slope errors were parameterized in terms of the PSD of the surface. Most of the results we quote in this paper are based on the assumption of a PSD which varies as a power-law in spatial frequency f , *i.e.*, $2W_1(f) = Cf^{-p}$. We allow the amplitude C and power-law index p to be free parameters. By convention, the amplitude of the PSD is represented in terms of the band-width limited integral for the total surface roughness

$$\sigma^2 = 2 \int_{f_1}^{f_2} W_1(f) df.$$

We quote results for the roughness per surface using limits of 1 mm^{-1} and 1000 mm^{-1} .

3. FWHM

The data corresponding to the full-width-half-maximum (FWHM) of the PRF of the VETA-I are shown in Fig. 1. This intensity distribution was made by stepping a 5μ diameter circular pinhole in 2μ steps through the core of the PRF, after an initial sequence of procedures demonstrated a relative tilt alignment between the optical elements of less than $0.1''$ and the location of the axial focus position to better than 25μ . The data were taken with an aluminum anode target which produced characteristic $K\alpha$ line emission at an (emission-weighted) energy of 1.488 keV. We extracted the total number of counts from a restricted range of pulse height (PH) channels of the observed proportional counter spectrum. No corrections for background, deadtime, or pulse pileup were applied since the relative correction from point to point was less than a few percent for these effects.

We present a study of the VETA-I FWHM using our raytrace model with the goal of identifying the dominant contributors to the FWHM performance of the VETA-I, whether test-induced (such as the finite source distance) or intrinsic to the mirror surface itself. Table 1 shows predicted FWHM values for several raytrace models where various mirror performance errors are introduced each in turn. In all cases the calculations are based on 5×10^5 rays of which about 1000 pass through the central pinhole, which ensures statistical precision of about 5% in the modelled FWHM values.

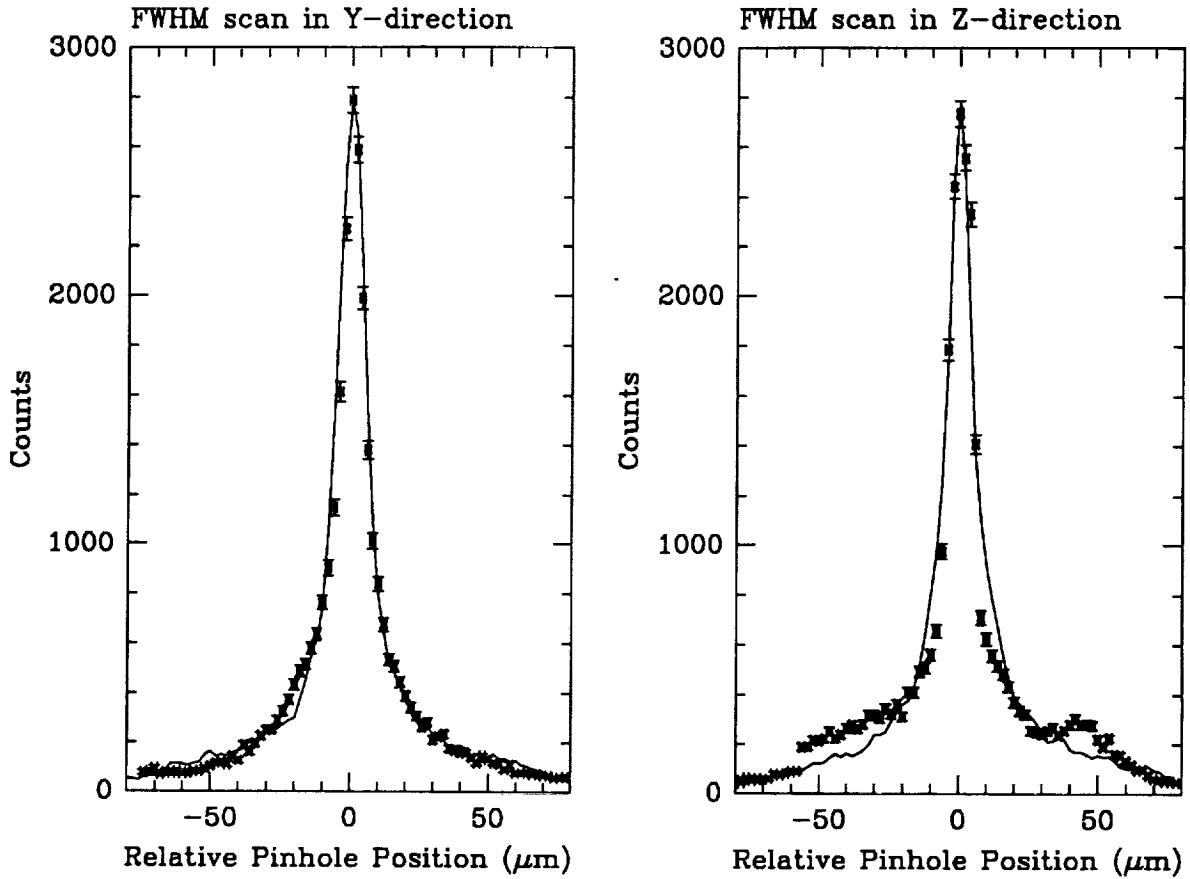


Figure 1 - The data points obtained during the FWHM scans of the core of the VETA-I point response function with a 5μ ($0.1''$) diameter pinhole moved in 2μ steps. The left panel shows results from scans along the Y-direction (horizontal), while the right panel shows scans along the Z-direction (vertical). The solid curves show the model assuming 3μ rad circumferential slope errors as discussed in the text.

Table 1 Predicted VETA-I FWHM		
	Y-FWHM (arcsec)	Z-FWHM (arcsec)
Measured Value	0.219 ± 0.030	0.221 ± 0.030
1. Grav., Finite Conj., Despace	0.132	0.140
2. Grav., Finite Conj., Despace, Source size	0.203	0.203
3. Case 2 plus Lev II Req axial slope errors	0.208	0.206
4. Case 2 plus Lev II Goal axial slope errors	0.209	0.210
5. Case 2 plus $\Delta\Delta R$ errors	0.201	0.206
6. Case 2 plus circum. slope errors	0.326	0.336
7. Case 2 plus axial sag	0.202	0.202

The first two models include no mirror degradation, and instead include only the so-called facility effects: the calculated residual gravitational distortion of the mirror, the finite source distance (finite conjugate), the mirror despace, and the finite source size. This last effect was included by inputting the actual measured intensity distribution of the XRCF X-ray source¹ to the raytrace model. Comparison of the predicted values in these two cases reveals that the finite size of the source is the dominant facility induced effect to the FWHM.

The remaining five cases show how the FWHM increases (or not) when various mirror performance error terms are included. Cases 3 and 4 include the axial slope errors which correspond to the Level II requirement and goal on HRMA performance as established by the AXAF project. Case 5 includes $\Delta\Delta R$ errors as discussed above. Case 6 includes circumferential slope errors with values, determined by HDOS metrology, of 6.446 μrad (on P1 after the sixth polishing cycle) and 9.745 μrad (on H1 after the fifth polishing cycle). The final case includes the maximal sag error (value plus quoted error), as known at the time of the test, 1585 Å (P1) and 447 Å (H1). Clearly the dominant mirror effect is the circumferential slope errors, for which metrology of the current optical surfaces (after 7 cycles of polishing) does not yet exist.

Given the large disparity between the predictions of the current raytrace model and the actual FWHM data, we thought that an attempt to determine a set of model parameters which better describe the data was warranted. The strong dependence of the FWHM on the circumferential slope errors, plus the fact of outdated metrology for this error term, suggested that a prudent and reasonable analysis would be to determine the average (*i.e.*, the root-sum-square [RMS] of errors on P1 and H1) circumferential slope error which best fit the data. We did not carry out a fit in the formal sense to the FWHM scan data, but rather searched for that value which gave nearly the same FWHM as measured. Table 2 summarizes the cases run. Note that the slope errors in the table are given as the RSS of P1 and H1. In contrast to the sensitivity study done above, these cases include axial slope errors (Level II requirement), $\Delta\Delta R$ errors, sag, as well as the facility effects. The best fit corresponds to an average slope error of 3.0 μrad per surface.

RSS Error μrad	Y-FWHM (arcsec)	Z-FWHM (arcsec)
0.0	0.209	0.208
4.27	0.223	0.223
5.80	0.234	0.238
8.63	0.285	0.276
11.68	0.326	0.321

Figure 1 shows the comparison with the entire FWHM curve for the best fit circumferential slope errors. Note that a fit was not performed to this curve and only scaling in intensity was done. The agreement with the Y-scan data is remarkable. Differences with the Z-scan data (particularly the intensity jumps near $\pm 50 \mu \approx 1''$) are probably a result of residual gravitational distortions due to the bonded flexure pads which support the optics. At this time, neither the finite element mechanical model nor our raytrace model can faithfully reproduce such high frequency distortions in the optic.

4. WING SCAN

The wing scan data were originally intended to allow estimation of the amount of X-ray flux scattered beyond the largest diameter (20 mm) pinhole available in the VETA-I test and to provide a (hopefully small)

correction to extrapolate to the effective area integrated over the whole focal plane.³ The test procedures called for stepping various size pinholes (from 3 mm diameter to 20 mm diameter) out to large offset angles from the beam center for various X-ray test energies. This data set has proved useful in characterizing the surface roughness of the optic as well as indicating the presence of surface particulate contamination.

Our approach was to assume that the observed surface brightness at large angles was a result of scattering from surface roughness. In this picture an in-surface spatial wavelength $1/f$ diffracts (or scatters) light of a given wavelength λ through an angle θ according to the the grating equation

$$f = \frac{\theta \sin \alpha}{\lambda},$$

with α as the mean grazing angle of the surface (here we use 51.2'). It is possible to relate⁴ the surface brightness $\psi(\theta)$ (at θ normalized to the total power in the focal plane) to the PSD of surface irregularities $W_1(f)$ through

$$2W_1(f) = \frac{f\psi(\theta)\lambda^4}{8\pi(\sin \alpha)^4}.$$

The wing scan data were background subtracted and corrected for possible temporal variations in source intensity by dividing by the counting rate in the normalization detector. We used the wing scan data themselves to estimate the total flux for normalizing $\psi(\theta)$. We assumed azimuthal symmetry (which was an excellent approximation based on a comparison of data taken in the orthogonal Y- and Z-directions) and integrated the flux from the 3 mm diameter pinhole scan out to a radius of 2.036 milliradians (21 mm). This was the only set of data which was available for nearly all the test energies and so this technique was used for consistency. The ψ values also had corrections applied to compensate for the fact that we were sampling a steeply falling surface brightness distribution with a circular pinhole of finite size. In no case was a correction larger than $\sim 10\%$ required. Figure 2 shows the wing scan data plotted in this representation.

Clearly the data in Fig. 2 are inconsistent with our main assumption, *i.e.*, that all the scattering is due to surface roughness, since there is an apparent dependence of roughness with wavelength. For example, the inferred surface roughness from the carbon data alone ($\lambda = 44 \text{ \AA}$) is 40 \AA per surface, while it is 11 \AA per surface from the molybdenum data ($\lambda = 5.3 \text{ \AA}$). This (in addition to other evidence²) suggests the presence of particulate contamination on the mirrors. A simple three parameter model of scattering from dust on the surface has been developed², combined with the surface scattering model, and fit to the data to yield the individual solid curves shown in Fig. 2 for each energy. We used a least-square minimization on the logarithmic data in lieu of a standard χ^2 minimization using purely statistical errors. The fitted parameters of the dust model are consistent with other measurements of the surface contamination.² In Fig. 2 the dashed curve shows the best-fit model for the surface PSD; the numerical values of this fit are $\sigma = 7.3 \pm 0.6 \text{ \AA}$ (per surface) and $p = 1.22 \pm 0.13$ (90% confidence errors for a single parameter).

Figure 4 shows two-dimensional contours for the amplitude and index of the power-law PSD from fits to the wing scan data (the dashed set of contours on the right side). The errors on the data used to produce this figure were estimated from the root-sum-square of the logarithmic residuals from the best-fit model (shown in the bottom panel of Fig. 2).

5. ENCIRCLED ENERGY

The encircled energy data were processed in detail to remove numerous test effects. These included background subtraction, pulse pileup, and deadtime, as well as corrections to remove the known spectral impurity of the incident X-ray spectrum, due mainly to continuum emission from electron bremsstrahlung in the X-ray target.⁵ Additional data reduction was implemented to remove the effects of the wire mesh

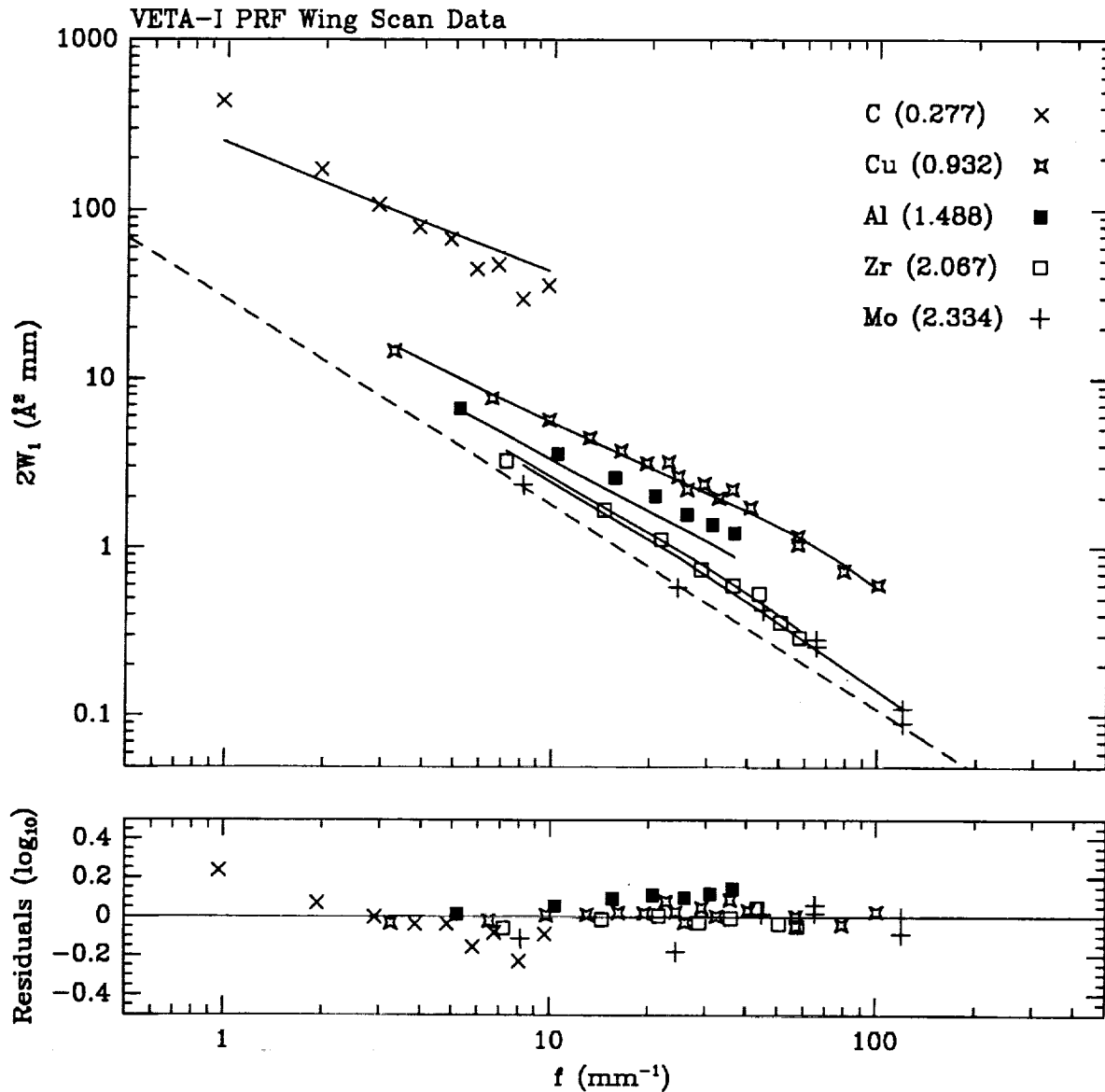


Figure 2 - Large angle scattering (wing scan) data from the five X-ray test energies scaled and plotted in terms of the PSD ($2W_1$) of surface irregularities vs. spatial frequency f . The dashed curve indicates what would be expected if only scattering from a rough surface were involved. The evident differences between the several test energies strongly indicate the presence of particulate contamination on the surface. The individual solid curves show the best-fit model for scattering from both surface roughness and particulate contamination for the various test energies. The lower panel shows the logarithmic residuals between the data and best-fit model.

supporting the thin polypropylene window of the low energy proportional counters used in the test.⁶ These processing steps allowed us to reduce the average fractional error on our encircled energy data from 3.8% to 0.9%.

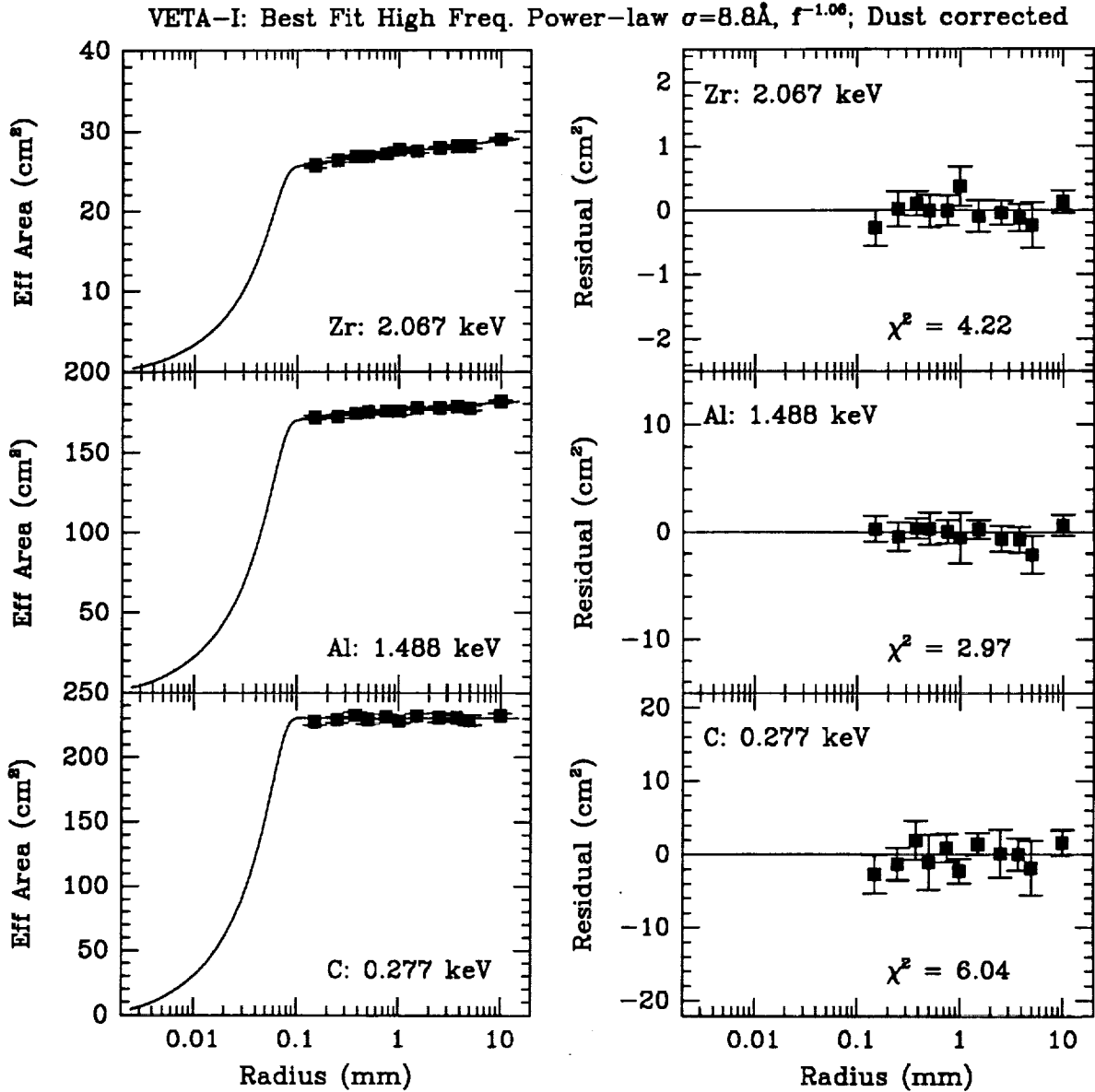


Figure 3 - Encircled energy data for three X-ray test energies. The panels on the left show the data and the best-fit raytrace model; the panels on the right show the residuals.

Figure 3 presents the encircled energy data at three test energies (labelled by the material composition of the anode target) for which it was possible to carry out the complete processing steps outlined above. The data are given in effective area units by referencing the number of X-ray events observed through each pinhole by the focal plane proportional counter to the corresponding number of counts observed in the (nominally identical) normalization proportional counter positioned at the entrance aperture of the VETA-1.

We compare the encircled energy data at three X-ray test energies with our raytrace model. Note that the results in this section include the updated value for the circumferential slope errors of $3.0 \mu\text{rad}$ per

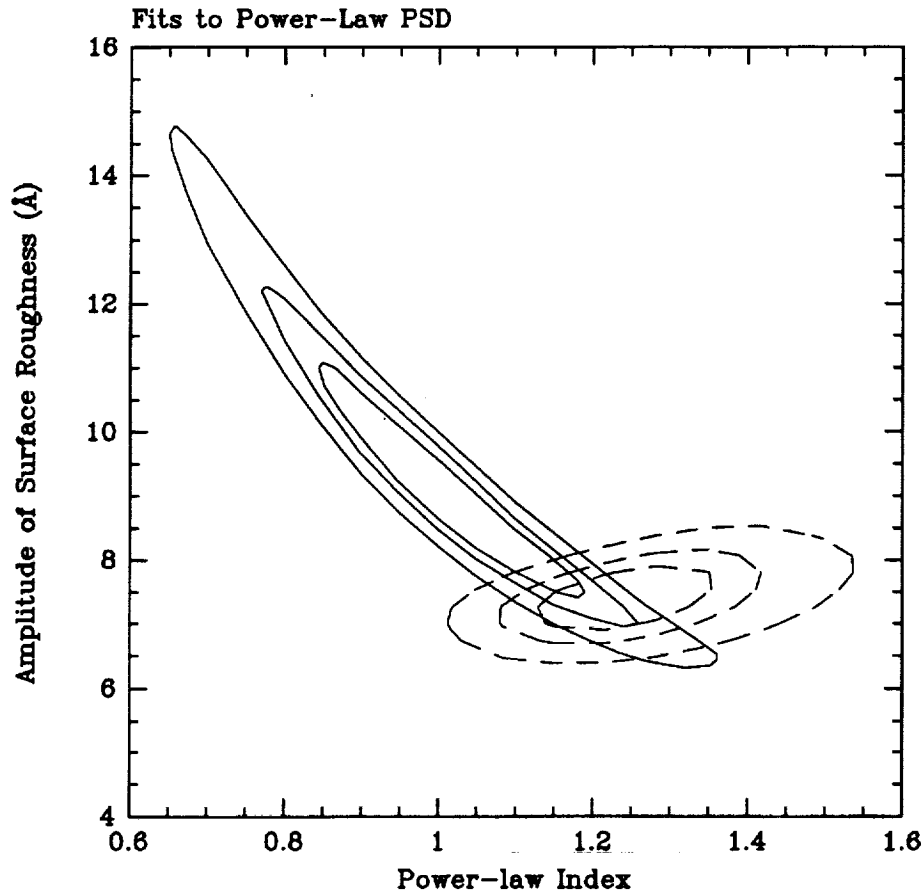


Figure 4 - Contours of constant χ^2 for fits of a power-law PSD for surface roughness to the wing scan data (dashed contours) and encircled energy data (solid contours). We show the 68%, 90%, and 99% confidence levels corresponding to 2 interesting free parameters: the power-law index (abscissa) and the amplitude of surface roughness (ordinate).

surface from the FWHM analysis presented in §3. We also incorporate the best-fit dust scattering model from the wing scan fits discussed in §4. The effect of dust scattering on the EE data is weak: from the smallest pinhole considered (0.3 mm diameter) to the largest (20 mm diameter) there is only a 2% difference in the encircled energy due to scattering from particulate contamination.

Some comments about how the model and data were normalized are needed. At the present time we are not able to accurately estimate the amount of X-ray flux scattered by the mirror beyond the largest pinhole used in these measurements and thus we do not know the total power (or transmitted energy) in the focal plane. As mentioned above, the data are given in effective area units, while the raytrace produces encircled energy models with values between zero and unity. In our model comparisons we scale the model to the data by determining the multiplicative normalization factor which minimizes χ^2 . This is done separately for the data at each X-ray energy. The multiplicative factor is the total effective area (integrated over the focal plane) at that energy.

In order to fit for the parameters of the power-law PSD we generated a large grid of model encircled energy distributions over a range of amplitudes and power-law indices. For each amplitude-index pair, three raytraces were run corresponding to each of the three X-ray test energies. At each point in this two-dimensional parameter space the data and models were compared (for each test energy separately) and a

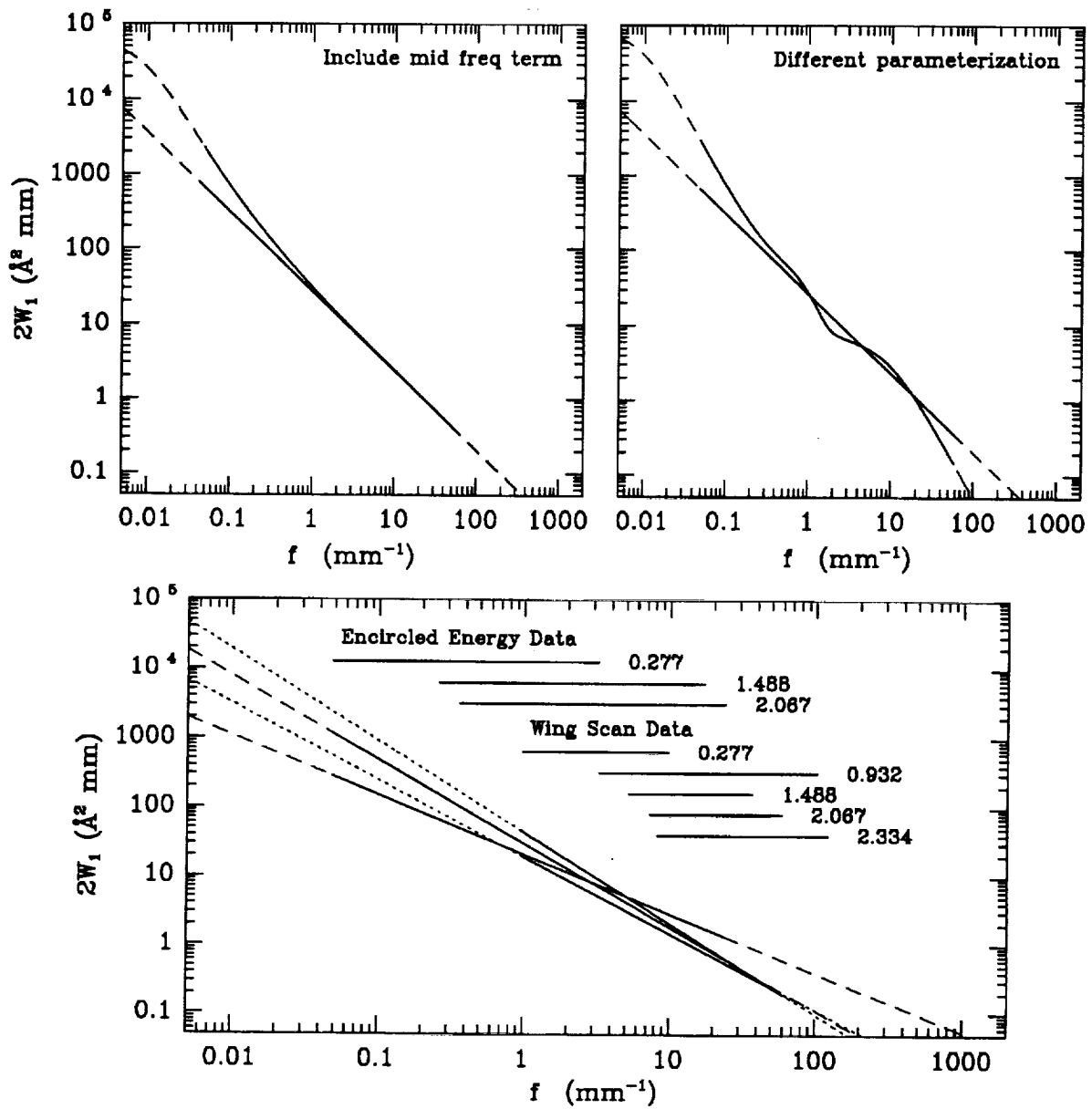


Figure 5 - Estimated PSD of the polished optical surface of the VETA-I based on the X-ray test measurements. The top two panels show two possible variations on the allowed shape of the PSD. The bottom panel shows the allowed range of surface PSD from fits of a pure power-law to the encircled energy and wing scan data. The range in f -values which was sampled by each data set is indicated in this panel. Extrapolations of the PSD beyond these ranges appear as dashed lines.

total χ^2 value for that point was determined. The best fit from these data occurred for $\sigma = 8.8_{-1.4}^{+2.2}$ Å and $p = 1.06_{-0.20}^{+0.15}$ with a grand combined $\chi^2 = 13.2$ for 28 d.o.f. The smooth curves shown in the left panels of Fig. 3 correspond to this best fit and the residuals are in the right panels. The fit for each of the test energies is good, as indicated by the individual χ^2 values labelling the panels.

The two-dimensional χ^2 contours for fits to the encircled energy data are shown in Fig. 4 as the solid contours toward the left side. These are consistent, even at the 68% confidence level, with the wing scan data results.

6. CONCLUSIONS

We have used X-ray measurements of the VETA-I to estimate the surface finish quality of the largest pair of AXAF mirror elements. We find that the narrow FWHM of the PRF requires that the circumferential slope errors be approximately $3.0 \mu\text{rad}$ per surface. Both the wing scan and encircled energy data can be well fit by a PSD for the surface roughness which falls as a power-law in spatial frequency with index 1.2 and amplitude $\sigma \approx 7.5$ Å. The wing scan data also reveal evidence for a significant level of particulate contamination on the VETA-I mirror.

The X-ray data are unable to make strong statements about the actual detailed functional dependence of the surface PSD on spatial frequency. For example the data allow the inclusion of a mid-spatial frequency term (with a correlation length of 18 mm) at a level of about 20 Å, as shown in the top left panel of Fig. 5. An entirely different parameterization of the surface PSD (based on the set of terms used to derive specifications on HRMA performance), also provides an acceptable fit to the X-ray data (see the top right panel of Fig. 5). The lower panel of the same figure shows the range of pure power-law PSD models allowed by the encircled energy data and the wing scan data. Although it is not possible to exclude a single power-law model as a description of the data, there may be some indication of a steepening of the PSD with increasing spatial frequency. We look forward to the final optical metrology data of the VETA-I, which will allow us to investigate these and other models characterizing the surface finish quality of the VETA-I.

This research was supported in part by NASA contract NAS8-36123.

7. REFERENCES

1. P. Zhao, E. M. Kellogg, D. A. Schwartz, M. A. Fulton, and C. Bower, these proceedings, 1992.
2. S. L. O'Dell, R. F. Elsner, J. J. Kolodziejczak, M. C. Weisskopf, J. P. Hughes, and L. Van Speybroeck, these proceedings, 1992.
3. E. M. Kellogg, G. Chartas, J. P. Hughes, L. Van Speybroeck, P. Zhao, M. C. Weisskopf, R. F. Elsner, and S. L. O'Dell, these proceedings, 1992.
4. P. Beckmann, and A. Spizzichino, *The Scattering of Electromagnetic Waves from Rough Surfaces*, (Oxford: Pergamon), 1963.
5. G. Chartas, K. Flanagan, J. P. Hughes, E. M. Kellogg, D. Nguyen, M. Zombeck, M. Joy, and J. Kolodziejczak, these proceedings, 1992.
6. P. Zhao, M. D. Freeman, J. P. Hughes, E. M. Kellogg, D. T. Nguyen, M. Joy, and J. J. Kolodziejczak, these proceedings, 1992.

The X-ray Reflectivity of the AXAF VETA-I Optics

E. Kellogg, G. Chartas, D. Graessle, J. P. Hughes, L. Van Speybroeck, P. Zhao
 Harvard/Smithsonian Center for Astrophysics
 60 Garden Street
 Cambridge, MA 02138

M. C. Weisskopf, R. F. Elsner, S. L. O'Dell
 Space Science Laboratory
 George C. Marshall Space Flight Center
 Huntsville, AL 35812

ABSTRACT

The x-ray reflectivity of the VETA-I optic, the outermost shell of the AXAF x-ray telescope, with a bare Zerodur surface, is measured and compared with theoretical predictions. Measurements made at energies of 0.28, 0.9, 1.5, 2.1, and 2.3 keV are compared with predictions based on ray trace calculations. The data were obtained at the x-ray calibration facility at Marshall Space Flight Center with an electron impact x-ray source located 528 m from the grazing incidence mirror. The source used photoelectric absorption filters to eliminate bremsstrahlung continuum. The mirror has a diameter of 1.2 m and a focal length of 10 m. The incident and reflected x-ray flux are detected using two proportional counters, one located in the incident beam of x-rays at the entrance aperture of the VETA-I, and the other in the focal plane behind an aperture of variable size. Results on the variation of the reflectivity with energy as well as the absolute value of the reflectivity are presented. We also present a synchrotron reflectivity measurement with high energy resolution over the range 0.26 to 1.8 keV on a flat Zerodur sample, done at NSLS. We present evidence for contamination of the flat by a thin layer of carbon on the surface, and the possibility of alteration of the surface composition of the VETA-I mirror perhaps by the polishing technique. The overall agreement between the measured and calculated effective area of VETA-I is between 2.6% and 10%, depending on which model for the surface composition is adopted. Measurements at individual energies deviate from the best-fitting calculation to 0.3 to 0.8%, averaging 0.6% at energies below the high energy cutoff of the mirror reflectivity, and are as high as 20.7% at the cutoff. We also discuss the approach to the final preflight calibration of the full AXAF flight mirror.

1. INTRODUCTION

In the following sections we discuss the techniques we used for the measurement of VETA-I effective area. We also discuss the techniques used for calculation of the predicted effective area from previously existing knowledge of the composition of the reflecting surface material, atomic scattering coefficients, and the geometry of the mirrors. We present a summary of the raytrace calculation procedure, and give the results of the comparison, compared with the data. We also present the results of the synchrotron reflectivity measurement for comparison.

The total effective area is defined in this work as the integral of the point response function (PRF) over the back hemi-

sphere of solid angle behind the optics. For observations with the AXAF observatory, one could consider whether this is really a useful quantity. It is of interest when comparing total reflected power with that predicted from scattering theory, but the scattering theory uses scattering coefficients obtained from experiments that are difficult to do precisely. Experimental measurements of reflection are very difficult to do out to scattering angles of $\pi/2$ because the flux density is so low at large angles, and the geometry of the optics prevents rays scattered at angles larger than about one degree from reaching the focal plane. Other measurements, such as total absorption, are also difficult. In this paper, we report estimates of the total effective area to $\pi/2$ based on extrapolation of measurements taken out to angles up to 17.5 arcmin, at which point the flux density is less than 10^{-10} of its peak central value.

2. MEASUREMENT TECHNIQUE

The general aspects of the VETA-I test are described by Kellogg et al¹. The measurement technique uses photometric x-ray detectors² with a series of circular mechanical apertures of increasing diameter centered on the peak of the PRF to define the geometric flux collecting area. The size of each aperture corresponds to an angle from the center of the point response function, out to which all flux is integrated. The largest aperture used was 20 mm diameter, which corresponds to 3.3 arcmin radius. At larger angles, the aperture was moved off-center from the PRF peak to measure the flux outside the maximum centered angle. These were known as wing scans.

The x-ray source is described in Chartas et al² and Zhao et al³. The targets used and resulting characteristic line energies are given in Table 1. The dominant line is α_1 in Siegbahn notation which corresponds to either the transition KL_{III} or $L_{III}M_V$.

The technique of Chartas et al² is used to define the x-ray energy. The contribution to the reflected flux from the VETA-I optic due to continuum from the x-ray source is subtracted, using a model of the mirror reflectivity vs. energy. What remains after the subtraction is the contribution from the characteristic line(s).

The apertures used are nominally circular with diameters ranging from 0.005 to 20 mm. The actual sizes and shapes deviate from ideal circles, so this effect must be taken into account. The details of these size and shape measurements are

described by Podgorski et al⁴.

Table 1: X-ray targets and Energies

Element	Z	Shell	Dominant Line Energy, keV	Mean Line Energy, keV
C	6	K	0.277	0.277
Cu	29	L	0.9297	0.932
Al	13	K	1.4867	1.488
Zr	40	L	2.04236	2.067
Mo	42	L	2.29316	2.334

A number of runs were carried out with the same x-ray target at different electron currents in order to determine the sensitivity of the results to the intensity of the X-ray beam. The error from such an effect was found to be much smaller than other errors.

Absolute normalization of the effective area was determined by taking the ratio of the flux in the x-ray line in the XDA detector to the flux in the x-ray line in the BND detector and multiplying by the open area of the BND detector, a 20 mm diameter aperture whose area was measured to be $100\pi = 314.16 \pm 0.08 \text{ mm}^2$ ($\pm 0.025\%$).⁴ That error is negligible in comparison with others, and so is ignored in the error analysis.

3. CALCULATION OF TOTAL REFLECTED ENERGY

We define the effective area as the integral of the PRF with the energy spectrum of the x-ray source, and the integral over angles with respect to the incident beam direction $0 < \theta < \pi/2$ and $0 < \phi < 2\pi$, polar and azimuthal angles, respectively. In this paper, we assume the PRF not to be a function of ϕ . We also assume that the PRF is composed of two functions of θ , a core $f_c(\theta)$ and a wing. We find that to a sufficient approximation⁵, the wing has a power law distribution $f_w(\theta) = K\theta^{-\alpha}$. The functional form of the PRF at large angles is obtained from a fit to the wing scan data, such as from Figure 1. Therefore, the integral of the PRF, or the Effective Area out to $\pi/2$ is

$$\text{EffectiveArea} = \text{Core}(\theta_2) + \text{Wing}(\theta_1)$$

$$= \int_0^{\theta_2} f_c(\theta) \theta d\Omega + \int_{\theta_1}^{\pi/2} (K\theta^{-\alpha}) d\Omega \quad \text{where } \theta_1 \text{ is the angle at}$$

which the contribution of the wing to the PRF is very small compared with the core and θ_2 is the angle at which the contribution of the core is very small compared to the wing.

The wing is then

$$\begin{aligned} \text{Wing}(\theta_1) &= \int_0^{2\pi} \int_{\theta_1}^{\pi/2} K\theta^{-\alpha} \sin\theta d\theta d\phi \\ &= 2\pi K \int_{\theta_1}^{\pi/2} \theta^{-\alpha} \sin\theta d\theta \end{aligned}$$

In Figure 1, we show the PRF of the VETA-I mirror at Al-K, 1.49 keV. The data at angles from 4.7×10^{-6} to 9×10^{-4}

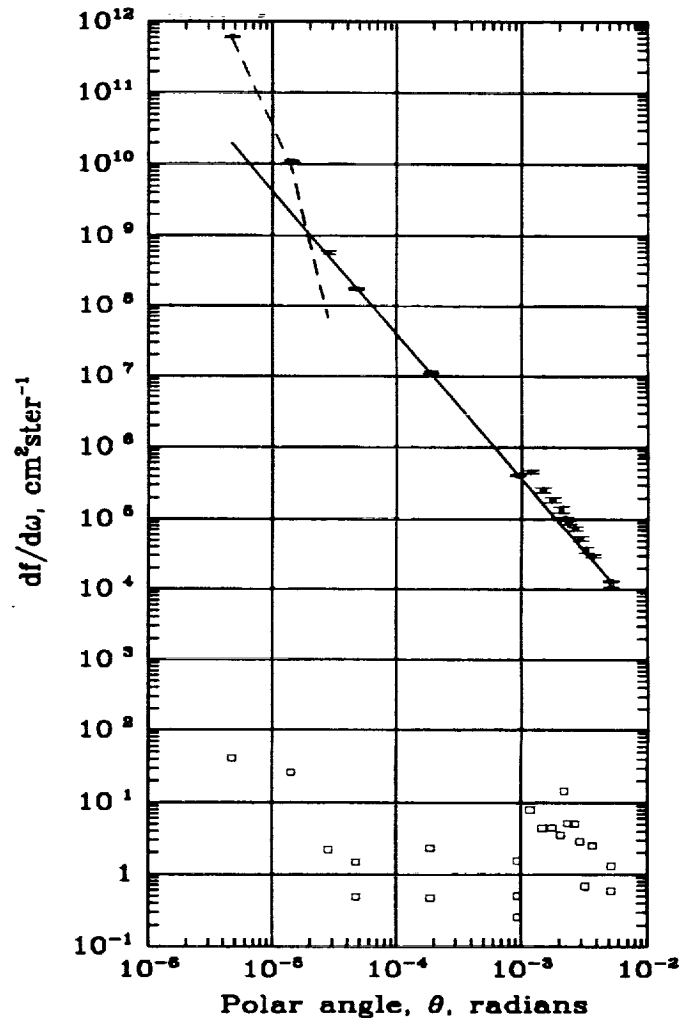


Figure 1. PRF of VETA-I at 1.49 keV. The open circles are the measured PRF, with 1σ error bars. The open squares are the deviations of the PRF from the power law fit to the wings of the PRF, which is the line of constant slope. The dashed line is the core PRF with the wing fit subtracted.

rad were taken using annular apertures consisting of an open annulus of a circle cut in solid metal, with four spokes to support the central opaque circle. The annulus has an inner diameter 0.9 of its outer diameter. The spokes obscure 10% of the

annulus at angles of 45° with the horizontal and vertical axes. At larger angles out to 5.2×10^{-3} rad, circular pinhole apertures offset from the center of the PRF were used. In Figure 1 a power law fit to the data at large angles is shown. The slope of the function with θ is given in Table 2. The equation fitted is $\log PRF = -\alpha \log \theta + \log b$. That component was subtracted from the PRF measured at the three smaller angles, resulting in the steeply rising curve in Figure 1 at small angles. The fit to the data was done only to the annuli data, since the pinholes must be corrected by a factor that depends on the ratio of their distance off axis to their size, and on the power law slope. The pinhole points lie above the curve, but approach it at larger angles, as the correction becomes smaller.

Therefore, we see that

- the PRF contains an outer component that is reasonably well represented by a power law
- the transition to the steeper inner component occurs at angles less than 10^{-4} rad.

As a result, it appears reasonable to use the power law to estimate the flux contained in the portion of the PRF outside the 20 mm pinhole (which subtends a half-angle of 9.8×10^{-4} rad).

The results of the wingscans at the other four energies are shown in Figure 2. The parameters of the logarithmic fits to the outer part of the PRF are also listed in Table 2. The slopes in

Table 2: Power Law Fits to the Outer Wings of the PRF

Line	Energy keV	α	$\log b$	Reduced χ^2
CK	0.277	2.381 ± 0.007	-1.904 ± 0.025	13.9
Cu L	0.930	2.004 ± 0.011	-0.488 ± 0.034	3.2
Al K	1.49	2.028 ± 0.007	-0.522 ± 0.023	4.3
Zr L	2.06	2.074 ± 0.046	-1.24 ± 0.16	1.4
Mo L	2.29	1.643 ± 0.075	-0.578 ± 0.215	4.6

Table 2 for the three middle energies, 0.93, 1.49 and 2.06 keV, are not significantly different, but the slope at 0.277 keV is significantly steeper, and the slope at 2.29 keV appears to be flatter, although it is based on only four data points. The slope is a result of the size distribution of features in the microroughness of the surface, as well as of any possible dust contamination that lies on the surface. This result suggests that some information about the size distributions may ultimately be obtained from the wing scans.

The large values of reduced χ^2 for the power law fits may come from a lack of azimuthal symmetry in the wings of the PRF, or because the model chosen doesn't fit the data well enough. For the Cu-L data, we did fits to the wing scans at four azimuths corresponding to scans in the vertical and horizontal directions, and the slopes were the same within error, but the normalizations differed by almost a factor of two. We attempted to improve the Al fit by averaging over azimuth

before fitting, but no significant improvement resulted.

We note that the fractional power in the wings increases with energy, as expected from scattering.

4. CHARACTERISTICS OF ZERODUR: COMPOSITION

In order to compare the measured effective area with that expected, we calculate the effective area from tabulated atomic scattering factors. Such a calculation can only be done if the composition of the reflecting surface is known. We initially assumed that the surface has the same composition as the bulk material. The Zerodur used to construct the AXAF mirrors was supplied by Schott. The composition is given in Table 3, in descending order of abundance⁶.

Table 3: Composition of AXAF Zerodur Mirrors

Compound	Fraction by weight	Compound	Fraction by weight
SiO ₂	0.555	ZrO ₂	0.019
Al ₂ O ₃	0.253	ZnO	0.014
P ₂ O ₅	0.079	MgO	0.010
Li ₂ O	0.037	Na ₂ O	0.005
TiO ₂	0.023	As ₂ O ₃	0.005

5. RAY TRACE CALCULATIONS

The effective area of the VETA-I was calculated using the OSAC raytrace code⁷. It was assumed that the optical elements were perfectly aligned, the despace was 109.03 mm and the X-ray source was on-axis. The actual finite source distance of 518160 mm (1730 ft.) was used. The reflectivity of Zerodur was calculated using the Henke et al⁸ optical constants for the mixture shown in Table 3 with a bulk density value of 2.53 g cm^{-3} .

There are stops along the optic axis defining the axial extent of the reflecting surfaces. The stops are: the apodizer located at the back of the P1, the mid-plane aperture plate, and the apodizer located at the back of the H1. However, due to the finite source distance and despace of the P1 and H1, only about 60% of the nominal flight length of the P1 optic was exposed, so the mechanical stops were not significant.

The figure of each optic was assumed to be a perfect conic section with the as-designed conic parameters. The large scale figure errors, either due to fabrication or to gravitational or thermal distortions, do not have any significant effect on calculations of total reflectivity in 2π ster, since they only redistribute power in the core of the PRF. Small scale microroughness and dust on the surface can have a significant effect, however.

Because of the assumptions of perfect alignment, an on-axis source position, and no distortion, and because we did not

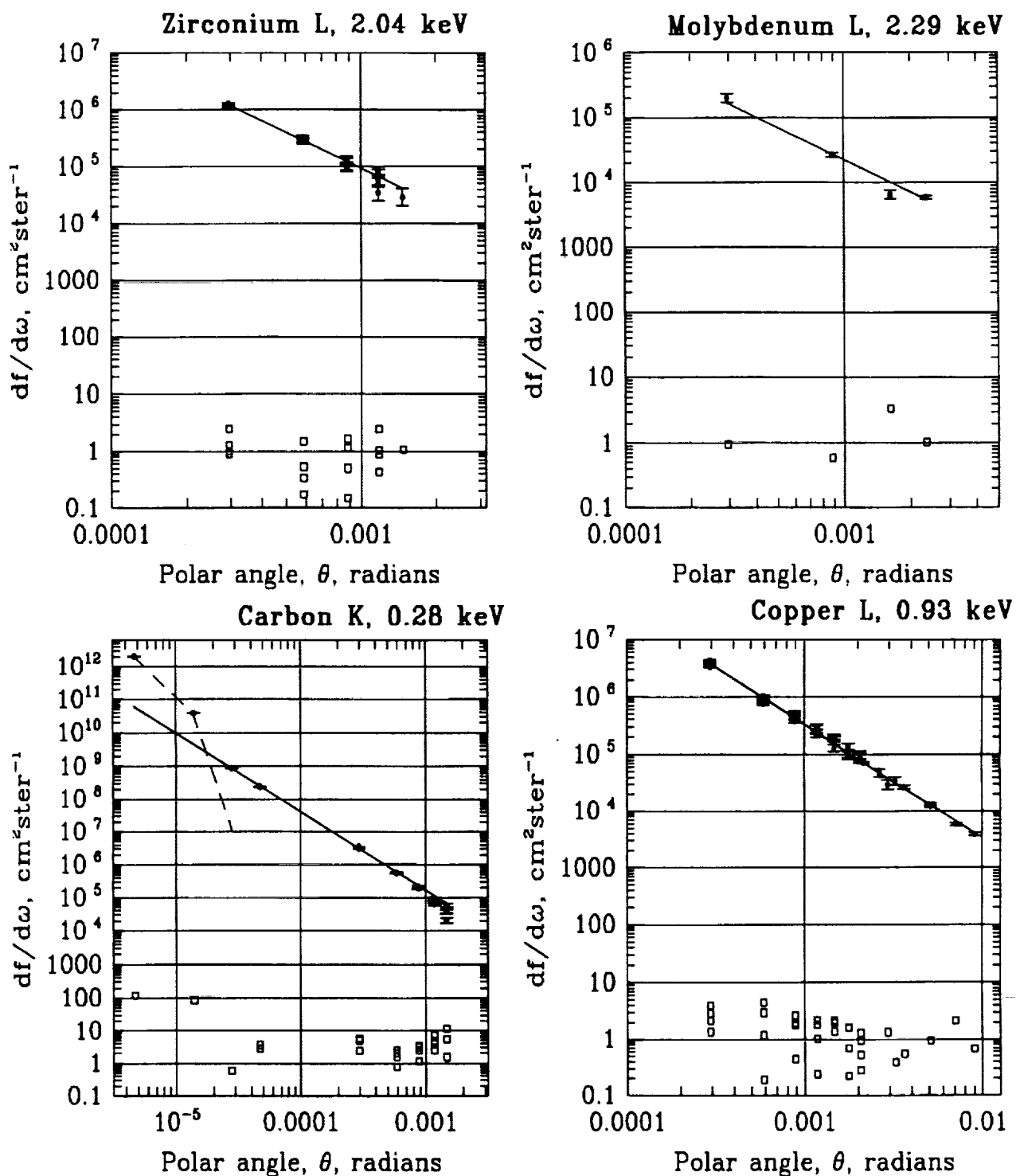


Figure 2. PRF of VETA-I at the four remaining energies. The circles are the measured PRF, with 1σ error bars. The open squares are the deviations of the PRF from the power law fit to the wings of the PRF, which is the line of constant slope. The dashed line for carbon-K is the core PRF with the wing fit subtracted.

do a detailed model of the azimuthal dependence of the obscuration by the support struts, the raytrace had rotational symmetry about the optical axis. Consequently it was possible to reduce the integration over the entrance pupil of the telescope to a one dimensional radial integration. This was implemented by placing 2000 rays at a single angular position over an annular entrance pupil. The emerging rays were collected in a ray file, which was then filtered at the focal plane to determine which ones passed through a specified pinhole aperture, to determine the fraction that were transmitted.

We quote the total effective area over 2π ster, that is, integrated over the entire focal plane. Obscuration due to the four mirror support struts (which were 76.2 mm thick) reduced the calculated area by 8%. The results showed some dependence of the flux in the wings on azimuth which may be due to the struts.

6. ATOMIC SCATTERING FACTORS

The x-ray reflection coefficients were calculated using the most recent Henke et al atomic scattering factors⁸, which are obtained by fitting a large quantity of experimental data. The factors are given as values of f_1 and f_2 from 10 to 30000 eV in logarithmic intervals, and represent the best available basis for comparison with previous measurements. Expressions for reflection from scattering coefficients are given in the original Henke et al⁹ paper.

7. RESULTS

Figure 3 shows the effective area of the VETA-I, calcu-

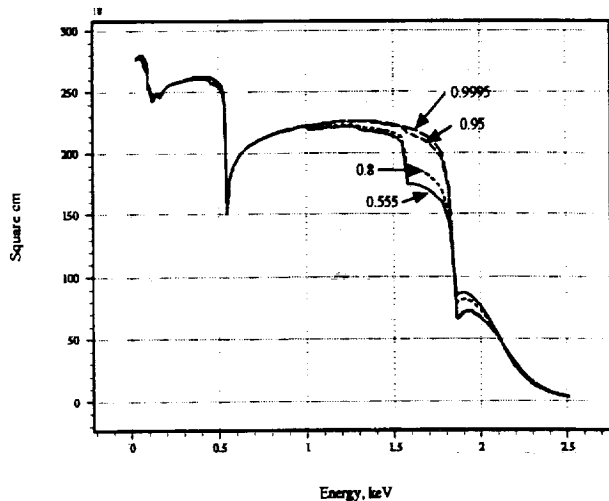


Figure 3. Calculated effective area of VETA-I for four different compositions. The labels indicate the fractional composition of SiO_2 . The nominal composition for Zerodur is 0.555.

lated using the methods described above, for several variations on the composition of the glass. These results were then compared with the measured effective area to see which composition would give the best fit to the measurements. The structure in the calculated curve due to edges of oxygen (532 eV), aluminum (1560 eV) and silicon (1840 eV), which are the main

constituents of Zerodur, is readily apparent.

The comparison between calculated and measured effective area is shown in Figure 4. The calculated curves were normalized to the measured points by minimizing χ^2 . The calculated area was multiplied by 0.974 for the pure SiO_2 , and 1.10 for Zerodur to obtain the minimum χ^2 . Thus, there is a slight preference for the surface composition of the glass being pure SiO_2 , rather than Zerodur, based on the better χ^2 (20 for 4 d.o.f. vs. 51 for Zerodur) and normalization.

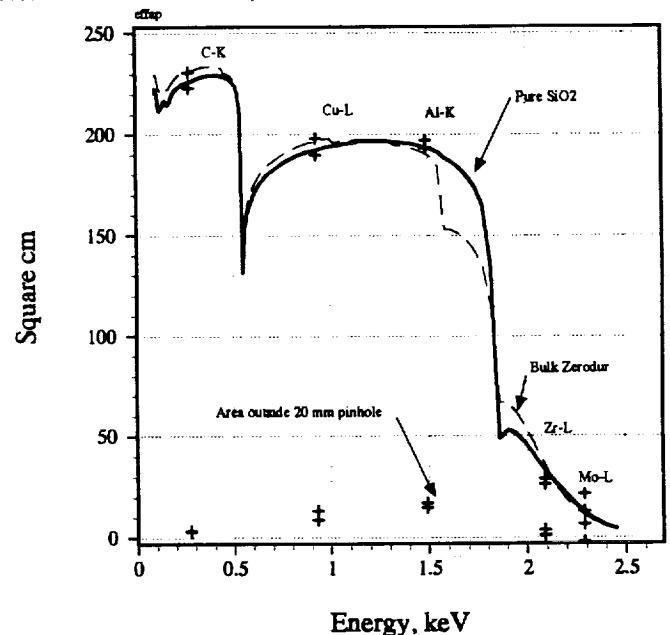


Figure 4. Calculated and measured effective area of VETA-I. The crosses are the measured results, giving the upper and lower limits of the estimated 1σ errors. In addition to the total effective area, the area outside the 20 mm pinhole, or 1 mrad angle, is plotted, which shows that the wings of the PRF are more important at higher energy.

A similar plot of the calculated effective area compared with the measured data is shown in Figure 5, for the case of Zerodur with a range of thicknesses of carbon from 0 to 80 Å. The measured effective area at 0.277 keV agrees best with the curve for no carbon layer.

8. SYNCHROTRON REFLECTIVITY MEASUREMENTS

The x-ray reflectivity of a flat polished sample (P1-1) of the VETA-I P1 paraboloid section material was measured at the NSLS, using techniques described by Graessle et al¹⁰. Figure 6 shows the results, compared with a calculation based on the Henke tables⁸. Obvious absorption features are present from carbon (284 eV), oxygen (532 eV), and aluminum (1560 eV). Incidentally, it is not surprising that the oxygen feature is much deeper than the Henke prediction; the latter are based on sparse data near edges. It should be noted that Figure 6 gives the reflectivity for *single* reflections from a *flat* mirror,

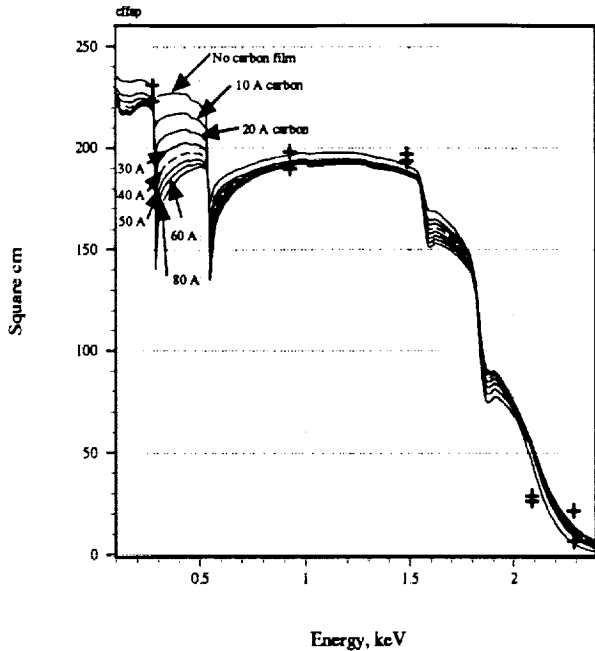


Figure 5. Calculated and measured effective area of VETA-I compared with calculations for Zerodur plus a thin film of hydrocarbon. A mean grazing angle approximation was used in this calculation.

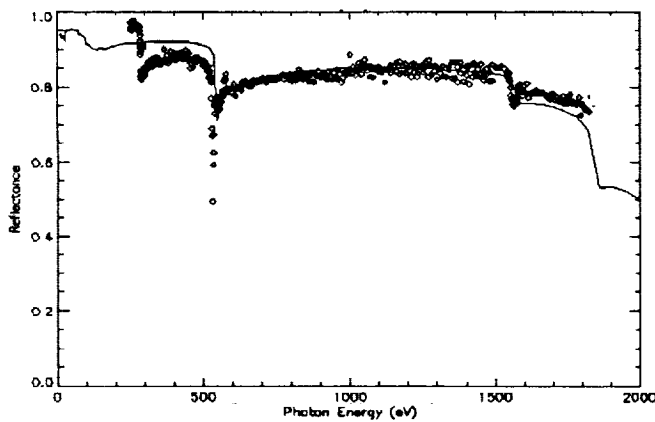


Figure 6. Reflectivity of P1-1 Zerodur sample flat, at an incident angle of 51.2 arcmin.

whereas the results in Figure 3, Figure 4 and Figure 5 are for double reflections from the VETA-I optic; while the same features are expected in both cases, their depth and gross energy dependences will differ.

There is a striking indication of the presence of carbon on the surface of the flat P1-1 sample, seen as the increase of reflectivity at energy below 284 eV, and the decrease above that energy, compared to the prediction for bare Zerodur.

9. DISCUSSION

9.1. Carbon contamination

The raytrace calculations for both Zerodur and pure SiO_2 are in good agreement with the measured effective area at 277 eV. We cannot yet make a statement with much certainty about the existence of hydrocarbon on the VETA-I, since the calculations we have done so far (see Figure 5) were only done with a mean grazing angle approximation, not a full raytrace. Also, It would be much better to have reflectivity measurements at energies just above and below the carbon edge to make the result less ambiguous.

For the flat, there is prima facie evidence for a carbon film. Therefore we conclude that the flat measured at the synchrotron was contaminated by carbon, and the VETA-I optic was probably not.

It is not surprising that the surface of the synchrotron test flat was contaminated by carbon, since no special prevention measures were taken. The VETA-I optic was, however, prepared under somewhat more stringent conditions, so it is again not surprising that the VETA-I shows no obvious contamination from a carbon film.

Carbon contamination will be important for AXAF operation in orbit, because such a film could be deposited at any time. If it happens before the final metal coating, it may interfere with proper adhesion at the least. If it happens after metal coating, the energy dependence of the PRF will be affected at the 5 - 10% level, much greater than our goal of 1-2% for knowledge of the PRF.

9.2. Possibility of changes in surface composition due to polishing

The formal χ^2 analysis supports the notion of a pure SiO_2 surface, although we recognize that there are difficulties with interpreting the data, especially in estimating the total power outside the 20 mm diameter apertures. There is room for a more sophisticated analysis in the future that may give a less ambiguous interpretation.

The better agreement between the prediction for pure SiO_2 and the VETA-I measured reflectivity vs. energy could be due to a change of surface composition during polishing at HDOS, causing the enhancement of SiO_2 . On the other hand, the synchrotron data from the flat show clear evidence for the Al edge at 1560 eV, so the polishing done at Marshall Space Flight Center did not affect the composition. The present VETA-I data and analysis are not sufficient to allow firm conclusions to be drawn.

Changes in surface composition of the Zerodur may not be significant for the AXAF flight mirrors. They will be coated with a high density metal film to improve their x-ray reflectivity, which will not be significantly affected by the composition of the underlying Zerodur.

9.3. Absolute normalization

We have very little information on the error in our knowledge of the absolute geometric area. Two possible contributors are centering errors and errors in placement of apodizers.

The normalization factor needed to minimize χ^2 for the fit in Figure 4 is 0.974 for pure SiO_2 , and 1.10 for Zerodur, which

gives us an overall agreement in the product of geometric area and reflectivity of 2.6% and 10% respectively. We would like to believe the better agreeing number, and that this shows the geometric errors to be negligible, but of course, even if the better number is true, there could always be a fortuitous cancelling of geometric errors and overall reflectivity calculation errors. For the final flight calibration of AXAF, it will be important to devise a way to estimate these geometric errors, and include them in our analysis.

9.4. Implications for final AXAF preflight calibration

The value of χ^2 for the best fit to the measured effective area, 20 for 4 d.o.f., is still not formally acceptable, so there is evidence for some remaining problem, which could be due to unknown errors in the measurement process, or in the calculations.

There is a great deal of structure expected in the reflectivity curve between 1800 and 2200 eV. If we had measured reflectivity of flats polished in the identical manner to the VETA-I using the synchrotron over that energy range, we probably could have resolved the composition issue. We may be able to do this on a Zerodur sample when the VETA-I is disassembled and cut to the proper length for the flight AXAF optics.

In Table 4, we show the deviations between the measured values of the VETA-I effective area from Figure 4 and the best fit calculation at each of the energies. The average value of the deviations from the full area is 1.2%, which is one measure of how accurately we have done the measurement. Another measure is the normalization factor, which gives us an overall agreement in the product of geometric area and reflectivity of 2.6% for our best fit composition of pure SiO₂. Therefore, we might surmise that in orbital operation (assuming we make no improvement in our measuring techniques prior to the final flight calibration planned for 1995-96), AXAF could make measurements of absolute flux over a broad spectral band to ~1%, but in a pessimistic view, might be in error as much as 10% of the geometric area overall. At higher energies, where the reflectivity cuts off and the effective area is much smaller, the errors could be larger, as high as ~20%, as shown in the fourth column of Table 4.

Careful analysis of the calibration data and comparison with complete synchrotron reflectivity energy scans taken on faithful witness flats may reduce the errors at selected energies by allowing us to weight the individual measurements appropriately. For the final calibration, we are also planning to use

Table 4: Effective Area Deviation vs. Energy

Energy keV	Line	Deviation from Measured Value to Best Fit,	
		normalized to full area at 0.277 keV	normalized to area at each energy
0.277	C-K	0.3%	0.3%

Table 4: Effective Area Deviation vs. Energy

Energy keV	Line	Deviation from Measured Value to Best Fit,	
		normalized to full area at 0.277 keV	normalized to area at each energy
0.93	Cu-L	0.7%	0.8%
1.49	Al-K	0.6%	0.7%
2.09	Zr-L	2.5%	20.7%
2.29	Mo-L	0.6%	8%

detectors with considerably better energy resolution, eliminating errors due to contamination from continuum in the spectrum of the x-ray beam used at the calibration facility. The single worst disagreeing measured data point was at 2.09 keV, Zr-L. We know that this measurement suffered from by far the highest contamination by bremsstrahlung continuum, about 33%, compared to values as low as about 8% at other energies.

We also plan to characterize the nature of the x-ray beam's spectrum much more carefully using high resolution spectrometers. We believe all three of these improvements are necessary to achieve the desired accuracy of effective area calibration, even up to the high energy cutoff of the mirror.

10. ACKNOWLEDGMENTS

There were many people at SAO, NASA, Hughes Danbury Optical Systems, TRW and Eastman Kodak who made this measurement possible. A few that we worked closely with and have not been recognized elsewhere are John Cobuzzi, Kathy Flanagan, John McDougal, John Roll, Dave Watson, and Marty Zombeck.

This work was partially supported under NASA Contract # NAS8-36123.

11. REFERENCES

1. E. Kellogg, R. Brissenden, K. Flanagan, M. Freeman, J. Hughes, M. Jones, M. Ljungberg, P. McKinnon, W. Podgorski, D. Schwartz, and M. Zombeck, "Calibration of the Verification Engineering Test Article-I (VETA-I) for AXAF using the VETA-I X-ray Detection System," *Proc. SPIE*, vol. 1546, pp.2-12, 1992.
2. G. Chartas, J. P. Hughes, E. M. Kellogg, M.V. Zombeck, M. K. Joy, J.J. Kolodziejczak, "Correcting x-ray spectra obtained from the AXAF VETA-I mirror calibration for pileup, continuum, background, and deadtime," *Proc. SPIE*, paper 1742-07, July 1992.

3. P. Zhao, E.M. Kellogg, D.A. Schwartz, M.A. Fulton, C.R. Bower, "Intensity distribution of the x-ray generator for the VETA-I test," *Proc. SPIE*, paper 1742-03, July 1992.
4. W.A. Podgorski, K.A. Flanagan, M.D. Freeman, E.M. Kellogg, T. Norton, P. Ouellette, A.G. Roy, D.A. Schwartz, "VETA-I x-ray detection system," *Proc. SPIE*, paper 1742-05, July 1992.
5. J. P. Hughes, D.A. Schwartz, A. Szentgyorgyi, L.P. Van Speybroeck, P. Zhao, "X-ray performance of the outer AXAF mirror pair based on measurements of the VETA-I," *Proc. SPIE*, paper 1742-11, July 1992.
6. German patent Jurgen Petzoldt D1902432.
7. Optical Surface Analysis Code (OSAC). 1982. Perkin-Elmer Optical Technology Division, Danbury, CT.
8. B. L. Henke, E. M. Gullikson and J. C. Davis, Atomic Data and Nuclear Data Tables (to be published).
9. Henke, B.L., Lee, P., Tanaka, T.J., Shimabukuro, R.L., and Fujikawa, B.K. 1982, Atomic Data and Nuclear Data Tables 27, 1-144. Academic Press.
10. D.E. Graessle, J.C. Cobuzzi, E.M. Kellogg, D.A. Schwartz, R.L. Blake, P.P. Gong, "Reflectance calibrations of AXAF mirror samples at absorption edges using synchrotron radiation," *SPIE*, paper 1742-16, July 1992.